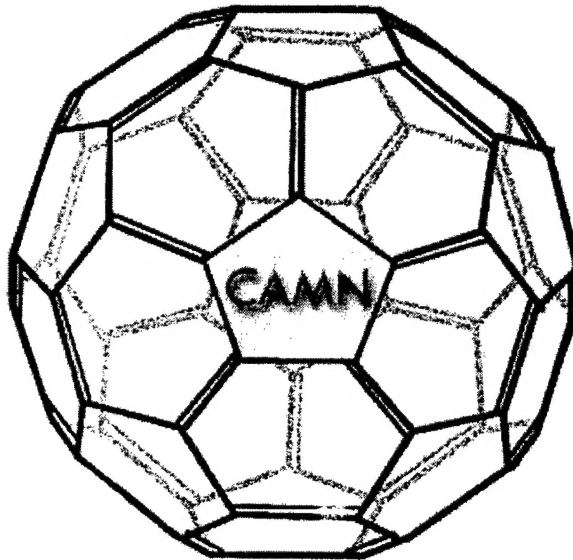


RECEIVED DEC 2 1 2004



## **FINAL REPORT**

### **Tailoring of Grain Boundary Chemistry to Produce Super Creep-Resistant Alumina**

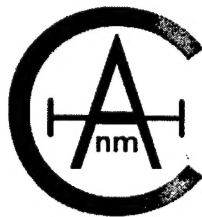
**Professors M.P. Harmer (PI), H. M.Chan (Co-PI), J.M. Rickman (Co-PI)**  
**Research Assistants M. Drahos and K. Bedu-Amissah**

**Sponsored by**  
**Air Force Office of Scientific Research (AFOSR)**

**Contract Number: F49620-01-1-0184, Mod. P00004**

**Report Period: 1 April 2001 – 30 September 2004**

**AFOSR Program Manager: Dr. Joan Fuller**



**CENTER FOR  
ADVANCED MATERIALS  
AND NANOTECHNOLOGY**

**DISTRIBUTION STATEMENT A**  
Approved for Public Release  
Distribution Unlimited

**20050125 144**

## Abstract

The Lehigh group has performed experimental and computational studies to determine the impact of dopants, especially rare earth elements, on the high temperature transport properties (including creep and densification) of alumina. We discovered, along with other groups, that the addition of trace amounts ( $< 1000$  ppm) of rare earth dopants, such as yttrium, lanthanum and neodymium, to fine-grained alumina (i.e., 1-3 micron grain size) reduces the creep rate by several orders of magnitude. The consensus emerging from this work is that these dopants segregate to grain boundaries due to a mismatch in ionic size and hinder diffusional transport and thereby Coble creep. Further investigation suggests that the observed behavior is associated with a solid solution effect. Complementary simulational work employing atomistic models confirms the propensity for dopant segregation and the increase in activation barriers for boundary diffusion that attend segregation. Furthermore, microstructural models reflect the interplay among transport and mechanical properties during creep. Finally, from our results, we have developed several doping strategies (i.e., selective codoping) to enhance creep resistance.

## REPORT DOCUMENTATION PAGE

AFRL-SR-AR-TR-05-

The public reporting burden for this collection of information is estimated to average 1 hour per response, including gathering and maintaining the data needed, and completing and reviewing the collection of information. Send comments, including suggestions for reducing the burden, to the Department of Defense, Executive Services at that notwithstanding any other provision of law, no person shall be subject to any penalty for failing to comply with a collection of information if it does not have a control number.

urces,  
tion of  
aware  
d OMB

PLEASE DO NOT RETURN YOUR FORM TO THE ABOVE ORGANIZATION.

1. REPORT DATE (DD-MM-YYYY) December 12, 2004		2. REPORT TYPE Final Report		3. DATES COVERED (From - To) April 1, 2001 - September 30, 2004	
4. TITLE AND SUBTITLE  Tailoring of grain Boundary Chemistry to Produce Super Creep-Resistant Alumina				5a. CONTRACT NUMBER F49620-01-1-0184, Mod. P00004	
				5b. GRANT NUMBER	
				5c. PROGRAM ELEMENT NUMBER	
6. AUTHOR(S)  Harmer, Martin P. Chan, Helen M. Rickman, Jeffrey M.				5d. PROJECT NUMBER	
				5e. TASK NUMBER	
				5f. WORK UNIT NUMBER	
7. PERFORMING ORGANIZATION NAME(S) AND ADDRESS(ES) Center for Advanced Materials and Nanotechnology Lehigh University 5 East Packer Avenue Bethlehem PA 18015				8. PERFORMING ORGANIZATION REPORT NUMBER  533054	
9. SPONSORING/MONITORING AGENCY NAME(S) AND ADDRESS(ES) Dr. Joan Fuller Air Force Office of Scientific Research 4015 Wilson Boulevard, Room 713 Arlington VA 22203-1954				10. SPONSOR/MONITOR'S ACRONYM(S)	
				11. SPONSOR/MONITOR'S REPORT NUMBER(S)	
12. DISTRIBUTION/AVAILABILITY STATEMENT  Distribution Statement A: Approved for public release. Distribution unlimited.					
13. SUPPLEMENTARY NOTES					
14. ABSTRACT  See attached.					
15. SUBJECT TERMS Alumina, Grain Boundary					
16. SECURITY CLASSIFICATION OF:			17. LIMITATION OF ABSTRACT	18. NUMBER OF PAGES	19a. NAME OF RESPONSIBLE PERSON
a. REPORT	b. ABSTRACT	c. THIS PAGE			Martin P. Harmer
U	U	U	SAR	98	19b. TELEPHONE NUMBER (Include area code) (610) 758-4227

## **TABLE OF CONTENTS**

- 1. Current Technical Report**
- 2. Publications, Reports and Presentations**
- 3. Awards, Honors and Patents**
- 4. Personnel**



## **1. CURRENT TECHNICAL REPORT**

## Final Report

### Tailoring of Grain Boundary Chemistry for the Development of Super Creep-Resistant Ceramic Oxides

The Lehigh group has performed an extensive series of experimental and computational studies to elucidate the impact of dopants, especially rare earth elements, on the high temperature transport properties (including creep and densification) of alumina. The results obtained in the program have been reported in numerous archival publications and presented in invited talks in various symposia. In this final report, we summarize some of our key findings, highlighting the novel and most significant aspects of our work.

#### I. Experimental Findings

In general, we discovered, along with other groups [1-3], that the addition of trace amounts ( $< 1000$  ppm) of rare earth dopants, such as yttrium, lanthanum and neodymium, to fine-grained alumina (i.e., 1-3 micron grain size) reduces the creep rate by several orders of magnitude. The suppression in the creep rate is also accompanied by an almost doubling of the activation energy from approximately 450 kJ/mol to 800 kJ/mol. The dopant influence is the same for concentration levels both above and below the solubility limit, confirming that the phenomenon is a solid solution effect. Many of our measurements are summarized below in Fig. 1. The importance of this work is reflected in both resulting commercial applications, such as creep resistant fibers fabricated by 3M Corporation based upon our doping strategy [4], and the interest of researchers in allied fields, such as those working to improve oxidation resistance in superalloys.

While there is still considerable debate as to the mechanisms underlying enhanced creep resistance in doped alumina, a consensus on several points has emerged from our work. For example, there is general agreement that the aforementioned rare earth elements segregate strongly to the grain boundaries in alumina due to their relatively large ionic size. This propensity for segregation has been quantified by us using a variety of analytical methods, including scanning transmission electron microscopy [5], extended x-ray absorption fine structure [6,7] and scanning ion mass spectroscopy [8].

Given the propensity for grain boundary segregation and the associated local atomic distortion in the grain boundary region, we and other researchers have maintained that the primary mechanism for creep retardation in alumina is the interference (blocking) with critical diffusional pathways at the grain boundaries. This admittedly oversimplified notion has guided us to develop co-

doping strategies for further increasing the creep resistance of alumina; specifically, simultaneous incorporation of ions of different size was carried out in order to block the grain boundary sites more effectively. This strategy has led to the development of the most creep resistant alumina composition to date [9]. Results such as these that make us optimistic about being able to control the oxidation in other systems, since there are many indications that grain boundary diffusion is also the dominant mechanism of oxidation in, for example, other oxides and carbides.

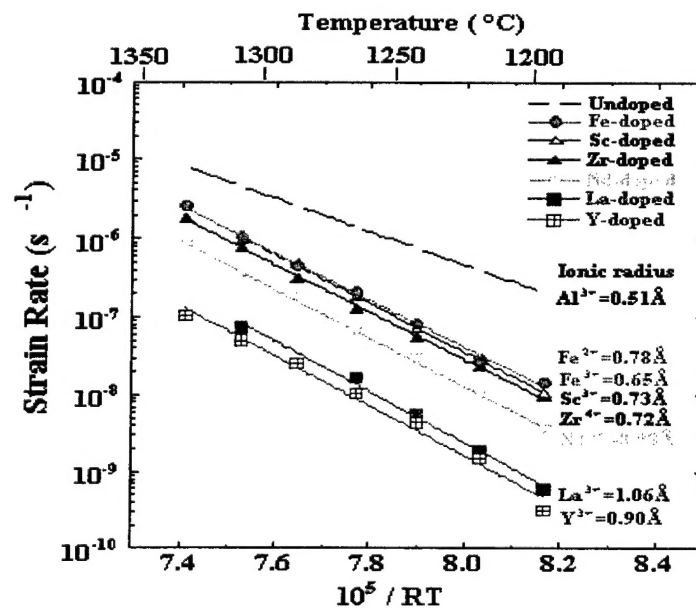


Figure 1. Influence of dopants of varying ionic size on the tensile creep of fine grained (2.4 micron) alumina.

With regard to other specific findings related to these general conclusions, we summarize below the salient points.

- Investigations of the impact of dopants on grain-boundary structure in alumina using electron backscattering to characterize grain misorientation show that the boundary structure is not significantly altered by the addition of, for example, yttrium. More specifically, the frequency of selected coincidence-site (CSL) boundaries was not significantly changed as a result of doping with cations such as yttrium. This preservation of boundary structure suggests that site-blocking may indeed be the operative mechanism for creep retardation.

- The level of segregation of impurities to boundaries in alumina was assessed with energy-dispersive x-ray and electron energy loss spectrometry [5]. These studies have confirmed the tendency of yttrium and lanthanum to segregate to grain boundaries.
- Selective codoping was found in some instances to result in a higher creep resistance than that found in a singly-doped oxide. In particular, it was found that in Nd/Zr codoped alumina the creep rate was reduced by 2-3 orders of magnitude relative to undoped alumina. This synergy suggests possible doping strategies to improve resistance.
- Finally, the role of oxidation state on kinetics was studied in densification experiments on iron and iron/yttrium codoped alumina [10]. The addition of Fe, for example, under oxidizing conditions was found to reduce the densification rate by a factor of five while, in a nitrogen atmosphere, the densification rate is similar to that of undoped alumina. Such densification experiments are useful in the interpretation of the boundary transport kinetics associated with diffusional creep. In summary, it has been found that  $\text{Fe}^{3+}$  reduces the densification rate and the creep rate relative to an undoped sample.

## II. Modeling and Simulation: Findings

Simulation studies effectively complement the various experimental probes outlined above in the investigation of the chemistry and mechanical properties of ceramic oxides. In addition, they have several advantages including, chiefly, the ability to describe "clean" systems containing only a few, controlled defects and the flexibility to systematically explore wide ranges in parameter space. Furthermore, it is possible to vary ionic size and charge in physically inaccessible regimes, permitting one to interrogate system chemistry for a spectrum of dopants. In the simulational components of this program we have employed atomistic computer simulation to model segregation in alumina and to determine the impact of dopant ions on the reaction coordinates associated with diffusion at grain boundaries. We have also employed mesoscale modeling to examine the impact of microstructural heterogeneity on grain-boundary diffusional (i.e., Coble) creep. Our main conclusions are summarized below.

- Using energy minimization techniques, we investigated the energetics of doping and segregation in both bulk alumina and ideal bicrystals. In particular, we examined the spatial distribution of free volume near boundaries using Voronoi tessellations to highlight cation substitutional sites

as well as voids. Such information is useful in determining the space available for boundary segregation and in the assessment of codoping possibilities. We also assessed the dependence of the driving force for segregation on misfit strain [11].

- We investigated the change in activation energy for boundary diffusion that attends segregation in aluminum oxide. By comparing different reaction coordinates, it was determined that oversized ions distort their local environment and thereby increase associated activation energies. Such increased energies are linked with hindered diffusion and suggest that boundary diffusion-mediated mechanisms may be strongly affected by the degree of segregation in doped materials.
- A microstructural model of steady-state creep coupling boundary transport, micromechanics and grain sliding was employed to highlight the impact of variable boundary diffusivities on creep behavior. In some limiting cases, approximate analytical forms for the creep rate and its dependence on stress and grain size were deduced [12].
- Finally, we are developing microstructural models of grain-boundary diffusion to assist in the extraction of boundary diffusivities from measured concentration profiles and mass uptakes. These models reflect the microstructural complexities inherent in a polycrystal.

## References

- 1.) S. Lartigue, C. Carry, and L. Priester, "Grain Boundaries in High Temperature Deformation of Yttria and Magnesia Co-doped Alumina," *J. Phys. (Paris)*, **C1-51** (1990) 985-90
- 2.) H. Yoshida, Y. Ikuhara, and T. Sakuma, "Transient Creep in Fine-Grained Polycrystalline  $\text{Al}_2\text{O}_3$  with  $\text{Lu}^{3+}$  Ion Segregation at Grain Boundaries," *J. Mater. Res.*, **16** (2001) 716-20
- 3.) P. Gruffel and C. Carry, "Effect of Grain Size on Yttrium Grain Boundary Segregation in Fine-Grained Alumina," *J. Eur. Ceram. Soc.*, **11**, (1993) 189-99
- 4.) D.M. Wilson and L.R. Visser, "Nextel 650 Ceramic Oxide Fiber: New Alumina-Based Fiber for High Temperature Composite Reinforcement," *Ceram. Eng. Sci. Proc.* **21** (2000), 363-373
- 5.) J. Bruley, J. Cho, Y. Z. Li, H. M. Chan, J. M. Rickman and M. P. Harmer "STEM Analysis of Grain Boundaries of Creep Resistant Y and La Doped Alumina," *J. Am. Ceram. Soc.*, **82** (1999) 2865-70
- 6.) C.M. Wang, G.S. Cargill III, H.M. Chan, and M.P. Harmer, "Structural Features of Y-Saturated and Supersaturated Grain Boundaries in Alumina," *Acta. Mat.* **48** (2000) 2579-91
- 7.) C.M. Wang, G.S. Cargill III, H.M. Chan, and M.P. Harmer, "Structure of Y and Zr Segregated Grain Boundaries in Alumina," *Interface Science*, **8** (2000) 243-55
- 8.) A.M. Thompson, K. K. Soni, H. M. Chan, M. P. Harmer, D. B. Williams, J. M. Chabala, and R. Levi-Setti, "Rare Earth Dopant Distributions in Creep-Resistant  $\text{Al}_2\text{O}_3$ ," *J. Am. Ceram. Soc.*, **80** (1997) 373-76
- 9.) Y. Z. Li, C. Wang, H. M. Chan, J. M. Rickman and M. P. Harmer, "Codoping of Alumina to Enhance Creep Resistance," *J. Am. Ceram. Soc.*, **82** (1999) 1497-1504
- 10.) M. Drahus, thesis (unpublished)
- 11.) J. Cho, J. M. Rickman, H. M. Chan, and M. P. Harmer, "Modeling of Grain-Boundary Segregation Behavior in Aluminum Oxide," *J. Am. Ceram. Soc.*, **83** (2000) 344-352

- 12.) W. S. Tong, J. M. Rickman, H. M. Chan, and M. P. Harmer, "Coble-Creep Response and Variability of Grain-Boundary Properties," J. Mater. Res., 17 (2002) 348-352

## **2. PUBLICATIONS, REPORTS AND PRESENTATIONS**



## 2. PUBLICATIONS, REPORTS AND PRESENTATIONS

### 2.1 Publications

#### A. Papers Published in Refereed Journals

J. Cho, C. Wang, H.M. Chan, J.M. Rickman and M.P. Harmer, "Role of Segregating Dopants on the Improved Creep Resistance of Aluminum Oxide," *Acta. Met. et. Mat.*, 47 (1999) 4197-207

C. Wang, G.S. Cargill III, M.P. Harmer, H.M. Chan and J. Cho, "Atomic Structural Environment of Grain Boundary Segregated Y and Zr in Creep Resistant Alumina from EXAFS," *Acta. Mater.* 47 (1999) pp.3411-22

J. Bruley, J. Cho, J.C. Fang, A.M. Thompson, Y.Z. Li, H.M. Chan, M.P. Harmer and J.M. Rickman, "STEM Analysis of Grain Boundaries of Creep Resistant Y and La Doped Alumina," *J. Amer. Ceram. Soc.* 82 (1999) pp.2865-70

Y.-Z. Li, C. Wang, H.M. Chan, J.M. Rickman, M.P. Harmer, J.M. Chabala, K.L. Gavrilov and R. Levi-Setti, "Codoping of Alumina to Enhance Creep Resistance," *J. Amer. Ceram. Soc.*, 82 (1999) pp.1497-504

J. Cho, J.M. Rickman, H.M. Chan and M.P. Harmer, "Modeling of Grain-Boundary Segregation Behavior in Aluminum Oxide," *J. Amer. Ceram. Soc.*, 83 (2000) pp. 344-52

J. Cho, J.M. Rickman, H.M. Chan and M.P. Harmer, "Modeling of Grain-Boundary Segregation Behavior in Aluminum Oxide," *J. Amer. Ceram. Soc.* 83 (2000) pp. 344-52

J. Cho, C. Wang, H.M. Chan, J.M. Rickman and M.P. Harmer, "Improved Tensile Creep Properties of Yttrium- and Lanthanum-Doped Alumina: A Solid Solution Effect," *J. Mater. Res.*, 16 (2000) 425-29

C. Wang, G.S. Cargill III, H.M. Chan and M.P. Harmer, "Structural Features of Y-Saturated and Supersaturated Grain Boundaries in Alumina," *Acta Mater.*, 48 (2000) pp.1-13

H.M. Chan, M.P. Harmer and J.M. Rickman, Reply to "Comment on 'Influence of Yttrium Doping on Grain Misorientation in Aluminum Oxide'," *J. Amer. Ceram. Soc.* 83 (2000) p. 1324

C. Wang, G.S. Cargill III, H.M. Chan and M.P. Harmer, "Structure of Y and Zr Segregated Grain Boundaries in Alumina," *Interface Science* 8 (2000) pp. 243-55

C. Wang, G.S. Cargill III, H.M. Chan, M.P. Harmer and D.B. Williams, "Atomic Structural Environment of Grain Boundary Segregated Y in Creep Resistant Alumina," Proc. IUMAS 2000, July 9-14, Kailua-Kona, HA, 2000 IOP Publishing Ltd, pp. 151-2

(2000)

① C.M. Wang, J. Cho, H.M. Chan, M.P. Harmer and J.M. Rickman, "Influence of Dopant Concentration on Creep Properties of Nd<sub>2</sub>O<sub>3</sub> Doped Alumina," J. Amer. Ceram. Soc., 84 (2001) pp. 1010-16

② W.S. Tong, J.M. Rickman, H.M. Chan and M.P. Harmer, "Coble-Creep Response and the Variability of Grain Boundary Properties," J. Mater. Res., 17 (2002) 348-52

③ C. Wang, G.S. Cargill III, H.M. Chan and M.P. Harmer, "X-Ray Absorption Near Edge Structure of Grain Boundary Segregated Y and Zr in Creep Resistant Alumina," J. Amer. Ceram. Soc., 85 (2002) 2492-98

④ C.-M. Wang, H.M. Chan and Martin P. Harmer, "Effect of Nd<sub>2</sub>O<sub>3</sub> Doping on the Densification and Abnormal Grain Growth Behavior of High Purity Alumina," J. Amer. Ceram. Soc., 87 (2004) 378-83

## **B. Non-Refereed Publications and Published Technical Reports**

None

## **2.2 PRESENTATIONS**

J.M. Rickman, H.M. Chan and Martin P. Harmer, "Enhanced Creep Resistance in Alumina," Workshop sponsored by the Max Planck Institute, sponsored Schloss Ringberg, Tegernese, Germany, March 1999

"Creep Properties and Microstructure of High Purity Alumina Doped with Rare Earth Oxides," Dept. of Materials Engineering, Drexel University, Philadelphia, PA, April 9, 2002.

C. Wang, J. Cho, H.M. Chan, M.P. Harmer and J.M. Rickman, "Creep Properties and Microstructure of High Purity Alumina Doped with Rare Earth Oxides," 101<sup>st</sup> Annual Meeting of the American Ceramic Society, Indianapolis, IN, April 1999

C. Wang, H.M. Chan, M.P. Harmer, J.M. Rickman and G.S. Cargill III, "Dopant Grain Boundary Supersaturation and Creep Resistance in Y and Zr Doped Alumina," 102<sup>nd</sup> Annual Meeting of the Amer. Ceram. Soc., St. Louis, MO, April 2000

C. Wang, H.M. Chan, M.P. Harmer and J.M. Rickman, "Creep Behavior of Y/Fe Co-Doped Alumina," 102<sup>nd</sup> Annual Meeting of the Amer. Ceram. Soc., St. Louis, MO, April 2000.

G.S. Cargill III, C.M. Wang, J.M. Rickman, H.M. Chan and M.P. Harmer, "Effect of Y and Zr Dopants on Grain Boundary Structure in Creep Resistant Polycrystalline Alumina," Fall Meeting, Materials Research Society, Boston MA, Nov. 2000.

M. Drahus, C.M. Wang, M.P. Harmer, H.M. Chan, G.S. Cargill III and J.M. Rickman, "New Insights on the Effect of Fe and Y/Fe Doping on Densification and Grain Growth in Alumina," 103<sup>rd</sup> Annual Meeting of the American Ceramic Society, Indianapolis, IN, April 22-25, 2001.

G.S. Cargill III, H.M. Chan, M.P. Harmer, J.M. Rickman and C.M. Wang, "Creep Behavior and Valence State of Fe in Y/Fe Co-Doped Alumina," 103<sup>rd</sup> Annual Meeting of the American Ceramic Society, Indianapolis, IN, April 22-25, 2001.

J.M. Rickman invited talk, Virginia Tech (Spring, 2001).

J.M. Rickman invited talk, University of California Santa Barbara (Spring, 2001).

J.M. Rickman invited talk, University of Wisconsin (Spring, 2001).

J.M. Rickman invited talk, Lawrence Berkeley National Laboratory (Spring 2001).

J.M. Rickman invited talk, Rockwell Science Center (Spring 2001).

J.M. Rickman invited talk, Spring MRS Meeting (2001).

M. Drahus, C. Turquat, M.P. Harmer, H.M. Chan and J.M. Rickman, "The Effect of Iron and Yttrium on the Densification and Microstructure of Alumina," 104<sup>th</sup> Annual Meeting of the American Ceramic Society, St. Louis, MO, April 28 - May 1, 2002.

C. Turquat, M.D. Drahus, H.M. Chan, J.M. Rickman and M.P. Harmer, "Doping Alumina in Order to Enhance its Creep Behavior," 104<sup>th</sup> Annual Meeting of the American Ceramic Society, St. Louis, MO, April 28 - May 1, 2002.

J.M. Rickman invited talk, Princeton University (Spring 2002).

J.M. Rickman, "Dislocation Energetics and Dynamics", Lawrence Livermore National Laboratory (Spring 2002).

J.M. Rickman, "Dislocation Energetics and Dynamics", Los Alamos National Laboratory (Spring 2002).

J.M. Rickman invited talk, Spring TMS Meeting (2002).

C.P. Turquat, M.D. Drahus, H.M. Chan, J.M. Rickman and M.P. Harmer, "Enhancing the Creep Resistance of Alumina by Low Concentration Additives" Gordon Research Conference on Solid State Studies in Ceramics, Meriden, NH, August 11 - 16, 2002

Jeffrey Rickman, Computational Materials Science - Education, TMS Meeting (Spring 2003)

J.M. Rickman, "Dislocation Energetics and Dynamics", Los Alamos National Laboratory - T-Division (Spring 2003).

J.M. Rickman, "Dislocation Energetics and Dynamics", University of Florida (Spring 2003).

J.M. Rickman, "Dislocation Energetics and Dynamics", Lawrence Livermore National Laboratory (Spring 2003).

M. Drahus, C. Turquat, H.M. Chan and M.P. Harmer, "The Effect of Iron on the Grain Boundary Segregation Behavior of Yttrium in Alumina," 105<sup>th</sup> Annual Meeting of the American Ceramic Society, Nashville, TN, April 27 - 30, 2003.

C. Turquat, M. Drahus, J.M. Rickman, H.M. Chan and M.P. Harmer, "Cerium-Doped Alumina: From Microanalysis to Creep," 105<sup>th</sup> Annual Meeting of the American Ceramic Society, Nashville, TN, April 27 - 30, 2003.

M. Drahus, C. Turquat, M.P. Harmer and H.M. Chan, "The Effect of Tungsten Doping on the Densification and Grain Growth of Alumina," 105<sup>th</sup> Annual Meeting of the American Ceramic Society, Nashville, TN, April 27 - 30, 2003.

J.M. Rickman, "Materials Modeling at Different Length Scales" - Lehigh Physics Dept. (Fall 2003).

J.M. Rickman, "Materials Modeling at Different Length Scales" - SUNY-Binghamton (Fall 2003).

J.M. Rickman, "Materials Modeling at Different Length Scales" - Wright-Patterson AFB (Fall 2003).

J. M. Rickman, "Dislocation Energetics and Dynamics" – 2nd International Workshop Multiscale Modeling of Strength and Fracture, Berkeley, CA (Spring 2004).

J. M. Rickman, "Multiscale Modeling of Materials" – California State University-Northridge (Spring 2004).

J. M. Rickman, "Multiscale Modeling of Materials" – Washington University (Spring 2004).

J. M. Rickman, "Multiscale Modeling of Materials" – Virginia Tech (Spring 2004).

J. M. Rickman, "Some Mathematical Methods in Materials Science" – Lehigh Mathematics Dept. (Spring 2004).

"Speeding and Crawling along Grain Boundaries in Ceramics," M.P. Harmer and H.M. Chan, 106<sup>th</sup> Annual Meeting of the American Ceramic Society, Indianapolis, IN, April 18 - 21, 2004.

M. Drahos, M.P. Harmer and H.M. Chan, "The Effect of Atmosphere on the Sintering of Iron Doped and Iron/Yttrium Codoped Alumina," 106<sup>th</sup> Annual Meeting of the American Ceramic Society, Indianapolis, IN, April 18 - 21, 2004.

J.M. Rickman, "Dislocation Energetics and Dynamics" – Gordon Research Conference, Physical Metallurgy (Summer 2004).

J.M. Rickman, Air Force Program Review – Ceramics (Summer 2004).

Martin P. Harmer, "Speeding and Crawling Along Grain Boundaries in Ceramics" 11th International Conference on Intergranular and Interphase Boundaries", Queens University, Belfast, Ireland, July 25-30, 2004.

M. Drahos, M.P. Harmer and H.M. Chan, "Densification and Creep Behavior of Fe-Doped and Fe/Y Codoped  $\alpha$ -Al<sub>2</sub>O<sub>3</sub>: Effect of Fe Valency," Gordon Research Conference on Solid State Studies in Ceramics, Meriden, NH, August 8-12, 2004

Martin P. Harmer, "Controlling Atom Movements In and Along Grain Boundaries", Gordon Research Conference on Solid State Studies in Ceramics, Kimball Union Academy, Meriden NH, August 8-13, 2004.

J.M. Rickman, Third Multiscale Modeling Workshop – DOE (Portland, Oregon – Fall 2004).

J.M. Rickman, "Simulation of Nucleation and Growth Processes" – Fall 2004 TMS meeting.

### 2.3 Books (and sections thereof)

**None**

## **SELECTED PUBLICATIONS**



PERGAMON

Acta mater. Vol. 47, No. 12, pp. 3411–3422, 1999  
 © 1999 Acta Metallurgica Inc.  
 Published by Elsevier Science Ltd. All rights reserved.  
 Printed in Great Britain  
 1359-6454/99 \$20.00 + 0.00

PII: S1359-6454(99)00210-4

## ATOMIC STRUCTURAL ENVIRONMENT OF GRAIN BOUNDARY SEGREGATED Y AND Zr IN CREEP RESISTANT ALUMINA FROM EXAFS

C. M. WANG, G. S. CARGILL III, M. P. HARMER†, H. M. CHAN and J. CHO

Materials Research Center, Lehigh University, Bethlehem, PA 18015, U.S.A.

(Received 12 April 1999; accepted 24 June 1999)

**Abstract**—Dopants Y and Zr at 100 p.p.m. level (Y or Zr to Al atomic ratio) in ultra-high purity polycrystalline alumina have been found to be mainly segregated to the alumina grain boundaries. The atomic structural environments around the Y and Zr segregants have been investigated by Extended X-ray Absorption Fine Structure (EXAFS). On average, Y ions in  $\alpha$ - $\text{Al}_2\text{O}_3$  grain boundaries are coordinated by four oxygens, at a distance of 2.30 Å, which corresponds nearly to the Y–O bond length in cubic  $\text{Y}_2\text{O}_3$ , and Zr ions are coordinated by five oxygens at a distance of 2.14 Å, which is approximately the same as the average Zr–O bond length in monoclinic  $\text{ZrO}_2$ . However, in the EXAFS radial distribution function, the Y-cation and Zr-cation next nearest neighbor shell cannot be clearly identified. These results suggest that Y and Zr at 100 p.p.m. concentrations in  $\alpha$ - $\text{Al}_2\text{O}_3$  occupy grain boundary sites with well defined nearest neighbor cation–oxygen bond lengths similar to those in their parent oxides but with the next nearest neighbor cation–cation distances varying considerably from site to site. From EXAFS, the Y grain boundary saturation concentration is estimated to be 6.0 atoms/nm<sup>2</sup>, which is consistent with the estimate from STEM of 4.4 atoms/nm<sup>2</sup>. The differences in the Zr–O and Y–O nearest neighbor distances and coordination numbers in  $\text{Al}_2\text{O}_3$  grain boundaries are related to the Y–Al and Zr–Al size mismatches. © 1999 Acta Metallurgica Inc. Published by Elsevier Science Ltd. All rights reserved.

**Keywords:** EXAFS; Alumina; Grain boundary segregation; Atomic structure; Y and Zr

### 1. INTRODUCTION

Dopant and impurity grain boundary segregation has been found in both metals and ceramics [1–4]. The grain boundary segregants may have either detrimental or beneficial effects on a material's microstructures and properties. An example of the detrimental aspects of grain boundary segregation is segregation-induced intergranular fracture embrittlement [5]. Beneficial effects of dopant segregation on material properties have been recently demonstrated in two systems. Doping superalloys with a trace amount of Y significantly improves their oxidation resistance [6]. Recently, it has been also systematically established that doping trace amounts of rare-earth oxide (typically 100–1000 p.p.m.) in high purity alumina induces a two to three orders of magnitude increase in the creep resistance [7–10]. A better understanding of the mechanisms by which such impurities influence material properties is the key to further exploiting these effects and for optimizing material properties.

Many efforts have been made over the last few years to correlate microstructural features with properties of rare earth doped high purity alumina. Based on transmission electron microscopy (TEM)

studies of grain boundaries in doped alumina specimens, Lartigue *et al.* [11] postulated that the role of the dopant ions was to modify the grain boundary structure in a manner so as to impede the accommodation of lattice dislocations, and hence limit grain boundary sliding. However, a recent study by Cho *et al.* [12] using Orientation Image Mapping (OIM) found no obvious difference in the distribution of the grain boundary types between undoped and doped alumina. The conclusion of Cho *et al.* is also consistent with a recent TEM survey of grain boundary type distribution in Y-doped alumina [13], where very few special boundary types were found. By using secondary ion mass spectroscopy (SIMS) mapping, Thompson *et al.* [3] have shown that Y and La dopants are segregated to all types of alumina grain boundaries. Motivated by those observations, the same group has proposed that the increased creep resistance in doped alumina be attributed to reduced grain boundary diffusivity caused by blocking of grain boundaries by the segregated oversized dopants [9, 14]. Further evidence in support of this grain boundary blocking model is as follows. (1) The same improvement in creep resistance was observed for dopant levels both above and below the solubility limit, confirming that the phenomenon is a solid solution effect [14]. (2) The creep resistance improvement shows dependence on

†To whom all correspondence should be addressed.



the ionic size of the dopant [14]. However, the structural details of the grain boundary with the segregated dopant remain to be established, both theoretically and experimentally. This information is needed for further understanding of the mechanisms by which segregation affects grain boundary related phenomena.

A variety of microscopic and spectroscopic methods have been employed to investigate the structural environment of the grain boundary segregated dopant ions. These methods have included auger electron spectroscopy (AES) [15], X-ray photoelectron spectroscopy (XPS) [16], energy dispersive X-ray spectroscopy (EDS) in a scanning electron microscope (SEM) and in a scanning transmission electron microscope (STEM) [17, 18], electron energy-loss spectroscopy (EELS), SIMS [3] and extended X-ray absorption fine structure (EXAFS) [19, 20]. AES, XPS, EDS and SIMS have been used mainly to investigate grain boundary segregation concentrations and segregant distribution profiles. STEM measurements by Bruley *et al.* [17] revealed that in the case of Y and La, the dopant ions were segregated to a narrow region at the alumina grain boundaries. Assuming a segregation layer thickness of  $\sim 1$  nm, the fraction of cation sites occupied by the impurity ions was determined to be  $\sim 9$ – $10\%$ . Attempts also have been made using EELS to investigate the local chemical bonding around the dopant ions in 1000 p.p.m.  $Y_2O_3$  and 500 p.p.m.  $La_2O_3$  doped alumina [17]. The structures of alumina grain boundaries with Ca and Zr segregation have also been investigated using high resolution transmission electron microscopy (HRTEM) [21, 22].

EXAFS is a powerful method for determining the atomic structural environment around impurities, particularly very dilute impurities, and it has been used to probe the local atomic structural configurations around impurities in various oxides and non-oxides [23–25], including  $Y_2O_3$  stabilized  $ZrO_2$  and 300 p.p.m. to 1 mol%  $Y_2O_3$  doped alumina [19, 20]. However, in an earlier study of  $Y_2O_3$  doped  $Al_2O_3$  [19], the  $Y_2O_3$  concentration exceeded the solid solution limit of the  $\alpha-Al_2O_3$ , so yttrium aluminum garnet ( $Y_3Al_5O_{12}$ , YAG), which precipitated as a secondary phase, masked the EXAFS signal from the grain boundary segregated Y ions. To obtain information about the structural environment of grain boundary segregated Y ions, measurements on more dilute yttrium doped alumina samples and more detailed data analysis were needed. Based on previous microscopic investigations, we have established for very dilute concentrations of doping, typically 100 p.p.m., that the Y and Zr ions are mainly segregated to the grain boundaries and that secondary phase precipitation is absent [14, 26]. In this paper, we report an EXAFS investigation of high purity alumina doped with  $Y_2O_3$  at concentrations of 100 p.p.m. and 1000 p.p.m., and  $ZrO_2$  at a nominal con-

centration of 100 p.p.m., giving information about the atomic structural environment of grain boundary segregated Y and Zr ions. Implications of the present results for the effects of the segregants on grain boundary mediated transport are discussed.

## 2. EXPERIMENTAL PROCEDURES

### 2.1. Materials

The samples were ultra-high purity  $Al_2O_3$  doped with either  $Y_2O_3$  or  $ZrO_2$ .  $Y_2O_3$  was doped at two levels, 100 and 1000 p.p.m. (Y/Al atomic ratio, hereafter referred to as samples 100Y and 1000Y), and  $ZrO_2$  at 100 p.p.m. nominally (Zr/Al atomic ratio, hereafter referred to as sample 100Zr). The doping process involves dispersing ultra-high purity alumina powder (Sumitomo AKP 53, with an average grain size of  $0.3 \mu m$ , and purity of 99.995%) in methanol. Y-doping was achieved by adding an yttrium nitrate (99.999%, Aldrich Chemical Co.) methanol solution to the  $Al_2O_3$  slurry. Zr-doping was achieved by ball milling the  $Al_2O_3$  slurry with  $ZrO_2$  grinding media (4.2 mol%  $Y_2O_3$  stabilized tetragonal zirconia, Tosoh U.S.A. Inc., Bridgewater, NJ) for 20 h. All powder processing was conducted in a class 100 clean room environment using acid washed containers. All the doped powders were hot-pressed using graphite dies in vacuum at 45 MPa for 30 min. The hot-pressing temperature for the 100Y powder was  $1450^\circ C$ , for the 1000Y powder was  $1475^\circ C$ , and for the 100Zr powder was  $1320^\circ C$ . The 100Y and 1000Y samples have a relative density higher than 99%, and the 100Zr sample has a relative density of 97%. The 100Zr and 100Y samples show a rather uniform grain size distribution, with the 100Y having an average grain size of  $\sim 1.5 \mu m$  [Fig. 1(a)], and the 100Zr having an average grain size of  $\sim 0.5 \mu m$  [Fig. 1(b)]. SEM and TEM reveal no secondary phase precipitates in the 100Y and 100Zr materials. The 1000Y material shows a bimodal grain size distribution, with a coarse grain size of  $\sim 5 \mu m$ , and fine grain size of  $\sim 1 \mu m$ . The 1000Y material also has secondary phase precipitates which are mainly in the fine grain size  $Al_2O_3$  regions [Fig. 1(c)]. Figure 2 shows STEM annular aperture dark field images and compositional mapping of the dopants. Both techniques reveal that the dopant is segregated narrowly at the grain boundaries, with a distribution width of less than 2 nm. STEM analysis indicates that the grain boundaries of 1000Y show similar features of Y segregation. Details of the microstructural features of these doped materials have been reported elsewhere [14].

### 2.2. X-ray absorption measurements

X-ray absorption measurements at the K edges of Y and Zr were made on Beamline X23A2 of the National Synchrotron Light Source (NSLS) at

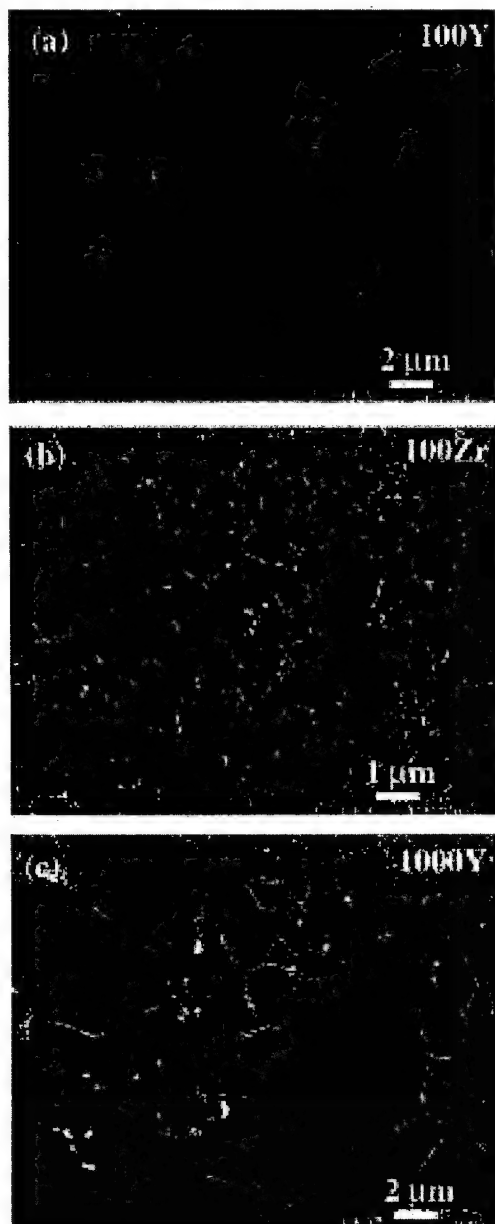


Fig. 1. SEM images of Y-doped and Zr-doped  $\text{Al}_2\text{O}_3$  samples: (a) 100 p.p.m.  $\text{Y}_2\text{O}_3$  doped  $\text{Al}_2\text{O}_3$ ; (b) 100 p.p.m.  $\text{ZrO}_2$  doped  $\text{Al}_2\text{O}_3$ ; and (c) 1000 p.p.m.  $\text{Y}_2\text{O}_3$  doped  $\text{Al}_2\text{O}_3$ . Grain boundaries are visible because of thermal grooving. In (c) some of the YAG precipitates are indicated by arrows.

Brookhaven National Laboratory under normal operating conditions (2.5 GeV, 100–200 mA) and using a Si (311) double crystal monochromator. For bulk materials, the spectra were measured in the fluorescence mode. The incident beam had a cross-section of  $3 \times 12 \text{ mm}^2$  and intersected with the specimen surface at 45 deg. An Ar-filled ion chamber was used as the fluorescence detector, posi-

tioned so that the detector window center line also intersected the specimen surface at 45° but was perpendicular to the incident beam direction. Absorption edge jumps in fluorescence were more than 20% of the pre-edge intensity for the 100Y sample and more than 30% for the 100Zr sample (see Fig. 3), so the fluorescence detector was used without filter foils. In order to reduce statistical errors, about 70 spectra were recorded and averaged for the 100Y sample and for the 100Zr sample. For the 1000Y sample only two spectra were collected and averaged to obtain similar statistical accuracy.

Samples of cubic  $\text{Y}_2\text{O}_3$  powder (purity 99.99%, Alfa, Johnson Matthey Company) and of monoclinic  $\text{ZrO}_2$  powder (purity 99.5%, Alfa, Johnson Matthey Company) were measured in transmission mode, and the data were used as standards for the analysis of data from the doped materials. Samples were prepared by encapsulating the powder between pieces of self-adhesive Scotch Magic tape. As a standard for analyzing secondary phase precipitates in the 1000Y material, bulk polycrystalline  $\text{Y}_3\text{Al}_5\text{O}_{12}$  (YAG), which includes 5 vol.%  $\text{Al}_2\text{O}_3$ , was also measured in fluorescence mode, but at a detector grazing angle of about 10°. For all the reference samples, at least five spectra were recorded and averaged.

### 2.3. EXAFS data analysis

For the bulk samples, the fluorescence intensity  $I_F(E)$  was normalized by the incident intensity  $I_0(E)$  to obtain the absorption spectrum,  $\mu(E) = I_F(E)/I_0(E)$ . For the powder samples, the transmitted intensity  $I_T(E)$  was normalized by the incident intensity  $I_0(E)$  to obtain the absorption spectrum,  $\mu(E) = -\ln[I_T(E)/I_0(E)]$ . A linear function was fitted to the pre-edge region of  $\mu(E)$  and was subtracted from  $\mu(E)$  in order to isolate the contributions from K-shell absorption,  $\mu_K(E)$ . The EXAFS function,  $\chi(k)$ , was extracted from  $\mu_K(E)$  using standard procedures [27]: a smooth background,  $\mu_0(E)$  was subtracted from  $\mu_K(E)$ , and then the spectra were normalized by the average value of  $\mu_0(E)$  throughout the EXAFS region ( $\mu_0(E)$ ). The values of  $E$  greater than the K-absorption edge energy  $E_0$  were converted to values of  $k$

$$k = \sqrt{8\pi^2 m(E - E_0)/h^2} \quad (1)$$

where  $m$  is electron mass and  $h$  is Planck's constant. The absorption edge energies were 17.034 keV for Y and 17.998 keV for Zr [28].

The resulting expression for the EXAFS function  $\chi(k)$  is

$$\chi(k) = \frac{\mu_K(E) - \mu_0(E)}{\langle \mu_0(E) \rangle} \quad (2)$$

The EXAFS distribution function  $\Phi_3(r)$  was calculated by Fourier transform of  $\chi(k)$

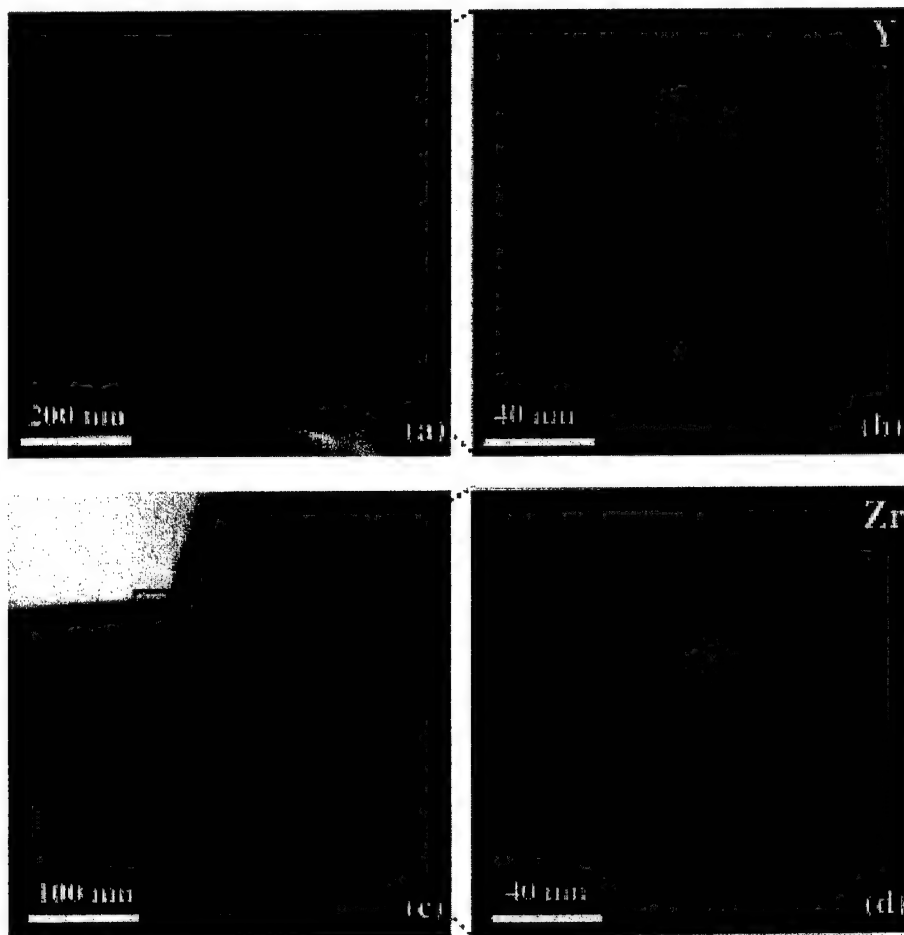


Fig. 2. STEM images, (a) and (c), and EDS maps, (b) and (d), reveal the segregation of the dopants in  $\alpha$ - $\text{Al}_2\text{O}_3$  grain boundaries: (a) annular aperture dark field image of 100 p.p.m.  $\text{Y}_2\text{O}_3$  doped material and (b) the EDS mapping of Y; (c) annular dark field image of 100 p.p.m.  $\text{ZrO}_2$  doped material and (d) the EDS mapping of Zr. In the EDS mapping, the electron beam diameter is optimized to 1 nm, and the mapping area is  $160 \times 160 \text{ nm}^2$  with a total pixel number of  $128 \times 128$ .

$$\Phi_3(r) = \int_{k_{\min}}^{k_{\max}} k^3 \chi(k) \exp(i2kr) dk. \quad (3)$$

The nearest neighbor contributions  $\chi_{\text{NN}}(k)$  were calculated by Fourier transform of  $\Phi_3(r)$  with the window functions centered on the nearest neighbor peaks of  $|\Phi_3(r)|$  (as shown later in Fig. 6).

The EXAFS spectra were analyzed using the standard EXAFS equation [27]

$$\chi(k) = \sum_j \frac{N_j}{kR_j^2} F_j(k) e^{-2\sigma_j^2 k^2} e^{-2R_j/\lambda} \sin[2kR_j + \phi_j(k)] \quad (4)$$

where  $F_j(k)$  is the backscattering amplitude from each of the  $N_j$  neighboring atoms of type  $j$  at distance  $R_j$  with a mean square relative displacement  $\sigma_j^2$ , and  $\phi_j(k)$  is the total phase shift experienced by the photoelectron including contributions from both the scatter and absorber. The factor  $e^{-2R_j/\lambda}$ ,

where  $\lambda$  is the photoelectron mean free path, accounts for inelastic scattering.

The average nearest neighbor coordination number,  $N$ , the average bond length,  $R$ , and the mean squared bond length dispersion,  $\sigma^2$ , around the grain boundary segregated dopant ions were obtained from EXAFS data by data fitting of  $\chi_{\text{NN}}(k)$  using Win-XAS (version 1.0) software [29] and an *ab initio* multiple scattering EXAFS code (FEFF program, version 7.0) [30]. In this approach, based on the crystallographic data of the model compounds (Table 1), we have calculated the cation-oxygen phase shift and backscattering amplitude functions and have fitted these to the nearest neighbor EXAFS spectra measured for the model compounds. The fitting parameters were  $S_0^2$ , the scaling factor which multiplies the theoretical backscattering amplitude and accounts for inelastic scattering;  $\Delta E_0$ , the adjustment to the absorption edge energy; and  $\sigma_j^2$ , the mean squared bond length dis-

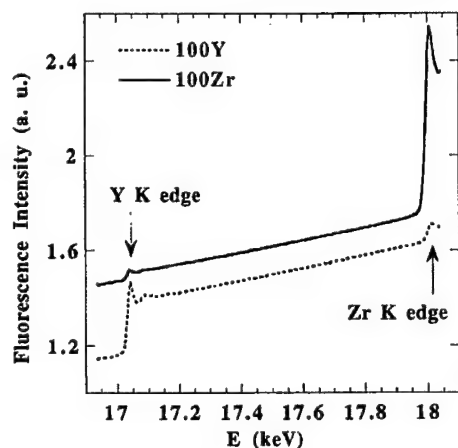


Fig. 3. Typical measurements of X-ray fluorescence intensity for Y and Zr in 100Y and 100Zr, showing that Zr exists as an impurity in 100 p.p.m.  $Y_2O_3$  doped  $\alpha-Al_2O_3$ , and also Y exists as an impurity in 100 p.p.m.  $ZrO_2$  doped  $\alpha-Al_2O_3$ . The curve for the 100Zr sample has been moved upwards by 0.3 for clarity.

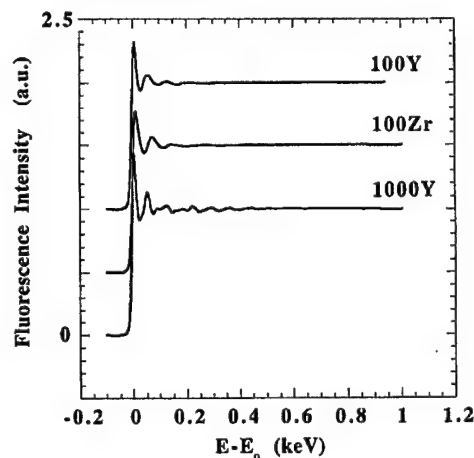


Fig. 4. Normalized X-ray absorption spectra for the doped samples.  $E_0$  is taken as 17.998 keV for Zr and 17.038 keV for Y. For clarity, the curves for 100Y and 100Zr have been moved upwards by 0.5 and 1.0, respectively.

persion. The same values of  $S_0^2$ ,  $\Delta E_0$ , phase shifts and backscattering amplitude functions were then used to fit the nearest neighbor EXAFS spectra for the Y- and Zr-doped  $Al_2O_3$  samples. From fitting either Y-O nearest neighbors in  $Y_2O_3$  or Zr-O nearest neighbors in  $ZrO_2$ , values obtained for  $S_0^2$  were 0.81, and for  $\Delta E_0$  were 0.67 eV.

The fluorescence EXAFS data for the YAG sample were corrected for finite thickness effects using the relationship derived by Jaklevic *et al.* [31] and discussed by Boehme *et al.* [32], together with the absorption coefficients from McMaster *et al.* [28].

### 3. RESULTS

Figure 3 shows typical measurements of fluorescence intensity as a function of energy for the 100Y and 100Zr samples. The energy range spans the K edges of both Y and Zr. It is interesting to note that the EXAFS signal is very sensitive to the impurity levels. Although the 100Y specimen is

nominally doped with only 100 p.p.m. Y, an edge jump at the Zr edge energy can also be seen, indicating that this sample also contains some Zr as an impurity. Based on the edge jump magnitude, the Y:Zr concentration ratio is estimated to be about 100:25. Such a high level of Zr impurity in the 100Y specimen is not expected, since all the raw materials used were ultra-high purity, as indicated in the specimen preparation section. One possible source of the Zr impurity may be surface contamination introduced during machining of the hot-pressed material. However, in the present analysis, we only concentrated on the Y edge in the 100Y specimen.

Similarly, in the 100Zr specimen there is an edge jump corresponding to Y. Based on the edge jump magnitude, Zr:Y = 100:5. Y impurity in the 100Zr specimen is expected, because the Zr dopant was obtained by milling of the alumina slurry with tetragonal  $ZrO_2$  milling media which contains 4.2 mol%  $Y_2O_3$  as stabilizer. This would give a Zr:Y ratio of 100:9, which is roughly consistent with the experimental value of 100:5.

Table 1. Crystallographic data for the model compounds<sup>a</sup>

Compound	Structure	Cation-oxygen bond length (Å)	Coordination number	Ref.
$Al_2O_3$	Rhombohedral	$3 \times 1.852$ ; $3 \times 1.972$ average: $6 \times 1.912$	6	[33]
$Y_2O_3$	Cubic	$6 \times 2.239$ ; $6 \times 2.289$ $6 \times 2.273$ ; $6 \times 2.333$ average: $6 \times 2.284$	6	[34]
$Y_3Al_5O_{12}$	Cubic	$4 \times 2.289$ ; $4 \times 2.412$ average: $8 \times 2.351$	8	[35]
$ZrO_2$	Monoclinic	$1 \times 2.051$ ; $1 \times 2.057$ ; $1 \times 2.151$ ; $1 \times 2.162$ ; $1 \times 2.189$ ; $1 \times 2.220$ ; $1 \times 2.284$ average: $7 \times 2.159$	7	[36, 37]

<sup>a</sup> Ionic radii (Å):  $O^{2-}$ (6): 1.40;  $Al^{3+}$ (6): 0.51;  $Y^{3+}$ (6): 0.90;  $Zr^{4+}$ (7): 0.78, in each case the coordination number is given in parentheses [38].

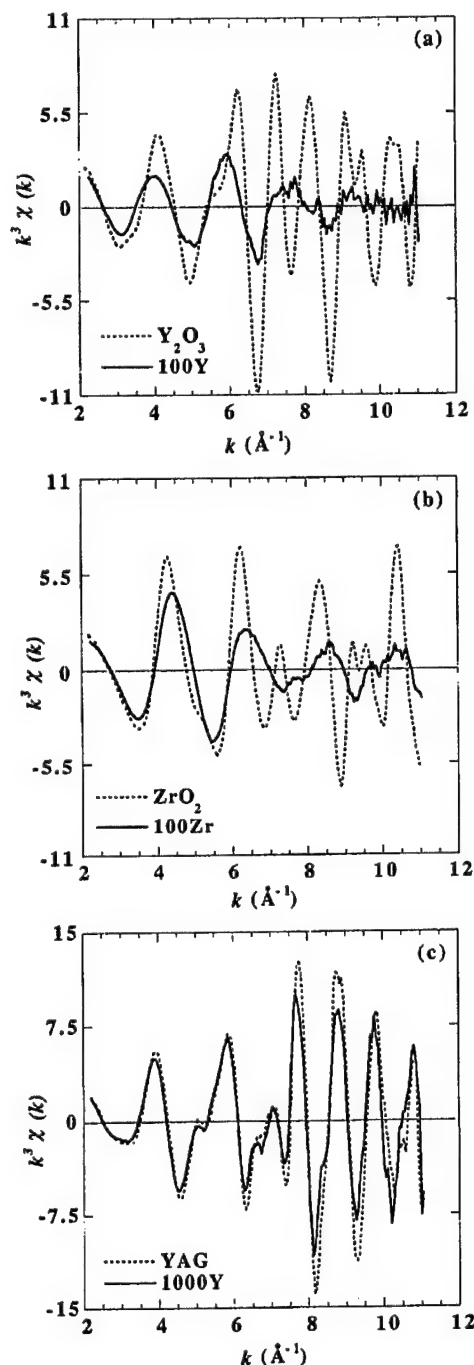


Fig. 5.  $k^3$  weighted  $\chi(k)$  EXAFS functions for (a) Y-K edge in 100Y and  $Y_2O_3$ ; (b) Zr-K edge in 100Zr and monoclinic  $ZrO_2$ ; and (c) Y-K edge in 1000Y and YAG.

Although the 100Y and 100Zr specimens are nominally doped with 100 p.p.m. Y and 100 p.p.m. Zr, respectively, the edge jump magnitude for Zr in the 100Zr specimen is about three times that for Y in the 100Y specimen. This indicates that the Zr

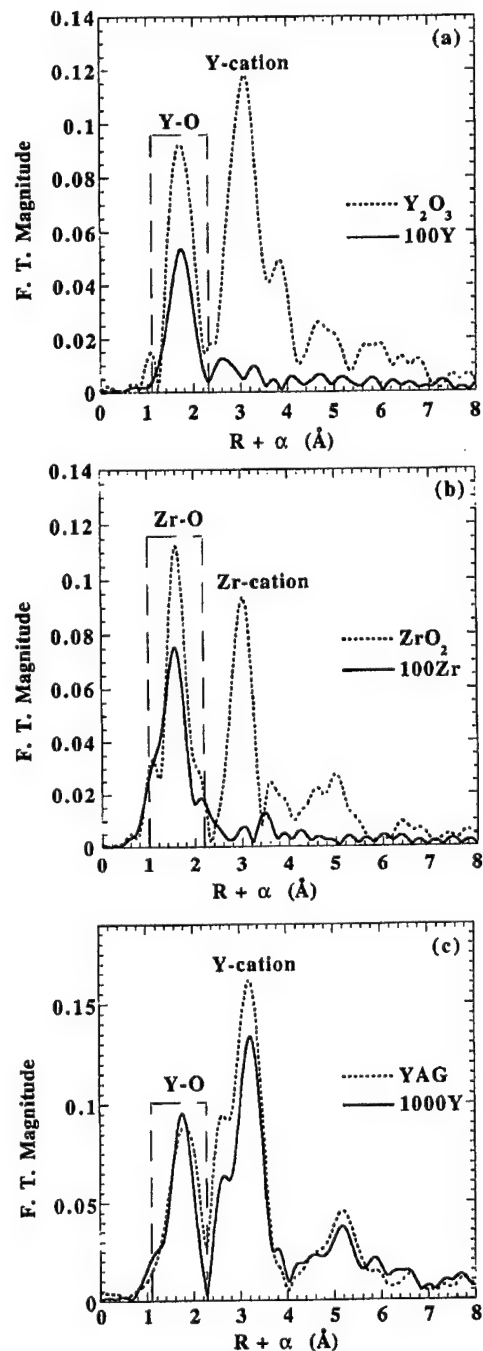


Fig. 6. Fourier transform magnitude  $|\Phi_3(r)|$  of the EXAFS spectra in Fig. 5: (a) 100Y and  $Y_2O_3$ ; (b) 100Zr and monoclinic  $ZrO_2$ ; and (c) 1000Y and YAG.  $\alpha$  represents the distance shift due to the phase shift function in the Fourier transformation. The dashed line window represents the Fourier filtering range for fitting nearest neighbors.

concentration in the 100Zr specimen is about three times larger than the Y concentration in the 100Y specimen. The actual doping concentration of Y is

Table 2. Fitting results for the doped materials<sup>a</sup>

	100Y Y-O	100Zr Zr-O	1000Y Y-O
Mean radial distance ( $\text{\AA}$ ): $R$	$2.30 \pm 0.01$	$2.14 \pm 0.01$	$2.36 \pm 0.01$
Coordination number: $N$	$4.2 \pm 0.5$	$5.0 \pm 0.5$	$7.5 \pm 0.7$
Distance dispersion ( $\text{\AA}^2$ ): $\sigma^2$	$0.009 \pm 0.001$	$0.010 \pm 0.001$	$0.008 \pm 0.0008$

<sup>a</sup> The uncertainties in fitted parameters correspond to a 10% increase in mean square difference between experimental and model  $k^3\chi(k)$  functions, when the other parameters are allowed to vary.

expected to be close to the nominal one, because the doping level of Y was obtained by weighing the diluted yttrium nitrate solution. However, the actual Zr doping level may easily differ from the nominal one, because it was only estimated from the time of ball milling.

Figure 4 shows the normalized X-ray absorption spectra for the 100Y, 1000Y, and 100Zr samples. Figures 5(a)–(c) show the Y and Zr  $\chi(k)$  EXAFS spectra weighted by  $k^3$  for both the doped alumina materials and the model compounds. The magnitudes of the Fourier transforms  $|\Phi_3(r)|$  of the  $k^3\chi(k)$  EXAFS functions in Fig. 5 are shown in Fig. 6. Although  $|\Phi_3(r)|$  gives the radial distribution around the absorbing atom, the EXAFS phase shift function in the Fourier transformation causes the peaks to be shifted to smaller distances [27]. This is indicated by including a peak shift  $\alpha$  symbolically in the ordinate for  $|\Phi_3(r)|$  in Figs 6 and 8. Qualitative comparisons of the radial distribution functions for the doped materials and the model compounds indicate that EXAFS in the 100Y [Figs 5(a) and 6(a)] and 100Zr [Figs 5(b) and 6(b)] samples are similarly dominated by the cation–oxygen nearest neighbor (NN) shell; the cation–cation next nearest neighbor (NNN) shell cannot be clearly identified. The radial distribution function for the 1000Y sample shows the same features as the YAG standard sample. The large difference in the radial distribution functions between the 100Y and 1000Y samples, and the very similar radial distribution functions for 1000Y and YAG samples, indicate that most of the dopant in the 1000Y sample is precipitated in the form of YAG, and this is consistent with the estimate from STEM data that ~87% of the total dopant in the 1000Y sample appears as the YAG phase [17]. There are no second phase precipitates in the 100Y and 100Zr samples, so the radial distribution functions for the 100Y and 100Zr reflect the structural environments of dopant sites in alumina grain boundaries, and to some extent in the bulk lattice.

Quantitative fitting of the first shell of the EXAFS data of the 100Y and 100Zr samples gives the average coordination number and the average NN cation–oxygen bond length around the largely grain boundary segregated Y and Zr, and those results are summarized in Table 2. Y–O and Zr–O nearest neighbor  $k^3\chi(k)$  function used in fitting for 100Y and 100Zr samples are shown in Fig. 7, in

which the Fourier filtering range for Y–O NN in the 100Y sample is from 1.1 to 2.3  $\text{\AA}$ , and for Zr–O NN in the 100Zr sample is 1.0–2.2  $\text{\AA}$ , as shown in Figs 6(a) and (b). Deviations between calculated and experimental  $k^3\chi(k)$  functions for the 100Y and 100Zr samples in Fig. 7 are similar to those obtained in fitting Y–O nearest neighbors in 1000Y and  $\text{Y}_2\text{O}_3$  samples or Zr–O nearest neighbors in  $\text{ZrO}_2$ , using theoretical phase shifts and backscattering amplitudes in all cases.

The grain boundary segregated Y is coordinated on average by approximately four oxygens at an average distance of 2.30  $\text{\AA}$ , which is approximately equal to the average Y–O NN bond length, 2.28  $\text{\AA}$ , in cubic  $\text{Y}_2\text{O}_3$  (Table 1), but is much larger than the Al–O NN bond length, 1.91  $\text{\AA}$ , in  $\alpha\text{-Al}_2\text{O}_3$ . However, in both  $\text{Al}_2\text{O}_3$  and  $\text{Y}_2\text{O}_3$ , the cation is coordinated by six oxygens (octahedral configuration). For the 1000Y sample, fitting gives an average Y–O NN bond length of 2.36  $\text{\AA}$ , which is approximately equal to that, 2.35  $\text{\AA}$ , in YAG

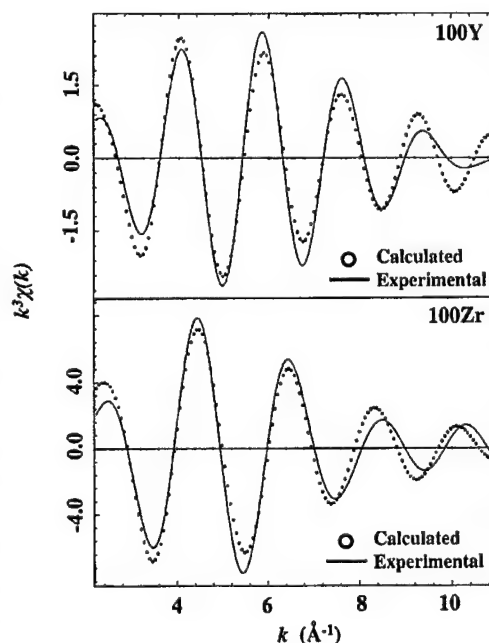


Fig. 7.  $k^3$  weighted nearest neighbor component of  $\chi(k)$  for Y in 100Y and Zr in 100Zr and fitted model calculations (open circles). The Fourier filtering range is 1.1–2.3  $\text{\AA}$  for Y, and 1.0–2.2  $\text{\AA}$  for Zr.

(Table 2). The grain boundary segregated Zr is coordinated on average by five oxygens at an average Zr-O NN distance of 2.14 Å, which is approximately equal to the average Zr-O NN bond length, 2.16 Å, in monoclinic ZrO<sub>2</sub>. However, this Zr-O coordination number is smaller than that of the zirconia polymorphs, for which the minimum Zr-O coordination number is 7.

#### 4. DISCUSSION

##### 4.1. Lattice solid solution, grain boundary segregation, and second phase precipitates

In any substitutional doping system with a tendency for dopant grain boundary segregation, if the dopant concentration is above the solid solution limit a secondary phase based on the dopant may precipitate. In this case, the EXAFS signal is expected to be a superposition of contributions from three different environments: dopant precipitated as a secondary phase, dopant segregated to the grain boundaries or other defects (such as dislocation cores), and dopant as a substitutional solute in the host lattice. Owing to the different atomic configurations in these three structures, the EXAFS spectra carry information about the relative proportion of each of these three states of the dopant. Based on this, the solid solution limit of the Y as a dopant in  $\alpha$ -Al<sub>2</sub>O<sub>3</sub> can be estimated using the EXAFS  $\chi(k)$ .

Significant difference in the EXAFS data of 100 and 1000 p.p.m. Y<sub>2</sub>O<sub>3</sub> doped materials, and the striking similarity between EXAFS data for the 1000 p.p.m. data and the YAG data, indicate that Y has a rather low solid solubility in the bulk or in grain boundaries of  $\alpha$ -Al<sub>2</sub>O<sub>3</sub>. This is consistent with the microstructural evidence that there are many YAG precipitates in the 1000 p.p.m. Y<sub>2</sub>O<sub>3</sub> doped material. If most of the Y atoms are in secondary phase precipitates, their EXAFS contributions will mask those of Y atoms segregated in grain boundaries or located in bulk substitutional sites. Using EXAFS, Loudjani *et al.* [19] attempted to determine the local atomic structure around Y in 1 mol% Y<sub>2</sub>O<sub>3</sub> doped alumina, but their fitted results were actually dominated by the YAG. Later, Loudjani *et al.* also studied 300 p.p.m. Y<sub>2</sub>O<sub>3</sub> doped alumina, and they obtained some information not dominated by the YAG phase [20]. They found a radial distribution function with a high Y-oxygen peak, consistent with our result for the 100Y sample. However, their data also showed a small peak attributed to Y-Al neighbors.

The present investigation of more dilute doping, at the level of 100 p.p.m., and with the materials in the grain size range of less than 2  $\mu$ m, avoids the uncertainties caused by secondary phase precipitates. For the 100Y and 100Zr doped alumina samples, our TEM observations show that at least

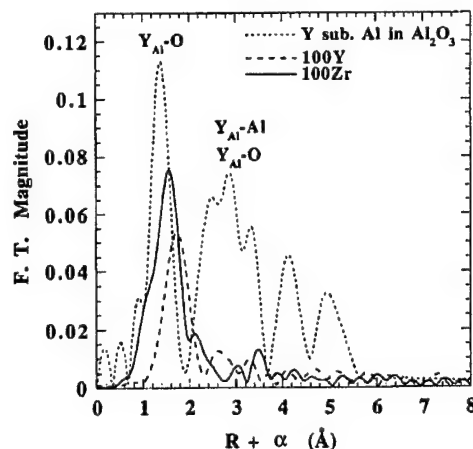


Fig. 8. Comparison of the experimentally obtained radial distribution functions for 100Y and 100Zr samples with that calculated supposing Y substitutes for Al in  $\alpha$ -Al<sub>2</sub>O<sub>3</sub> without relaxing the Y<sub>Al</sub>-O bond length. Note the significant Y<sub>Al</sub>-Al and Y<sub>Al</sub>-O next nearest neighbor peaks in the calculated function which are not present in the experimental functions.

99% of the grains are dislocation free. However, in principle, EXAFS spectra from the 100Y and 100Zr samples are still superpositions of two contributions, one from the dopant in substitutional sites of the  $\alpha$ -Al<sub>2</sub>O<sub>3</sub> lattice and another from the dopant segregated to the Al<sub>2</sub>O<sub>3</sub> grain boundaries.

Figure 8 is a comparison of the radial distribution functions for the 100Y and 100Zr samples with those calculated for Y in a substitutional cation site in  $\alpha$ -Al<sub>2</sub>O<sub>3</sub>. For simplicity, the calculation was without relaxation of the Y<sub>Al</sub>-O bond length. The calculated distribution function has next nearest neighbor Y-Al and Y-oxygen peaks which are nearly as strong as the nearest neighbor Y-oxygen peak. Absence of a significant Y-Al peak for the 100Y sample, or a Zr-Al peak for the 100Zr sample, indicates that most of the Y and Zr atoms in these samples are not in bulk substitutional sites, but are grain boundary segregated, so the resulting atomic configurational parameters describe the dopant surroundings in  $\alpha$ -Al<sub>2</sub>O<sub>3</sub> grain boundaries.

These results also indicate that the solubility of Y and Zr in the bulk lattice of  $\alpha$ -Al<sub>2</sub>O<sub>3</sub> is very low. Available literature data on the lattice solid solution limit of Y and Zr in  $\alpha$ -Al<sub>2</sub>O<sub>3</sub> are quite limited. Based on AES analysis, McCune *et al.* [39] suggested that Y in  $\alpha$ -Al<sub>2</sub>O<sub>3</sub> has a solid solution limit of less than 10 p.p.m.

Based on the observation that grain boundary segregated Y only gives a Y-O NN coordination peak as in the 100Y sample [Figs 5(a) and 6(a)], using the  $k^3\chi(k)$  functions of the 100Y [Fig. 5(a)], 1000Y [Fig. 5(c)], and YAG standard samples [Fig. 5(c)], the ratio of the Y in the grain boundaries and that precipitated as YAG in the 1000Y sample may be estimated. Based on superposition of grain



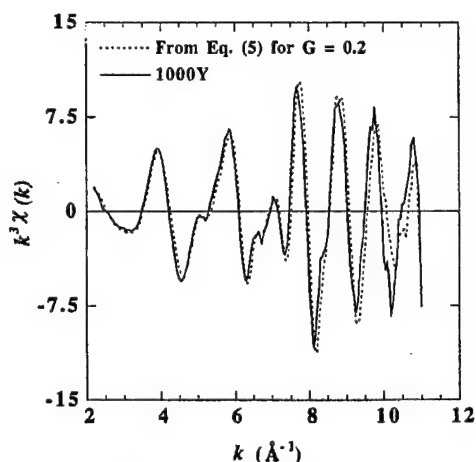


Fig. 9. Comparison of the experimentally obtained  $k^3\chi(k)$  function for the 1000Y sample with that obtained by adding together the  $k^3\chi(k)$  functions of the 100Y and YAG with  $G = 0.2$  in equation (5).

boundary and precipitate contributions for the 1000Y sample, the fraction of the Y segregated in the grain boundaries of alumina in the 1000Y,  $G$ , can be obtained from the following equation:

$$Gk^3\chi_{100Y}(k) + (1 - G)k^3\chi_{YAG}(k) = k^3\chi_{1000Y}(k) \quad (5)$$

where  $k^3\chi_{100Y}(k)$  is the  $k^3\chi(k)$  function for 100Y,  $k^3\chi_{YAG}(k)$  is the  $k^3\chi(k)$  function for YAG, and  $k^3\chi_{1000Y}(k)$  is the  $k^3\chi(k)$  function for 1000Y. Equation (5) gives a  $G$  value of approximately 0.2, and the nearly exact superposition, shown in Fig. 9, for the simulated  $k^3\chi_{1000Y}(k)$  calculated from equation (5) with  $G = 0.2$  and the experimental  $k^3\chi_{1000Y}(k)$  confirm this value. From this result, we conclude that of the 1000 p.p.m.  $Y_2O_3$  in the 1000Y sample, ~20% is segregated to the grain boundaries (200 p.p.m. in the grain boundaries and this corresponds to Y grain boundary excess of ~6.0 atoms/nm<sup>2</sup>) and ~80% is precipitated as YAG.

This result is fairly consistent with the estimate from STEM data for the same material that ~130 p.p.m. of the dopant is segregated to the alumina grain boundaries [17]. We calculated the latter value from the grain boundary excess dopant amount given in Ref. [17] and the average grain size of the doped material.

#### 4.2. Grain boundary segregation sites and relaxation around the segregant

It has been proposed that the ionic size mismatch between the solute and the matrix lattice is the dominant driving force for solute grain boundary segregation [2, 4]. The Y and Zr ions are larger than the Al ions, and they show strong tendency for segregating to  $\alpha-Al_2O_3$  grain boundaries. Information about the sites in  $\alpha-Al_2O_3$  grain boundaries occupied by segregants has been sought both from experiments and from theoretical calculations

[17, 20, 40]. Although the Zr and Y have different ionic sizes, the similarity in their EXAFS radial distribution functions [Figs 6(a), (b), and 8] strongly suggests that the Y and Zr have similar environments, at least within the range of the nearest and next nearest neighbors (within 3 Å). Both distribution functions show prominent cation-oxygen nearest neighbors but no well defined more distant neighbors. This implies that the Y and Zr are indeed similarly and mainly segregated to the alumina grain boundaries. The most plausible sites in the grain boundary of  $\alpha-Al_2O_3$  for the segregants Y and Zr are the substitutional Al ion sites. If Y and Zr substitute for Al ions in the  $Al_2O_3$  grain boundaries, this requires relaxation of the oxygen ions around the segregants. The present results indicate that the oxygens surrounding the Y and Zr are completely relaxed to the same bond lengths as in  $Y_2O_3$  and  $ZrO_2$ . This corresponds to the nearest neighbor oxygen atoms around the yttrium moving outward by 19%, and to those around the zirconium moving outward by 13% with respect to the normal Al-O distance.

Calculations of cation-oxygen relaxation have been reported for both bulk and grain boundary sites. Ching *et al.* [41] have conducted an *ab initio* calculation in which an yttrium replaces an aluminum ion in a supercell of  $\alpha-Al_2O_3$  containing 120 atoms. They found that the nearest neighbor oxygen atoms around the Y moved outward by 8%. This is less than half the relaxation indicated by the present EXAFS measurements if they are interpreted as Y substituting for Al in the grain boundary of  $\alpha-Al_2O_3$ . Cho [40] has also treated the substitution of Al by La and Yb in the basal twin boundary of  $\alpha-Al_2O_3$ . The results confirm that large cation-oxygen relaxation can occur for rare earth dopants in  $Al_2O_3$  grain boundaries.

A good way to view the difference between grain boundary substitutional sites and bulk lattice substitutional sites may be to observe that in the undoped grain boundary some cation sites are locally compressed and some are locally dilated, whereas in the bulk lattice all cation sites are identical. In the grain boundary, the misfitting dopants, which have larger ionic sizes than Al, preferentially occupy the larger sites, so only small local distortions are required to obtain the ideal nearest neighbor distances, like those in the parent oxides. Larger, higher energy distortions would be required in the bulk. The grain boundary sites are energetically favored compared with the bulk substitutional sites, which makes solubility of the dopants in the grain boundaries much higher than in the  $Al_2O_3$  bulk.

#### 4.3. Coordination numbers

The reduced cation-oxygen coordination numbers for the grain boundary segregated Y ( $N = 4.2$ ) and Zr ( $N = 5.0$ ) ions obtained from the EXAFS measurements are believed to be significant. We



estimate uncertainties in these coordination numbers to be only  $\pm 0.5$ , as shown in Table 2. In the perfect lattices of  $\alpha$ - $\text{Al}_2\text{O}_3$  and  $\text{Y}_2\text{O}_3$ , Al and Y each have six oxygen nearest neighbors, and in the polymorphs of zirconia, each Zr has at least seven oxygen nearest neighbors. In this section, we first discuss generally the reduced cation-oxygen coordination number for grain boundary segregated Y and Zr compared with their parent oxides and with  $\alpha$ - $\text{Al}_2\text{O}_3$ . We then discuss the difference in the grain boundary cation-oxygen coordination numbers between Y and Zr.

We believe that the smaller cation-oxygen coordination numbers of the grain boundary segregated Y and Zr, compared with those in their parent oxides and in  $\alpha$ - $\text{Al}_2\text{O}_3$ , are related to the intrinsic structure of alumina grain boundaries [42]. Both theoretical modeling and STEM energy-loss near-edge structure (ELNES) studies of a near  $\Sigma 11$  grain boundary in  $\alpha$ - $\text{Al}_2\text{O}_3$  have established that in this boundary some Al ions are coordinated by only four O atoms [43–45]. Similar results have also been obtained by ELNES analysis of more general grain boundaries in 0.1 mol%  $\text{ZrO}_2$  doped alumina [21]. Apparently, distortions in cation arrangements in  $\alpha$ - $\text{Al}_2\text{O}_3$  grain boundaries, which optimally join together adjacent misoriented crystalline grains, are accommodated by reduced cation-oxygen coordination. The presently observed overall low oxygen coordination number around the grain boundary segregated Y and Zr seems to be consistent with these theoretical models and ELNES observations of grain boundaries in pure and doped  $\alpha$ - $\text{Al}_2\text{O}_3$ .

In considering the reduced cation-oxygen coordination numbers in  $\alpha$ - $\text{Al}_2\text{O}_3$  grain boundaries, it may be useful to think of the grain boundary as being formed by bringing together the free surfaces of two misoriented grains. On the clean, free surfaces, Al ions will, on average, have reduced oxygen coordinations of about 4.5, consisting of three oxygen atoms shared with other Al ions within the bulk, and one or two non-bridging oxygen atoms. When the free surfaces are brought together, with rotations or displacements to accommodate the grain-to-grain misorientation, some of the Al atoms adjacent to the boundary will have a cation-oxygen coordination less than six, and some will have more than six. The undercoordinated sites may be the energetically preferred sites for Y or Zr to substitute for Al.

In  $\alpha$ - $\text{Al}_2\text{O}_3$  and MgO-doped  $\alpha$ - $\text{Al}_2\text{O}_3$ , the thermal grooving induced grain boundary dihedral angles are  $\sim 110^\circ$ , which implies that the grain boundary energy is approximately equal to the air-exposed  $\alpha$ - $\text{Al}_2\text{O}_3$  surface energy [46]. This suggests that the atom coordination in the grain boundary may be similar to that in the free surface, which may retain its cation-oxygen under coordination. However, for a free surface, it is likely that additional oxygen is added by chemisorption from the air, typically as

hydroxyl attachments. We recognize that this discussion is quite speculative. Further experimental studies, combining HRTEM, STEM and EXAFS, together with modeling and simulation calculations, are needed to develop a detailed structural picture of dopant segregation in grain boundaries.

We note that Loudjani *et al.* [20] have used EXAFS to determine the oxygen coordination number around the Y in 300 p.p.m.  $\text{Y}_2\text{O}_3$  doped alumina. They found that the nearest oxygen coordination number around the Y to be only about 2.7 (with a Y–O distance of 2.32 Å). They also noticed an additional shell of oxygen at 2.85 Å with a coordination number of 1.7. Adding those two shells together gives a total Y–O coordination number of 4.4, which is within the range we have obtained, although the second shell Y–O distance is larger than we obtained.

The experimentally observed difference in the cation-oxygen coordination numbers for Y and Zr may be due to differences in the ionic sizes and valences between Y and Zr. Since Y is larger than Zr, and both are larger than Al, large local distortions or structural modifications will be required if Y or Zr replace Al in a grain boundary, the more so for Y than for Zr. To allow relaxation of cation-oxygen nearest neighbor distances to those which are energetically favorable for the larger cations, while retaining a local cation concentration of at least 50% Al, local removal of oxygens, or introduction of oxygen vacancies, may be required. This would lead to a reduced cation-oxygen coordination number for Y and for Zr, with a larger reduction expected for the larger Y atom, as observed experimentally.

The smaller ionic size of Zr compared with Y might lead to greater substitutional solubility of Zr in the  $\text{Al}_2\text{O}_3$  grains. This would give rise to a higher cation-oxygen coordination number for Zr. However, if there were significant substitutional solubility of Zr in the  $\text{Al}_2\text{O}_3$  grains, second neighbor Zr–Al contributions would be expected in the Zr EXAFS distribution functions, which are not found in the present experimental results.

The larger ionic valence of Zr, +4, compared with that of Y, +3, may also play a role in Zr having a larger cation-oxygen coordination number than Y. Simply replacing an  $\text{Al}^{3+}$  ion by a  $\text{Zr}^{4+}$  ion would require a coordination of oxygen around Zr of more than six to maintain local charge neutrality. Similar effects may occur in the grain boundary, leading to  $\text{Zr}^{4+}$  having a larger cation-oxygen coordination than  $\text{Y}^{3+}$ .

#### 4.4. Further implications

Based on the present EXAFS results, the atomic structural environment around the grain boundary segregated Y and Zr may be as illustrated schematically in Fig. 10. In this figure, the classic two-dimensional representations of amorphous and crys-

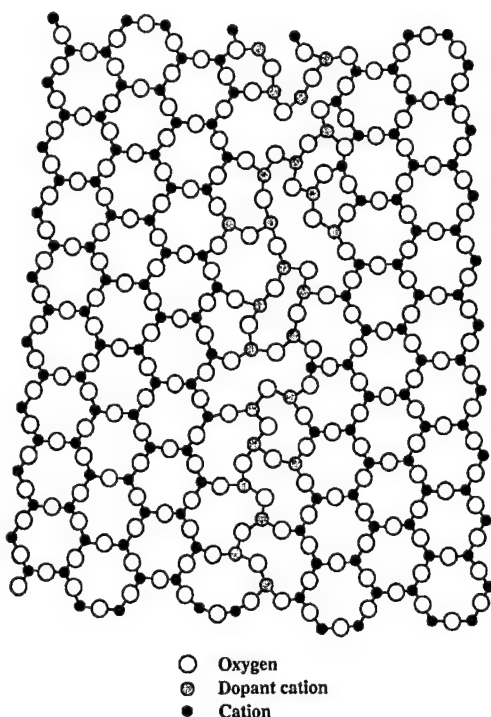


Fig. 10. A two-dimensional schematic drawing showing that each dopant ion segregated to the grain boundary is coordinated by oxygen nearest neighbors at well defined distances, while the next nearest neighbor distances are changing from site to site. The grain boundary segregated ion concentration and the grain boundary width are exaggerated in this drawing.

talline phases are used, such that the oxygens surrounding each dopant ion are ordered and have fixed bond lengths, while the dopant-cation next nearest neighbors are disordered. However, both the concentration of the dopant segregated to the grain boundary and the dopant distribution width around the grain boundary are exaggerated in this illustration.

Also relevant to the present observations is the equilibrium glassy film in liquid phase sintered silicon nitride. This  $\sim 1$  nm thick film composed of  $\text{Si}(\text{N})\text{O}_4$  tetrahedra is sandwiched between the  $\text{Si}_3\text{N}_4$  crystalline grains [47]. Configurationally, the arrangement of the dopant-oxygen cluster in the alumina grain boundary may be similar to the  $\text{Si}(\text{N})\text{O}_4$  tetrahedral arrangement in the glass film between silicon nitride grains. In both cases, the cation-oxygen distance is very well defined, while the cation-cation distance is changing from site to site. However, it should be noted that HRTEM observations indicate that grain boundaries of Y and Zr doped alumina have no more than one or two monolayers of disordered material [21].

It would be expected, in a co-doping system, that the larger dopant ions will selectively occupy the larger sites, and the smaller dopant ions will occupy

the smaller sites. In comparison with random substitutional site occupancy, this would give a more efficient filling of the grain boundary free space when co-doping alumina with two dopants having different ionic sizes. This would also provide a structural basis for the synergistic effect of Nd and Zr co-doping improving the creep resistance of alumina, which has been attributed to the co-doping providing more efficient inhibition of grain boundary mediated transport [14].

The complete relaxation of the cation-oxygen bond lengths to that in the parent oxides observed in the EXAFS measurements for the 100Y and 100Zr samples is noteworthy. A complete relaxation of the bond length between the dopant and the oxygen suggests that the grain boundary segregated ions are in stable positions. However, it remains to be established how the segregant may itself modify the grain boundary structure.

## 5. CONCLUSIONS

EXAFS analysis of  $\text{Y}_2\text{O}_3$  and  $\text{ZrO}_2$  doped ultra-high purity alumina indicates that dopants at the level of 100 p.p.m. are mainly segregated to the alumina grain boundaries. This is generally consistent with SIMS and STEM studies of the grain boundary segregation behavior of rare earth and  $\text{ZrO}_2$  doped alumina. EXAFS data indicate that the grain boundary segregated Y and Zr ions have well defined dopant (Y, Zr)-O nearest neighbor coordinations, but that the dopant (Y, Zr)-cation next nearest neighbor coordination is changing from site to site. The dopant (Y, Zr)-oxygen nearest neighbor bond length in the grain boundary, on average, is fully relaxed to that in the dopant cation parent oxides. However, the dopant (Y, Zr)-O nearest neighbor coordination number is  $\sim 30\%$  smaller than that in their parent oxides.

It may be speculated that the grain boundary segregated Y and Zr occupy substitutional Al sites in the boundaries. The overall pattern of those local atomic structural features around the grain boundary segregated dopant ions reflects two factors: the intrinsic structural imperfection of the alumina grain boundary and the role of the ionic size mismatch between the dopant and the host lattice. However, it remains to be established to what degree the valence difference between the dopant cation  $\text{Zr}^{4+}$  and the host cation  $\text{Al}^{3+}$  influences the local structure.

*Acknowledgements*—The authors would like to thank Joseph Woicik and Zugen Fu of NIST for assistance in beamline operation and data acquisition, and for beneficial discussions; and Y. Ito and J. M. Rickman for further helpful discussions. This research is supported by the U.S. Air Force Office of Scientific Research under Contract No. F49620-98-1-0117 (monitored by A. Pechenik) and by the U.S. Office of Naval Research under Contract No. N00014-99-1-0236 (monitored by S. Fishman). EXAFS

*old grant*

measurements were made at NSLS, Brookhaven National Laboratory, which is supported by the DoE.

# REFERENCES

- Rittner, J. D. and Seidman, D. N., *Acta mater.*, 1997, **45**, 3191.
- Li, C. W. and Kingery, W. D., in *Advances in Ceramics, Vol. 10, Structure and Properties of MgO and Al<sub>2</sub>O<sub>3</sub> Ceramics*, ed. W. D. Kingery. American Ceramic Society, Columbus, OH, 1984, pp. 368–378.
- Thompson, A. M., Soni, K. K., Chan, H. M., Harmer, M. P., Williams, D. B., Chabala, J. M. and Levi-Setti, R., *J. Am. Ceram. Soc.*, 1997, **80**, 373.
- Johnson, W. C., *Metall. Trans. A*, 1977, **8A**, 1413.
- Hondros, E. D. and Seah, M. P., *Int. metall. Rev.*, 1977, **22**, 262.
- Gall, M. L., Huntz, A. M., Lesage, B., Monty, C. and Bernardini, J., *J. Mater. Sci.*, 1995, **30**, 201.
- French, J. D., Zhao, J., Harmer, M. P., Chan, H. M. and Miller, G. A., *J. Am. Ceram. Soc.*, 1994, **77**, 2857.
- Wakai, F., Nagano, T. and Iga, T., *J. Am. Ceram. Soc.*, 1997, **80**, 2361.
- Cho, J., Harmer, M. P., Chan, H. M., Rickman, J. M. and Thompson, A. M., *J. Am. Ceram. Soc.*, 1997, **80**, 1013.
- Lartigue, S., Carry, C. and Priester, L., *J. Phys. (Paris)*, 1990, **C1(51)**, 985.
- Lartigue, S., Priester, L., Dupau, F., Gruffel, P. and Carry, C., *Mater. Sci. Engng*, 1993, **A164**, 211.
- Cho, J., Chan, H. M., Harmer, M. P. and Rickman, J. M., *J. Am. Ceram. Soc.*, 1998, **81**, 3001.
- Gulgun, M. A., Putlayev, V. and Ruhle, M., *J. Am. Ceram. Soc.*, 1999, **82**, 1849.
- Li, Y., Wang, C. M., Chan, H. M., Rickman, J. M., Harmer, M. P., Chabala, J. M., Gavrilov, K. L. and Levi-Setti, R., *J. Am. Ceram. Soc.*, 1999, **82**, 1497.
- Cook, R. F. and Schrott, A. G., *J. Am. Ceram. Soc.*, 1988, **71**, 50.
- Taylor, R. I., Coad, J. P. and Brook, R. J., *J. Am. Ceram. Soc.*, 1974, **57**, 539.
- Bruley, J., Cho, J., Chan, H. M., Harmer, M. P. and Rickman, J. M., *J. Am. Ceram. Soc.*, in press.
- Clarke, D. R., *J. Am. Ceram. Soc.*, 1980, **63**, 339.
- Loudjani, M. K., Roy, J. and Huntz, A. M., *J. Am. Ceram. Soc.*, 1985, **68**, 559.
- Loudjani, M. K., Huntz, A. M. and Cortes, R., *J. Mater. Sci.*, 1993, **28**, 6466.
- Kaneko, K., Gemming, T., Tanaka, I. and Mulleijans, H., *Phil. Mag. A*, 1998, **77**, 1255.
- Kaplan, W. D., Mulleijans, H., Ruhle, M., Rodel, J. and Claussen, N., *J. Am. Ceram. Soc.*, 1995, **78**, 2841.
- Tang, C., Georgopoulos, P. and Cohn, J. B., *J. Am. Ceram. Soc.*, 1982, **65**, 625.
- Li, P., Chen, I. W. and Penner-Hahn, J. E., *J. Am. Ceram. Soc.*, 1994, **77**, 118.
- Kavanagh, K. L. and Cargill, G. S. III, *Phys. Rev. B*, 1992, **45**, 3323.
- Wang, C. M., Cho, J., Chan, H. M., Harmer, M. P. and Rickman, J. M., *J. Am. Ceram. Soc.*, submitted.
- Teo, B. K., *EXAFS: Basic Principles and Data Analysis*. Springer-Verlag, New York, 1986.
- McMaster, W. H., Kerr Del Grande, N., Mallett, J. H. and Hubbell, J. H., Compilation of X-ray cross section, Report No. UCRL-50174 Sec. II, Rev. 1, Lawrence Radiation Laboratory, Livermore, CA, May 1969. National Technical Information Service, Springfield, VA.
- WinXAS 97, version 1.0, written by Thorsten Ressler, available from T. Ressler, E-mail: Ressler@FHI-Berlin.mpg.de.
- Rehr, J. J., Mustre de Leon, J., Zabinsky, S. I. and Albers, R. C., *J. Am. chem. Soc.*, 1991, **113**, 5135.
- Jaklevic, J., Kirby, J. A., Klein, M. P., Robertson, A. S., Brown, G. S. and Eisenberger, P., *Solid St. Commun.*, 1977, **23**, 679.
- Boehme, R. F., Cargill, G. S. III, Weber, W. and Jackson, T., *J. appl. Phys.*, 1985, **58**, 811.
- Ishizawa, N., Miyata, T., Minato, I., Marumo, F. and Iwai, S., *Acta crystallogr.*, 1980, **B36**, 228.
- Bonnet, M. and Delapalme, A., *Acta crystallogr.*, 1975, **A31**, 264.
- Euler, F. and Bruce, J. A., *Acta crystallogr.*, 1965, **19**, 971.
- Smith, D. K. and Newkirk, H. W., *Acta crystallogr.*, 1965, **18**, 983.
- Howard, C. J., Kisi, E. H., Roberts, R. B. and Hill, R. J., *J. Am. Ceram. Soc.*, 1990, **73**, 2828.
- Shannon, R. D., *Acta crystallogr.*, 1976, **A32**, 751.
- McCune, R. C., Donlon, W. T. and Ku, R. C., *J. Am. Ceram. Soc.*, 1986, **69**, C196.
- Cho, J., Ph.D. thesis, Lehigh University, 1998.
- Ching, W. Y., Xu, Y. N. and Ruhle, M., *J. Am. Ceram. Soc.*, 1997, **80**, 3199.
- Exner, M. and Finnis, M. W., *Mater. Sci. Forum*, 1996, **207–209**, 225.
- Kenway, P. R., *J. Am. Ceram. Soc.*, 1994, **77**, 349.
- Hoche, T., Kenway, P. R., Kleebe, H. J., Ruhle, M. and Morris, P. A., *J. Am. Ceram. Soc.*, 1994, **77**, 339.
- Mo, S. D., Ching, W. Y. and French, R. H., *J. Am. Ceram. Soc.*, 1996, **79**, 627.
- Handwerker, C. A., Dynys, J. M., Cannon, R. M. and Coble, R. L., *J. Am. Ceram. Soc.*, 1990, **73**, 1371.
- Kleebe, H. J., Cinibulk, M. K., Tanaka, I., Bruley, J., Vetrano, J. S. and Ruhle, M., in *Tailoring of Mechanical Properties of Si<sub>3</sub>N<sub>4</sub> Ceramics*, ed. M. J. Hoffmann and G. Petzow. Kluwer Academic, Dordrecht, 1993, pp. 259–274.

# Coble-creep response and variability of grain-boundary properties

W.S. Tong, J.M. Rickman, H.M. Chan, and M.P. Harmer

*Department of Materials Science and Engineering, Lehigh University, Bethlehem, Pennsylvania 18015*

(Received 24 September 2001; accepted 12 November 2001)

A microstructural model of steady-state creep that couples grain-boundary transport, micromechanics, and grain sliding is employed to investigate the grain-boundary diffusional creep response of an idealized microstructure with variable boundary diffusivities. Both numerical and analytical methods were used to determine the stress state and, in some cases, the strain rate associated with an applied uniaxial, tensile stress. Various types of boundaries are considered, and the implications of our results for more general microstructures are discussed.

## I. INTRODUCTION

The long-time strain response of creeping systems subjected to a uniaxial stress is an important design consideration for both metals and ceramics. The creep behavior of these systems is often complex and governed by various mechanisms, including those involving diffusional transport and grain-boundary dislocation motion. In particular, diffusional creep occurs via a mass flux in either the bulk and/or at grain boundaries driven by a gradient in the chemical potential field attending the stressed state<sup>1–8</sup> while dislocation-based creep occurs via the climb and glide of grain-boundary dislocations.<sup>9–12</sup> The dominant mechanism for a given system can sometimes be inferred from the power-law dependence of the strain rate on stress and average grain size by a comparison of extracted exponents with those predicted by simple calculations.

The functional form of the grain-boundary diffusional creep law has been determined analytically from highly idealized microstructural models that couple mass transport and grain micromechanics and are based on either the behavior of a representative grain<sup>3,13</sup> or the response of spatially uniform systems consisting of a repeat unit.<sup>14,15</sup> The restrictive assumptions inherent in these simple models make them tractable while inevitably limiting their applicability to real systems. More sophisticated microstructural models are amenable to numerical analysis and have been employed recently to assess the impact of variable grain size and shape on aggregate creep response.<sup>16,17</sup> It should be noted, however, that in many cases the strain rate dependence on grain size is unchanged in more complex microstructures, apart from a prefactor, as can be seen from dimensional analysis.

An important factor affecting creep behavior that has not been considered in earlier microstructural models is the variability in grain-boundary properties, especially

the diffusivity. In general, the boundary diffusivity correlates with detailed boundary geometry, and some empirical relations have been formulated to quantify this interrelationship between structure and kinetics.<sup>18,19</sup> Furthermore, there is evidence that grain-boundary segregation can inhibit diffusion in some systems by constricting nominally fast diffusion pathways.<sup>20</sup> Indeed, this “blocking” effect has been invoked to explain the observed decrease in secondary creep rate in selectively doped ceramic oxides.<sup>20–22</sup>

With this in mind, the purpose of this short paper is to model both analytically and numerically the grain-boundary diffusional creep response of an idealized microstructure with variations in boundary diffusivity to investigate the stress state of this system and deduce an appropriate creep law. This is accomplished by modifying a microstructural model of creep that combines grain-boundary transport, micromechanics, and grain sliding to determine the stress state, strain rate, and initial microstructural changes in the steady-state regime. Having obtained results for selected boundary configurations, we then consider the implications of our work for more realistic configurations and explore the origin of an anomalous stress dependence of the creep response.<sup>23</sup>

## II. METHODOLOGY

### A. General

The methodology that we employ here is, apart from small differences, discussed in some detail elsewhere,<sup>16,17</sup> and so we simply outline below the salient features of the approach. We wish to describe the onset of the steady-state diffusional creep response of a microstructure subjected to an applied uniaxial, tensile stress  $\sigma_A$  at temperature  $T$ . We employ a two-dimensional, regular hexagonal network, consisting of  $N$  rigid grains,

enclosed in a unit cell that is either periodic or, in this work, subjected to a set of prescribed stress or flux boundary conditions. In particular, we inscribe the network in a rectangular unit cell so the requisite number of half segments terminates on the cell boundary and the appropriate constraints can be applied at the boundary nodes.

In this system it is assumed that creep is dominated by grain-boundary diffusion, and therefore from the theory of linear irreversible thermodynamics,<sup>24</sup> there is a flow of matter induced by gradients in the chemical potential, subject to the constraints of mechanical equilibrium. The local chemical potential is a function of the normal stress  $\sigma$  on a boundary segment and the associated flux is given by

$$j = \frac{D}{kT} \frac{d\sigma}{dw} \quad (1)$$

where  $D$  is the local grain boundary diffusivity,  $w$  is the coordinate along the segment,  $T$  is the absolute temperature, and  $k$  is Boltzmann's constant.

For a given boundary the speed of recession or approach of neighboring grains is

$$v = - \frac{\delta D \Omega}{kT} \frac{d^2 \sigma}{dw^2} \quad (2)$$

If it is further assumed that the plating speed is constant (i.e.,  $v$  is constant) along a segment, then the corresponding boundary stress may be parameterized by a quadratic form in  $w$ . Thus, a complete solution to this problem amounts to calculating the three unknown stress parameters for every segment. This is accomplished by imposing the following constraints: (i) The boundary conditions are applied at the external (i.e., boundary) nodes. (ii) The flux is conserved at each internal node. (iii) Normal stress  $\sigma$  is continuous at each internal node. (iv) The net force on each grain is zero. (v) The plating and sliding rates are compatible such that a contiguous structure is produced without boundary cracks on internal segments.<sup>16</sup>

## B. Implementation

For convenience, the conservation laws and boundary conditions listed above are written in terms of the inhomogeneous matrix equation  $Ax = b$ , where  $A$  is the matrix of coefficients corresponding to the conservation laws and boundary conditions listed above,  $x$  is a column vector consisting of the stress parameters, and  $b$  contains information on the boundary conditions and external forces. The inversion of this equation is problematic for two reasons: (i) the coefficients in the plating-rate equations are divergent for a regular, hexagonal structure, and (ii)  $A$  may be poorly conditioned. The former difficulty is

overcome by a slight (random) displacement of the nodes, although this breaks translational symmetry, while the latter difficulty is addressed by applying specialized numerical techniques.

One approach that can be used to invert an ill-conditioned matrix is singular-value decomposition,<sup>25</sup> a procedure that amounts to identifying and then removing eigenvectors in the nullspace of  $A$  prior to inversion. Alternatively, it is possible to regularize the matrix system,<sup>25</sup> and we employ a variation on this method here by solving the following modified system of equations

$$[A^T A + \lambda I] X = A^T b + \lambda X_0 \quad (3)$$

where  $\lambda$  is a tunable parameter controlling the extent of regularization and  $X_0$  is a trial solution for  $X$ . Equation (3) is obtained by finding the extremum of a weighted functional of  $X$  and a judiciously chosen  $X_0$ , thereby constraining the solution vector to be "near"  $X_0$ . In practice, we choose for  $X_0$  the solution corresponding to a regular, hexagonal lattice with all segments having the same diffusivity (see below) and then adjust  $\lambda$  so as to minimize the residual  $|AX - b|$ . It has been found that this scheme is both robust and reversible; i.e.,  $X_0$  can be recovered as a solution vector upon starting from a different trial solution.

## III. RESULTS

We now present the results of several calculations that were performed for a model system consisting of 125 grains under uniaxial tension and were subjected to a zero-flux boundary condition, as seen in Fig. 1(a). Consider, for example, a simple benchmark in which there is a single grain-boundary diffusivity  $D$  such that all trijunctions are equivalent. By invoking the aforementioned conservation laws and symmetry arguments, one deduces the stress profiles<sup>14</sup> along the two inequivalent segment types [see Fig. 1(b)] to be

$$\begin{aligned} \frac{\sigma_1}{\sigma_A} &= -6s^2 + 6s + \frac{1}{2} \quad , \\ \frac{\sigma_2}{\sigma_A} &= +3s^2 - 3s + \frac{1}{2} \quad , \end{aligned} \quad (4)$$

where  $s = w/G$  is a dimensionless segment coordinate and  $G$  is the segment length. (It should be noted that for the zero-flux boundary conditions implemented here, the range of  $s$  for some half segments [0.5, 1]. For these segments, the corresponding stress coefficients can be obtained by the substitution  $s \rightarrow s + 1/2$ .) Figure 2 shows, as expected, the excellent agreement between the numerical and the analytical results [Eq. (4)] obtained for the path highlighted in Fig. 1(a).

Next consider two illustrative cases in which there are distinct diffusivities  $D$  and  $D^*$  such that  $D^*/D = \alpha$ . For simplicity, it is assumed that all plates are flat despite the variable diffusivities. In the first case all segments normal to the direction of the applied stress (i.e., vertical segments) have diffusivities  $D^*$  while the remaining segments have the baseline diffusivity  $D$ . Again, all trijunctions are equivalent in this system, and therefore, proceeding as above, one obtains

$$\frac{\sigma_1}{\sigma_A} = \frac{-18}{2 + \alpha} s(s-1) + \frac{3\alpha}{2(2 + \alpha)},$$

$$\frac{\sigma_2}{\sigma_A} = \frac{+9}{2 + \alpha} s(s-1) + \frac{3\alpha}{2(2 + \alpha)}. \quad (5)$$

Figure 3 shows the excellent agreement between stresses obtained both numerically and analytically along the chosen path for  $\alpha = 0.6$  and  $\alpha = 2.5$ .

In the second case the diffusivity of a single, defected vertical segment is taken to be  $D^*$  while the remaining segments have the baseline diffusivity  $D$ . Unlike the previous examples, the trijunctions here are inequivalent, and so an analytical approximation to the stresses is possible only within the limits of perturbation theory (i.e.,  $|\alpha - 1|$  is small). Figure 4 illustrates the simplifying assumptions needed for a tractable analysis here, namely that (i) despite the broken translational symmetry there

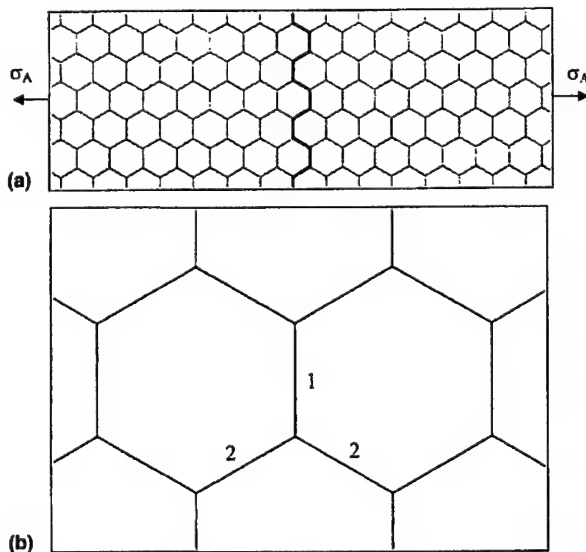


FIG. 1. (a) Model microstructure consisting of 125 regular hexagonal grains under uniaxial tension. The stress profiles are determined along the highlighted path when the system is subject to zero-flux boundary conditions. (b) The two inequivalent segment types as employed in Eq. (4). Note that for this configuration material plates onto segments of type 1 and off of type 2.

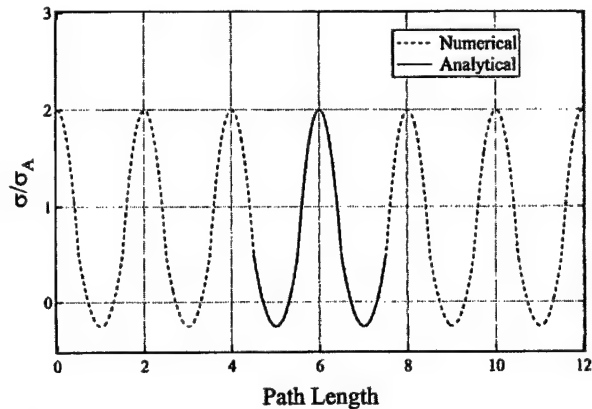


FIG. 2. The normalized stress  $\sigma/\sigma_A$  profile for the path shown in Fig. 1(a) with the assumption that all grain boundaries have the same diffusivity. The numerical and analytical results shown here are in excellent agreement.

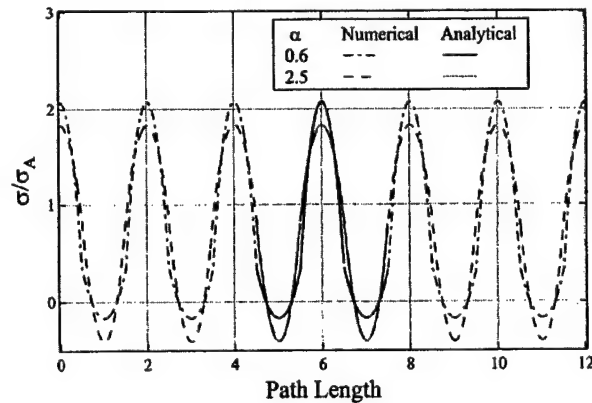


FIG. 3. The normalized stress profile for the path shown in Fig. 1(a) with the assumption that the ratio of the diffusivities on segment types 1 and 2 is  $\alpha$ . The numerical and analytical results shown here for  $\alpha = 0.6$  and 2.5 are in excellent agreement.

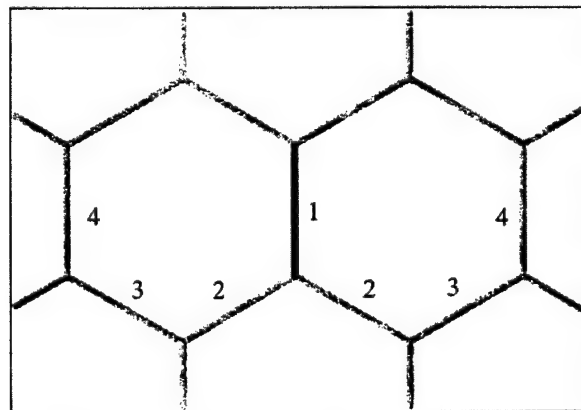


FIG. 4. A portion of a microstructure containing a single, defective segment. Segment types 2-4 represent those with nontrivial responses to the defect (segment 1). Note that two mirror planes of symmetry pass through the defect segment (through and at the perpendicular bisector). Like Fig. 1, material plates onto the vertical segment types (1,4) and off of the zig-zag segment types (2,3).



remain both vertical and horizontal mirror planes through the defected segment and (ii) the associated stress perturbation decays over a distance of one grain diameter. These assumptions have the benefit of reducing the number of independent segments considered here, although this consequently limits the accuracy of the predicted  $\sigma(s)$  (but not the plating rates) of nearby vertical segments. The stress distributions for the four segment types modified by the defect are found to be

$$\begin{aligned}\frac{\sigma_1}{\sigma_A} &= \frac{-48}{1+7\alpha} s(s-1) + \frac{4(-1+2\alpha)}{1+7\alpha}, \\ \frac{\sigma_2}{\sigma_A} &= \frac{+3(3+13\alpha)}{2(1+7\alpha)} s^2 + \frac{-3(3+5\alpha)}{1+7\alpha} s + \frac{1}{2}, \\ \frac{\sigma_3}{\sigma_A} &= \frac{+3(-1+9\alpha)}{1+7\alpha} s(s-1) + \frac{1}{2}, \\ \frac{\sigma_4}{\sigma_A} &= \frac{-48\alpha}{1+7\alpha} s(s-1) + \frac{1}{2}.\end{aligned}\quad (6)$$

Figure 5 shows the stresses obtained both analytically and numerically along the chosen path for  $\alpha = 0.8$  and  $\alpha = 1.5$ . The agreement between the two stress profiles is impressive given that the required movement of the nodes and the imposition of zero-flux boundary conditions further break the translational symmetry in the numerical calculation. The results from this last case permit us to determine the strain response for a system containing a dilute concentration of identically defected segments. In this limit the strain rate is approximately

$$\dot{\epsilon} = A (\rho^*) \frac{\sigma_A}{G^3}, \quad (7)$$

where the prefactor  $A$  is given by

$$A(\rho^*) = - \left( \frac{2\delta\Omega}{\sqrt{3}kT} \right) [D^*B^*\rho^* + 2DB'\rho^* + DB(1-3\rho^*)], \quad (8)$$

and  $\rho^*$  is the fraction of vertical defected segments. The plating constants for the defected segment, its neighbor, and a perfect segment are  $B^* = -96/(1+7\alpha)$ ,  $B' = -96\alpha/(1+7\alpha)$ , and  $B = -12$ , respectively. We note that  $A(0) = 4\sqrt{3}\delta\Omega/(kT)$  in agreement with previous calculations.<sup>14</sup>

As might be expected intuitively, it should be noted that the overall change in creep response modifies only the prefactor for a dilute solution of defected segments given that each defected segment is essentially independent in this limit. We discuss below the possible change in stress and grain size exponents that might result from spatial correlations among such segments.

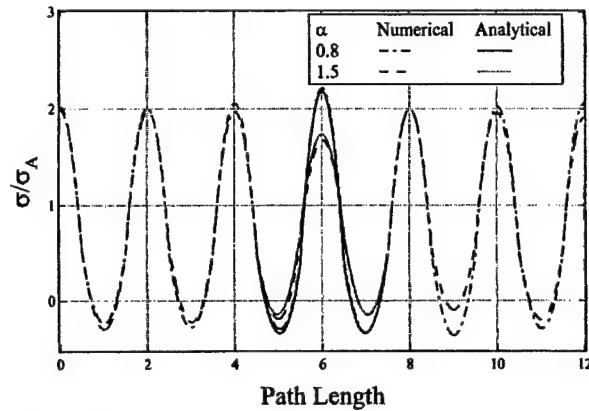


FIG. 5. The normalized stress profile along the path shown in Fig. 1(a) with the assumption that there is a single, defective segment. The numerical and approximate analytical results shown here for  $\alpha = 0.8$  and  $1.5$  are in good agreement even though  $\alpha - 1 = 0.5$  in the latter case.

#### IV. DISCUSSION AND CONCLUSIONS

The diffusional creep response of a microstructure having variable grain-boundary diffusivities was investigated here for several prototypical systems. In each case the spatial distribution of stresses was calculated, both numerically and analytically, and the steady-state strain rate determined in the limit of a dilute concentration of defected segments. In this limit the power-law expression for the strain rate [Eq. (7)] is modified by a change in the overall prefactor  $A$ .

We note that while the methodology employed here is based on that introduced in earlier work,<sup>16,17</sup> the incorporation of variability in grain-boundary diffusivities presents new challenges that, to our knowledge, have not been treated quantitatively elsewhere. The variability of properties in this combined microstructural-mechanical model sometimes leads to numerical difficulties in solving the associated system of coupled equations, as discussed above. Indeed, the identification of a solution that is consistent with the constraint of plating-rate compatibility is often nontrivial. For example, in the case of a single, defective vertical segment, a numerical solution to the problem is needed to fully reflect the imposed boundary conditions and the different plating rates on the various boundary segments. The perturbative solution outlined in the previous section does, however, provide some insight into the nature of this solution. Having obtained a solution, this single segment can then serve as a building block for more complex structures with many defected segments.

More generally, it is of interest to determine the creep response for a system in which defect-defect correlations are significant. Such correlations can, in some cases, lead to relatively large local stresses and a number of preferred diffusion pathways. Other workers have suggested

that boundary correlations can change the effective length scales in the system,<sup>26-28</sup> and so certain material properties, including creep response, may depend on the linear dimensions of clusters of grains sharing the same type of boundary. Thus, the effective stress and grain-size exponents in the creep law may be modified, and our model can be generalized to include nonlinear stress-dependent driving forces. An assessment of the impact of boundary correlations on creep, as inferred from a configurational average of creep response, is the subject of ongoing work.

## ACKNOWLEDGMENTS

We gratefully acknowledge helpful interactions with Dr. P. Hazzledine and Dr. J. Schneibel. We also wish to thank the United States Air Force Office of Scientific Research for their support under Grant No. F49620-94-1-0284, F49620-98-1-0117, and F49620-01-1-0184. W.S. Tong wishes to also thank the Pennsylvania Department of Community and Economic Development through the Pennsylvania Technology Development Authority.

*Current*

## REFERENCES

1. F.R.N. Nabarro, *Phil. Mag.* **16**, 75 (1948).
2. C. Herring, *J. Appl. Phys.* **21**, 437 (1950).
3. H.W. Green II, *J. Appl. Phys.* **41**, 1679 (1970).
4. B. Burton, *Trans Tech Publications, Diffusional Defect Monogr. Ser.* (1977).
5. I.M. Lifshitz, *Sov. Phys. JETP* **14**, 909 (1963).
6. R. Raj and M.F. Ashby, *Metall. Trans.* **2**, 113 (1971).
7. M.F. Ashby, *Surf. Sci.* **31**, 498 (1972).
8. M.F. Ashby, R. Raj, and R.C. Gifkins, *J. Am. Ceram. Soc.* **71**, 832 (1970).
9. A. Arieli and A.K. Mukherjee, *Mater. Sci. Eng.* **45**, 61 (1980).
10. A. Ball and M.M. Hutchison, *J. Metal. Sci.* **3**, 1 (1969).
11. J.H.H. Gittus, *J. Eng. Mater. Tech. Ser. H*, **99**, 244 (1977).
12. H.W. Hayden, S. Floreen, and P.D. Goodell, *Metall. Trans.* **3**, 244 (1972).
13. R.L. Coble, *J. Appl. Phys.* **34**, 1679 (1963).
14. J.R. Spingarn and W.D. Nix, *Acta Metall.* **26**, 1389 (1978).
15. J.H. Schneibel, R.L. Coble, and R.M. Cannon, *Acta Metall.* **29**, 1285 (1981).
16. P.M. Hazzledine and J.H. Schneibel, in *Superplasticity in Metals, Ceramics, and Intermetallics*, edited by M.J. Mayo, M. Kobayashi, and J. Wadsworth (Mat. Res. Soc. Symp. Proc. **196**, Pittsburgh, PA, 1990), p. 15.
17. P.M. Hazzledine and J.H. Schneibel, *Acta. Metall. Mater.* **41**, 1253 (1993).
18. V.T. Borisov, V.M. Golikov, and G.V. Scherbedinskiy, *Phys. Met. Metall.* **17**, 80 (1964).
19. A.P. Sutton and R.W. Balluffi, *Interfaces in Crystalline Materials* (Clarendon Press, Oxford, United Kingdom, 1995).
20. Y. Li, C. Wang, H.M. Chan, J.M. Rickman, and M.P. Harmer, *J. Am. Ceram. Soc.* **82**, 1497 (1999).
21. J. Cho, M.P. Harmer, H.M. Chan, J.M. Rickman, and A.M. Thompson, *J. Am. Ceram. Soc.* **80**, 1013 (1997).
22. J. Cho, H.M. Chan, M.P. Harmer, and J.M. Rickman, *J. Am. Ceram. Soc.* **81**, 3001 (1998).
23. Y-Z. Li, C. Wang, H.M. Chan, J.M. Rickman, M.P. Harmer, J. Chabala, K.L. Gavrilov, and R. Levi-Setti, *J. Am. Ceram. Soc.* **82**, 1497 (1999).
24. S.R. deGroot and P. Mazur, *Non-equilibrium Thermodynamics* (North-Holland, New York, 1962).
25. W.H. Press, S.A. Teukolsky, W.T. Vetterling, and B.P. Flannery, *Numerical Recipes in Fortran: The Art of Scientific Computing* (Cambridge University Press, Cambridge, 1992).
26. C.S. Nichols, R.F. Cook, D.R. Clarke, and D.A. Smith, *Acta Metall. Mater.*, **39**, 1657 (1991).
27. C.S. Nichols, R.F. Cook, D.R. Clarke, and D.A. Smith, *Acta Metall. Mater.* **39**, 1667 (1991).
28. C.S. Nichols and D.R. Clarke, *Acta. Metall. Mater.* **39**, 995 (1991).



# X-ray Absorption Near-Edge Structure of Grain-Boundary-Segregated Y and Zr in Creep-Resistant Alumina

C. M. Wang,<sup>\*,†</sup> G. Slade Cargill III, Helen M. Chan,<sup>\*</sup> and Martin P. Harmer<sup>\*</sup>

Materials Research Center, Lehigh University, Bethlehem, Pennsylvania 18015

X-ray absorption near-edge structure (XANES) depends on stereochemical features of coordination polyhedra around probe atoms. *K*-edge XANES of Y and Zr segregated in alumina grain boundaries has been obtained and analyzed using metallic Y and Zr,  $Y_2O_3$ , YAG, and monoclinic  $ZrO_2$  as standards. Grain-boundary-segregated Y and Zr show a positive chemical shift, and the magnitude of the shift, as compared with that of  $Y_2O_3$  and  $ZrO_2$ , respectively, is different for Y and Zr, indicating that, relative to  $Y_2O_3$  and  $ZrO_2$ , charge transfers for the grain-boundary-segregated Y and Zr are different. This result is also supported by the strength of the threshold resonance. A pre-edge shoulder is seen in *K*-edge XANES for grain-boundary-segregated Y and Zr but not for  $Y_2O_3$  and  $ZrO_2$ . This shoulder is attributed to the  $1s \rightarrow 4d$  transition, which is normally forbidden, but can occur because of *d-p* mixing, which is favored by a tetrahedral coordination configuration. These results suggest that some of the grain-boundary-segregated Y and Zr have coordination configurations with a well-defined tetrahedral symmetry. The XANES results are compared with those obtained from EXAFS. Implications of these results for understanding of the enhanced creep resistance in alumina are also discussed.

## I. Introduction

DOPANTS Y and Zr at the level of 100 to 1000 ppm have been found to enhance alumina creep resistance by up to 2 orders of magnitude.<sup>1-8</sup> A variety of microscopic and spectroscopic methods have been used to investigate the structural environment of the grain-boundary-segregated dopant ions. These methods have included Auger electron spectroscopy (AES),<sup>9</sup> X-ray photoelectron spectroscopy (XPS),<sup>10</sup> energy dispersive X-ray spectroscopy (EDS) in a scanning electron microscope (SEM) and in a scanning transmission electron microscope (STEM),<sup>11-13</sup> electron energy-loss spectroscopy (EELS), SIMS<sup>14</sup> and extended X-ray absorption fine structure (EXAFS).<sup>15-18</sup> AES, XPS, EDS, and SIMS have been used mainly to investigate grain boundary segregation concentrations and segregant distribution profiles. The structures of alumina grain boundaries with Ca and Zr segregation have also been investigated using high-resolution transmission electron microscopy (HRTEM).<sup>19,20</sup> STEM measurements by Bruley *et al.*<sup>11</sup> revealed that Y and La dopant ions were segregated to a narrow region at alumina grain boundaries. Assuming a segregation layer thickness of  $\sim 1$  nm, the fraction of cation sites occupied by the

impurity ions in the boundaries was determined to be  $\sim 9\%$ – $10\%$ . EELS has been used to investigate the local chemical bonding around the dopant ions in 1000-ppm- $Y_2O_3$ - and 500-ppm- $La_2O_3$ -doped alumina.<sup>11</sup>

Based on such microscopic and spectroscopic studies, several explanations have been proposed for the effect of dopants on creep properties.<sup>4,5,21</sup> A plausible explanation is based on observed dopant grain boundary segregation behavior and the results of computer simulation and modeling of grain boundary structures. In this explanation oversized dopant ions impede (via long-range strain fields) or effectively block fast diffusive paths at grain boundaries. This proposition is supported by two experimental observations:<sup>6</sup> (i) the degree of enhanced creep resistance generally correlates with dopant ionic size; and (ii) codoping is sometimes synergistic, resulting in a further diminution of the creep rate. Also, recent atomistic computer simulations indicate that oversized, segregated dopants can modify diffusive paths along special grain boundaries.<sup>22</sup> Finally, and more recently, Ching *et al.*<sup>23</sup> have conducted first-principles molecular orbital calculations of the bonding states in the Y–Al–O system. They found that the relative bonding strengths of Y–O and Y–Al in different crystal structures ( $Y_3Al_5O_{12}$ ,  $Y_4Al_2O_9$ , and  $Y_2O_3$ ) depend on details of the atomic environments. Similarly, calculations by Yoshida *et al.*<sup>2</sup> have shown that the Al–O bond strength is altered by bulk doping with lanthanides. These results suggest that the enhanced creep resistance of doped alumina may be attributed to stronger bonding at grain boundaries with dopant segregated.

A detailed knowledge of the atomic structures of dopant-segregated grain boundaries will aid understanding of the dopant effect and will advance computer simulation and modeling of phenomenon related to dopant grain boundary segregation. X-ray absorption spectroscopy, including EXAFS and X-ray absorption near-edge structure (XANES), is an element-specific local probe which is sensitive to low concentrations of dopants.<sup>24-27</sup> Generally speaking, EXAFS spectra provide information about the coordination chemistry of the probe atom such as average bond lengths and coordination numbers at the probe atom. XANES probes more directly the density of unoccupied electronic states. It is complementary to EXAFS and provides information on stereochemical features of the coordination polyhedron around the probe atom, including bonding configuration, ligand-field symmetry, and valence state. XANES has been used to investigate the ligand symmetry in dopant stabilization of zirconia.<sup>28-33</sup>

By using EXAFS and high-resolution scanning transmission electron microscopy, Wang *et al.*<sup>17,18</sup> have determined the atomic structural features for grain-boundary-segregated Y and Zr, and for Y the dependence of those structural parameters on the grain boundary dopant concentration. Y–O and Zr–O bond lengths for Y and Zr in  $\alpha-Al_2O_3$  are all relaxed to values found in their respective parent oxides, but the average nearest-neighbor coordination numbers around the grain-boundary-segregated Y and Zr are  $\sim 4$  and  $5$ , respectively, compared with coordination numbers of 6 or 7 for  $\alpha-Al_2O_3$ ,  $Y_2O_3$ , and monoclinic  $ZrO_2$ . Local atomic structures of the grain boundaries also depend on the dopant grain boundary concentration. With an increase of the dopant concentration, grain boundary dopant behavior occurs in three stages, corresponding to dilute to saturated concentrations, supersaturated

T. E. Mitchell—contributing editor

*o/d grant*

Manuscript No. 187243. Received December 26, 2001; approved June 28, 2002. This research is supported by the U.S. Air Force Office of Scientific Research under Contract No. F49620-98-1-0117 (monitored by Dr. A. Pechenik) and by the U.S. Office of Naval Research under Contract No. N00014-99-1-0236 (monitored by Dr. S. Fishman). EXAFS measurements were made at NSLS, Brookhaven National Laboratory, which is supported by the Department of Energy.

<sup>\*</sup>Member, American Ceramic Society.

<sup>†</sup>Present address: Pacific Northwest National Laboratory, Richland, Washington 99352. E-mail: chongmin.wang@pnl.gov.

concentrations, and grain boundary concentration equilibrated with precipitates.<sup>18</sup> For supersaturated concentrations, some of the dopant ions are believed to occupy near-boundary layers, and within these layers the dopant ions are in substitutional Al sites.

In this paper, we report *K*-edge XANES spectra of alumina grain-boundary-segregated Y and Zr, analyzed using the metallic Y and Zr,  $Y_2O_3$ , monoclinic  $ZrO_2$ , and YAG as standards. *K*-edge XANES of Y for different grain boundary Y concentrations and for Y absorbed on the free surface of  $\alpha-Al_2O_3$  were also obtained. Structural information inferred from XANES was compared with that from EXAFS. The same materials were used in this XANES study and in the earlier EXAFS study, thus avoiding effects of microstructural differences in comparing the EXAFS and XANES results. The significance of the present results in understanding of the creep resistance is also discussed.

## II. Experimental Procedure

### (1) Materials

Fabrication of materials used in this study has been described in detail in Refs. 17 and 18. In brief, ultra-high-purity  $\alpha-Al_2O_3$  was doped with either  $Y_2O_3$  or  $ZrO_2$ .  $Y_2O_3$  was doped at two levels, 100 and 1000 ppm (Y/Al atomic ratio, hereafter referred to as samples 100Y and 1000Y), and  $ZrO_2$  at 100 ppm (Zr/Al atomic ratio, hereafter referred to as sample 100Zr). The 100Zr and 100Y samples show a rather uniform grain size distribution, with the 100Y having an average grain size of  $\sim 1.5 \mu m$  and the 100Zr having an average grain size of  $\sim 0.5 \mu m$ . SEM and TEM reveal no secondary-phase precipitates in the 100Y and 100Zr materials. A part of the as-hot-pressed 100Y sample was further annealed for 40 h at  $1475^\circ C$  in air, which increased the average grain size from  $\sim 1.5$  to  $\sim 4.0 \mu m$ . As noted in Ref. 18, for this sample, designated 100Y-SS, alumina grain boundaries are supersaturated with Y without formation of YAG precipitates. The 1000Y material shows a bimodal grain size distribution, with a coarse grain size of  $\sim 5 \mu m$ , and a fine grain size of  $\sim 1 \mu m$ . The 1000Y material also has  $Y_3Al_5O_{12}$  (YAG) as secondary-phase precipitates which are mainly distributed in the fine grain size  $Al_2O_3$  regions. Based on STEM and EXAFS analysis, it has been estimated that in the 1000Y sample, 80% of the Y exists as YAG and the rest is segregated to alumina grain boundaries.<sup>17</sup> Figure 1 shows a representative STEM annular aperture dark-field image and compositional map of the 100Y sample. Both techniques reveal that the dopant is segregated to grain boundaries with a distribution width of less than 2 nm. Another sample was prepared with Y adsorbed on the surface of  $0.3 \mu m$   $Al_2O_3$  particles, by dispersing the powder in an yttrium methanol solution, giving an Y/Al atomic ratio of 100 ppm, followed by annealing at  $700^\circ C$  for 8 h, as described in Ref. 18. This sample is designated 100Y-SURF.

### (2) X-ray Absorption Measurements

X-ray absorption measurements at the *K*-edges of Y and Zr were made on Beamline X23A2 of the National Synchrotron Light Source (NSLS) at Brookhaven National Laboratory under normal operating conditions (2.5 GeV, 100–200 mA) and using a Si (311) double-crystal monochromator. The setup for the XANES measurement was the same as that for the EXAFS measurement described in detailed in Refs. 17 and 18, except that a 0.5 mm entrance slit was used for the XANES measurement to improve energy resolution. To reduce statistical errors, about 50 spectra were recorded and averaged for the 100Y and 100Zr samples. For the 1000Y sample only two spectra were collected and averaged to obtain similar statistical accuracy. To monitor any energy drift during the repeated scans of the 100Y and 100Zr specimens, a pure Y or Zr metallic foil was scanned before and after the total specimen scans. *K*-edge XANES of metallic Y and Zr foils, cubic  $Y_2O_3$  powder (purity 99.99%, Alfa, Johnson Matthey Co.), and monoclinic  $ZrO_2$  powder (purity 99.5%, Alfa, Johnson Matthey Co.) were measured in transmission mode, and those spectra were used as standards for the interpretations of XANES from grain-

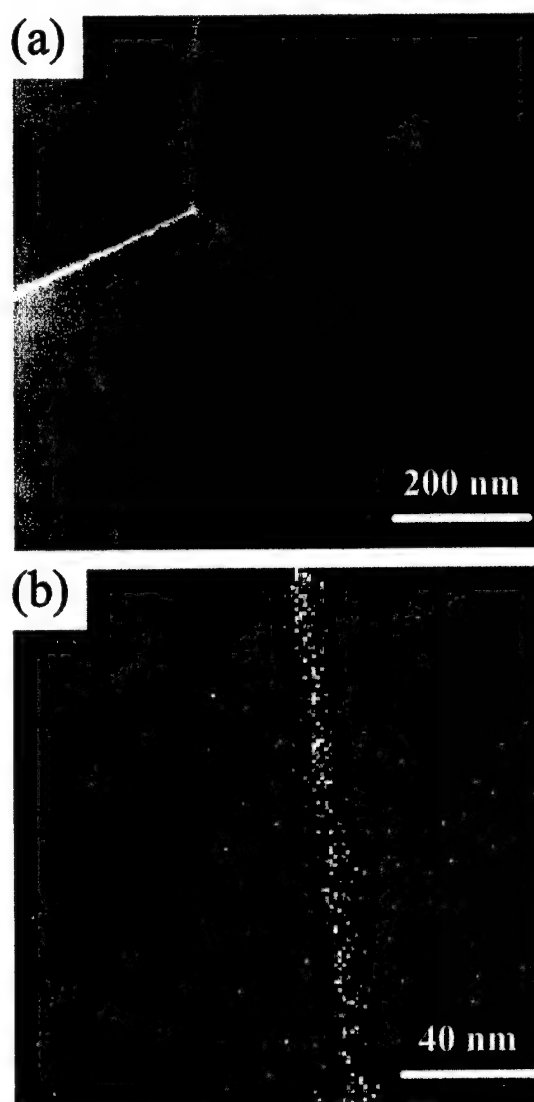


Fig. 1. STEM annular aperture dark-field image of 100-ppm- $Y_2O_3$ -doped material (a), and the EDS mapping of Y (b). In the EDS mapping, the electron beam diameter is optimized to 1 nm, and the mapping area is  $160 \times 160 \text{ nm}^2$  with a total pixel number of  $128 \times 128$ .

pre-edge background was removed by subtracting a single, first-order polynomial from the data. The result was then multiplied by a scale factor either to bring the main peak to the same magnitude for measuring the chemical shift or to bring the background corrected data to the same magnitude for  $E-E_0 \sim 30 \text{ eV}$  to determine the strength of the threshold resonance.

## III. XANES Results

Representative *K*-edge XANES spectra for metallic Y,  $Y_2O_3$ , 100Y, and 1000Y are shown in Fig. 2(a). XANES for metallic Zr, monoclinic  $ZrO_2$ , and 100Zr are shown in Fig. 2(b). To take first derivatives, the spectra for the 100Y and 100Zr are Fourier smoothed. The unsmoothed original spectrum for the 100Y is shown in Fig. 4. The first derivatives of the XANES spectra are shown as an inset in the Figs. 2(a) and (b).

### (1) Chemical Shifts

The chemical shifts with respect to the elemental metals were taken from the absorption edge energies at half of the absorption step maximum.<sup>34</sup> The chemical shifts for the 100Y, 1000Y, and

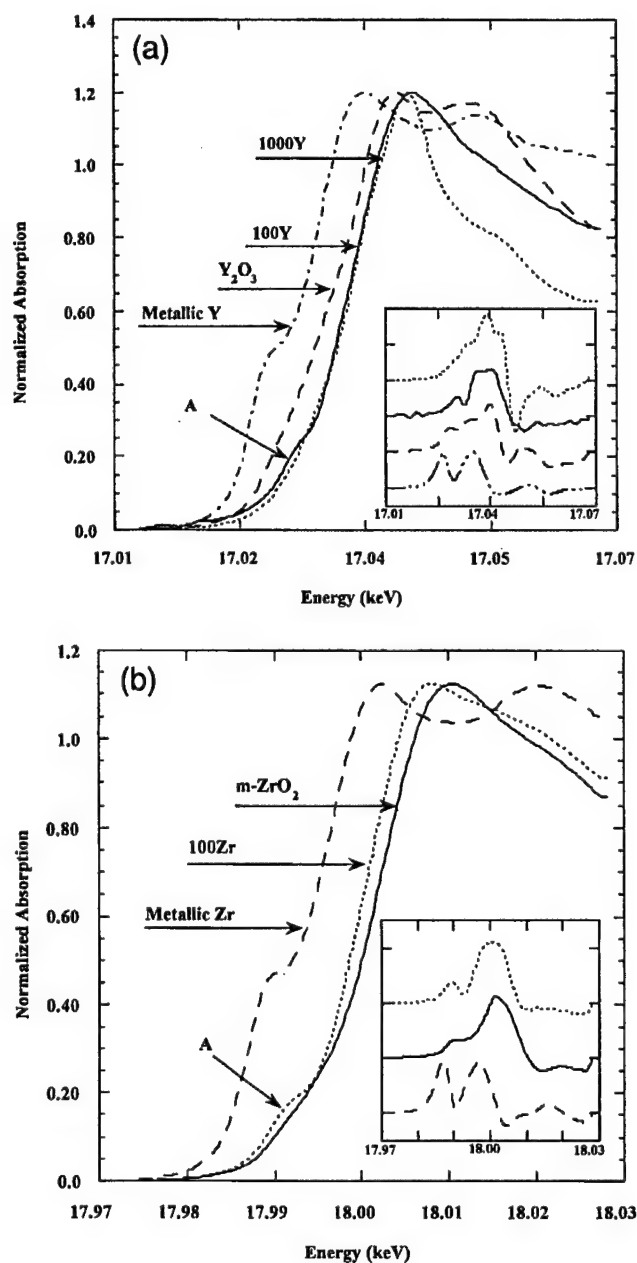


Fig. 2. K-edge XANES spectra: (a) Y in metallic Y, Y<sub>2</sub>O<sub>3</sub>, 100Y, and 1000Y; and (b) Zr in metallic Zr, 100Zr, and m-ZrO<sub>2</sub>. First derivatives of the spectra are shown in the inset. The shoulder marked A is attributed to  $1s \rightarrow 4d$  transition.

The Y K-edges of 100Y and 1000Y samples show positive chemical shifts of 5.5 and 5.8 eV, respectively, which are larger than that of Y<sub>2</sub>O<sub>3</sub> (3.5 eV). The Zr K-edge of the 100Zr sample shows a chemical shift of 6.0 eV, which is smaller than that of monoclinic ZrO<sub>2</sub> (7.2 eV).

## (2) Pre-edge Features

Comparing the pre-edge features of 100Y and 100Zr with those of the standard oxides, it is seen that grain-boundary-segregated Y and Zr have a small shoulder below the principal peak, marked by an arrow in Fig. 2, which is more apparent in the first-derivative plots. However, this kind of shoulder is barely resolved for Y in Y<sub>2</sub>O<sub>3</sub> or for Zr in monoclinic ZrO<sub>2</sub>. This shoulder is also not well resolved in the 1000Y specimen, implying that it is also absent in

Table I. Observed Chemical Shifts Relative to Metallic Elements

Samples	Chemical shift (eV)
100Y	5.5
1000Y	5.8
Y <sub>2</sub> O <sub>3</sub>	3.5
Y <sub>3</sub> Al <sub>5</sub> O <sub>12</sub>	6.0 <sup>†</sup>
100Zr	6.0
m-ZrO <sub>2</sub>	7.2

<sup>†</sup>Calculated from  $\Delta E_{1000Y} = 0.8\Delta E_{YAG} + 0.2\Delta E_{100Y}$ ;  $\Delta E$  is the chemical shift.

## (3) Y-Supersaturated Grain Boundaries and Y Absorbed on the Free Surface of $\alpha$ -Al<sub>2</sub>O<sub>3</sub>

Figure 4 shows Y K-edge XANES spectra for dilute (100Y) and supersaturated Y grain boundary concentrations (100Y-SS), together with spectra for Y absorbed on the free surface of  $\alpha$ -Al<sub>2</sub>O<sub>3</sub> (100Y-SURF). When the Y grain boundary concentration is supersaturated, the chemical shifts approach that for Y atoms absorbed on the free surface of  $\alpha$ -Al<sub>2</sub>O<sub>3</sub>.

## IV. Interpretation of Experimental Results

Generally speaking, there are two ways to interpret XANES spectra. One is the fingerprint method in which XANES of the material of interest is compared with XANES of other materials of known structures to identify structural similarities. Another method is to compare XANES of the materials of interest with results of molecular orbital density of state calculations, since the XANES spectrum is a reflection of the empty states above the Fermi energy. The fingerprint method has been used in this study.

Our analysis focuses on three aspects of the XANES spectra: (1) the chemical shift, which is defined as the absorption edge energy shift of the atom in the compound relative to the edge energy of elemental metals; (2) the threshold resonance; and (3) the pre-edge features. In the following, we describe and interpret these three features of XANES spectra of 100Y, 1000Y, and 100Zr samples. Previous STEM and EXAFS analyses have indicated that for the 100Y and 100Zr samples, the doped Y and Zr atoms were mainly segregated to the alumina grain boundaries.<sup>17</sup> Thus the features of the XANES spectra of the 100Y and 100Zr samples represent grain-boundary-segregated Y and Zr. For the 1000Y sample, ~80% of the Y atoms are in YAG precipitates and only ~20% are segregated to grain boundaries. Thus the XANES spectra of the 1000Y samples are a superposition of spectra from YAG precipitates and spectra from grain-boundary-segregated Y.

## (1) Chemical Shifts

Chemical shifts are typically discussed in terms of effective nuclear charge,<sup>35</sup> oxidation state,<sup>36</sup> coordination number, type of chemical bonding, electronegativity,<sup>37,38</sup> hybridization, relaxation energy, screening, and inner level shifts.<sup>39,40</sup> However, there are no simple, quantitative relationships to correlate these factors with the magnitudes of chemical shifts. For transition-metal oxides and vanadium compounds it has been found experimentally that chemical shifts increase with increasing valence of the metal atoms in the oxides or compounds, and it has been shown empirically that the chemical shift is linearly proportional to the coordination charge,  $\eta$ , of the probe atoms.<sup>41,42</sup> As introduced by Batsanov,<sup>43</sup> the coordination charge is given by

$$\eta = m - CN \quad (1)$$

where  $m$  is the formal valence of the central atom,  $N$  is its coordination number,  $C = 1 - i$  is the degree of covalency, and  $i$  is the multiple-bond ionicity. For a purely ionic material like NaCl,

valence of the absorber atom. The multiple-bond ionicity  $i$  given by

$$i = 1 - \frac{m}{N} \exp \left[ -\frac{1}{4} (X_A - X_B)^2 \right] \quad (2)$$

can be expressed in terms of the single-bond ionic character  $I$ , or ionicity, introduced by Pauling,<sup>44</sup>

$$I = 1 - \exp \left[ -\frac{1}{4} (X_A - X_B)^2 \right] \quad (3)$$

where  $X_A$  and  $X_B$  are the electronegativities of atoms A and B. Combining Eqs. (1) to (3) one obtains

$$\eta = mI \quad (4)$$

From Eq. (4), the coordination charge is given by the product of the formal valence,  $m$ , and the ionicity,  $I$ , of the metal atom with its coordination ligands. For the same coordination ligands around the probe atom, oxygen for the present case, the chemical shifts of the absorption edge are an indication of the net charge on the probe atom. Conceptually, this may be understood as the valence electrons being pulled away from the metal atom by the electronegativity  $X_B$  of the coordinating ligands, and all of the other electrons of the central atom becoming more tightly bound to shield the metal atom's nuclear charge. Hence, a  $K$ -shell transition is expected to increase in energy with an increase in the product of formal valence and ionicity. The coordination charge should be regarded as only a rough measure of the actual net charge.

If we correlate the chemical shift of the  $K$ -edges of Y and Zr in the present samples with the coordination charge around the Y and Zr for different coordination ligands around the Y and Zr, the coordination charge for Y is ordered as  $Y_2O_3 < 100Y < 1000Y$  ( $<YAG$ ), and for Zr as  $100Zr < ZrO_2$ . This qualitative analysis implies that the grain-boundary-segregated Y has a higher net charge than Y in  $Y_2O_3$ , but less than Y in YAG. Bhide *et al.*<sup>45</sup> have found that the Y–O bond in  $Y_2O_3$  possesses 20% covalence. Xu *et al.*<sup>46</sup> have calculated the net charge for Y in  $Y_2O_3$  and in YAG and have concluded that the net charge for Y in both is 2.50. They also found that the Y–O bond in YAG is more ionic than in  $Y_2O_3$ . These results from molecular orbital calculations are consistent with our present experimental observations that the chemical shift for Y in YAG is larger than in  $Y_2O_3$ . This is also consistent with the fact that the Y–O bond length in YAG is longer than that in  $Y_2O_3$ , and that in YAG each Y is coordinated by 8 oxygen atoms while in  $Y_2O_3$  each Y is coordinated by only 6 oxygen atoms. Jollet *et al.*<sup>47</sup> have studied the electronic structure of stoichiometric  $Y_2O_3$  and nonstoichiometric, reduced  $Y_2O_3$  in which oxygen vacancies reduce the average Y–O coordination numbers compared with that for stoichiometric  $Y_2O_3$ . They concluded that reducing  $Y_2O_3$  causes the Y–O bond to become more covalent or less ionic.<sup>47</sup>

## (2) $K$ Threshold Resonances

Free atom electron configurations for Y and Zr are  $[Kr]4d^1 5s^2$  and  $[Kr]4d^2 5s^2$ . In electronic transitions, the dipole selection rule requires that  $\Delta l = \pm 1$ , where  $l$  is the electron angular momentum quantum number. For the  $K$ -edges of Y and Zr, the main absorption peaks can be assigned to  $1s \rightarrow 5p$  transitions.<sup>28,29</sup> The splitting of the main peak in pure  $Y_2O_3$  has been previously reported. The present observed splitting of 9.2 eV (Fig. 2(a)) is close to the 9.0 eV splitting reported by Li *et al.*,<sup>29</sup> but is larger than the 7.0 eV splitting reported by Thromat *et al.*<sup>48</sup> and by Jollet *et al.*<sup>49</sup>

Lytle *et al.*<sup>50</sup> have developed a spectral difference method for quantifying the degree of the threshold resonance, in which the normalized spectrum for a metal is subtracted from that for a compound, and the resulting difference spectrum is related to the difference in the electronic structure of the absorber atom in the two environments. In this method, the absorption edge position

larger the magnitude of the difference, the stronger is the threshold resonance. By applying this method to our XANES (Fig. 3), it is seen that the  $K$  threshold resonance for Y and Zr, either segregated to the alumina grain boundaries or in the pure oxides or compounds, is stronger than that for metallic Y and Zr. Similar results have been reported for other metallic oxide systems.<sup>50</sup> Comparing the  $K$ -edge XANES spectra of 100Y, 1000Y, and  $Y_2O_3$ , the 1000Y sample has the strongest  $K$  threshold resonance, followed by 100Y and  $Y_2O_3$ . For 100Zr and monoclinic  $ZrO_2$ , Zr in monoclinic  $ZrO_2$  shows a slightly stronger  $K$  threshold resonance. A stronger resonance can be attributed to a higher density of the vacant  $p$ -electronic states.

Based on  $L_{III}$ -edge XANES of Ir, Pt, and Au, Lytle *et al.*<sup>50</sup> found the strengths of the XANES resonances of those metal oxides to be linearly proportional to the coordination charge. Li *et al.*<sup>29</sup> have reported that the  $K$ -edge threshold resonance for Y in solid solution with  $ZrO_2$  is stronger than that for Y in  $Y_2O_3$ ,

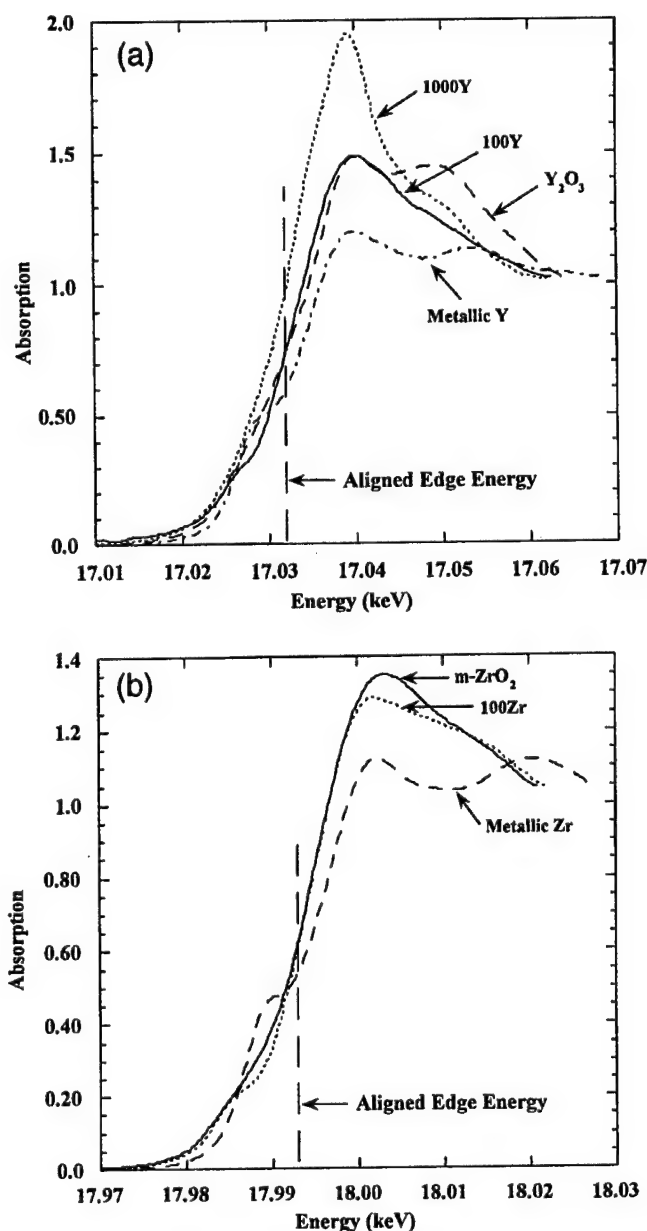


Fig. 3.  $K$ -edge XANES spectra: (a) Y in metallic Y,  $Y_2O_3$ , 100Y, and 1000Y; and (b) Zr  $K$ -edge for metallic Zr, 100Zr, and  $m$ - $ZrO_2$ . All of the spectra were aligned at the absorption edge energy of the pure metallic element to correct for chemical shifts (Table I). Note the dependence of the



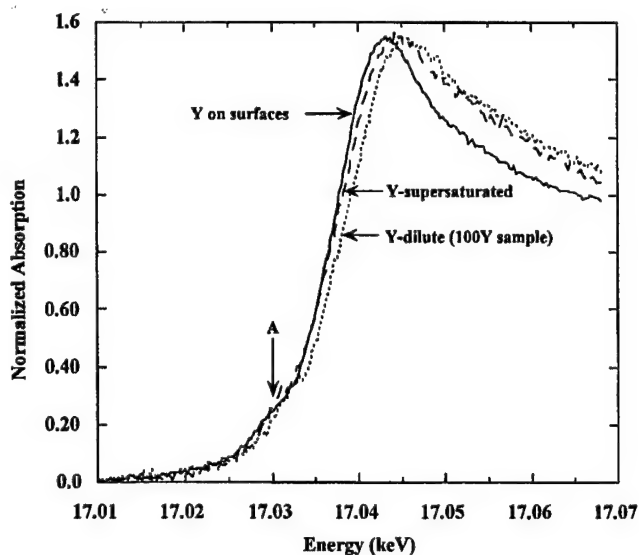


Fig. 4. Comparison of *K*-edge XANES spectra for Y at dilute (100Y) and supersaturated (100Y-SS) concentrations, and for Y coated on the free surface of  $\alpha$ - $\text{Al}_2\text{O}_3$  (100Y-SURF).

indicating a more ionic Y–O bond when Y is in solid solution with  $\text{ZrO}_2$  as compared with  $\text{Y}_2\text{O}_3$ . This is consistent with a higher coordination number and a larger Y–O distance of Y in  $\text{ZrO}_2$ . If we relate our present observations of the strength of *K* threshold resonances with the coordination charge around the Y and Zr for different environments of Y and Zr, the coordination charges for Y may be arranged in the order of  $\text{Y}_2\text{O}_3 \leq 100\text{Y} < 1000\text{Y} (< \text{YAG})$ , given that 1000Y is a superposition of 80% YAG and 20% 100Y, and for Zr may be arranged as  $100\text{Zr} < \text{ZrO}_2$ . These orderings are consistent with those inferred from the *K*-edge threshold resonance features discussed in Section IV(1).

### (3) Pre-edge Features

Pre-edge features provide information about coordination ligand symmetry. In general, XANES features within  $\sim 10$  eV below the edge threshold are due to electronic transitions to unoccupied high-energy states near the Fermi level. These transitions are particularly sensitive to the local geometry of first anion neighbors of cation probe atoms in ionic compounds. In the case of transition metals, this pre-edge absorption indicates a tetrahedral environment around the absorbing metal atoms.<sup>28,29,51,52</sup> This characteristic pre-edge absorption is also found in *K*-edge spectra of vanadium in fourfold coordination.<sup>42</sup> In the *K*-edge XANES of tetragonal  $\text{ZrO}_2$ , Li *et al.*<sup>28,29,31,33</sup> also observed a pre-edge shoulder. They attributed this to the  $1s \rightarrow 4d$  transition due to *d*–*p* mixing, which is promoted by the Zr–O tetrahedral coordination geometry. In tetragonal  $\text{ZrO}_2$  the Zr–O geometry can be regarded as two sets of nonequivalent Zr–O tetrahedra.<sup>28,33</sup> Similar results have also been reported for  $\text{Fe}_2\text{O}_3$ – $\text{ZrO}_2$  solid solutions.<sup>31</sup>

Since we have attributed the principal peak at the *K*-edge to a  $1s \rightarrow 5p$  dipole-allowed transition, the shoulder in the rising absorption edge for grain-boundary-segregated Y and Zr may be attributed to the  $1s \rightarrow 4d$  transition resulting from mixing of unoccupied *d* final states with *p*-character final states. Such *d*–*p* mixing is forbidden for a centrosymmetric (e.g., octahedral) environment, but it is allowed in a noncentrosymmetric (e.g., tetrahedral) environment. Indeed, tetrahedral geometry is known to enhance *d*–*p* mixing. The pre-edge shoulders for the 100Y and 100Zr samples indicate that the oxygen coordination ligands around at least a fraction of the grain-boundary-segregated Y and Zr are tetrahedrally arranged. The forbidden  $1s \rightarrow 4d$  transition shoulder also exist for Y supersaturated grain boundaries and for Y

## V. Discussion

### (1) XANES and EXAFS Results

This XANES study of alumina grain-boundary-segregated Y and Zr suggests that at least a fraction of the grain-boundary-segregated Y and Zr have nearest-neighbor oxygens arranged in a tetrahedral configuration, although this is not necessarily an indication of the grain-boundary-segregated Y and Zr having an oxygen coordination number of 4. In tetragonal  $\text{ZrO}_2$ , each Zr has 8 oxygens as the nearest neighbors, but they are arranged in two nonequivalent tetrahedra, thus leading to the appearance of the  $1s \rightarrow 4d$  transitions.<sup>28,33</sup>

Our EXAFS study of the 100Y and 100Zr samples has indicated that grain-boundary-segregated Y and Zr, on average, have oxygen coordination numbers of  $\sim 4$  and 5, respectively.<sup>17</sup> Loudjani *et al.*<sup>53</sup> have also used EXAFS to study the Zr–O bond length and the coordination number for grain-boundary-segregated Zr. They similarly concluded that, on average, grain-boundary-segregated Zr has  $\sim 4$  oxygens as the nearest neighbors. Considering both XANES and EXAFS results, the tetrahedral configuration of the oxygens around the grain-boundary-segregated Y and Zr, as suggested by the XANES pre-edge features, suggests that at least some of the Y or Zr segregated to the  $\alpha$ - $\text{Al}_2\text{O}_3$  grain boundary indeed are coordinated by 4 oxygens with well-defined distance.

The low coordination numbers around the grain-boundary-segregated Y and Zr indicated by EXAFS are somewhat surprising,<sup>54</sup> especially for the larger Y atom to have such a low coordination number. In the case of crystalline YAG, the ionic size of Y is larger than that of Al and Y has eight oxygens as the nearest neighbors, while 60% of the Al atoms have four oxygen nearest neighbors and 40% of the Al atoms have six oxygen nearest neighbors. However, grain boundaries are distorted regions, and ions in such regions may be intrinsically undercoordinated. The atomic arrangement of the near  $\Sigma = 11$  boundary in  $\alpha$ - $\text{Al}_2\text{O}_3$  was modeled by Kenway,<sup>55</sup> and its electronic structure was calculated by Mo *et al.*<sup>56</sup> They both concluded that, in this special boundary, some Al atoms are coordinated by only four oxygens. More generally, based on an electron energy-loss near-edge structure study of grain boundaries in  $\alpha$ - $\text{Al}_2\text{O}_3$ , Kaneko *et al.*<sup>19</sup> have concluded that, for a general boundary in  $\alpha$ - $\text{Al}_2\text{O}_3$ , some Al atoms are likely to be coordinated by four oxygens.

We also recognize that it may be possible that the oxygen coordination number around the grain-boundary-segregated Y and Zr may be close to that for the ideal structure to satisfy the valence bonding requirements for Y (coordination number of at least 6) and Zr (coordination number of at least 7).<sup>54</sup> However, because of the distorted structural nature of grain boundaries, the Y–O and Zr–O distances are not uniformly defined for each Y and Zr. This may result in unrealistically low coordination numbers from fitting EXAFS spectra for the grain-boundary-segregated Y and Zr.

### (2) Correlation of the Creep Resistance with the Electronic Structure in Doped Alumina

Recently progress has been made in correlating the enhanced creep resistance of alumina with their electronic structure after doping. Experimentally, it has been found that YAG has much better creep resistance than alumina. Ching *et al.*<sup>23,46</sup> have calculated the electronic structures of Y–Al–O systems, including four compounds with different Al/Y ratios:  $\text{Y}_3\text{Al}_5\text{O}_{12}$  (YAG),  $\text{YAlO}_3$  (YAP), and  $\text{Y}_4\text{Al}_2\text{O}_9$  (YAM). In the YAG phase, Y ions are dodecahedrally coordinated to eight O ions. There are two different sites for Al:  $\text{Al}_{\text{oct}}$  atoms occupy sites with octahedral point symmetry and  $\text{Al}_{\text{tet}}$  atoms occupy sites with tetrahedral point symmetry. The ratio of  $\text{Al}_{\text{tet}}/\text{Al}_{\text{oct}}$  is 3/2. For YAP, both Y and Al are coordinated by distorted octahedra of six O atoms. In monoclinic YAM, there are nine O, four Y, and two Al sites. Two of the Y ions (Y1, Y3) are sevenfold coordinated, and the other two (Y2 and Y4) are sixfold coordinated. Both Al1 and Al2 are tetrahedrally coordinated. Based on electronic structure calculations for these three compounds, Ching *et al.* have concluded that in YAG there is direct bonding interaction between the tetrahedrally

is relatively weak because of the shielding of the  $Al_{oct}$  by the six oxygens. They also speculate that the effect of alumina grain-boundary-segregated Y on the creep properties is related to the interaction of the Y and Al ions in grain boundaries. Consistent with this picture is the work of Sakuma *et al.*,<sup>2,57</sup> in which they have calculated the electronic structure of alumina with lanthanides and Y dissolved in the lattice. They have correlated the dopant effect with enhanced Al–O ionic bonding and with covalent bonding between the dopant and the Al ions, as compared with the undoped alumina.

The chemical shift and the threshold resonance indicate a degree of charge transfer in Y- and Zr-doped alumina, which indicates interaction of the dopant with the surrounding cations and anions, as discussed by Sakuma *et al.*<sup>2,57</sup> A larger chemical shift in 100Y than in  $Y_2O_3$  indicates a stronger Y–O bond in the 100Y material. Furthermore, the undercoordinated dopant ions in grain boundaries may also allow the interaction of dopants with Al ions, as suggested by Sakuma *et al.* and Ching *et al.* in the modeling. This implies that the dopant-enhanced creep resistance may also be related to the stronger bonding in the grain boundaries after the dopant segregation.

It has been generally realized that supersaturation of dopants in the alumina grain boundaries induces abnormal grain growth and abnormal creep behavior, although the reasons for this are yet to be fully established. The present observations are that for supersaturation of grain boundaries the chemical shift and the threshold resonance are more like the free surface. This suggests similarities between grain boundary structure and free surface, especially when dopant concentrations approach the supersaturation limit.<sup>17,18,58</sup>

## VI. Conclusions

Alumina grain-boundary-segregated Y and Zr show different magnitudes of chemical shift relative to  $Y_2O_3$  and monoclinic  $ZrO_2$ , indicating different degrees of charge transfer for the grain-boundary-segregated Y and Zr. The existence of a pre-edge shoulder for the grain-boundary-segregated Y and Zr suggests that there is  $d-p$  mixing, which is known to be favored by tetrahedral configuration of cation–anion first-shell neighbors. This indicates that the oxygens around the grain-boundary-segregated Y and Zr, at least partially, possess tetrahedral coordination configurations. This is consistent with the energy-loss near-edge structure (ELNES) analysis of a pure alumina grain boundary, in which it has been found that some Al atoms have a coordination of 4. Atomic structural parameters obtained by EXAFS and XANES provide important parameters for computer calculations and modeling of the dopant-segregated grain boundaries. More thorough interpretations of these spectra may be possible through molecular orbital calculations.

## Acknowledgments

We thank Dr. Joseph Woicik and Dr. Zugen Fu of NIST for assistance with operation of the beamline and data acquisition and for beneficial discussions, and Dr. P. E. D. Morgan of Rockwell Science Center for discussions about chemical bonding and for reading the manuscript. Beneficial discussions with Professor K. Klier of Lehigh University are also greatly appreciated.

## References

- J. D. French, J. Zhao, M. P. Harmer, H. M. Chan, and G. A. Miller, "Creep of Duplex Microstructure," *J. Am. Ceram. Soc.*, **77**, 2857–65 (1994).
- H. Yoshida, Y. Ikuhara, and T. Sakuma, "High Temperature Creep Resistance in Lanthanoid Ion-Doped Polycrystalline  $Al_2O_3$ ," *Philos. Mag. Lett.*, **79**, 249–56 (1999).
- F. Wakai, T. Nagano, and T. Iga, "Hardening in Creep of Alumina by Zirconium Segregation at the Grain Boundaries," *J. Am. Ceram. Soc.*, **80**, 2361–66 (1997).
- S. Lartigue, C. Carry, and L. Priester, "Grain Boundaries in High Temperature Deformation of Ytria and Magnesia Co-Doped Alumina," *J. Phys. (Paris)*, **C1**, 51, 985–90 (1990).
- S. Lartigue, L. Priester, F. Dupau, P. Gruffel, and C. Carry, "Dislocation Activity and Differences Between Tensile and Compressive Creep of Ytria Doped Alumina," *Y. Li, C. M. Wang, H. M. Chan, J. M. Rickman, M. P. Harmer, J. M. Chabala, K. L. Gavrilov, and R. Levi-Setti, "Codoping of Alumina to Enhance Creep Resistance," J. Am. Ceram. Soc.*, **82**, 1497–504 (1999).
- J. Cho, C. M. Wang, H. M. Chan, M. P. Harmer, and J. M. Rickman, "Role of Segregating Dopants on the Improved Creep Resistance of Aluminum Oxide," *Acta Mater.*, **47**, 4197–207 (1999).
- J. Cho, M. P. Harmer, H. M. Chan, J. M. Rickman, and A. M. Thompson, "Effect of Yttrium and Lanthanum on the Tensile Creep Behavior of Aluminum Oxide," *J. Am. Ceram. Soc.*, **80**, 1013–17 (1997).
- R. F. Cook and A. G. Schrott, "Calcium Segregation to Grain Boundaries in Alumina," *J. Am. Ceram. Soc.*, **71**, 50–58 (1988).
- R. I. Taylor, J. P. Coad, and R. J. Brook, "Grain Boundary Segregation in  $Al_2O_3$ ," *J. Am. Ceram. Soc.*, **57**, 539–40 (1974).
- Bruley, J. Cho, H. M. Chan, M. P. Harmer, and J. M. Rickman, "Scanning Transmission Electron Microscopy Analysis of Grain Boundaries in Creep-Resistant Yttrium- and Lanthanum-Doped Alumina," *J. Am. Ceram. Soc.*, **82**, 2865–70 (1999).
- D. R. Clarke, "Grain Boundary Segregation in an  $MgO$ -Doped  $Al_2O_3$ ," *J. Am. Ceram. Soc.*, **63**, 339–41 (1980).
- C. W. Li, and W. D. Kingery, "Solute Segregation at Grain Boundaries in Polycrystalline  $Al_2O_3$ ," pp. 368–78 in *Advances in Ceramics*, Vol. 10, *Structure and Properties of  $MgO$  and  $Al_2O_3$  Ceramics*. Edited by W. D. Kingery. American Ceramic Society, Columbus, OH, 1984.
- Thompson, K. K. Soni, H. M. Chan, M. P. Harmer, D. B. Williams, J. M. Chabala, and R. Levi-Setti, "Dopant Distributions in Rare-Earth-Doped Alumina," *J. Am. Ceram. Soc.*, **80**, 373–76 (1997).
- M. K. Loudjani, J. Roy, and A. M. Huntz, "Study by Extended X-ray Absorption Fine Structures Technique and Microscopy of the Chemical State of Yttrium in  $\alpha$ -Polycrystalline Alumina," *J. Am. Ceram. Soc.*, **68**, 559–62 (1985).
- M. K. Loudjani and R. Cortes, "X-ray Absorption Study of the Local Structure and the Chemical State of Yttrium in Polycrystalline Alumina," *J. Eur. Ceram. Soc.*, **14**, 67–75 (1994).
- M. Wang, G. S. Cargill III, M. P. Harmer, H. M. Chan, and J. Cho, "Atomic Structural Environment of Grain Boundary Segregated Y and Zr in Creep Resistant Alumina from EXAFS," *Acta Mater.*, **47**, 3411–22 (1999).
- M. Wang, G. S. Cargill III, H. M. Chan, and M. P. Harmer, "Structural Features of Y-Saturated and Supersaturated Grain Boundaries in Alumina," *Acta Mater.*, **48**, 2579–91 (2000).
- K. Kaneko, T. Gemming, I. Tanaka, and H. Mulleljans, "Analytical Investigation of Random Grain Boundaries of Zr-Doped Sintered  $\alpha$ - $Al_2O_3$  by Transmission Electron Microscopy and Scanning Transmission Electron Microscopy," *Philos. Mag. A*, **77**, 1255–72 (1998).
- W. D. Kaplan, H. Mulleljans, M. Ruhle, J. Rodel, and N. Claussen, "Calcium Segregation to Basal Surfaces in  $\alpha$ -Alumina," *J. Am. Ceram. Soc.*, **78**, 2841–44 (1995).
- J. Cho, H. M. Chan, M. P. Harmer, and J. M. Rickman, "Influence of Yttrium Doping on Grain Misorientation in Aluminum Oxide," *J. Am. Ceram. Soc.*, **81**, 3001–3004 (1998).
- J. Cho, J. M. Rickman, H. M. Chan, and M. P. Harmer, "Modelling of Grain Boundary Segregation Behavior in Aluminum Oxide," *J. Am. Ceram. Soc.*, **83**, 344–52 (2000).
- Y. Ching and Y. N. Xu, "Nonscalability and Nontransferability in the Electronic Properties of the Y–Al–O System," *Phys. Rev. B*, **59**, 12815–21 (1999).
- B. K. Teo, *EXAFS: Basic Principles and Data Analysis*. Springer-Verlag, New York, 1986.
- J. C. J. Bart, "Near-Edge X-ray Absorption Spectroscopy in Catalysis," *Adv. Catal.*, **34**, 203–97 (1986).
- R. F. Egerton, *Electron Energy Loss, Spectroscopy in the Electron Microscope*, 2nd Ed. Plenum, New York, 1996.
- U. C. Srivastava and H. L. Nigam, "X-ray Absorption Edge Spectrometry (XAES) as Applied to Coordination Chemistry," *Coord. Chem. Rev.*, **9**, 275–310 (1973).
- P. Li, I.-W. Chen, and J. E. Penner-Hahn, "X-ray Absorption Studies of Zirconia Polymorphs: I, Characteristic Local Structures," *Phys. Rev. B*, **48**, 10063–73 (1993).
- P. Li, I.-W. Chen, and J. E. Penner-Hahn, "X-ray Absorption Studies of Zirconia Polymorphs: II, Effect of  $Y_2O_3$  Dopant on  $ZrO_2$  Structure," *Phys. Rev. B*, **48**, 10074–81 (1993).
- P. Li, I.-W. Chen, and J. E. Penner-Hahn, "X-ray Absorption Studies of Zirconia Polymorphs: III, Static Distortion and Thermal Distortion," *Phys. Rev. B*, **48**, 10082–89 (1993).
- P. Li, I.-W. Chen, and J. E. Penner-Hahn, "Effect of Dopants on Zirconia Stabilization—An X-ray Absorption Study: I, Trivalent Dopants," *J. Am. Ceram. Soc.*, **77**, 118–28 (1994).
- P. Li, I.-W. Chen, and J. E. Penner-Hahn, "Effect of Dopants on Zirconia Stabilization—An X-ray Absorption Study: II, Tetravalent Dopants," *J. Am. Ceram. Soc.*, **77**, 1281–88 (1994).
- P. Li, I.-W. Chen, and J. E. Penner-Hahn, "Effect of Dopants on Zirconia Stabilization—An X-ray Absorption Study: III, Charge-Compensating Dopants," *J. Am. Ceram. Soc.*, **77**, 1289–95 (1994).
- L. A. Grunes, "Study of the Edges of 3d Transition Metals in Pure and Oxide Form by X-ray-Absorption Spectroscopy," *Phys. Rev. B*, **27**, 2111–31 (1983).
- S. I. Salem, C. N. Chang, and T. J. Nash, "Energy Shift and Structure of the K-Absorption Edge of Vanadium in Some Vanadium Compounds," *Phys. Rev. B*, **18**, 5168 (1978).
- V. Kunzl, "Edge Shift and Valency of Metal Ions in Oxide," *Collect. Czech. Commun.*, **4**, 213 (1932).
- S. Kawata and K. Maeda, "Effect of Chem. Combination on the X-ray  $L_{III}$  Absorption Limits of Mo, Rh, Pd, Ag, and Cd," *J. Phys. F*, **3**, 167 (1973).
- S. Kawata and K. Maeda, "X-ray Absorption Discontinuities of Cr and Fe,"

- <sup>39</sup>C. Mançé and V. B. Sapre, "Chemical Shifts in X-ray Absorption Spectra" pp. 287–301 in *Advances in X-ray Spectroscopy*. Edited by C. Bonnelle and C. Mande. Pergamon Press, Oxford, U.K., 1982.
- <sup>40</sup>K. S. Srivastava and V. Kumar, "Chemical Shifts of X-ray K or L Absorption Edges of Solids," *J. Phys. Chem. Solids*, **42**, 275 (1981).
- <sup>41</sup>S. P. Cramer, T. K. Eccles, F. W. Kutzler, K. O. Hodgson, and L. E. Mortenson, "Molybdenum X-ray Absorption Edge Spectra, the Chemical State of Molybdenum in Nitrogenase," *J. Am. Chem. Soc.*, **98**, 1287–88 (1976).
- <sup>42</sup>J. Wong, F. W. Lytle, R. P. Messmer, and D. H. Maylotte, "K-edge Absorption Spectra of Selected Vanadium Compounds," *Phys. Rev. B*, **30**, 5596–610 (1984).
- <sup>43</sup>I. A. Ovsyannikova, S. S. Batsanov, L. I. Nasonova, L. R. Batsanova, and E. A. Nekrasova, *Bull. Acad. Sci. USSR, Phys. Ser. (Engl. Transl.)*, **31**, 936 (1967).
- <sup>44</sup>L. Pauling, *The Nature of the Chemical Bond*, 2nd Ed.; p. 69. Cornell University Press, Ithaca, NY, 1948.
- <sup>45</sup>V. G. Bhide and N. V. Bhat, "X-ray K-Absorption Edge of Yttrium in Some Yttrium Compounds," *J. Chem. Phys.*, **48**, 3103–108 (1968).
- <sup>46</sup>Y. N. Xu and W. Y. Ching, "Electronic Structure of Yttrium Aluminum Garnet ( $Y_3Al_5O_{12}$ )," *Phys. Rev. B*, **59**, 10530–35 (1999).
- <sup>47</sup>F. Jollet, C. Noguera, M. Gautier, N. Thromat, and J. Duraud, "Influence of Oxygen Vacancies on the Electronic Structure of Yttrium Oxide," *J. Am. Ceram. Soc.*, **74**, 358–64 (1991).
- <sup>48</sup>N. Thromat, C. Noguera, M. Gautier, and J. P. Duraud, "Electronic Structure and Atomic Arrangement around Zr Substituted for Y in  $Y_2O_3$ ," *Phys. Rev. B*, **44**, 7904 (1991).
- <sup>49</sup>F. Jollet, C. Noguera, N. Thromat, M. Gautier, and J. P. Duraud, "Electronic Structure of Yttrium Oxide," *Phys. Rev. B*, **42**, 7587 (1990).
- <sup>50</sup>W. Lytle, P. S. P. Wei, R. B. Gregor, G. H. Via, and J. H. Sinfelt, "Effect of Chemical Environment on Magnitude of X-ray Absorption Resonance at  $L_{III}$  Edges, Studies on Metallic Elements, Compounds, and Catalysts," *J. Chem. Phys.*, **70**, 4849–55 (1979).
- <sup>51</sup>L. Rao, D. J. Schneider, R. J. Mayer, J. W. Pyrz, J. Widom, and L. Que Jr., "X-ray Absorption Spectroscopy of Iron-Tyrosinate Proteins," *J. Am. Chem. Soc.*, **106**, 1676–81 (1984).
- <sup>52</sup>J. Frandon, B. Brousseau, and F. Pradal, "Electronic Excitations in Some Transition Metals and Their Oxides," *Phys. Status Solidi B*, **98**, 379–84 (1980).
- <sup>53</sup>M. K. Loudjani and R. Cortes, "Study of the Local Environment around Zirconium Ions in Polycrystalline  $\alpha$ -Alumina in Relation with Kinetics of Grain Growth and Solute Drag," *J. Eur. Ceram. Soc.*, **20**, 1483–91 (1994).
- <sup>54</sup>P. E. D. Morgan; private communication.
- <sup>55</sup>P. R. Kenway, "Calculated Structures and Energies of Grain Boundaries in  $\alpha$ - $Al_2O_3$ ," *J. Am. Ceram. Soc.*, **77**, 349–55 (1994).
- <sup>56</sup>S. D. Mo, W. Y. Ching, and R. H. French, "Electronic Structure of a Near  $\Sigma 11$   $a$ -axis Tilt Grain Boundary in  $\alpha$ - $Al_2O_3$ ," *J. Am. Ceram. Soc.*, **79**, 627–33 (1996).
- <sup>57</sup>Y. Takigawa, Y. Ikuhara, and T. Sakuma, "Grain Boundary Bonding State and Fracture Energy in Small Amount of Oxide-Doped Fine-Grained  $Al_2O_3$ ," *J. Mater. Sci.*, **34**, 1991–97 (1999).
- <sup>58</sup>C. A. Handwerker, J. M. Dynys, R. M. Cannon, and R. L. Coble, "Dihedral Angles in Magnesia and Alumina: Distributions from Surface Thermal Grooves," *J. Am. Ceram. Soc.*, **73**, 1371–77 (1990). □

# Effect of Nd<sub>2</sub>O<sub>3</sub> Doping on the Densification and Abnormal Grain Growth Behavior of High-Purity Alumina

Chong-Min Wang\*

Pacific Northwest National Laboratory, Richland, Washington 99352

Helen M. Chan\* and Martin P. Harmer\*

Center for Advanced Materials and Nanotechnology, Lehigh University, Bethlehem, Pennsylvania 18015

The densification behavior and microstructural development of high-purity Al<sub>2</sub>O<sub>3</sub> doped with different levels of Nd<sub>2</sub>O<sub>3</sub> were investigated. Dopant levels ranged from 100–1000 ppm (Nd/Al atomic ratio). The densification behavior of the doped powders was studied using constant heating rate dilatometry. It was found that neodymium additions inhibited densification, with a corresponding increase in the apparent activation energy. The level of grain-boundary segregation was studied using high-resolution analytical electron microscopy. At dilute concentrations, the degree of neodymium grain-boundary excess was found to be consistent with a simple geometrical model relating this quantity to the overall dopant concentration and average grain size. For certain combinations of dopant level and heat treatment, supersaturation of the grain boundaries was observed, which was found to correlate with the onset of abnormal grain growth. Possible explanations for this behavior are discussed.

## I. Introduction

FOR the last several decades, the effect of impurities and additives on the sintering and microstructural development of alumina has received widespread attention. More recently, there has been work focusing on the influence of rare-earth additions. Interest in this class of dopant has arisen primarily because of the discovery that, even at parts-per-million (ppm) levels, rare-earth elements can greatly reduce the creep rate of alumina.<sup>1–4</sup> Using techniques such as secondary ion mass spectrometry (SIMS) and analytical electron microscopy (AEM), it is now well established that dopants such as yttrium and lanthanum segregate strongly to the alumina grain boundaries.<sup>5–9</sup> Given that the ionic radii of these ions are significantly greater than that of Al<sup>3+</sup>, the driving force for segregation is believed to arise primarily from elastic strain energy considerations.

With respect to the effect of the rare-earth dopant on densification and grain growth, the most widely studied additive is that of yttria.<sup>9–14</sup> Fang *et al.*<sup>11</sup> have observed that for alumina doped with 1000 ppm yttrium, the densification mechanism (at 1350°C) was consistent with control by grain-boundary diffusion, and densification kinetics were slowed by approximately one order of magnitude relative to undoped alumina. Voytovich *et al.*<sup>12</sup> studied the influence of yttrium over a range of temperatures and reported that, although yttrium doping inhibited densification at 1450°C, it had little effect at 1550°C, and no effect at 1650°C. These workers

rationalized their findings by suggesting a transition (with increasing temperature) from grain boundary to lattice diffusion control.

There is currently a body of research that attributes the development of abnormal grain growth in alumina to the presence of glass-forming impurities.<sup>15–18</sup> This phenomenon has also been investigated in alumina with yttrium additions. Unpublished research by the present authors has shown that, although alumina doped with 100 ppm yttrium exhibits a uniform microstructure consisting of equiaxed grains, samples doped with 1000 ppm yttrium often developed a bimodal grain structure. There are several studies in the literature that suggest that abnormal grain growth in yttrium-containing aluminas initiates at a critical grain-boundary impurity level.<sup>13</sup> The work of Voytovych and co-workers<sup>14</sup> showed that, although yttrium alone did not induce abnormal grain growth, the level of silicon required to trigger abnormal grain growth was reduced when yttrium was also present.

Although less studied, additions of the rare-earth neodymium have also been shown to be highly beneficial with regard to the tensile creep behavior of alumina.<sup>19–20</sup> For example, at 1200°C, the addition of 100 ppm neodymium reduces the creep rate of alumina by more than two orders of magnitude. Li *et al.*<sup>19</sup> reported that for alumina codoped with neodymium and zirconium, the enhancement in creep resistance was greater than achieved by doping with either neodymium or zirconium alone. As in the case of yttrium, SIMS mapping has shown that neodymium segregates to alumina grain boundaries;<sup>20</sup> a result that is hardly surprising, given that the ionic radius of Nd<sup>3+</sup> (0.98 Å) is slightly higher than that of Y<sup>3+</sup> (0.90 Å). To date, however, there have been no published reports that directly address the effect of neodymium additions on the densification and microstructural development of alumina; hence, the rationale for the present study.

## II. Experimental Procedure

### (1) Materials Preparation

Samples were prepared using ultra-pure α-Al<sub>2</sub>O<sub>3</sub> powder (AKP-53, Sumitomo Chemical America, New York, NY); the powder purity was 99.995%, with a mean particle size of 0.35 μm and a specific surface area of 12.7 m<sup>2</sup>/g. Doping of the powder was accomplished by a wet chemical process using neodymium nitrate of semiconductor grade; details of the procedure have been described elsewhere.<sup>19</sup> The Al<sub>2</sub>O<sub>3</sub> powder was nominally doped with Nd<sub>2</sub>O<sub>3</sub> at three concentration levels: 100, 350, and 1000 ppm (Nd/Al atomic ratio). These samples will subsequently be referred to as Nd100, Nd350, and Nd1000, respectively. Before sintering, the doped powder was calcined in air at 750°C for 5 h to remove possible organic contaminants and to decompose the neodymium nitrate. The dopant content of the powders was also determined using inductively coupled plasma atomic emission spectroscopy (ICP). A comparison of the nominal doping levels with the corresponding values measured using ICP is shown in Fig. 1. It can be seen that reasonably good agreement was obtained, confirming

J. E. Blendell—contributing editor



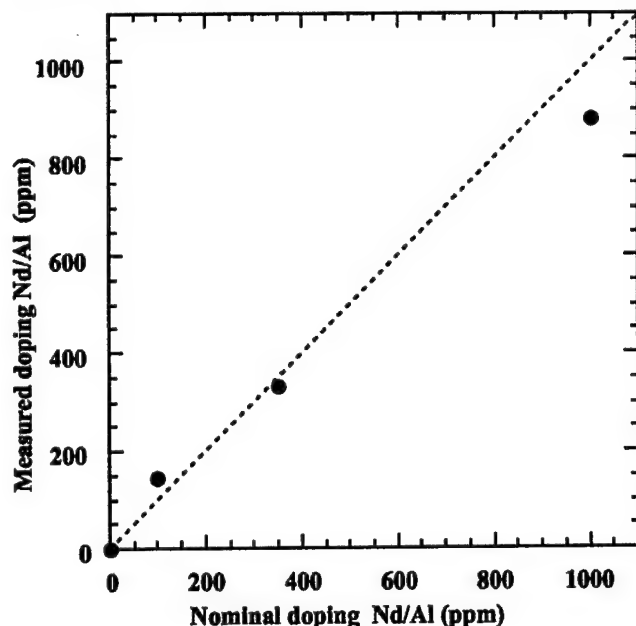


Fig. 1. Analysis of doped powders: a comparison between the nominal dopant levels and the measured levels using ICP.

the efficacy of the wet chemical approach for adding trace amounts of dopants to alumina.

Bulk samples were prepared by vacuum hot pressing in a graphite die (76.2 mm in diameter) at 50 MPa for 30 min. The hot-pressing temperatures were varied to achieve samples with approximately the same starting grain size. Hence, the undoped alumina was hot pressed at 1350°C, the Nd100 material was hot pressed at 1425°C, and the Nd350 and Nd1000 samples were hot pressed at 1450°C. These specimens were subsequently annealed in air at 1450°C for different times to coarsen the grain structure. The silicon content of the as hot-pressed samples was determined and found to be ~130 ppm.

## (2) Densification and Grain Growth

Green compacts for sintering were obtained by isostatic pressing of the powders in a cylindrical rubber tube at 300 MPa. This resulted in a green body cylindrical rod of ~5 mm in diameter, from which test samples (~10 mm length) were cut. The densification behavior was characterized by dilatometric studies, which were conducted under both isothermal annealing and constant heating rate (CHR) conditions. The isothermal annealing studies were conducted at 1450°C for periods up to 8 h. The CHR dilatometry was performed at a heating rate of 10°C/min.

Comparison of changes in the lateral and axial directions confirmed that the sample shrinkage was isotropic. The value of the density at any given time  $t$  ( $\rho_t$ ) was calculated from the following expression:

$$\rho_t = \left(\frac{L_f}{L_t}\right)^3 \cdot \rho_f \quad (1)$$

Where  $L_f$  is the final length of the specimen,  $L_t$  is specimen length at time  $t$ , and  $\rho_f$  is the final density as measured by the Archimedes method.

The sintered samples were sectioned, ground, and polished to a 1  $\mu\text{m}$  finish, and subsequently thermally etched at 1400°C for 0.5 h for examination by scanning electron microscopy (SEM).

## (3) STEM Analysis of Grain-Boundary Dopant Concentration

For selected samples, analysis of the grain-boundary neodymium concentration was conducted using scanning transmission

by the standard methods of diamond wheel slicing, thinning, dimpling, and finally ion-beam thinning to perforation. To prevent charging during the analysis, a thin carbon film was evaporated on the surface of the thin foils. Quantitative chemical analysis was performed on a dedicated STEM (model HB603, Vacuum Generators, UK) operating at 300 keV with a 30-mm virtual-objective aperture. The incident probe size was optimized to <1 nm, and the beam current was ~0.5 nA. Characteristic Al-K, Nd-K, and Y-K X-ray lines were measured using a windowless Si(Li) EDX detector (Oxford Instruments, Concord, MA). Net intensities of these lines were determined by the background subtraction and characteristic line peak-integration programs in a multichannel analyzer (Model eXL, Oxford Instruments). EDX spectra were quantified using the Cliff-Lorimer equation;<sup>21</sup> second-phase precipitates of  $\text{NdAlO}_3$  (present in the 1000 ppm neodymium-doped samples) were used as calibration standards. The value of the neodymium to aluminum atomic sensitivity factor ( $k_{\text{Nd/Al}}$ ), was determined to be 0.56. No corrections were made for either mass absorption or fluorescence, because calculations revealed that under the conditions of the present study, these quantities were negligible.

To convert the measured intensity ratio,  $I_{\text{Nd}}/I_{\text{Al}}$ , to a segregant grain-boundary excess amount, a square window method was used.<sup>22</sup> The dopant grain-boundary excess ( $\Gamma$ ), which is defined as the amount of solute present per unit area of grain boundary in excess of the amount of solute that would be present if there were no grain boundary, can be calculated as

$$\Gamma = w n_{\text{Al}} k_{\text{Nd/Al}} \left[ \left( \frac{I_{\text{Nd}}}{I_{\text{Al}}} \right)_{\text{gb}} - \left( \frac{I_{\text{Nd}}}{I_{\text{Al}}} \right)_{\text{bl}} \right] \quad (2)$$

where  $w$  is the width of the electron beam scan area perpendicular to the boundary in nanometers,  $n_{\text{Al}}$  is the atomic density of aluminum in  $\text{Al}_2\text{O}_3$  (47.1 atoms/nm<sup>3</sup>), and the subscripts gb and bl refer to the grain boundary and bulk lattice, respectively. In addition to the compositional analysis, high-resolution TEM observation of the grain boundaries was conducted in a field-emission gun electron microscope (Model JEM 2010F, JEOL, Tokyo, Japan) with a GIF (Gatan Imaging Filter, Gatan, Inc., Warrendale, PA) installed in the column.

## III. Results and Discussion

### (1) Densification

The dilatometry-derived densification curves for isothermal annealing at 1450°C are shown in Fig. 2. Neglecting grain size considerations, it can be seen that the additions of 100 and 350 ppm neodymium retard the densification kinetics relative to undoped alumina. Constant heating rate densification curves for  $\text{Al}_2\text{O}_3$  doped with different levels of  $\text{Nd}_2\text{O}_3$  are shown in Fig. 3(a). During the heating process, all the samples undergo considerable densification; in the case of the undoped  $\text{Al}_2\text{O}_3$ , on reaching 1450°C, the sample density is 95% of theoretical. With increasing dopant content, the density at any given temperature relative to the undoped alumina was progressively lower. A method for estimating the activation energy based on constant heating rate sintering data has been developed by Young and Cutler;<sup>23</sup> in the case where grain boundary diffusion was assumed to be the predominant mechanism, these workers showed that:

$$\left( \frac{\Delta L}{L_0} \right)^3 = \frac{A}{T} \cdot \exp \left( - \frac{Q}{RT} \right) \quad (3)$$

Where  $\Delta L$  is the linear shrinkage,  $L_0$  is the initial length of the sample,  $Q$  is the activation energy, and  $R$  is the gas constant. The parameter  $A$  was assumed to be a constant by Young and Cutler,<sup>23</sup> but as subsequently pointed out by Wang and Raj,<sup>24</sup> incorporates terms involving the density and grain size. It can be seen from Eq. (3) that, in principle, the apparent activation energy can be derived

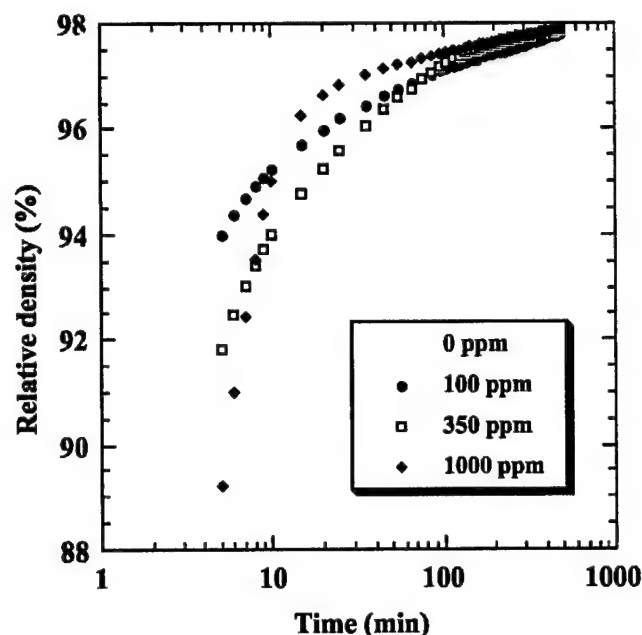


Fig. 2. Effect of neodymium content on densification: dilatometry data showing relative density as a function of time for isothermal annealing at 1450°C.

The CHR dilatometry data are plotted in this manner in Fig. 3(b). For the undoped alumina, this analysis gives an activation energy of 420 kJ/mol, which is consistent with values obtained from other work.<sup>25,26</sup> For the doped samples, the deviation from linearity is more marked than in the undoped case, so that quantitative determination of  $Q$  is more open to question. Possible explanations for this include variability in the starting particle-size distributions and differences in the relative effect of the dopant on densification and grain growth.<sup>24</sup> This seems quite likely, given that for yttrium- and lanthanum-doped alumina, the work of Fang *et al.*<sup>11</sup> showed that both of these dopants decreased the coarsening rate relative to the densification rate, thus shifting the grain

size/density trajectory to a higher density for a given grain size. These considerations notwithstanding, it is clear that for samples containing neodymium, there is an associated increase in the activation energy. Furthermore, the activation energy values for the three dopant levels tested appear to be roughly comparable. These observations are consistent with results obtained from creep data on the same compositions, where it was shown that the creep activation energies of the undoped, Nd100, Nd350, and Nd1000 samples were 475, 700, 860, and 900 kJ/mol, respectively.<sup>20</sup>

## (2) Microstructure Development and Abnormal Grain Growth

The hot-pressed and pressureless sintered samples showed very similar features with regard to microstructure development. SEM micrographs of the polished and thermally etched surfaces of the as-hot-pressed samples are depicted in Fig. 4. Note that no second-phase precipitates were observed in the 100 ppm sample, either by SEM or TEM. In contrast to the uniform microstructures of the undoped and Nd100 samples, the grain structure of the Nd350 sample was bimodal, comprising coarse grains ( $\sim 10$  mm diameter) dispersed in a fine-grained matrix ( $d \sim 1.5$  mm). Although no second phase was visible in the SEM, compositional mapping in the STEM occasionally revealed neodymium-enriched regions at grain triple points, which were believed to be nascent  $\text{NdAlO}_3$  particles (Fig. 5). The Nd1000 sample contained a mixture of coarse and fine-grained regions. Doping with neodymium at the 1000 ppm level was clearly in excess of the solubility limit, as evidenced by the numerous second-phase particles, which were situated almost exclusively at triple points in the fine-grain regions.

## (3) Dopant Grain-Boundary Segregation Behavior

As described earlier, the EDS peak intensity data can be used to calculate  $\Gamma$ , the grain-boundary excess. This parameter is a quantitative measure of the degree of segregation, and is defined as the amount of solute present per unit area of grain boundary, in excess of the amount present in the bulk. Assuming negligible solubility of the dopant in the bulk, Wang *et al.*<sup>27</sup> have shown that

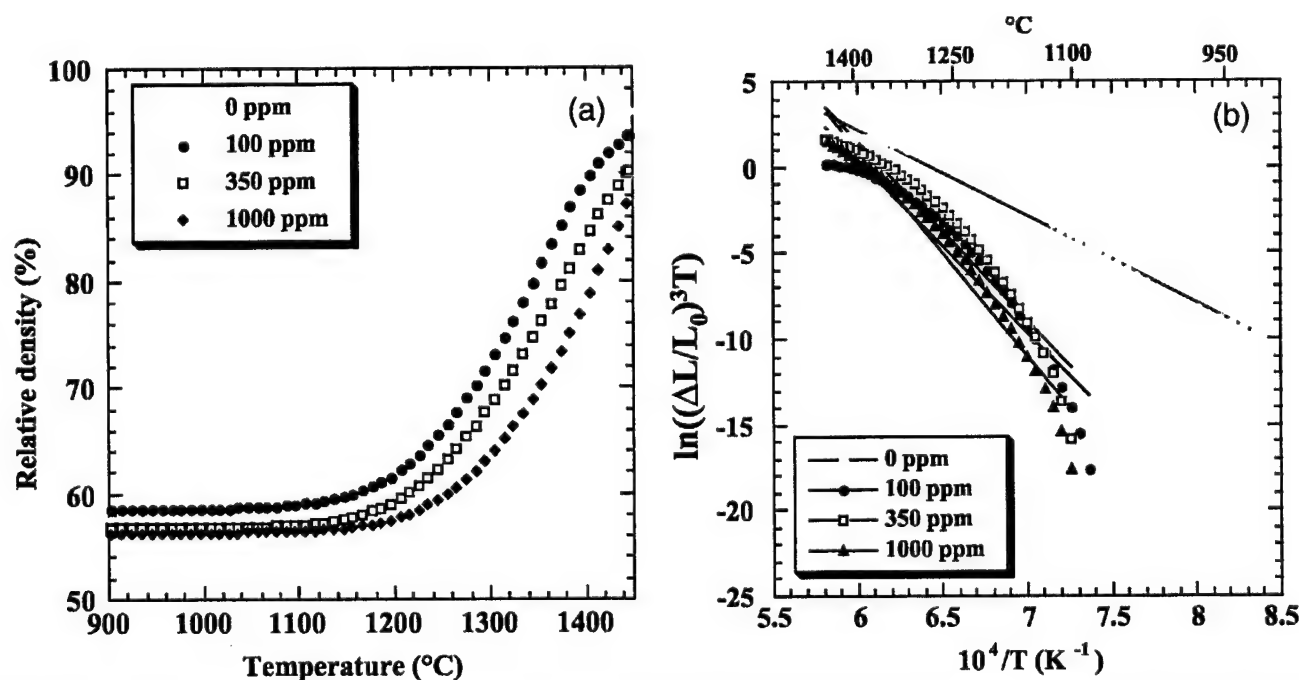


Fig. 3. (a) Constant heat rate (10°C/min) densification curves for alumina doped with differing levels of neodymium; (b) Arrhenius plot of the data from

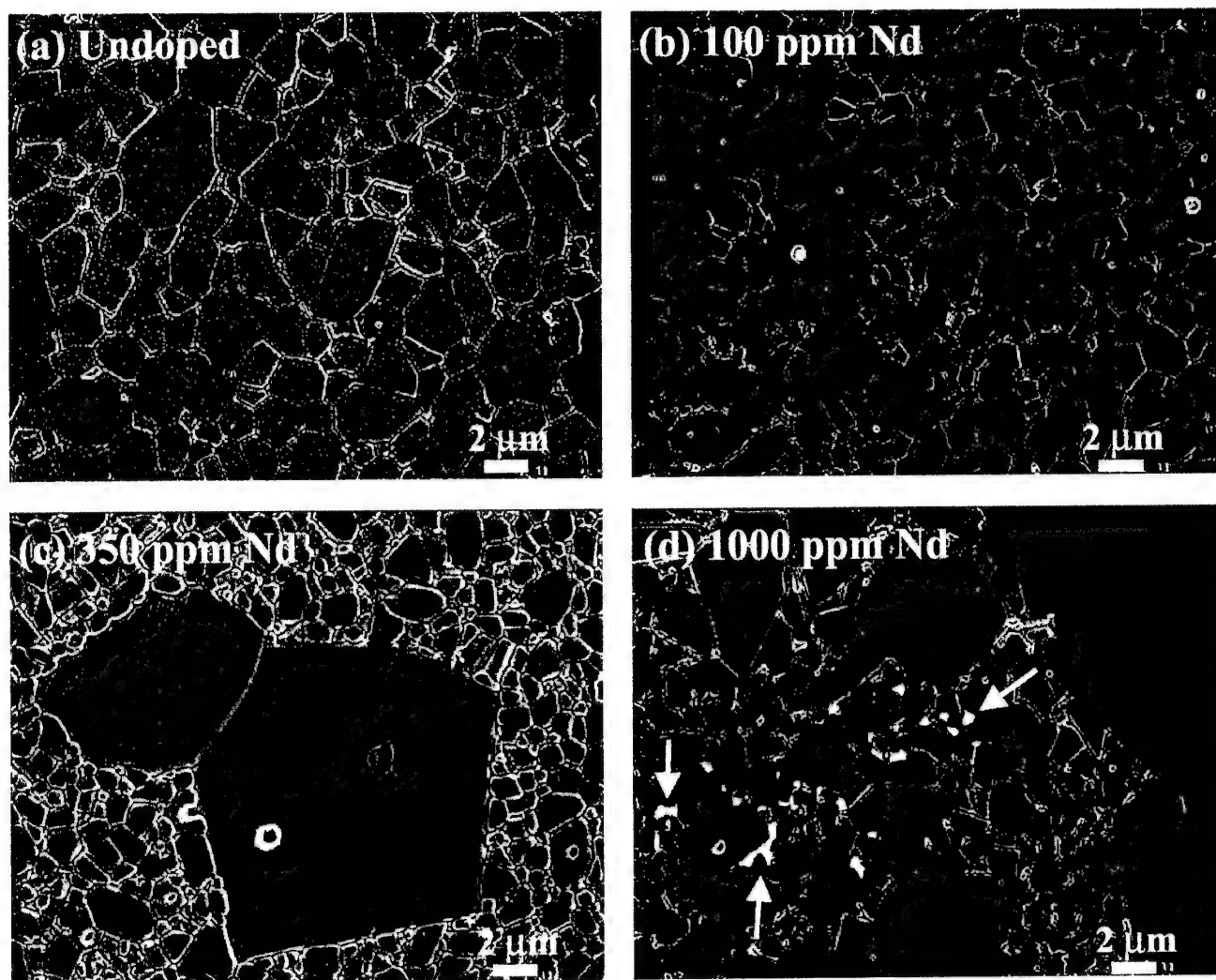


Fig. 4. SEM micrographs showing microstructure of as hot-pressed samples: (a) undoped alumina, (b) 100 ppm neodymium, (c) 350 ppm neodymium, and (d) 1000 ppm neodymium.

$\Gamma$  can also be expressed in terms of the grain size ( $d$ ) and initial dopant concentration ( $C_0$ ) as follows:

$$\Gamma = \frac{2N_{\text{Av}}p_0}{3W_{\text{Al}}} dC_0 \quad (4)$$

Where  $N_{\text{Av}}$  is Avogadro's constant,  $W_{\text{Al}}$  is the molecular weight, and  $r_0$  is the theoretical density of  $\alpha\text{-Al}_2\text{O}_3$ . The expression predicts that below the solubility limit the grain-boundary excess is proportional to the product of the initial dopant concentration ( $C_0$ ) and the average grain size ( $d$ ).

Figure 6 shows the measured values of neodymium grain-boundary excess, plotted as a function of  $dC_0$ . If one considers the data points in order of increasing  $dC_0$ , they correspond to the hot-pressed Nd100, Nd350, and Nd1000 samples, respectively. (For the purposes of comparison, data obtained in previous work corresponding to yttrium-doping are also plotted.<sup>27</sup>) It can be seen that the values of grain-boundary excess ( $\Gamma$ ) for the neodymium-doped samples initially show a linear dependence on  $dC_0$ . Moreover, the slope of the linear portion agrees reasonably well with the value expected from Eq. (4). With increasing  $dC_0$ ,  $\Gamma$  reaches a peak value, which corresponds to the supersaturation of the grain boundary with the dopant ions. Following the supersaturation,  $\Gamma$  drops to a constant value, reflecting the nucleation of the secondary phase precipitates. The saturation behavior of the neodymium-doped alumina is thus directly comparable to that of the yttrium-

A comparison of the magnitude of the grain-boundary excess and the microstructural development for each of the different neodymium-dopant levels clearly indicates that initiation of abnormal grain growth is correlated with the dopant grain-boundary supersaturation. One explanation that could be put forward based on classical solute drag theory is that select boundaries (which were initially in the supersaturated state) become "unpinned" because of the nucleation of second-phase particles.<sup>28</sup> Thus, the higher mobility of such "freed" boundaries would result in the development of abnormal grains. The possible role of solute interactions needs also to be considered. Baik and co-workers<sup>17</sup> have demonstrated that abnormal grain growth in alumina results from the presence of glass-forming impurities (silicon, calcium, potassium, sodium). For any given overall impurity concentration, therefore, it is argued that there exists a grain size at which the impurities attain a critical level sufficient to form a stable intergranular glassy phase. Similarly, as alluded to earlier, Gulgun *et al.*<sup>13</sup> have reported that abnormal grain growth in yttrium-doped alumina is triggered by a critical level of specific impurities segregated at grain boundaries. Based on these findings, high-resolution transmission electron microscopy was used in the present study to specifically look for amorphous grain-boundary phases. It was found that, for the 30 or so boundaries examined in this manner, no glassy films were detected. Nonetheless, the roles of intergranular

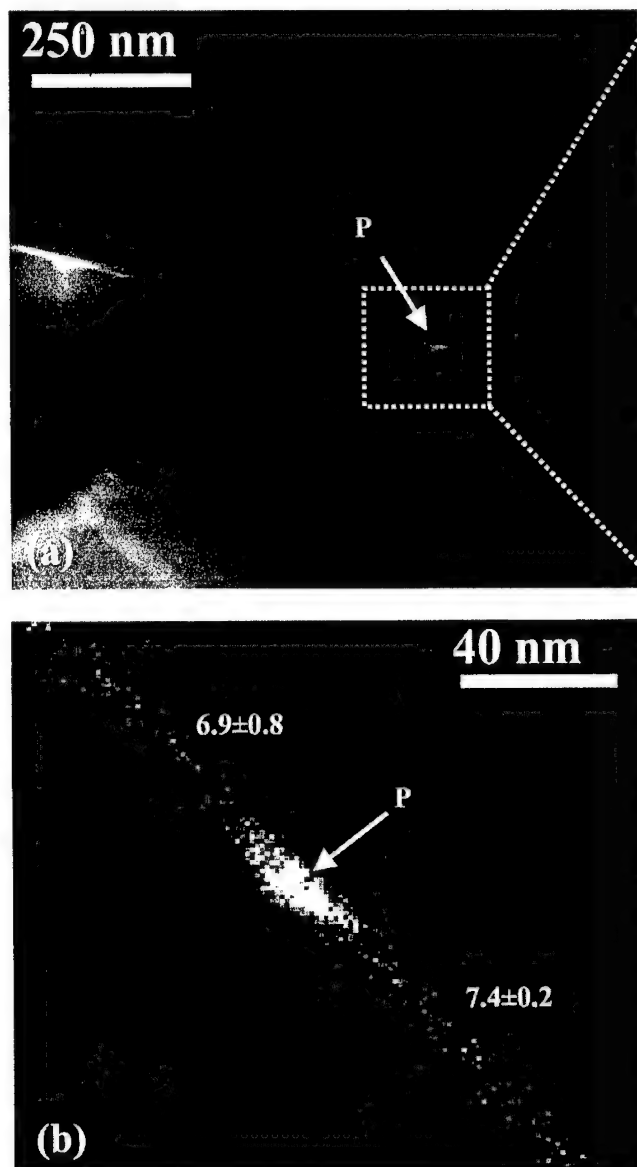


Fig. 5. STEM micrographs of the 350 ppm neodymium sample (as hot-pressed), showing neodymium enrichment at triple points.

Evidence also exists to support the model that structural differences in supersaturated boundaries may give rise to increased mobility and hence abnormal grain growth. For alumina powders containing both  $\text{MgO}$  and  $\text{Y}_2\text{O}_3$ , Sato and Carry<sup>29</sup> observed anomalous second peaks during constant heating rate densification studies. These workers interpreted their data to be the result of the inhibition of densification by yttrium at low grain-boundary concentrations, but the enhancement of densification in the near saturation regime. In high-temperature deformation studies of alumina doped with yttrium, Gruffel and Carry<sup>5</sup> and Lartigue *et al.*<sup>30</sup> observed that, with increasing grain size, a plateau in the creep strain rate developed for grain sizes in the range of 1–4  $\mu\text{m}$ . These researchers postulated that the plateau corresponded to rapid mass transport induced by yttria saturation at the grain boundaries. Most recently, Lartigue-Korinek and co-workers<sup>9</sup> proposed an increase in grain-boundary diffusivity due to a disordered “fluid-like” grain-boundary region that was associated with yttrium supersaturation. This type of model has some commonality with the EXAFS observations of Wang *et al.*<sup>27,31</sup> which established that in alumina a dopant supersaturated grain boundary can be considered to be composed of three layers: a grain-boundary core region and two sub-boundary regions. One could speculate that the presence of the more disordered outer sub-boundary regions increases mass transport, and thus contributes to the onset of abnormal

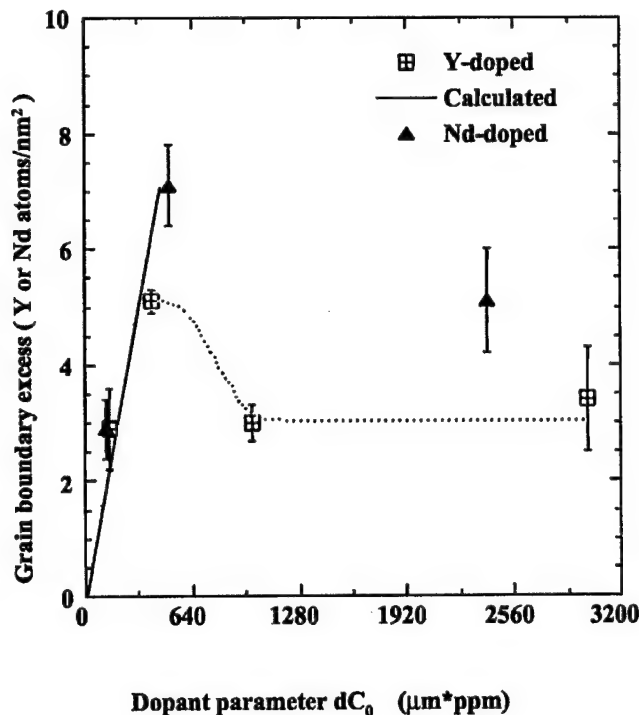


Fig. 6. Graph of grain-boundary excess ( $\Gamma$ ) versus the product of the grain size ( $d$ ) and overall dopant concentration ( $C_0$ ) for hot-pressed neodymium-doped samples. Data corresponding to yttrium-doping included for comparison.<sup>27</sup>

At present, it is not possible to distinguish unambiguously between the different roles of the segregant rare-earth ion. It is clear that a concentration regime exists in which select grain boundaries exhibit anomalous transport properties. Further study, however, is necessary to resolve whether such properties arise when the boundaries are in the supersaturated state, or immediately after the supersaturation is relieved. An important implication of the present work is the confirmation of the fact that the microstructure of dilutely doped alumina is not microscopically stable. Typically, during high-temperature service of a component, dynamical grain growth will lead to an overall increase of dopant grain-boundary concentration. If supersaturation and subsequent precipitation of second phase occurs, abnormal grain growth can develop. From the standpoint of microstructural stability, therefore, it may be desirable to use a sufficiently high concentration of dopant such that second-phase precipitates are nucleated, thus maintaining the grain-boundary dopant at equilibrium concentration.

#### IV. Summary

The influence of neodymium additions on the densification and microstructure development of alumina has been studied at dopant levels of 100, 350, and 1000 ppm. Doping was achieved using a wet chemical process, and good agreement was obtained between the nominal and measured levels. Results of dilatometric densification studies showed that the densification kinetics are inhibited relative to undoped alumina, and that there is an increase in the apparent activation energy. The degree of grain-boundary segregation was measured using STEM, and it was found that under dilute conditions, the measured grain-boundary excess of neodymium was consistent with a geometrical model relating this quantity to the overall dopant concentration and grain size. Furthermore, it was observed that under certain conditions, supersaturation of the alumina grain boundaries can occur, and that this is associated with abnormal grain growth. It was speculated that

supersaturated grain boundaries, which gave rise to enhanced boundary transport.

### Acknowledgments

The authors are grateful to Y.-Z. Li and J. Cho for many valuable discussions concerning the work, and to M. J. Watson for assistance with the dilatometry study.

### References

- <sup>1</sup>S. Lartigue, C. Carry, and L. Priester, "Grain Boundaries in High Temperature Deformation of Ytria and Magnesia Co-doped Alumina," *J. Phys. (Paris)*, **C1-51**, 985-90 (1990).
- <sup>2</sup>J. D. French, J. Zhao, M. P. Harmer, H. M. Chan, and G. A. Miller, "Creep of Duplex Microstructures," *J. Am. Ceram. Soc.*, **77**, 2857-65 (1994).
- <sup>3</sup>J. Cho, M. P. Harmer, H. M. Chan, J. M. Rickman, and A. M. Thompson, "Effect of Yttrium and Lanthanum on the Tensile Creep Behavior of Aluminum Oxide," *J. Am. Ceram. Soc.*, **80**, 1013-17 (1997).
- <sup>4</sup>H. Yoshida, Y. Ikuhara, and T. Sakuma, "Transient Creep in Fine-Grained Polycrystalline  $\text{Al}_2\text{O}_3$  with  $\text{Lu}^{3+}$  Ion Segregation at Grain Boundaries," *J. Mater. Res.*, **16**, 716-20 (2001).
- <sup>5</sup>P. Gruffel and C. Carry, "Effect of Grain Size on Yttrium Grain Boundary Segregation in Fine-Grained Alumina," *J. Eur. Ceram. Soc.*, **11**, 189-99 (1993).
- <sup>6</sup>A. M. Thompson, K. K. Soni, H. M. Chan, M. P. Harmer, D. B. Williams, J. M. Chabala, and R. L. Setti, "Dopant Distribution in Rare-Earth-Doped Alumina," *J. Am. Ceram. Soc.*, **80**, 373-76 (1997).
- <sup>7</sup>J. Bruley, J. Cho, H. M. Chan, M. P. Harmer, and J. M. Rickman, "STEM Analysis of Grain Boundaries of Creep Resistant Y- and La-Doped Alumina," *J. Am. Ceram. Soc.*, **82**, 2865-70 (1999).
- <sup>8</sup>M. A. Gulgun, R. Voytovych, I. MacLaren, and M. Ruhle, "Cation Segregation in an Oxide Ceramic with Low Solubility: Yttrium Doped  $\alpha\text{-Al}_2\text{O}_3$ ," *Interface Sci.*, **10**, 99-110 (2002).
- <sup>9</sup>S. Lartigue-Korinek, C. Carry, and L. Priester, "Multi-Scale Aspects of the Influence of Yttrium on the Microstructure, Sintering and Creep of Alumina," *J. Eur. Ceram. Soc.*, **22**, 1525-41 (2002).
- <sup>10</sup>M. A. Gulgun, V. Putlayev, and M. Ruhle, "Effect of Yttrium Doping  $\alpha\text{-Alumina}$ : I, Microstructure and Microchemistry," *J. Am. Ceram. Soc.*, **82**, 1849-56 (1999).
- <sup>11</sup>J. Fang, A. M. Thompson, M. P. Harmer, and H. M. Chan, "Effect of Y and La on the Sintering Behavior of Ultra-High-Purity  $\text{Al}_2\text{O}_3$ ," *J. Am. Ceram. Soc.*, **80**, 2005-12 (1997).
- <sup>12</sup>R. Voytovych, I. MacLaren, M. A. Gulgun, R. M. Cannon, and M. Ruhle, "The Effect of Yttrium on Densification and Grain Growth in  $\alpha\text{-Al}_2\text{O}_3$ ," *Acta Mater.*, **50**, 3453-63 (2002).
- <sup>13</sup>M. A. Gulgun, R. Voytovych, E. Bischoff, R. M. Cannon, and M. Ruhle, "Microstructural Development in  $\alpha\text{-Al}_2\text{O}_3$ ," *Ceram. Trans.*, **118**, 115-25 (2000).
- <sup>14</sup>R. Voytovych, M. Gulgun, and M. Ruhle, "Microstructural Evolution in Y-Doped Polycrystalline Alumina," *Trans. JWRI*, **30**, 425-30 (2001).
- <sup>15</sup>C. A. Handwerker, P. A. Morris, and R. L. Coble, "Effects of Chemical Inhomogeneities on Grain Growth and Microstructure in  $\text{Al}_2\text{O}_3$ ," *J. Am. Ceram. Soc.*, **72**, 130-36 (1989).
- <sup>16</sup>C. A. Bateman, S. F. Bennison, and M. P. Harmer, "Mechanism for the Role of MgO in the Sintering of  $\text{Al}_2\text{O}_3$  Containing Small Amounts of a Liquid Phase," *J. Am. Ceram. Soc.*, **72**, 1241-44 (1989).
- <sup>17</sup>S. I. Bae and S. Baik, "Determination of Critical Concentrations of Silica and/or Calcia for Abnormal Grain Growth in Alumina," *J. Am. Ceram. Soc.*, **76**, 1065-67 (1993).
- <sup>18</sup>J.-C. Nam, I.-J. Bae, and S. Baik, "Origin and Control of Abnormal Grain Growth in Alumina," pp. 323-29 in *Ceramic Microstructures: Control at the Atomic Level*. Edited by A. P. Tomsia and A. Glaeser. Plenum Press, New York, 1998.
- <sup>19</sup>Y.-Z. Li, C. Wang, H. M. Chan, J. M. Rickman, M. P. Harmer, J. M. Chabala, K. L. Gavrilov, and R. Levi-Setti, "Codoping of Alumina to Enhance Creep Resistance," *J. Am. Ceram. Soc.*, **82**, 1497-504 (1999).
- <sup>20</sup>C.-M. Wang, J. Cho, H. M. Chan, M. P. Harmer, and J. M. Rickman, "Influence of Dopant Concentration on Creep Properties of  $\text{Nd}_2\text{O}_3$ -Doped  $\text{Al}_2\text{O}_3$ ," *J. Am. Ceram. Soc.*, **84**, 1010-16 (2001).
- <sup>21</sup>G. Cliff and G. W. Lorimer, "The Quantitative Analysis of Thin Specimens," *J. Microsc.*, **103**, 203-207 (1975).
- <sup>22</sup>U. Alber, H. Müllehan, and M. Ruhle, "Improved Quantification of Grain Boundary Segregation by EDS in a Dedicated STEM," *Ultramicroscopy*, **69**, 105-16 (1997).
- <sup>23</sup>W. S. Young and I. B. Cutler, "Initial Sintering with Constant Rates of Heating," *J. Am. Ceram. Soc.*, **53**, 659-63 (1970).
- <sup>24</sup>J. Wang and R. Raj, "Estimate of the Activation Energies for Boundary Diffusion from Rate-Controlled Sintering of Pure Alumina, and Alumina Doped with Zirconia or Titania," *J. Am. Ceram. Soc.*, **73**, 1172-75 (1990).
- <sup>25</sup>J. Zhao and M. P. Harmer, "Sintering of Ultra-High Purity Alumina Doped Simultaneously with MgO and FeO," *J. Am. Ceram. Soc.*, **70**, 860-66 (1987).
- <sup>26</sup>J. Zhao and M. P. Harmer, "Sintering Kinetics for a Model Final-Stage Microstructure: A Study of  $\text{Al}_2\text{O}_3$ ," *Philos. Mag. Lett.*, **63**, 7-14 (1991).
- <sup>27</sup>C. M. Wang, G. S. Cargill III, H. M. Chan, and M. P. Harmer, "Structural Features of Y Saturated and Supersaturated Grain Boundaries in Alumina," *Acta Mater.*, **48**, 2579-91 (2000).
- <sup>28</sup>S. J. Bennison and M. P. Harmer, "A History of the Role of MgO in the Sintering of  $\alpha\text{-Al}_2\text{O}_3$ ," pp. 13-49 in *Ceramic Transactions, Vol. 7, Sintering of Advanced Ceramics*. Edited by C. A. Handwerker, J. E. Blendell, and W. A. Kaysser. American Ceramic Society, Westerville, OH, 1990.
- <sup>29</sup>E. Sato and C. Carry, "Ytria Doping and Sintering of Submicrometer-Grained  $\alpha\text{-Alumina}$ ," *J. Am. Ceram. Soc.*, **79**, 2156-60 (1996).
- <sup>30</sup>S. Lartigue, L. Priester, F. Dupau, P. Gruffel, and C. Carry, "Dislocation Activity and Differences between Tensile and Compressive Creep of Ytria Doped Alumina," *Mater. Sci. Eng. A*, **164**, 211-15 (1997).
- <sup>31</sup>C. M. Wang, G. S. Cargill III, M. P. Harmer, H. M. Chan, and J. Cho, "Atomic Structural Environment of Grain Boundary Segregated Y and Zr in Creep Resistant Alumina from EXAFS," *Acta Mater.*, **47**, 3411-22 (1999). □



# Scanning Transmission Electron Microscopy Analysis of Grain Boundaries in Creep-Resistant Yttrium- and Lanthanum-Doped Alumina Microstructures

John Bruley,<sup>†</sup> Junghyun Cho,\* Helen M. Chan,\* Martin P. Harmer,\* and Jeffrey M. Rickman\*

Materials Research Center and Department of Materials Science and Engineering, Lehigh University, Bethlehem, Pennsylvania 18015

High-spatial-resolution analytical electron microscopy using energy-dispersive X-ray (EDX) and electron energy-loss spectrometry (EELS) of yttrium- and lanthanum-doped  $\text{Al}_2\text{O}_3$  has been conducted to ascertain the level of segregation of these impurities to grain boundaries. Line profile analyses indicate that the segregation is confined to a layer thickness of  $<3$  nm. Similar amounts of excess solute have been observed in both dopant systems:  $4.4 \pm 1.5$  and  $4.5 \pm 0.9$  at./nm<sup>2</sup> for yttrium and lanthanum, respectively. Assuming all the segregant is uniformly distributed within  $\pm 0.5$  nm of the boundary, this excess corresponds to  $9 \pm 3$  at.% for yttrium-doped  $\text{Al}_2\text{O}_3$  and  $10 \pm 2$  at.% for lanthanum-doped  $\text{Al}_2\text{O}_3$ . For both dopant systems, examination of the spatially resolved electron energy-loss near-edge structures (ELNES) on the  $\text{Al-L}_{2,3}$  edge suggests a loss in octahedral symmetry and a slight  $\text{Al-O}$  bond-length expansion. No significant change is noted in the  $\text{O-K}$  edge.

## I. Introduction

THE controlled doping of ultra-high-purity  $\text{Al}_2\text{O}_3$  with small amounts ( $<1000$  ppm) of rare-earth elements, such as lanthanum and yttrium, dramatically alters sintering and creep rates in these systems.<sup>1-4</sup> Furthermore, the introduction of similar dopants in many metal alloys reportedly influences their high-temperature oxidation properties.<sup>5</sup> Given these observations, considerable effort has been directed at elucidating the function of dopants in rate-dependent processes in ceramic oxides. Because the dopants under consideration have relatively low solubilities in  $\text{Al}_2\text{O}_3$ , most studies have noted that dopant grain-boundary segregation is generally favorable and have, therefore, focused on the structural and chemical changes at boundaries that attend segregation. In particular, several investigations have identified (a) the misfit strain energy of solute ions and (b) the presence of space-charge layers comprising charged point defects near boundaries as two important factors that correlate with the propensity for segregation as well as boundary transport rates.<sup>6-11</sup>

A consistent picture of boundary segregation is beginning to emerge from studies in  $\text{Al}_2\text{O}_3$ . For example, from measurements of segregation profiles using energy-dispersive X-ray (EDX) with scanning transmission electron microscopy (STEM), Li and Kingery<sup>12</sup> have concluded that the primary driving force for the segregation of isovalent cations is the

strain energy associated with ionic misfit. Recent calculations are consistent with this conclusion.<sup>4,13,14</sup> The impact of a segregant on boundary structure also has been of some interest. Indeed, prompted by recent speculation that yttrium doping enhances the population of special "near coincidence" boundaries in hot-pressed  $\text{Al}_2\text{O}_3$ ,<sup>1,15</sup> Cho *et al.*<sup>16</sup> have shown that the grain-boundary structure in  $\text{Al}_2\text{O}_3$  (as characterized by the frequency of selected coincident lattice site boundaries (CSLs) and the grain-boundary misorientation distribution) is not significantly altered by the addition of yttrium. This observation is also consistent with the TEM work of Gülgün *et al.*,<sup>17</sup> who studied the same yttrium-doped material as examined in the present work. These researchers have characterized more than 100 grain boundaries in yttrium-doped  $\text{Al}_2\text{O}_3$ , and they have found very few special boundaries. Thus, the beneficial influence of yttrium-doping appears not to be primarily through its effect on the grain-boundary structure. Moreover, yttrium has been found to segregate to all grain boundaries, having a maximum coverage on dense (0112) planes. Although a somewhat decreased level of yttrium on the basal (0001) planes is observed (although a significant amount of silicon is present), even apparently "clean" boundaries have shown significant segregation to grain-boundary dislocation cores.

Striking visual evidence of grain-boundary segregation has been provided by other probes. Most notably, Thompson *et al.*<sup>3</sup> have used scanning ion mass spectrometry (SIMS) mapping to vividly demonstrate the widespread uniformity of grain-boundary segregation of lanthanum and yttrium in doped  $\text{Al}_2\text{O}_3$ . The images indicate qualitatively that segregation is essentially isotropic, with very few boundaries denuded of segregant ions. Although this technique provides elemental maps with parts-per-million sensitivity, it is, unfortunately, not yet sufficiently reliable for quantification. Furthermore, the lateral spatial resolution of SIMS, which is of the order of  $0.1 \mu\text{m}$ , is inadequate for modeling of grain-boundary segregation structures.

The goal of the present work is to use EDX and electron energy loss spectroscopy (EELS) in a dedicated STEM to analyze quantitatively the grain-boundary segregation profiles in the same doped, high-purity aluminas examined earlier.<sup>2-4</sup> Another goal is to investigate the coordination environment of the aluminum and oxygen ions in the vicinity of the boundary, using spectrum-line profiling. This is accomplished by examining the characteristic near-edge structures of the elemental ionization edges. Taken together, this information provides valuable new understanding on grain-boundary structure and chemistry near segregated interfaces in  $\text{Al}_2\text{O}_3$ .

## II. Experimental Procedure

The two samples selected for this analysis were processed using procedures described in earlier studies.<sup>2-4</sup> In brief, the first specimen was composed of high-purity commercial  $\text{Al}_2\text{O}_3$  powder (AKP-53, Sumitomo Chemicals, Tokyo, Japan) doped with 1000 at. ppm yttrium and hot pressed at  $1475^\circ\text{C}$  under

A. H. Carim—contributing editor

*o/d grant*

Manuscript No. 189681. Received December 21, 1998; approved April 27, 1999. Supported by the U.S. Air Force Office of Scientific Research under Contract No. F49620-94-1-0284 (monitored by Dr. A. Pechenik). Support for J.B. was provided by the National Science Foundation (DMR 93 06253).

\*Member, American Ceramic Society.

<sup>†</sup>Present address: IBM, Fishkill, NY.

vacuum to >99% of theoretical density. An inspection of the sample microstructure indicated the presence of yttrium aluminum garnet (YAG) precipitates and an average  $\text{Al}_2\text{O}_3$  grain size of  $2 \pm 1 \mu\text{m}$ . The second sample was doped with 500 ppm lanthanum, hot-pressed at  $1450^\circ\text{C}$ ; it also contained second-phase particles. Some isolated elongated grains were observed, and the average grain size of the lanthanum-doped sample was  $1.7 \pm 0.8 \mu\text{m}$ . The presence of a second phase in these two systems indicated that the solubility limit of the bulk and grain-boundary regions had been exceeded. The samples were prepared for analytical electron microscopy (AEM) by conventional polishing and dimpling, followed by ion milling.

Analytical microscopy was conducted in dedicated STEMs (Models HB603 and the HB501, VG Microscopes, East Grinstead, U.K.) operated at 300 and 100 keV, respectively. The 300 keV microscope was fitted with a windowless Si(Li) detector (Link Systems, Boston, MA) that enabled the highest spatial resolution and best detection sensitivity for EDX analysis. The 100 keV instrument, fitted with a parallel EELS detector (Gatan, Inc., Pleasanton, CA), was used predominantly for the EELS analysis. In both cases, the machines were operated to provide a beam current of  $\sim 0.5 \text{ nA}$  with a probe diameter of  $\sim 1.0 \text{ nm}$ , although these values were not explicitly determined for this study. For a typical foil thickness of  $\sim 50 \text{ nm}$ , the electron beam broadening for 300 keV electrons was expected to be  $\sim 2 \text{ nm}$ .<sup>18</sup> Only those boundaries that appeared planar and edge-on to the beam were examined to accomplish the analysis. Two analytical procedures were followed. The first involved acquiring spectral data while simultaneously scanning the probe over a small square area of sample (typically  $64 \text{ nm}^2$ ). The second approach involved data acquisition at discrete points across a line perpendicular to the boundary using digital beam control. EELS "spectrum-lines" were acquired using a custom function<sup>†</sup> operating within commercial software.

### III. Results

#### (1) Compositional Information

(A) *Yttrium-Doped  $\text{Al}_2\text{O}_3$* : To ascertain the level of yttrium segregation to grain boundaries in  $\text{Al}_2\text{O}_3$ , we begin by examining a boundary image and its associated EDX spectrum. Figure 1 shows a typical EDX spectrum recorded with the beam located over a grain boundary. Superimposed is the corresponding spectrum from an adjacent region within the grain, recorded under identical conditions. The marked difference in the intensity of the yttrium peaks is evident, indicating that the boundary region is yttrium-rich. Examination of the boundaries using conventional TEM imaging has revealed no evidence of a continuous grain-boundary phase. Figure 2 shows a high-angle annular dark-field (ADF) (or Z-contrast) image of a particular grain boundary; the bright contrast at the boundary confirms the segregation of the (higher atomic number) yttrium ions to the boundary plane. (The ADF inner angle was  $\sim 30 \text{ mrad}$ .) A bright, second-phase, particle pinning the grain boundary also is present. Comparable data have been recorded at seven other grain boundaries, each indicating similar segregation behavior. No distinction is made here between special and general boundaries.

Quantification of the EDX spectra was accomplished by application of the Cliff-Lorimer equation.<sup>19</sup> The yttrium-to-aluminum atomic sensitivity  $k$ -factor for the lines was determined using  $\text{Y}_3\text{Al}_5\text{O}_{12}$  powder (Alfa Aesar, Ward Hill, MA) as a standard and found to be  $k_{\text{YAl}} = 0.53$ . The mass absorption correction factor was estimated to be  $>0.97$  for a 50 nm thick foil and, therefore, neglected. A summary of the analyses is given in Table I. The following simple geometric model was

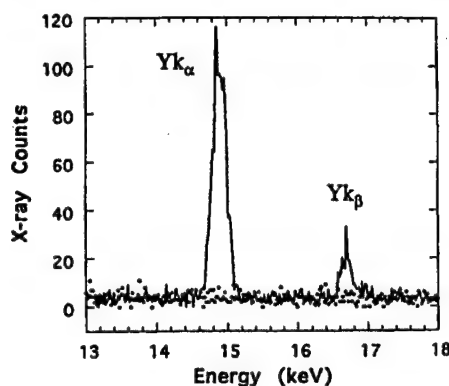


Fig. 1. EDX spectrum taken from grain-boundary region in yttrium-doped  $\text{Al}_2\text{O}_3$  ((•) data taken from the grain interior).

used to convert the measured intensity ratio,  $I_i/I_{\text{Al}}$ , to a segregated grain-boundary excess amount. The interaction volume was assumed to be the thickness multiplied by the irradiated area,  $d^2$ , where  $d$  was the larger dimension of the beam raster or probe size. The area of grain boundary illuminated was the product of  $d$  and the foil thickness. The grain-boundary excess (per unit area),  $\Gamma_i$ , of element  $i$  is then given by

$$\Gamma_i = d\rho_{\text{Al}}k_{\text{Al}} \frac{I_i}{I_{\text{Al}}}$$

where  $\rho_{\text{Al}}$  is the atomic density of aluminum in  $\alpha\text{-Al}_2\text{O}_3$ . The data in the fourth column of Table I represent the amount of yttrium, assuming that it was homogeneously distributed within a 1 nm thick boundary layer. The average yttrium content of the boundary was  $4.4 \pm 1.5 \text{ at.}/\text{nm}^2$ , which was equivalent to a cation fraction of  $9 \pm 3 \text{ at.}\%$ . No other significant level of impurity segregant was detected (sensitivity limit of  $\sim 0.5 \text{ at.}\%$  in 1 nm). Moreover, high-resolution electron microscope (HREM) imaging of the grain boundary (see, for example, Fig. 3), did not reveal a continuous glassy phase.

Further insight into the segregation behavior at grain bound-

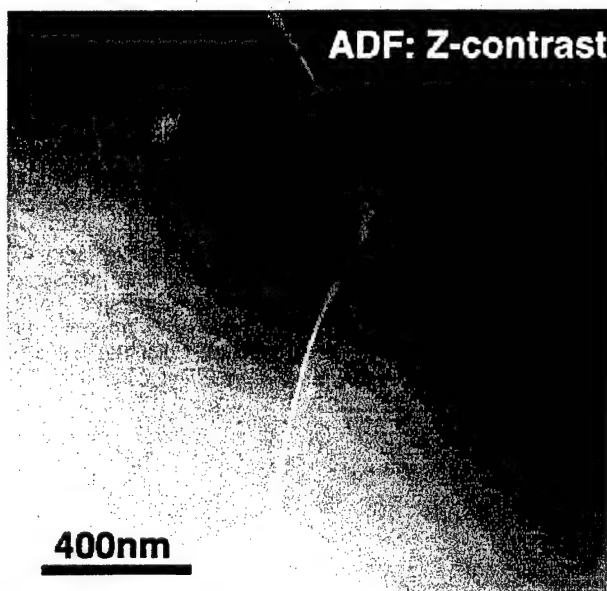


Fig. 2. ADF image of grain-boundary region in yttrium-doped sample. Enhanced brightness corresponds to increased mass thickness associated with yttrium segregation.

<sup>†</sup>Written by G. Düscher, Max-Planck Institut, Stuttgart, Germany.

Table I. Grain-Boundary EDX Analysis of Yttrium-Doped  $\text{Al}_2\text{O}_3$

$N_Y/N_{\text{Al}}$	$d$ (nm)	$\Gamma_Y$ (at./nm <sup>2</sup> ) <sup>†</sup>	$\rho_Y/\rho_{\text{Al}}$ in 1 nm <sup>2</sup>
0.0046	12	2.6	0.06
0.0020	43	4.1	0.08
0.0035	43	7.1	0.13
0.0027	43	5.5	0.12
0.0117	4	2.2	0.05
0.0556	2	5.2	0.11
0.0509	2	4.8	0.10
0.0420	2	4.0	0.08
		$\langle 4.4 \pm 1.5 \rangle$	$\langle 0.09 \pm 0.03 \rangle$

<sup>†</sup> $\Gamma_{\text{Al}}$  on (0006) in  $\alpha\text{-Al}_2\text{O}_3$  = 10 at./nm<sup>2</sup>. <sup>‡</sup> $\rho_{\text{Al}}$  = 47.1 at./nm<sup>2</sup>.

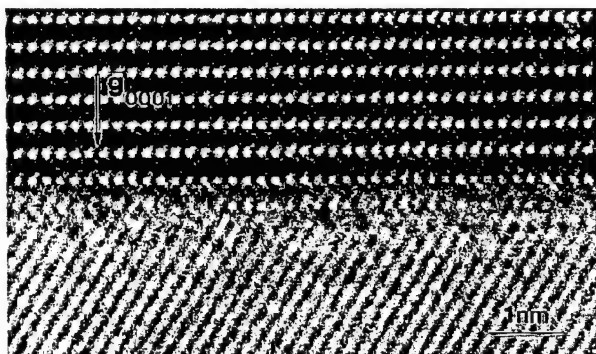


Fig. 3. HREM image of a grain boundary parallel to (0001) plane (note absence of a glassy grain-boundary phase). (Courtesy of M. A. Gülgün and M. Rühle.)

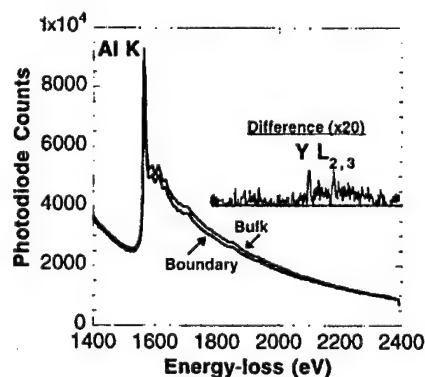


Fig. 4. EELS spectrum of grain boundary in yttrium-doped  $\text{Al}_2\text{O}_3$ . Spatial difference approach used to expose the  $L_{2,3}$  edge onset at 2080 eV.

aries has been obtained using EELS. Figure 4 shows an EELS spectrum revealing the onset of the weak  $\text{Y-L}_{2,3}$  edge at 2080 eV superimposed on an intense background. The  $\text{Al-K}$  edge onset is located at 1560 eV. Because of the very low signal to background ratio ( $<0.05$ ), evidence of the yttrium edge is poor. As a consequence, conventional background subtraction procedures, such as power-law fitting, are not feasible. An alternative method involves using the "spatial difference" approach, where the background is simply modeled using a standard spectrum taken under identical conditions from a neighboring  $\text{Al}_2\text{O}_3$  matrix. The spatial difference is then the residual given by the difference between the boundary and standard spectra. The as-recorded spectrum-line data set can be envisaged in three dimensions with beam position and energy loss plotted on

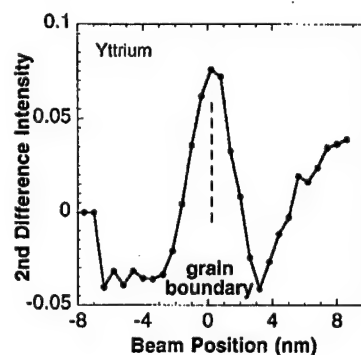


Fig. 5. Profile resulting from application of top-hat filter to spectrum-line data. Individual spectra in the spectrum-line series were normalized to the same intensity within a 50 eV pre-edge window so as to eliminate the effects of grain-boundary grooving on the intensity profile.

the x- and y-axes, respectively, and intensity plotted on the z-axis (see, for example, Fig. 7).

A relatively novel procedure was devised to extract the yttrium segregation profile from the above data, whereby a one-dimensional top-hat filter<sup>20</sup> was passed along the beam position coordinate, and the net counts within a 100 eV energy window centered on 2130 eV was determined. The spectra in the line series were first normalized in a 100 eV wide energy window centered at 2030 eV to minimize the effects of grain-boundary grooving. The optimum choice of the lobe dimensions of the top-hat filter depended on the pixel sample density, the instrumental probe, the counting statistics in the data, and the actual distribution of the segregant. In the limit of high sampling, good statistics, and narrow lobes on the filter, a profile was equivalent to a second derivative of the concentration distribution along the line-profile. Figure 5 represents such a profile generated from the yttrium-edge spectrum-line for a filter that had lobes 3 nm in width. In this case, the resultant width of the profile was probably determined by the spatial resolution of the microscope. The profile clearly illustrated the effectiveness of the filtering technique in revealing the change in yttrium content at the  $\text{Al}_2\text{O}_3$  boundary.

(B) *Lanthanum-Doped  $\text{Al}_2\text{O}_3$* : As in the case of yttrium, lanthanum was segregated at all the boundaries examined. A line profile extracted from a series of EDX spectra taken across one such boundary showed that the lanthanum was localized to a region of full-width half-height equal to 3 nm (see Fig. 6). This width was almost certainly limited by experimental conditions: the probe size was  $\sim 1$  nm, and beam broadening due to multiple electron scattering was  $\sim 2$  nm for a 50 nm thick  $\text{Al}_2\text{O}_3$

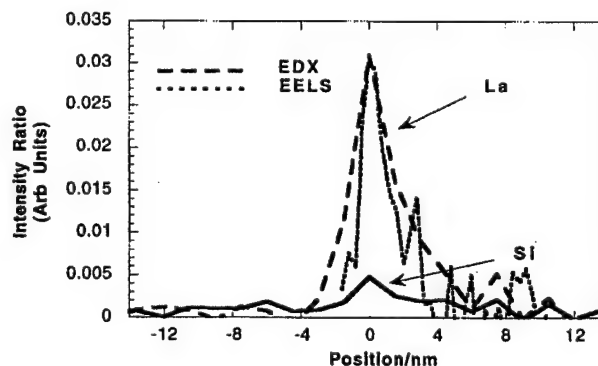


Fig. 6. Comparison of EDX and EELS profiles across boundary of lanthanum-doped  $\text{Al}_2\text{O}_3$ . The full width of the segregant layer is  $<2$  nm.



foil. For the purposes of quantitative analysis, the thin-film lanthanum to aluminum atomic  $k$ -factor was determined using a  $\text{LaAlO}_3$  powder (Alfa Aesar) as a standard. The resulting value was  $k_{\text{LaAl}} = 0.51$ ; effects due to absorption and/or fluorescence were ignored. The lanthanum analysis results (for eight separate boundaries) are summarized in Table II. The average lanthanum excess at the boundary was  $4.5 \pm 0.9$  at./nm<sup>2</sup>, which is equivalent to  $10 \pm 2$  at.% of the cation population uniformly distributed within a 1 nm thick layer.

In addition to the presence of lanthanum, a small concentration of silicon was segregated to the boundary, as shown in Fig. 6. The amount was estimated to be  $\sim 2$  at.% within  $\pm 0.5$  nm of the boundary and was too small to be associated with a continuous siliceous intergranular layer. The line-profile showing lanthanum segregation determined using EELS was slightly narrower than that determined from EDX, i.e., a full-width half-height of 1.5 nm, as compared with 3 nm.

## (2) Near-Edge Structure Analysis

In addition to compositional information, EELS is able to provide the density of unoccupied electronic states lying above the Fermi energy, through the fine structures on the ionization edges. The form of the  $\text{Al-L}_{2,3}$  and the  $\text{O-K}$  energy-loss near-edge structures (ELNES) can yield insight on the local bonding and coordination of the aluminum and oxygen ions.<sup>21–27</sup> Figure 7 displays a spectrum-line series, consisting of 30 spectra of the  $\text{Al-L}_{2,3}$  edge recorded along a line perpendicular to the grain boundary. Figure 8 shows the  $\text{O-K}$  edge series recorded across the same 30 nm long line. In both cases, the data have been processed to remove the smooth power-law background. The boundary plane is readily located at the region corresponding to the reduction in intensity of the aluminum and oxygen edges, most likely due to slight grain-boundary grooving. Preliminary inspection of the oxygen series reveals no grain-boundary-dependent component of the near-edge structure. On the other hand, there is evidence that the shape of the  $\text{Al-L}_{2,3}$  edge is slightly modified by the presence of the boundary. Specifically, in the boundary region, the initial peak intensity at 79 eV (corresponding to the transition from the  $2p$  core state to the  $3s$  conduction band), appears somewhat attenuated relative to the remaining ELNES absorption features located at 5 eV above threshold at 83 eV. This modification of the loss spectra is also observed at other boundaries in the lanthanum-doped sample and is similar to preliminary ELNES observations taken from boundaries in the yttrium-doped  $\text{Al}_2\text{O}_3$ . The statistical significance of these qualitative observations has been confirmed using principal components analysis (PCA), which is a matrix transformation tool that results in a list, in order of significance, of series of principal components (eigenvectors) of the original data set.<sup>28</sup> The application of this method has been described previously,<sup>29–31</sup> and, hence, the details are not reproduced here. Finally, to aid in the interpretation of the observed spectral changes in the  $\text{Al-L}_{2,3}$  ELNES at grain boundaries, the data is compared to the ELNES of two lanthanum aluminate compounds,  $\text{LaAlO}_3$  and  $\text{LaAl}_{11}\text{O}_{18}$ . The  $\text{Al-L}_{2,3}$  edges of these materials are shown in Fig. 9.

Table II. Grain-Boundary EDX Analysis of Lanthanum-Doped  $\text{Al}_2\text{O}_3$

$N_{\text{La}}/N_{\text{Al}}$	$d$ (nm)	$\Gamma_{\text{La}}$ (at./nm <sup>2</sup> )	$P_{\text{La}}/P_{\text{Al}}$ in 1 nm
0.011	8	4.1	0.09
0.010	8	3.8	0.08
0.013	8	4.9	0.10
0.015	8	5.7	0.12
0.015	8	5.7	0.12
0.026	4	4.9	0.10
0.012	5	2.8	0.06
0.047	2	4.4	0.09
		$\langle 4.5 \pm 0.9 \rangle$	$\langle 0.10 \pm 0.02 \rangle$

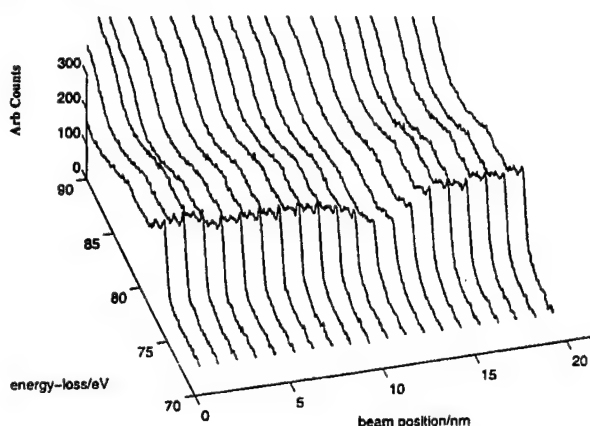


Fig. 7. Spectrum-line of  $\text{Al-L}_{2,3}$  edge in lanthanum-doped  $\text{Al}_2\text{O}_3$  after power-law background subtraction. Subtle changes to the edge are discernible in the grain-boundary region.

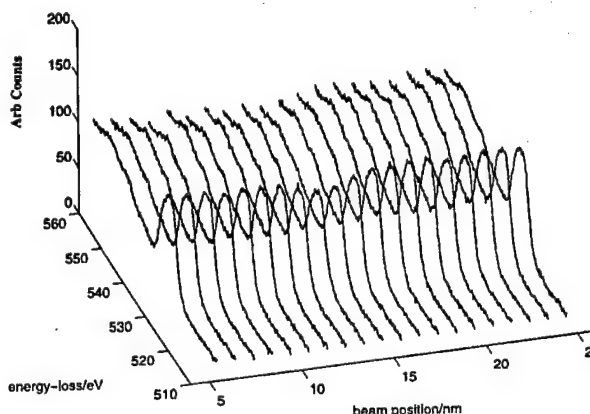


Fig. 8. Spectrum-line of  $\text{O-K}$  edge in lanthanum-doped  $\text{Al}_2\text{O}_3$  across same line as in Fig. 7. No changes are observed at the boundary.

## IV. Discussion

A comparison of average composition data measured here with those reported by SIMS<sup>3</sup> indicated agreement for the yttrium-doped sample, but a factor of 5 discrepancy for the lanthanum-doped sample (the present study yielding the higher values). This difference was greater than could be accounted for by experimental error alone and, may, in part, have been due to the difference in grain-boundary sampling. For the SIMS technique, data were acquired over micrometer-sized regions containing several grains, whereas, for the AEM measurements undertaken in the present work, only a limited subset of boundaries were present as flat and edge-on to the electron probe. A further possible contribution to the discrepancy could have been inaccuracy of the SIMS calibration. According to Thompson *et al.*,<sup>3</sup> the amount of segregant was determined by measuring the boundary signal relative to the total signal, collected over a large sample area. This ratio then was multiplied by the nominal concentration of dopant to give the grain-boundary content. If, for any reason, there was a nonuniform distribution of lanthanum within the sample, and the local dopant concentration within the sampled region was higher than the global content, then the grain-boundary content could have been underestimated by a significant factor.

The aforementioned factor of 5 difference between the SIMS and EDX data for lanthanum segregation has implications for modeling the grain-boundary structure. Table III shows the calculated values of the effective layer width of grain-boundary

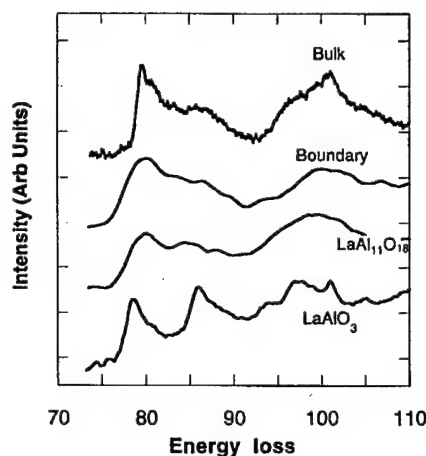


Fig. 9. Comparison of Al- $L_{2,3}$  edge spectra from bulk and grain-boundary regions in lanthanum-doped  $\text{Al}_2\text{O}_3$ , bulk  $\text{LaAlO}_3$ , and bulk  $\text{LaAl}_{11}\text{O}_{18}$ . (Boundary spectrum was smoothed using a 0.7 eV Gaussian filter.)

second phase ( $\text{LaAlO}_3$  or  $\text{LaAl}_{11}\text{O}_{18}$ ) for the various quantification results. A layer thickness of less than the atomic dimension represents the possibility of submonolayer coverage, a situation that leads to difficulties in the computer simulation of boundary segregation. Comparison of these widths with the lattice parameters for the La-Al-O compounds suggests that there is not enough segregant to form a complete unit-cell thickness of any known compound, but there might be enough to form a single plane or two of characteristic structure units.

Another finding of this study, reached by comparing the ELNES structure obtained from the grain-boundary region of the lanthanum-doped samples with that of the two lanthanum aluminates (Fig. 9), is that the  $\text{LaAlO}_3$  phase is most likely not present. Several observations lead to this conclusion. First, the sharp edge at 86 eV, which is present in the  $\text{LaAlO}_3$  spectrum, is conspicuously absent in the boundary spectrum. Second, covalent overlap between the Al  $s$  and Al  $d$  states with the narrow atomic-like La  $f$  states leads to the sharp onset of the Al- $L_{2,3}$  edge in  $\text{LaAlO}_3$ , a feature that is attenuated in the boundary spectrum. However, the edge structure is similar to that of aluminum in the  $\text{LaAl}_{11}\text{O}_{18}$  phase. This finding is consistent with the  $\text{Al}_2\text{O}_3$ - $\text{La}_2\text{O}_3$  phase diagram, where the  $\text{LaAl}_{11}\text{O}_{18}$  phase is the most  $\text{Al}_2\text{O}_3$ -rich of the intermediate compounds and would be expected to be the first to form if the solubility limit of  $\text{La}_2\text{O}_3$  were exceeded. The analytical results are consistent with the formation of up to 1 nm of the aluminum-rich second phase or the equivalent of about one-half of the unit-cell thickness. It is tempting to speculate that grain-boundary saturation of lanthanum corresponds to the formation of a monolayer of characteristic lanthanate structural units.

A simpler picture is that of direct lanthanum substitution for aluminum at the boundary. Such a substitution of the large lanthanum cation (ionic radius of 1.0 Å) might be expected to locally "separate" the (0001) close-packed oxygen basal

planes, thereby decreasing the octahedral symmetry about the smaller neighboring aluminum ions (ionic radius of 0.51 Å). Theory predicts this would lead to mixing of the 3s and 3p final states in the conduction band, which would remove the sharp edge onset characteristic of Al- $\text{O}_6$  structural units. Such a diffuse edge is observed in  $\gamma\text{-Al}_2\text{O}_3$ ,<sup>30</sup> inverse spinel,<sup>23</sup> and pure  $\text{Al}_2\text{O}_3$  grain-boundary structures,<sup>24</sup> and it is a feature characteristic of tetrahedral units. Further evidence of such dilatation is given by the position of the shape resonance at ~100 eV. The energy of this resonance above the Fermi energy has been shown to scale inversely with the square of the average Al-O bond length.<sup>32</sup> Assuming the Fermi energy remains fixed in the middle of the bandgap across the boundary, the resonance for bulk  $\text{Al}_2\text{O}_3$  is 25.1 eV, whereas that at the boundary is 23.6 eV. According to the inverse quadratic scaling law, this 1.5 eV reduction corresponds to a local 3% Al-O bond-length expansion.

Finally, similar changes in the oxygen data are absent, a result that is somewhat surprising, because some hybridization might have been expected between the O  $p$  states with the La  $f$  states. An electronic structure model would be needed here to affirm that, with only 10 at.% of segregant, the oxygen density-of-states is unaffected in the boundary region (within the detection sensitivity of the EELS technique).

## V. Conclusions

Chemical composition profiles indicate that segregation of yttrium and lanthanum is localized to within ~2 nm of the grain boundary, i.e., about the width of a single unit cell. In both cases, the amount is ~9 at.% within 1 nm of the boundary, which is consistent with the formation of a single layer of aluminum-rich second phase, although none has been confirmed yet. Modification of the Al- $L_{2,3}$  near-edge structure for the lanthanum-doped sample indicates a significant alteration in the cation bonding with a 3% Al-O bond length expansion. Such changes to the grain-boundary structure and cation-binding energy are consistent with the significant alteration in the diffusional creep properties as reported in the literature.<sup>4,33</sup>

**Acknowledgments:** Specimens for this research were generously provided by Drs. Y. Li, J. C. Fang, and A. M. Thompson. Discussions with Drs. K. Soni, M. A. Gülgün, and M. Rühle are gratefully acknowledged.

## References

- <sup>1</sup>S. Lartigue-Korinek and F. Dupau, "Grain Boundary Behavior in Superplastic Mg-Doped Alumina with Yttria Codoping," *Acta Metall. Mater.*, **42** [1] 293-302 (1994).
- <sup>2</sup>J. C. Fang, A. M. Thompson, M. P. Harmer, and H. M. Chan, "Effect of Yttrium and Lanthanum on the Final-Stage Sintering Behavior of Ultrahigh-Purity Alumina," *J. Am. Ceram. Soc.*, **80** [8] 2005-12 (1997).
- <sup>3</sup>A. M. Thompson, K. K. Soni, H. M. Chan, M. P. Harmer, D. B. Williams, J. M. Chabala, and R. Levi-Setti, "Dopant Distribution in Rare-Earth-Doped Alumina," *J. Am. Ceram. Soc.*, **80** [2] 373-76 (1997).
- <sup>4</sup>J. Cho, M. P. Harmer, H. M. Chan, J. M. Rickman, and A. M. Thompson, "Effect of Yttrium and Lanthanum on Tensile Creep Behavior of Aluminum Oxide," *J. Am. Ceram. Soc.*, **80** [4] 1013-17 (1997).
- <sup>5</sup>M. L. Gall, A. M. Huntz, B. Lesage, C. Monty, and J. Bernardini, "Self-Diffusion in  $\alpha\text{-Al}_2\text{O}_3$  and Growth Rate of Alumina Scales Formed by Oxidation: Effect of  $\text{Y}_2\text{O}_3$  Doping," *J. Mater. Sci.*, **30**, 201-11 (1995).
- <sup>6</sup>K. L. Kliever and J. S. Koehler, "Space Charge in Ionic Crystals. I. General Approach with Application to NaCl," *Phys. Rev. [Sect.] A*, **140** [4] 1226-39 (1965).
- <sup>7</sup>M. F. Yan, R. M. Cannon, and H. K. Bowen, "Space Charge, Elastic Field, and Dipole Contributions to Equilibrium Solute Segregation at Interfaces," *J. Appl. Phys.*, **54** [2] 764-78 (1983).
- <sup>8</sup>S. K. Tikku and F. A. Kröger, "Effect of Space Charge, Grain-Boundary Segregation, and Mobility Differences between Grain Boundary and Bulk on the Conductivity of Polycrystalline Alumina," *J. Am. Ceram. Soc.*, **63** [3-4] 183-89 (1980).
- <sup>9</sup>R. L. Coble, "A Model for Boundary Diffusion Controlled Creep in Polycrystalline Materials," *J. Appl. Phys.*, **34**, 1679-82 (1963).
- <sup>10</sup>R. M. Cannon, W. H. Rhodes, and A. H. Heuer, "Plastic Deformation of Fine-Grained Alumina ( $\text{Al}_2\text{O}_3$ ): I. Interface-Controlled Diffusional Creep," *J. Am. Ceram. Soc.*, **63** [1-2] 46-53 (1980).
- <sup>11</sup>K. R. Venkatchari and R. Raj, "Superplastic Flow in Fine-Grained Alumina," *J. Am. Ceram. Soc.*, **69** [2] 135-38 (1986).
- <sup>12</sup>C.-W. Li and W. D. Kingery, "Solute Segregation at Grain Boundaries in Polycrystalline  $\text{Al}_2\text{O}_3$ ," pp. 368-78 in *Advances in Ceramics*, Vol. 10, *Structure*

Table III. Thickness of Lanthanum Aluminate Phases for Mean Coverage Measured by SIMS and AEM Techniques

	Thickness (nm) <sup>†</sup>	
	SIMS measurement (2 at.%)	AEM measurement (10 at.%)
$\text{LaAlO}_3$ (cubic; $a_0 = 3.8$ Å)	0.04	0.2
$\text{LaAl}_{11}\text{O}_{18}$ (hexagonal; $a_0 = 5.5$ Å, $c = 22$ Å)	0.2	1.0

<sup>†</sup>Thickness <0.2 nm corresponds to submonolayer coverage.

and Properties of MgO and Al<sub>2</sub>O<sub>3</sub> Ceramics. Edited by W. D. Kingery. American Ceramic Society, Columbus, OH, 1984.

<sup>13</sup>M. Exner and M. W. Finnis, "Atomistic Simulation of Grain Boundaries in Alumina," *Mater. Sci. Forum*, **207–209**, 225–28 (1996).

<sup>14</sup>J. Cho, J. M. Rickman, H. M. Chan, and M. P. Harmer, "Modeling of Grain-Boundary Segregation in Aluminum Oxide," *J. Am. Ceram. Soc.*, in press.

<sup>15</sup>D. Bouchet, F. Dupau, and S. Lartigue-Korinek, "Structure and Chemistry of Grain Boundaries in Yttria-Doped Aluminas," *Mater. Sci. Forum*, **207–209**, 205–208 (1996).

<sup>16</sup>J. Cho, H. M. Chan, M. P. Harmer, and J. M. Rickman, "Influence of Yttrium Doping on Grain Misorientation in Aluminum Oxide," *J. Am. Ceram. Soc.*, **81** [11] 3001–3004 (1998).

<sup>17</sup>M. A. Gülgün, V. Putlayev, and M. Rühle, "Effects of Yttrium Doping in  $\alpha$ -Alumina: I. Microstructure and Microchemistry," *J. Am. Ceram. Soc.*, **82** [7] 1849–56 (1999).

<sup>18</sup>D. B. Williams, J. R. Michael, J. I. Goldstein, and A. D. Romig Jr., "Definition of the Spatial Resolution of X-ray Microanalysis in Thin Foils," *Ultramicroscopy*, **47**, 121–32 (1992).

<sup>19</sup>J. I. Goldstein, D. B. Williams, and G. Cliff, *Principles of Analytical Electron Microscopy*, p. 155. Edited by D. C. Joy, A. D. Romig, and J. I. Goldstein. Plenum, New York, 1986.

<sup>20</sup>D. B. Williams and C. B. Carter, *Transmission Electron Microscopy*, p. 603. Plenum, New York, 1996.

<sup>21</sup>A. Balzarotti and A. Bianconi, "Electronic Structure of Aluminum Oxide as Determined by X-ray Photoemission," *Phys. Status Solidi B*, **76**, 689–94 (1976).

<sup>22</sup>A. Balzarotti, F. Antonangeli, R. Gilanda, and G. Martino, "Core Excitons in Corundum," *Solid State Commun.*, **44** [2] 275–78 (1982).

<sup>23</sup>J. Bruley, M. W. Tseng, and D. B. Williams, "Spectrum-Line Profile Analysis of a Magnesium Aluminate Spinel/Sapphire Interface," *Microsc., Microanal., Microstruct.*, **6**, 1–18 (1995).

<sup>24</sup>J. Bruley, "Spatially Resolved Electron Energy-Loss Near-Edge Structure

Analysis of a Near  $\Sigma=11$  Tilt Boundary in Sapphire," *Microsc. Microanal. Microstruct.*, **4**, 23–39 (1993).

<sup>25</sup>R. Brydson, H. Sauer, W. Engel, and E. Zeitler, "EELS as a Fingerprint of the Chemical Coordination of Light Elements," *Microsc. Microanal. Microstruct.*, **2**, 159–69 (1991).

<sup>26</sup>R. Brydson, H. Sauer, W. Engel, J. M. Thomas, and E. Zeitler, "Coordination Fingerprints in Electron Loss Near-Edge Structures—Determination of the Local Site Symmetry of Aluminum and Beryllium in Ultrafine Minerals," *J. Chem. Soc. Chem. Commun.*, **15**, 1010–12 (1989).

<sup>27</sup>P. L. Hansen, R. Brydson, D. W. McComb, and I. Richardson, "EELS Fingerprint of Al-Coordination in Silicates," *Miscrosc., Microanal., Microstruct.*, **5**, 173–82 (1994).

<sup>28</sup>E. R. Malinowski and D. G. Howery, *Factor Analysis in Chemistry*. Robert E. Krieger Publishing, Malabar, FL, 1989.

<sup>29</sup>S. J. Splinter, J. Bruley, and D. A. Smith, "Decomposition of Electron Energy Loss Spectrum Line Profiles by Target Factor Analysis," p. 274 in *Proceedings of Microscopy and Microanalysis 95*. Edited by G. W. Bailey, M. H. Ellisman, R. A. Hennigar, and N. J. Zaluzec. Jones and Begell Publishing, New York, 1995.

<sup>30</sup>I. A. Brytov and Y. N. Romaschenko, "X-ray Spectroscopic Investigation of the Electronic Structure of Silicon and Aluminum Oxides," *Sov. Phys. Solid State*, **20** [3] 384–89 (1978).

<sup>31</sup>N. Bonnet, M. Brun, and C. Colliex, "Extracting Information from Sequences of Spatially Resolved EELS Spectra Using Multi-Variate Statistical Analysis," *Ultramicroscopy*, **77** [3] 97–112 (1999).

<sup>32</sup>A. Bianconi, M. Dell'Arriccia, A. Gargano, and C. R. Natoli, *Springer Series in Chemical Physics: EXAFS and Near Edge Structure*, p. 57. Edited by A. Bianconi, L. Incoccia, and S. Stipcich. Springer Verlag, Berlin, Germany, 1983.

<sup>33</sup>Y.-Z. Li, C. Wang, H. M. Chan, J. M. Rickman, M. P. Harmer, J. M. Chabala, K. L. Gavrilov, and R. Levi-Setti, "Codoping of Alumina to Enhance Creep Resistance," *J. Am. Ceram. Soc.*, **82** [6] 1497–504 (1999). □

# Modeling of Grain-Boundary Segregation Behavior in Aluminum Oxide

Junghyun Cho,\* Jeffrey M. Rickman,\* Helen M. Chan,\* and Martin P. Harmer\*\*

Materials Research Center and Department of Materials Science and Engineering,  
Whitaker Laboratory, Lehigh University, Bethlehem, Pennsylvania 18015

It is believed that the segregation of oversized dopant ions to grain boundaries in  $\text{Al}_2\text{O}_3$  hinders grain-boundary diffusion, thereby reducing the tensile creep rate in this system by  $\sim 2$ – $3$  orders of magnitude. In order to explain this improvement in creep behavior, it is helpful to characterize both the effective cation and interstitial volumes at grain boundaries, because the relative openness of some boundary structures suggests a great accommodation of oversized ions. In this study, the boundary volume is determined by a spatially local Voronoi construction, which highlights cation ( $\text{Al}^{3+}$ ) substitutional sites as well as large interstitial voids. In particular, we examine the spatial distribution of free volume near grain boundaries and, in addition, the dependence of the driving force for segregation on misfit strain in doped  $\text{Al}_2\text{O}_3$ . We interpret our results in light of recent evidence that selective codoping can provide a more efficient means of filling available space near boundaries, thereby further enhancing creep resistance.

## I. Introduction

GIVEN their relative mechanical stability and refractory nature, ceramic materials have been used extensively for high-temperature structural applications. However, because of the limited utility of monolithic ceramics in some extreme conditions, ceramic-matrix composites (CMCs) have received considerable attention in recent years. For example, under conditions in which high oxidation resistance at high temperatures is required, ceramic oxides, such as  $\text{Al}_2\text{O}_3$ , are possible candidates for both fiber and matrix materials. In this regime, the creep properties of  $\text{Al}_2\text{O}_3$  limit its applicability. Given this constraint, it is of interest to identify a subset of  $\text{Al}_2\text{O}_3$ -based oxides having superior creep resistance. We note that significant progress toward this goal occurred when it was discovered that the tensile creep rate of  $\text{Al}_2\text{O}_3$  decreased by  $\sim 2$ – $3$  orders of magnitude by the addition of  $\text{Y}_2\text{O}_3$  or  $\text{La}_2\text{O}_3$ .<sup>1,2</sup>

While the exact mechanism for enhanced creep resistance in these promising doped oxides is not yet known, emerging evidence suggests that grain boundaries play a dominant role in this behavior. One such observation is that oversized cation dopants strongly segregate to grain boundaries. This segregation tendency was highlighted in the work of Li and Kingery<sup>3</sup> and, more recently, in secondary ion mass spectroscopy (SIMS) mapping<sup>4</sup> and dedicated scanning transmission electron microscopy (STEM) studies.<sup>5</sup> Unfortunately, the complexity of grain-boundary geometries, particularly in the presence of dopants, makes it difficult to connect

boundary structure with boundary transport and, ultimately, diffusional creep. Consequently, the interaction between cation ( $\text{Al}^{3+}$ ) grain-boundary diffusion, which is believed to control creep in this study,<sup>1,6,7</sup> and dopant segregants has not been clearly identified. One purpose of this work, therefore, is to characterize systematically and model grain-boundary structure in doped  $\text{Al}_2\text{O}_3$  in order to connect boundary structure with the propensity for segregation. The long-term goal is to describe grain-boundary transport kinetics in the presence of dopants and, thereby, further elucidate the mechanisms for observed creep behavior.

Specifically, we focus here on the local free volume associated with grain boundaries in order to identify those regions that might accommodate (oversized) segregants. Thus, we use a local Voronoi construction consisting of space-filling polyhedra in the vicinity of grain boundaries under consideration to quantify this volume. For convenience, the grain boundaries selected here are special, coincidence-site lattice (CSL) boundaries with a common [0001] rotation axis, even though we expect to use the results to obtain generic information applicable to a broader spectrum of boundaries. The procedure for generating and relaxing these boundaries is summarized below.

The systematic analysis undertaken here is also useful in understanding certain experimental synergies associated with selective codoping. For example, it has been found that codoping  $\text{Al}_2\text{O}_3$  with neodymium and zirconium enhances its creep resistance beyond that observed in  $\text{Al}_2\text{O}_3$  systems singly doped with either ion.<sup>8</sup> This observation has led to the conjecture that, in some circumstances, a combination of large and small ions can fill the grain-boundary region more efficiently than can either ion individually, thereby greatly inhibiting diffusion and creep. In principle, then, the characterization of grain-boundary volume can suggest optimal doping strategies in  $\text{Al}_2\text{O}_3$  that lead to improved creep resistance.

## II. Simulation Methodology

### (1) Energetics

Various combinations of interionic potentials are used to describe the energetics of both pure and doped oxides. In particular, the lattice energy,  $U$ , of an oxide containing  $N$  ions is calculated with a pair potential having two contributions: a short-range combination of Born–Mayer and attractive van der Waals interactions and a long-range Coulombic interaction that together are given by

$$U = \frac{1}{2} \sum_{i=1}^N \sum_{j=1, j \neq i}^N \left[ V(r_{ij}) + \frac{z_i z_j}{r_{ij}} \right] \quad (1)$$

where  $z$  is the ionic charge,  $r_{ij}$  the separation between ions  $i$  and  $j$ , and  $V(r_{ij})$  the short-range interaction

$$V(r_{ij}) = A_{ij} \exp\left(-\frac{r_{ij}}{\rho}\right) - \frac{C}{r_{ij}^6} \quad (2)$$

The empirical parameters  $A$ ,  $\rho$ , and  $C$  are determined from fits to perfect crystal data, such as the lattice parameter, elastic constants, and cohesive energy.

R. Raj—contributing editor

*o/L Quant*

Manuscript No. 189878. Received September 11, 1998; approved July 12, 1999.  
Supported by the U.S. Air Force Office of Scientific Research under Contract No. F49620-98-1-0117. (Monitored by Dr. A. Pechenik.)

Presented at the 460th Annual Meeting of the American Ceramic Society, Cincinnati, OH, May 4, 1998 (Computational Modeling of Materials and Processing Symposium, Paper No. SV-014-98).

\*Member, American Ceramic Society.

\*\*Fellow, American Ceramic Society.

Table I. Empirically Fitted Potential Parameters and Shell Constants for  $\alpha$ -Al<sub>2</sub>O<sub>3</sub> and M<sub>2</sub>O<sub>3</sub> Systems<sup>†</sup>

Parameter	$\alpha$ -Al <sub>2</sub> O <sub>3</sub>	Fe <sub>2</sub> O <sub>3</sub>	Yb <sub>2</sub> O <sub>3</sub>	Eu <sub>2</sub> O <sub>3</sub>	La <sub>2</sub> O <sub>3</sub>
$A(+/-)$ (eV)	1460.3	3219.335	991.029	847.868	5436.827
$\rho(+/-)$ (Å)	0.29912	0.2641	0.3515	0.3791	0.2939
$C(+/-)$ (eV · Å <sup>6</sup> )	0.0	0.0	0.0	0.0	0.0
$A(-/-)$ (eV)	22764.3				
$\rho(-/-)$ (Å)	0.1490				
$C(-/-)$ (eV · Å <sup>6</sup> )	27.879				
$Y_+$ ( ē )	1.3830	1.971	-0.278	-0.991	5.149
$k_+$ (eV · Å <sup>-2</sup> )	92.488	179.58	308.91	304.92	173.90
$Y_-$ ( ē )	-2.8106				
$k_-$ (eV · Å <sup>-2</sup> )	103.07				

<sup>†</sup> $Y$  = shell charge,  $k$  = spring constant. In all cases, cation-cation potential is taken to be purely Coulombic (taken from Catlow *et al.*<sup>9</sup> and Bush *et al.*<sup>29</sup>).

In this study, the potential parameters by Catlow *et al.*<sup>9</sup> are used, as summarized in Table I, wherein only oxygen-oxygen and (repulsive) oxygen-aluminum interactions are considered, and where cutoff radii of 8.0 Å are imposed for both interactions. We note, however, that the long-range, Coulombic potential requires special treatment. Because this interaction falls off rather slowly in space, one can not establish arbitrary cutoff radii, because the summations indicated in Eq. (1) are only conditionally convergent.<sup>10</sup> This problem is remedied, as usual, by using a three-dimensional Ewald summation<sup>11,12</sup> to obtain the relevant contribution to the cohesive energy and associated Madelung constant. We also note the additional complication that a space-charge layer can form near extended defects.<sup>13,14</sup> This effect is not considered explicitly below, because the focus of this study is isovalent cation impurities.

Because defect interactions in ionic crystals depend strongly on the electrical polarization of the lattice, the description above is incomplete, because it does not incorporate the dielectric response of the material. For this purpose, the shell model, used by Dick and Overhauser<sup>15</sup> in their treatment of the dielectric properties of alkali halides, is implemented here. In this idealized model, an ion,  $i$ , is composed of both core and shell pieces that are connected by an elastic spring contributing an additional quadratic interaction potential

$$V_{sc}^i = \frac{1}{2} k_i (r_{si} - r_{ci})^2 \quad (3)$$

where  $k_i$  is a spring constant associated with ion,  $i$ , and  $r_{si}$  and  $r_{ci}$  the ionic shell and core positions, respectively. The corresponding shell charges and spring constant are again obtained from the dielectric properties of bulk crystals,<sup>9</sup> as summarized in Table I. While the core and shell positions are taken to coincide initially, the final equilibrium configuration in a defect region often consists of many core-shell displacements, given its lower symmetry relative to the bulk environment, if the associated polarization energy is compensated by decreases in energy elsewhere.

Having evaluated the energy for a given perfect or defect configuration, the equilibrium, ground-state energy is found using the conjugate-gradient technique, wherein forces are calculated at each step in the relaxation.<sup>16</sup> In many cases, we compare these energies with those obtained by zero-temperature Monte Carlo (MC) simulation. These experiments are performed by using a rectangular or rhombic supercell of dimension  $1 \times 1 \times n$ , where  $n$  is variable, with periodic boundary conditions imposed in three directions (see Table II). As a result, in the case of extended defects, such as surfaces and grain boundaries, a spatially periodic superlattice is constructed, and  $n$  is adjusted until extended defect-defect interactions have been substantially reduced or eliminated, sometimes using extrapolation. Grain-boundary superlattices have been investigated by others using a similar methodology.<sup>17</sup> The height,  $z$ , of the simulation cell is also variable, permitting us to adjust the stress component,  $\sigma_{zz}$ . Finally, we are also able to add an excess volume fraction,  $\delta$ , near an interface by incorporating a gap and then minimizing the total energy with

respect to the distance between two crystals. Given the time-consuming nature of the atomic relaxation procedure, gap optimization is performed, in practice, in the unrelaxed state.

## (2) Grain-Boundary Geometry

While grain boundaries can be characterized by various geometric parameters,<sup>18</sup> it is convenient here to classify boundary geometry in terms of a CSL model. The fundamental quantity in this description is the multiplicity,  $\Sigma$ , defined as the volume ratio of the CSL unit cell to that of the original unit cell. For our purposes, Grimmer *et al.*<sup>19</sup> have tabulated all coincidence orientations with multiplicities  $\Sigma \leq 36$  for rhombohedral lattices with axial ratios,  $cla$ , for corundum-type structures (i.e.,  $2.696 < cla < 2.765$ ). Among these interfaces, we have selected six basal-plane grain boundaries, namely  $\Sigma 3$ , 7, 13, 19, 21, and 31, which are constructed here via rotation around the [0001] axis. From related geometric considerations, one can show that common rotations (in which the same relative orientation of two halves of a bicrystal can be described also by a rotation around the three-fold axis by an angle  $\theta$  so that  $3^{1/2} \tan \theta/2$  is rational)<sup>19</sup> result in the coincidence of a fraction  $1/\Sigma$  of translation vectors in rhombohedral lattices. We note here that electron backscattered Kikuchi diffraction results for experimentally hot-pressed polycrystalline Al<sub>2</sub>O<sub>3</sub> samples reveal the presence of both  $\Sigma 3$  and  $\Sigma 13$  boundaries, albeit in rather limited proportions.<sup>20</sup>

For the purpose of illustration, Fig. 1 shows the ionic positions associated with a  $\Sigma 13$  boundary, while also highlighting the associated CSL unit cell, and Table II summarizes the salient features of the CSL boundaries used in this study. Finally, we note that, during relaxation to equilibrium, the translations parallel to the boundary plane (i.e.,  $x$ - and  $y$ -directions) are fixed,<sup>17</sup> and we do not consider explicitly the role of point defects in the possible stabilization of some grain boundaries.<sup>21</sup>

## (3) Voronoi Polyhedra

As discussed above, we wish to examine quantitatively the volume associated with grain-boundary regions in the oxides under consideration.<sup>22,23</sup> Our approach has been to partition space in a slab of prescribed thickness near a (relaxed) boundary using a

Table II. Selected CSLs around the [0001] Axis and the Associated  $1 \times 1 \times n$  Simulation Cells Used in This Study

$\Sigma$	$\theta$ (degrees)	$n$	Number of ions in the simulation cell
3	60.00	4	1920
7	38.21	4	2520
13	27.80	4	3120
19	46.83	2	2280
21	21.79	4	3360
31	17.90	4	7440



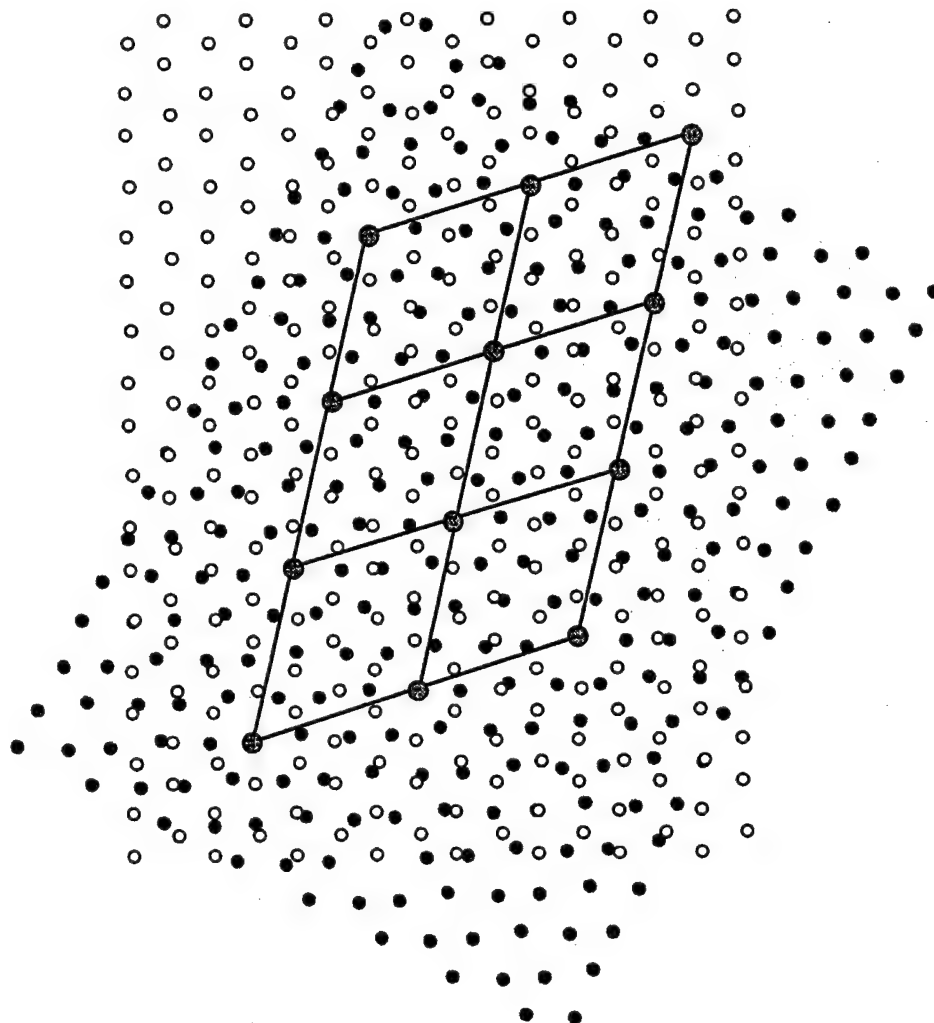


Fig. 1. Rotation of two crystals by  $27.80^\circ$  to build a  $\Sigma 13$  boundary. This is viewed along the  $[0001]$  axis, and the coincidence sites and the corresponding unit cells are indicated. ((○) or (●) = oxygen; (⊙) = coincidence site.)

Voronoi construction.<sup>24,25</sup> In particular, two measures of interfacial volume are determined: the spatial distribution of cation volume and the distribution of void volume, by associating each element of space with either a cation or a void, respectively. In the cation case, a Voronoi polyhedron is constructed from the envelope of planes that bisect each line, which connects the cation to a neighboring anion. Thus, in a bulk environment, each cation is octahedrally coordinated and associated with a cubic Voronoi cell (Fig. 2). Interstices are characterized by a similar procedure. For convenience, in both cases, the average "radius" (the average distance from a cation site to six neighboring faces) of the Voronoi cell is used as a measure of cell size given that the determination of cell volume is rather tedious for general polyhedra.

While this approach is quite useful in that it provides data on the distribution and frequency of possible segregation sites, it is worth noting two limitations. First, this subdivision of space is complicated by ambiguities in identifying void locations in a defect region, by the polarizability of ions in low-symmetry positions and by relatively large ionic relaxations in some cases. Second, it is essentially a geometric description of an interfacial region that does not incorporate explicitly local charge considerations. Nevertheless, as is seen below, the Voronoi construction is quite informative.

#### (4) Isovalent Doping of $\alpha\text{-Al}_2\text{O}_3$

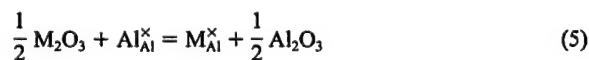
A more complete picture of the propensity for grain-boundary segregation incorporates the elastic deformation that attends the

introduction of impurities in the boundary region. Such deformations are particularly relevant here, because experimental evidence indicates that oversized isovalent ions, such as yttrium and lanthanum, strongly segregate to grain boundaries, suggesting that the main driving force for segregation is size mismatch (despite reports that yttrium can behave as a donor).<sup>26,27</sup> The strain energy associated with this mismatch has been given in the continuum limit by Eshelby and is proportional to the square of the misfit strain, as given by the square of the difference,  $\Delta r$ , between dopant and host ion radii.<sup>28</sup> In fact, for a related elastically isotropic system, one can write

$$U_s = \frac{6\pi r^3(\Delta r/r)^2 B}{(1 + 3B/4G)} \quad (4)$$

where  $B$  is the bulk modulus of the solute ion and  $G$  the shear modulus of the matrix.

In this study, we consider the interchange of a generic trivalent cation,  $M$ , with an aluminum cation. This substitution, which can be performed conveniently in a simulation, might arise in practice, for example, from the reaction



The short-range interaction between dopant and oxygen ions is incorporated in the simulation by using empirical potential parameters obtained by Bush *et al.* for a series of metal oxides, as

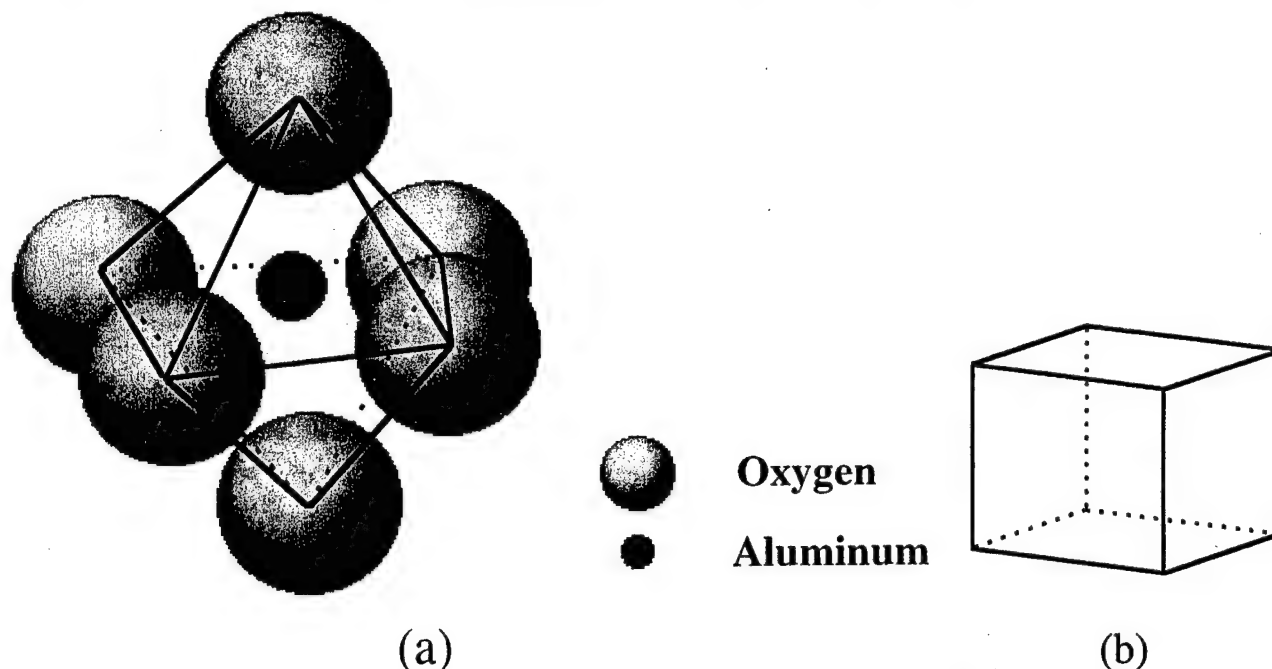


Fig. 2. (a) Octahedral environment of oxygen anions for an aluminum cation in bulk. (b) Corresponding Voronoi cell is a cube.

summarized in Table I.<sup>29</sup> Various dopants, ranging in size from iron (0.64 Å) to lanthanum (1.06 Å), are used here. Now, the Langmuir-McLean theory predicts that

$$C_{gb} \approx C_i \exp\left(-\frac{\Delta H}{kT}\right) \quad (6)$$

where  $C_{gb}$  is the occupation fraction (impurity/host ions) at the grain boundary,  $C_i$  the bulk fraction, and  $\Delta H$  the segregation enthalpy of interaction between the solute ion and the boundary.<sup>30</sup> We note that, in writing Eq. (6), we have used a dilute solution approximation and also neglected entropic contributions to the free energy. With this definition, then, a negative  $\Delta H$  implies segregation. Thus, if the strain energy is the main driving force for segregation,  $\Delta H$  is essentially proportional to

$$-\Delta H = kT \ln\left(\frac{C_{gb}}{C_i}\right) \propto \left(\frac{\Delta r}{r}\right)^2 \quad (7)$$

In the following section, the validity of this relation is assessed via an identification of favorable boundary sites that most relieve the strain energy. For this purpose, segregation enthalpy is calculated and related to boundary geometry.

### III. Results and Discussion

We summarize here the energetic and geometric information obtained from simulation. As indicated above, relaxed, equilibrium structures are obtained primarily via conjugate-gradient energy minimization, and these results are compared, in some cases, with those calculated via the zero-temperature MC method in order to validate the methodology. The data obtained from these two complementary relaxation schemes are presented in Table III for a bulk system, a basal free surface, and an (oxygen-terminated) basal twin boundary. It is worth pointing out that our results for the energies of the perfect crystal, the basal free surface, and point-defect formation energies (such as the Schottky quintet, Frenkel anion, and Frenkel cation) agree very well with previous simulation studies that have used this potential.<sup>9,31</sup>

For the CSL boundaries considered in this study, grain-boundary excess energies (per unit area) are calculated and shown in Fig. 3 as a function of misorientation angle. As is evident from

Table III. Energetic Comparison between Two Energy Minimization Procedures

	Monte Carlo method	Conjugate-gradient method
Perfect lattice (eV/formula unit)	-160.62	-160.62
(0001) Free surface (960 ions) (J/m <sup>2</sup> )	2.93	2.92
(0001) Twin boundary (960 ions) (J/m <sup>2</sup> ) <sup>†</sup>	3.89	3.86

<sup>†</sup>Based on oxygen-terminated twin boundary; twin boundary energy was 3.10 J/m<sup>2</sup> when it was extrapolated to an infinite system to avoid interactions between the two twins.

Fig. 3, the boundary energies lie in the range of ~2.8–3.2 J/m<sup>2</sup>, with the  $\Sigma 3$  basal twin boundary having the lowest energy in this series of CSLs. It should be noted that the energy of this  $\Sigma 3$

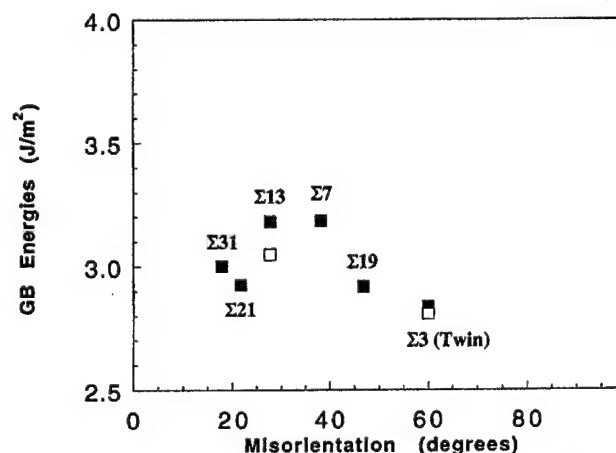


Fig. 3. Grain-boundary energy versus misorientation angle for selected CSLs around the [0001] axis. Twin boundary forms at a misorientation of 60°. (□) indicates grain-boundary energy with an incorporated gap between two half crystals.)

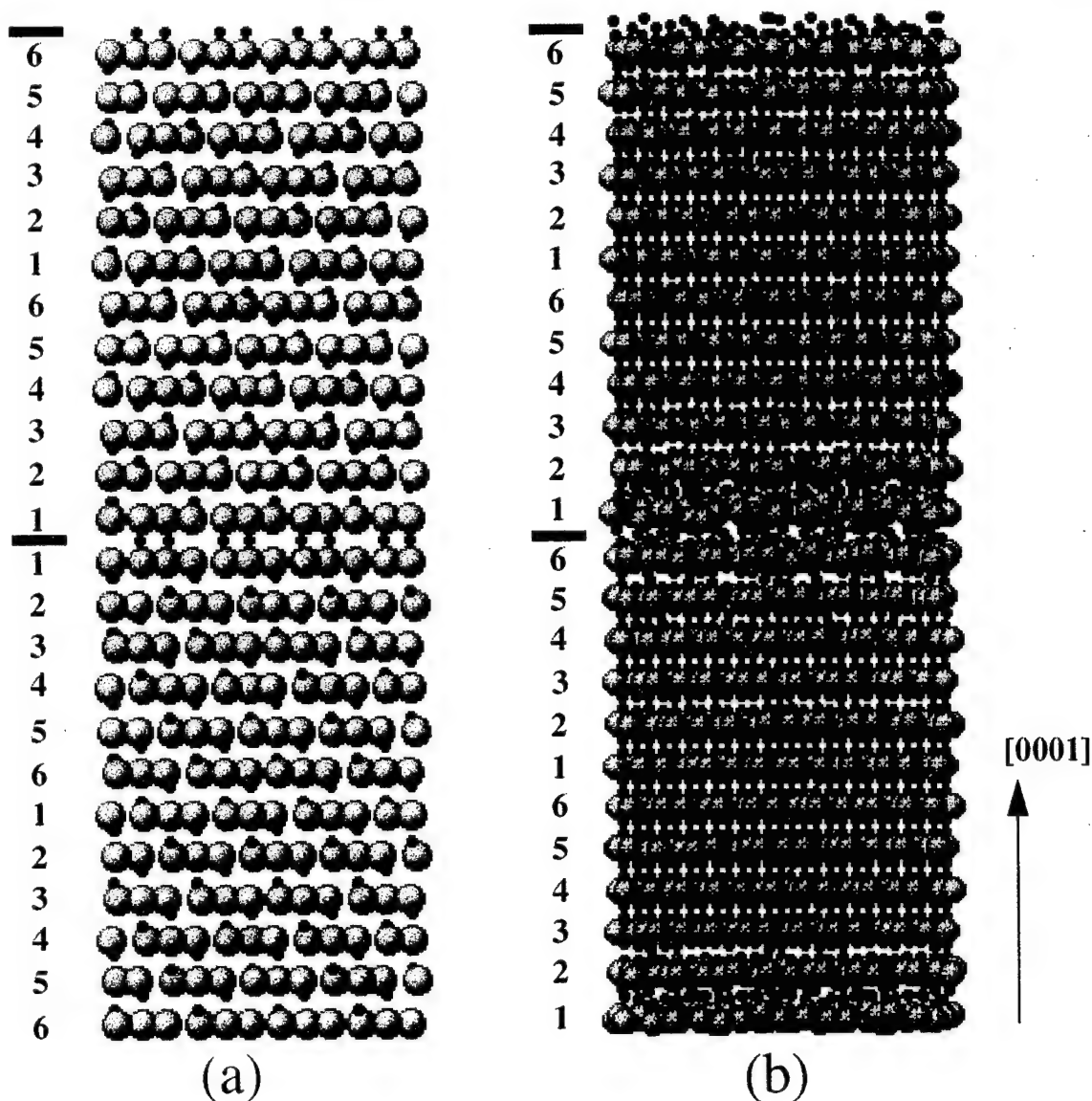


Fig. 4. Relaxed structures from (a)  $\Sigma 3$  (twin) and (b)  $\Sigma 13$  boundary. Location of boundaries is indicated by a bold line. Number shows the oxygen stacking sequence, and arrow indicates the  $[0001]$  direction. (( $\odot$ ) = oxygen; ( $\bullet$ ) = aluminum.)

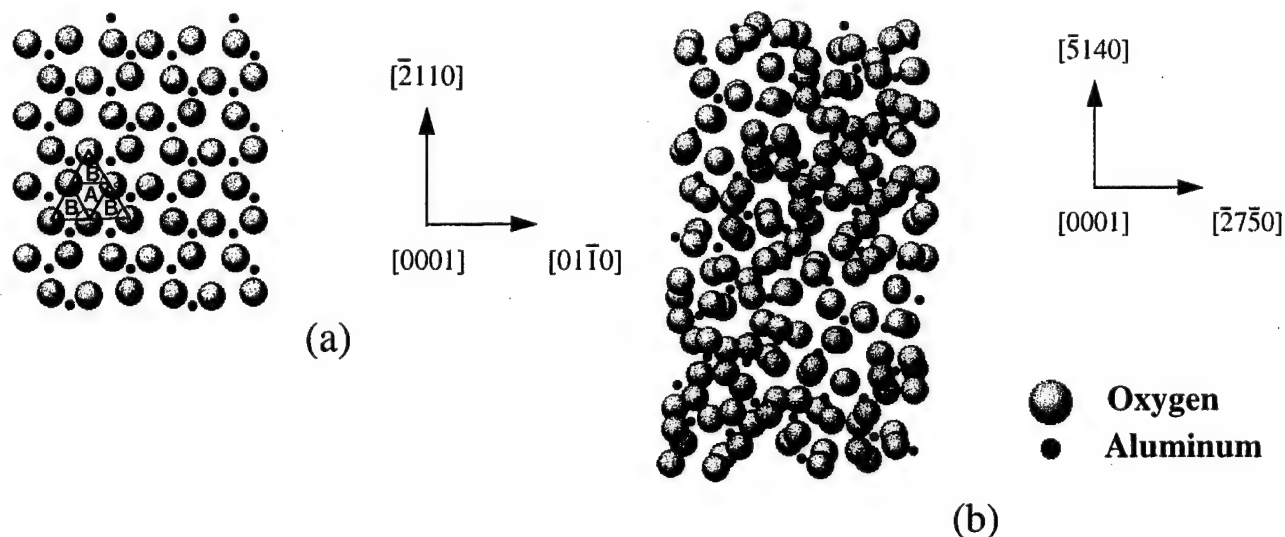


Fig. 5. Same structure as in Fig. 4 focusing on three boundary planes (O-Al-O), as viewed along the  $[0001]$  axis: (a)  $\Sigma 3$  boundary voids characterized by the trigonal prisms of A (large) and B (small); (b)  $\Sigma 13$  boundary.



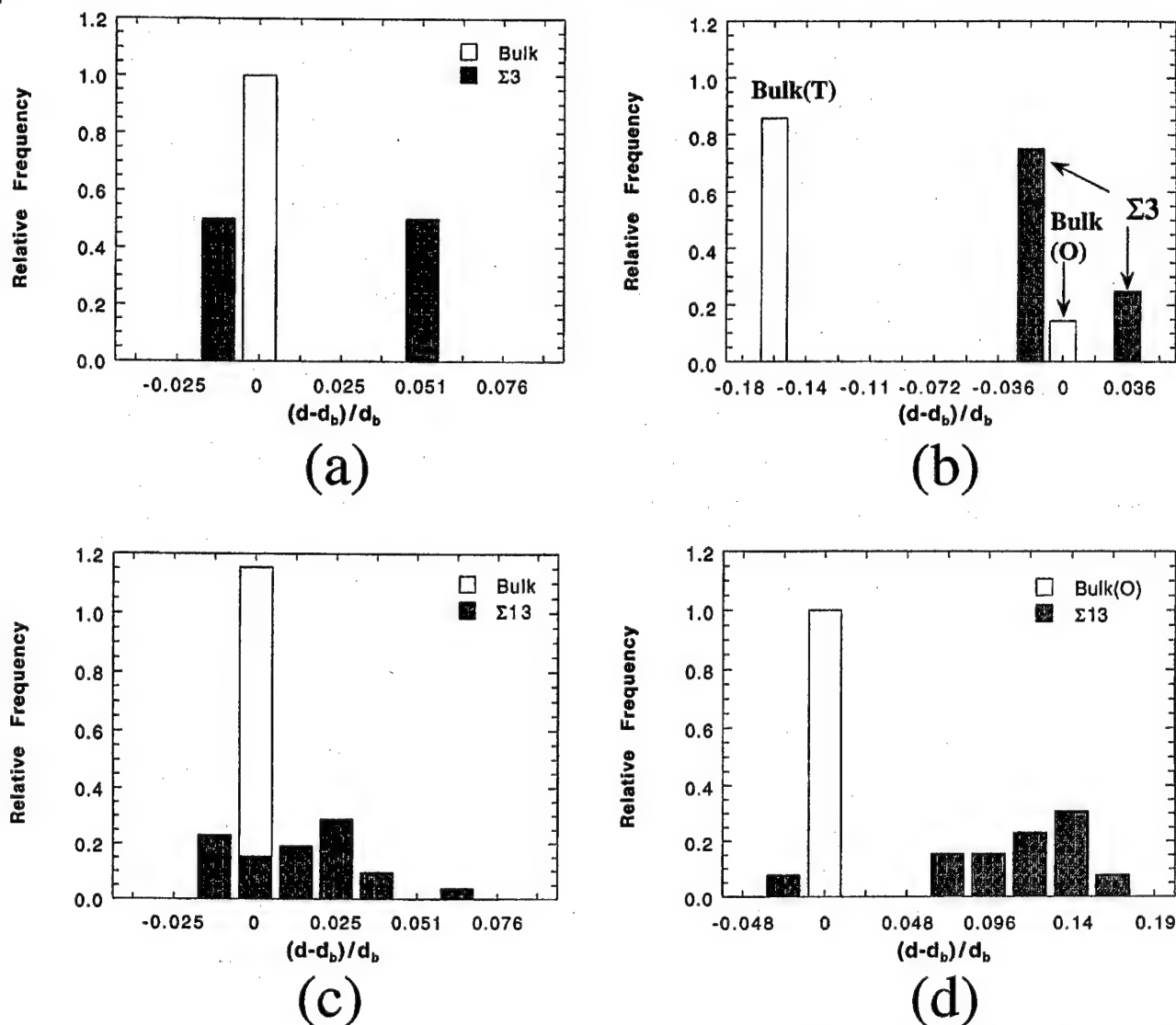


Fig. 6. Voronoi cell characterization of a boundary plane, as compared to bulk environment: (a)  $\Sigma 3$ , substitutional; (b)  $\Sigma 3$ , interstitial; (c)  $\Sigma 13$ , substitutional; (d)  $\Sigma 13$ , interstitial. (T = tetrahedral site, O = octahedral site,  $d$  = Voronoi cell radius,  $d_b$  = Voronoi cell radius for the bulk sites.)

boundary is lower than that of the corresponding oxygen-terminated basal twin (see Table III), and that, more generally, all of these boundary energies are each less than twice the calculated (0001) surface energy, indicating stability against spontaneous grain-boundary separation.

We note here, as mentioned above, that in-plane (i.e.,  $x$  and  $y$ ) boundary translations have not been considered in this study. While such translations can facilitate grain-boundary relaxation in some cases, they are not easily incorporated in this superlattice model, given the two interfaces created per cell. Further, it is often difficult to determine, *a priori*, the optimal displacement vectors associated with relaxation. An alternative to this description is the Mott-Littleton approach, wherein the crystal is divided into region I, surrounding an interface, and an outer region II, modeled as a dielectric continuum.<sup>9</sup> The drawback of this approach is, however, that the usual Ewald summation technique must be modified to account for the loss of periodicity in one direction. Thus, we have adopted the view that the superlattice model is adequate for the segregation studies reviewed here, because, although grain-boundary translation can affect the detailed locations of potential segregation sites, the overall distribution of excess grain-boundary volume is likely to be less sensitive to such translations. The incorporation of grain-boundary sliding into segregation studies is a subject for future work.

Figure 4 shows the corresponding relaxed grain-boundary structures, based for simplicity only on ionic core positions, for both the  $\Sigma 3$  and  $\Sigma 13$  boundaries. In the former case, the grain-boundary region remains relatively coordinated, with the requisite mirror symmetry across the boundary. By contrast, the latter ( $\Sigma 13$ ) boundary region is more disordered, exhibiting a rumpled structure in the oxygen layers ( $\Delta z \approx 1 \text{ \AA}$  at plane 1) near the boundary plane. Given this difference in the degree of disorder, these two boundaries serve as prototypes in the discussion below.

Note, however, from Fig. 4(b) that the terminating boundary plane is not easily located, unlike that for the  $\Sigma 3$  boundary. Indeed, one might imagine alternative starting configurations, such as, for example, the one obtained by placing the boundary plane between two aluminum layers (i.e., splitting two aluminum layers between oxygen layers). In fact, the relaxation of this configuration yields a different boundary structure with a correspondingly (slightly) higher energy ( $\sim 1\%$ ). This result implies that there can be various metastable local energy minima corresponding to different initial structures. Such minima can, in fact, be artifacts of the simplified potential used here that neglect short-range, cation-cation interactions (see Table I). In any case, we focus on the structure presented in Fig. 4(b), while hoping to identify a global minimum with simulated annealing in future work.

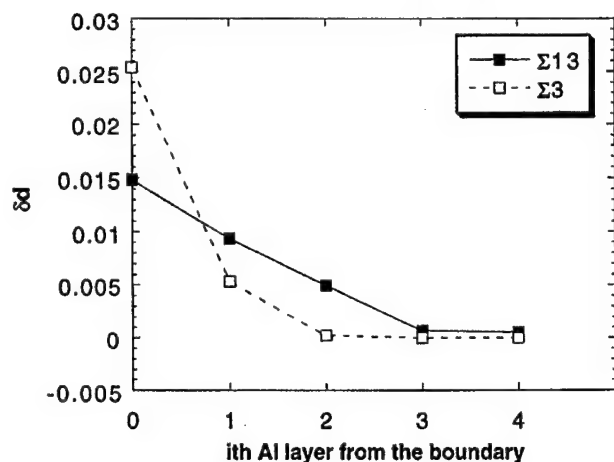


Fig. 7. Excess parameter,  $\delta d$ , a measure of excess volume of large boundary substitutional sites as a function of  $i$ th aluminum layer (which increases upon moving away from the boundary).  $\Sigma 3$  shows narrow distribution and so approaches the bulk value more quickly.

A somewhat more detailed description of the boundary structure is possible, in some cases, upon viewing several planes along the [0001] axis (Fig. 5). For example, one can view the  $\Sigma 3$  boundary interstices in terms of two types of trigonal prisms (located at sites A and B), which have a relative radii of  $d/d_b = 1.03$  and  $0.986$ , respectively, where  $d$  is the average radius of the trigonal prisms and  $d_b$  the radius of bulk octahedral interstitial sites (Fig. 5(a)). However, the disorder associated with the  $\Sigma 13$  boundary precludes this simple analysis and leads to several types of interstices of varying size (Fig. 5(b)).

Based solely on geometrical arguments, it is expected that areas of larger interfacial volume can serve as potential sites for dopant segregation. Thus, in order to identify the most likely candidate sites, we compiled a frequency histogram of Voronoi volumes for the  $\Sigma 3$  and  $\Sigma 13$  boundaries. As is evident in the histogram for substitutional sites (Fig. 6(a)), the  $\Sigma 3$  boundary has broken the degenerate, bulk unimodal size distribution into an essentially bimodal distribution of sites with widely disparate sizes. The situation for interstitial sites (Fig. 6(b)) is rather similar, yet complicated by the fact that there are now both octahedral and more numerous tetrahedral bulk sites. It is found that one-fourth of the boundary interstices are larger than these bulk sites. In the case of the  $\Sigma 13$  boundary, several potential substitutional sites, many larger than the corresponding bulk sites, are available for segregation in addition to some interstitial sites (see Figs. 6(c) and (d)).

Finally, the Voronoi analysis is extended to layers near each boundary. In Fig. 7, the excess volume available is plotted as a function of  $i$ th aluminum layer from the boundary (0 is at the boundary) near the  $\Sigma 3$  and  $\Sigma 13$  grain boundaries. One measure of this excess volume is the excess parameter,  $\delta d$ , characterized by

$$\delta d = \frac{1}{N} \sum_{i=1}^N (d_i - d_b) \times \Theta(d_i - d_b) \quad (8)$$

where  $N$  is total number of sites,  $d_i$  ( $d_b$ ) the average radius of site  $i$  (a bulk site), and  $\Theta(d_i - d_b)$  a step function. From Fig. 7, it is concluded that, because of the more-localized excess volume associated with the  $\Sigma 3$  boundary, segregation is likely to occur near this boundary (within  $\sim 2.0$  Å), whereas, in the case of the  $\Sigma 13$  boundary, a segregant concentration profile likely extends over several layers. Electron microscopy studies have reported essentially no segregation of yttrium to the basal twin boundary, whereas they have detected segregation to other boundaries.<sup>32</sup>

The relevance of the relative excess radius,  $(d - d_b)/d_b$ , in this segregation study can be seen by examining Fig. 8, which shows the simulation result of unrelaxed substitutional energy (relative to bulk) of europium in the  $\Sigma 13$  boundary as a function of  $(d - d_b)/d_b$

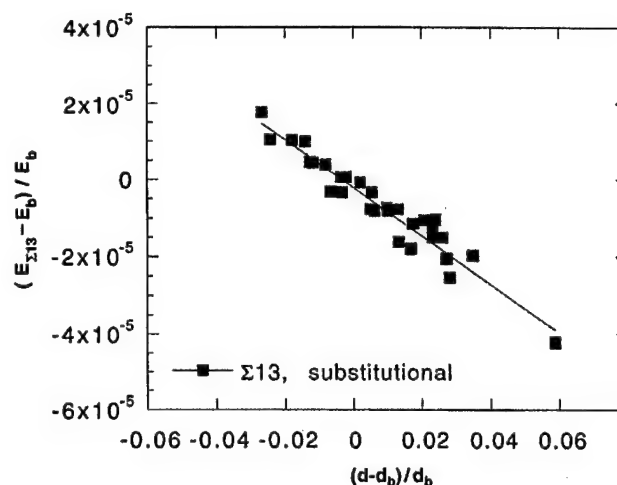


Fig. 8. Unrelaxed substitutional energy of europium in  $\Sigma 13$  boundary as a function of boundary space, showing linear relationship. ( $E_{\Sigma 13}$  = unrelaxed substitutional energy at  $\Sigma 13$ ,  $E_b$  = unrelaxed substitutional energy in the bulk.)

for sites of various sizes. Europium is an intermediate-sized lanthanide ion having a radius of  $0.95$  Å. The substitutional energy shows a roughly linear relationship with the relative excess radius, indicating the larger volume can more easily accommodate oversized ions. Further, those sites with zero excess radius have nearly zero corresponding excess energies, implying that such sites are essentially bulklike and that the size of the local Voronoi cell is the best indicator of the propensity for segregation. A more complete description must, of course, incorporate ionic relaxation.

Having characterized the volume in boundary regions, we next determine zero-temperature (substitutional) segregation enthalpies,  $\Delta H$ , for relaxed boundary and bulk sites. Such information can, in principle, be used in an equilibrium statistical mechanical calculation of a segregation profile, although our aim here is only to identify likely segregation sites based on volume and complementary energetic considerations. For this purpose, our results are perhaps best illustrated in the case of the  $\Sigma 13$  boundary.

The segregation enthalpy,  $\Delta H$ , is displayed in Fig. 9 for four dopants (iron, yttrium, europium, and lanthanum) of varying size as a function of  $(\Delta r)^2$  for three types of boundary substitutional sites. These sites, labeled 1, 2, and 3 and ordered based on size, have relative radii,  $d/d_b$ , of 1.067, 1.018, and 0.9813, respectively. For type 1 sites, the observed linear relationship suggests that the main driving force for segregation is indeed size mismatch. As the site volume decreases, segregation enthalpy also expectedly increases and is positive for type 3 sites, which are smaller than their bulk counterparts. Similar trends exist for substitutional sites near the boundary. In summary, these results not only indicate which subset of sites are preferred for segregation but also suggest that (1) site exhaustion can lead to a saturation of segregation behavior and that (2) selective codoping schemes can be used to enhance segregation, particularly in the case of the  $\Sigma 13$  boundary with its multiplicity of potential sites. The possibility of segregation saturation is consistent with the observation of similar segregation profiles in systems with relatively large ionic impurities, such as yttrium- and lanthanum-doped  $\text{Al}_2\text{O}_3$ ,<sup>5</sup> while the advantages of codoping are discussed above in relation to the neodymium-zirconium codoped  $\text{Al}_2\text{O}_3$  system.<sup>8</sup>

It is of interest to explore the implications of these results for transport processes in ceramic oxides. In particular, it has been shown in preliminary work that the presence of segregating ions near grain boundaries can alter (possibly fast) diffusive paths in interfacial regions.<sup>20,33</sup> We are, in fact, now in the process of correlating these diffusion studies with investigations of the kinetics of creep. Therefore, to the extent that grain-boundary diffusion controls the long-time mechanical response of the material, as exemplified by its creep rate, the propensity for segregation

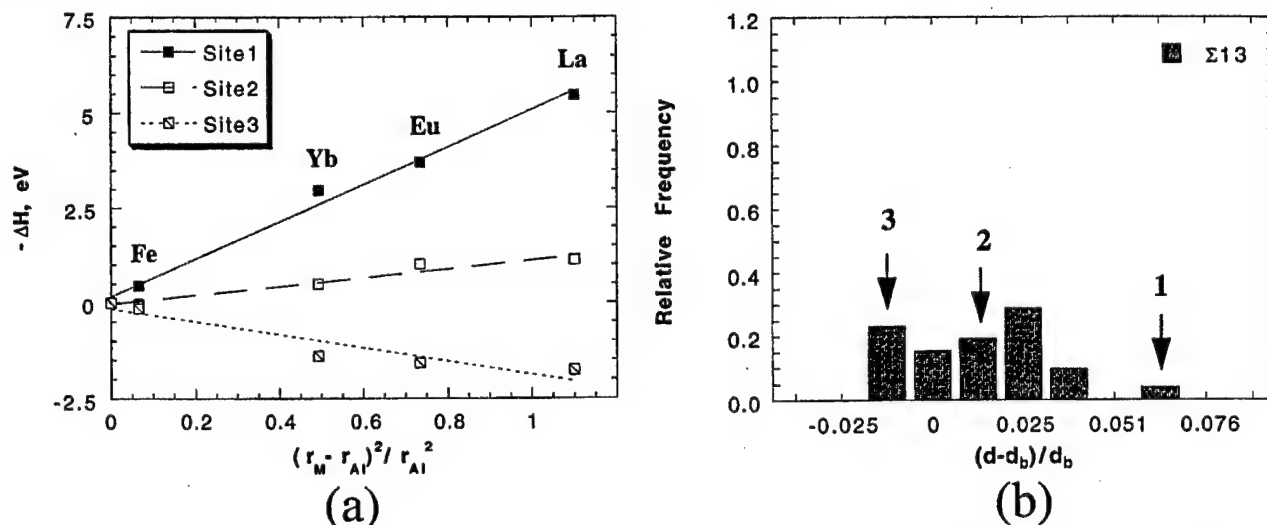


Fig. 9. (a) Segregation enthalpy,  $\Delta H$ , versus square of the difference in radii for four different dopant ions at three different sites in the same boundary plane of  $\Sigma 13$ . (b) Three different sites representing largest ( $d/d_b = 1.067$ ), intermediate (1.018), and smallest (0.9813), as shown in this histogram.

likely governs this response. From this perspective, one can envision scenarios in which a relatively small impurity concentration at the boundary can substantially improve creep resistance by blocking or modifying a few, critical diffusive pathways. Such synergies in yttrium- and lanthanum-doped  $Al_2O_3$  are described in the Introduction.

Finally, the results of this study of  $Al_2O_3$  grain boundaries correlate roughly with some experimental findings, namely that the largest substitutional sites represent  $\sim 4\%$  of the  $\Sigma 13$  boundary sites, translating to the 5%–10% of dopant coverage found in both SIMS and STEM work.<sup>4,5</sup> It should be noted, however, that our simulations are clearly idealized in certain respects. For example, the present work was performed at 0 K, where vacancy formation is not a factor; whereas, at higher temperatures, the presence of vacancies can alter detailed boundary structure<sup>34</sup> and presumably, therefore, detailed segregation profiles. Also, while general grain boundaries are clearly present in the experimental systems studied to date, we have confined our investigations to a subset of special boundaries given the constraints of spatial periodicity and system size. Thus, we have focused here only on two prototypical special boundaries on the basal plane. A more extensive study of other special boundaries, with a possible extrapolation to general boundaries, is contemplated for future work.

#### IV. Summary

In this study, the volumes associated with several special grain boundaries in  $Al_2O_3$  were characterized by a spatially local Voronoi construction in order to identify potential sites for impurity segregation. In particular, both the  $\Sigma 3$  (twin) and the  $\Sigma 13$  basal boundaries were examined in some detail in order to determine the frequency and spatial distribution of these sites. In conjunction with this geometrical study, a complementary energetic analysis yielded site segregation enthalpies and shed some light on observed experimental behavior. The dependence of enthalpy on ionic radius was examined by simulating ionic size mismatch using a variety of isovalent dopants, and it was found that the strain energy associated with this mismatch contributed significantly to the driving force for segregation.

As indicated above, a better understanding of boundary segregation behavior in polycrystalline  $Al_2O_3$  systems is key to describing the enhancement of time-dependent mechanical properties given that segregation is likely to alter boundary transport. Thus, future efforts are directed at linking segregation to transport properties at grain boundaries and at investigating boundary segregation in codoped  $Al_2O_3$  by using computer simulation. In

this way, one may be able to identify which dopants and which boundaries have the greatest impact on observed creep behavior.

#### Acknowledgments:

The authors would like to thank Professor F. Lange and Dr. C. Wang for helpful discussions.

#### References

- <sup>1</sup>J. Cho, M. P. Harmer, H. M. Chan, J. M. Rickman, and A. M. Thompson, "Effect of Yttrium and Lanthanum on the Tensile Creep Behavior of Aluminum Oxide," *J. Am. Ceram. Soc.*, **80** [4] 1013–17 (1997).
- <sup>2</sup>J. D. French, J. Zhao, M. P. Harmer, H. M. Chan, and G. A. Miller, "Creep of Duplex Microstructures," *J. Am. Ceram. Soc.*, **77** [11] 2857–65 (1994).
- <sup>3</sup>C.-W. Li and W. D. Kingery, "Solute Segregation at Grain Boundaries in Polycrystalline  $Al_2O_3$ ," pp. 368–78 in *Advances in Ceramics*, Vol. 10, *Structure and Properties of MgO and  $Al_2O_3$  Ceramics*. Edited by W. D. Kingery. American Ceramic Society, Columbus, OH, 1984.
- <sup>4</sup>A. M. Thompson, K. K. Soni, H. M. Chan, M. P. Harmer, D. B. Williams, J. M. Chabala, and R. Levi-Setti, "Rare Earth Dopant Distributions in Creep-Resistant  $Al_2O_3$ ," *J. Am. Ceram. Soc.*, **80** [2] 373–76 (1997).
- <sup>5</sup>J. Bruley, J. Cho, H. M. Chan, M. P. Harmer, and J. M. Rickman, "Scanning Transmission Electron Microscopy Analysis of Grain Boundaries of Creep-Resistant Yttrium- and Lanthanum-Doped Alumina Microstructures," *J. Am. Ceram. Soc.*, **82** [10] 2865–70 (1999).
- <sup>6</sup>R. M. Cannon and R. L. Coble, "Review of Diffusional Creep of  $Al_2O_3$ ," pp. 61–100 in *Deformation of Ceramic Materials*, Proceedings of a Symposium on Plastic Deformation of Ceramic Materials (Pennsylvania State University, July 1974). Edited by R. C. Bradt and R. E. Tressler, Plenum, New York, 1975.
- <sup>7</sup>A. H. Chokshi and T. G. Langdon, "Diffusion Creep in Ceramics: A Comparison with Metals," pp. 1205–26 in *Diffusion in Metals and Alloys DIMETA 88*, Defect and Diffusion Forum, Vols. 66–69 (Balatonfured, Hungary, September 1988). Edited by F. J. Kedves and D. L. Bake. Sci-Tech Publications, Brookfield, VT, 1990.
- <sup>8</sup>Y.-Z. Li, C. Wang, H. M. Chan, J. M. Rickman, and M. P. Harmer, "Codoping of Alumina to Enhance Creep Resistance," *J. Am. Ceram. Soc.*, **82** [6] 1497–504 (1999).
- <sup>9</sup>C. R. W. Catlow, R. James, W. C. Mackrodt, and R. F. Stewart, "Defect Energetics in  $\alpha-Al_2O_3$  and Rutile  $TiO_2$ ," *Phys. Rev. B: Condens. Matter*, **25** [2] 1006–26 (1982).
- <sup>10</sup>N. W. Ashcroft and N. D. Mermin, *Solid State Physics*. Holt, Rinehart, and Winston, New York, 1976.
- <sup>11</sup>P. P. Ewald, "Die Berechnung Optischer und Elektrostatistischer Gitterpotentiale," *Ann. Phys. (Leipzig)*, **64**, 253–87 (1921).
- <sup>12</sup>M. P. Allen and D. J. Tildesley, *Computer Simulation of Liquids*, pp. 156–62. Oxford Press, Oxford, U.K., 1987.
- <sup>13</sup>K. L. Klier and J. S. Koehler, "Space Charge in Ionic Crystals. I. General Approach with Application to  $NaCl$ ," *Phys. Rev. A*, **140** [4A] 1226–39 (1965).
- <sup>14</sup>D. M. Duffy and P. W. Tasker, "Space-Charge Regions around Dipolar Grain Boundaries," *J. Appl. Phys.*, **56** [4] 971–77 (1984).
- <sup>15</sup>B. G. Dick and A. W. Overhauser, "Theory of the Dielectric Constants of Alkali Halide Crystals," *Phys. Rev.*, **112**, 90–103 (1958).
- <sup>16</sup>W. H. Press, S. A. Teukolsky, W. T. Vetterling, and B. P. Flannery, *Numerical Recipes in Fortran: The Art of Scientific Computing*, 2nd ed., pp. 413–18. Cambridge, New York, 1992.

- <sup>17</sup>J. D. Rittner, D. Udler, and D. N. Seidman, "Solute-Atom Segregation at Symmetric Twist and Tilt Boundaries in Binary Metallic Alloys on an Atom-Scale," *Interface Sci.*, **4**, 65–80 (1996).
- <sup>18</sup>A. P. Sutton and R. W. Balluffi, *Interfaces in Crystalline Materials*; pp. 3–68. Clarendon, Oxford, U.K., 1995.
- <sup>19</sup>H. Grimmer, R. Bonnet, S. Lartigue, and L. Priester, "Theoretical and Experimental Descriptions of Grain Boundaries in Rhombohedral  $\alpha$ - $\text{Al}_2\text{O}_3$ ," *Philos. Mag. A*, **61** [3] 493–509 (1990).
- <sup>20</sup>J. Cho, "Role of Rare-Earth Dopants on the Improved Creep Properties of Aluminum Oxide"; Ph.D. Thesis, Lehigh University, Bethlehem, PA, 1998.
- <sup>21</sup>D. Wolf, "Energy and Structure of (001) Coincidence-Site Twist Boundaries and the Free (001) Surface in MgO: Theoretical Study," *J. Am. Ceram. Soc.*, **67** [1] 1–13 (1984).
- <sup>22</sup>M. F. Ashby, F. Spaepen, and S. Williams, "The Structure of Grain Boundaries Described as a Packing of Polyhedra," *Acta Metall.*, **26**, 1647–63 (1978).
- <sup>23</sup>H. J. Frost, "A First Report on a Systematic Study of Tilt-Boundaries in Hard Sphere F.C.C. Crystals," *Scr. Metall.*, **14**, 1051–56 (1980).
- <sup>24</sup>J. L. Finney, "Random Packings and the Structure of Simple Liquids I. The Geometry of Random Close Packing," *Proc. R. Soc. London A*, **319**, 479–93 (1970).
- <sup>25</sup>D. Srolovitz, K. Maeda, S. Takeuchi, T. Egami, and V. Vitek, "Local Structure and Topology of a Model Amorphous Metal," *J. Phys. F: Met. Phys.*, **11**, 2209–19 (1981).
- <sup>26</sup>M. M. El-Aiat and F. A. Kröger, "Yttrium, an Isoelectric Donor in  $\alpha$ - $\text{Al}_2\text{O}_3$ ," *J. Am. Ceram. Soc.*, **65** [6] 280–83 (1982).
- <sup>27</sup>M. K. Loudjani, A. M. Huntz, and R. Cortès, "Influence of Yttrium on Microstructure and Point Defects in  $\alpha$ - $\text{Al}_2\text{O}_3$  in Relation to Oxidation," *J. Mater. Sci.*, **28**, 6466–73 (1993).
- <sup>28</sup>J. D. Eshelby, "The Continuum Theory of Lattice Defects," *Solid State Phys.*, **3**, 79 (1956).
- <sup>29</sup>T. S. Bush, J. D. Gale, C. R. A. Catlow, and P. D. Battle, "Self-Consistent Interatomic Potentials for the Simulation of Binary and Ternary Oxides," *J. Mater. Chem.*, **4** [6] 831–37 (1994).
- <sup>30</sup>D. McLean, *Grain Boundaries in Metals*, Clarendon, Oxford, U.K., 1957.
- <sup>31</sup>P. W. Tasker, "Surfaces of Magnesia and Alumina"; see Ref. 3, pp. 176–89.
- <sup>32</sup>M. A. Gülgün, V. Putlayev, and M. Rühle, "Effects of Yttrium Doping in  $\alpha$ -Alumina: I. Microstructure and Microchemistry," *J. Am. Ceram. Soc.*, **82** [7] 1849–56 (1999).
- <sup>33</sup>J. Cho, C. M. Wang, H. M. Chan, and J. M. Rickman, "Role of Segregating Ions on the Improved Creep Resistance of Aluminum Oxide," *Acta Mater.*, in press.
- <sup>34</sup>M. P. Harmer, H. M. Chan, J. M. Rickman, J. Cho, and C. M. Wang, "Grain Boundary Chemistry and Creep Resistance of Oxide Ceramics"; pp. 139–44 in *The Science of Engineering Ceramics II*. Edited by K. Niihara, T. Sekino, E. Yasuda, and T. Sasa. Trans Tech Publication Ltd., Aedermannsdorf, Switzerland, 1998. □



PERGAMON

*Acta mater.* Vol. 47, Nos 15, pp. 4197–4207, 1999  
© 1999 Acta Metallurgica Inc.  
Published by Elsevier Science Ltd. All rights reserved.  
Printed in Great Britain  
1359-6454/99 \$20.00 + 0.00

PII: S1359-6454(99)00278-5

## ROLE OF SEGREGATING DOPANTS ON THE IMPROVED CREEP RESISTANCE OF ALUMINUM OXIDE

J. CHO, C. M. WANG, H. M. CHAN, J. M. RICKMAN and M. P. HARMER†

Materials Research Center, Whitaker Laboratory, Lehigh University, Bethlehem, PA 18015, U.S.A.

**Abstract**—Recent studies have demonstrated that p.p.m. levels of rare-earth dopant ions (e.g. Y, La, Nd) wield a beneficial and highly potent influence on the creep properties of alumina. In addition, codoping with ions of disparate sizes (Nd, Zr) resulted in even further enhancement of the creep behavior. In all cases, the dopant ions were found to strongly segregate to grain boundaries. Creep rates were not influenced by the presence of second phase precipitates, verifying that the creep improvement is a solid solution effect. In an attempt to clarify the exact mechanism(s) that controls creep behavior of the doped aluminas, various advanced characterization techniques have been applied including: secondary ion mass spectrometry, scanning transmission electron microscopy, orientation image microscopy, and extended X-ray absorption fine structure as well as atomistic computer simulation and studies of the creep kinetics. Although no definitive mechanism has been established, a logical explanation is that outsize ions segregate to more energetically favorable grain boundary sites, and improve creep resistance by blocking a few critical diffusive pathways. This mechanism is sufficiently general that it may be applicable to other ceramic systems. © 1999 Acta Metallurgica Inc. Published by Elsevier Science Ltd. All rights reserved.

**Keywords:** Oxides; Interface diffusion; Grain boundaries; Segregation; Creep

### 1. INTRODUCTION

It has been discovered recently that the addition of trace amounts ( $<1000$  p.p.m.) of rare-earth dopants such as yttrium, lanthanum or neodymium, to fine-grained alumina (1–2  $\mu\text{m}$  grain size) can reduce the creep rate by several orders of magnitude [1–3]. In order to fully exploit this opportunity for developing polycrystalline materials with significantly enhanced creep resistance, over the past several years we have been conducting a comprehensive study aimed at elucidating the underlying mechanism(s) associated with this improved mechanical response. This has included kinetic studies of the tensile creep rate as a function of temperature, applied stress, grain size, dopant type and concentration [3, 4]; detailed microstructural and microchemical analyses of grain boundaries using advanced electron microscopy techniques, high resolution secondary ion mass spectrometry (SIMS) and orientation image mapping [5–7]; a study of the atomic structural environments around Y and Zr segregants using extended X-ray absorption fine structure (EXAFS) [8]; atomistic computer simulation of dopant segregation to surfaces and grain boundaries, and calculations of the migration energy for grain boundary diffusion along grain boundaries with and without segregants [9]. The objective of the present work is to assimilate the findings of these earlier component studies, along with other related studies in the literature, with

a view to identify or at least suggest the underlying scientific mechanism involved. What emerges is a clear correlation between creep retardation and the segregation of solute at the grain boundaries. The exact mechanism is still debatable; however, a role involving site blocking of a few critical diffusive pathways is strongly implied. From that it becomes apparent that there is indeed a realistic potential for tailoring materials with superior creep resistance, guided by a mechanism-based approach.

### 2. CREEP BEHAVIOR

Work by Carry and Mocellin showed that the addition of Y reduced the strain rate during superplastic deformation of fine-grained, MgO-doped alumina [10]. Independently, French *et al.* [1] demonstrated that Y doping resulted in two to three orders of magnitude improvements in the tensile creep behavior of alumina. Since that time, researchers at Lehigh have extended this study to encompass a wide range of both singly doped, and codoped systems. The specimen preparation and testing procedures have been described in detail elsewhere [1–3], and hence will only be mentioned briefly here. It should be noted, however, that ultra-high purity starting powders were used throughout, and extreme care was taken to avoid the introduction of impurities (aside from the intended dopant ions). Dog-bone shaped specimens were machined from fully dense, hot-pressed billets. Tensile creep tests were undertaken under various temperatures

†To whom all correspondence should be addressed.

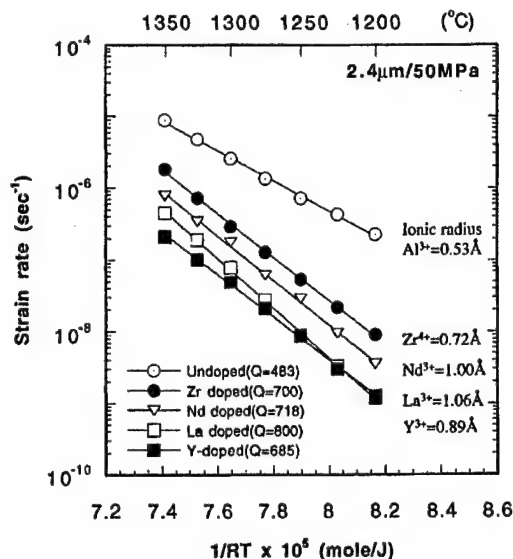


Fig. 1. Arrhenius plot of normalized steady-state creep rates, showing the influence of dopant size on the tensile creep rate for various dopant systems. The plots were normalized to a 2.4  $\mu\text{m}$  grain size.  $Q$  is the activation energy (kJ/mol).

and applied stresses [2, 11], with the gauge length established by two SiC flags. A laser extensometer was used to measure strain, and the strain rates were determined from a well-defined steady-state creep regime. The most important findings emerging from this work are described in the following.

### 2.1. Tensile creep of singly doped aluminas

The steady-state creep rates of various singly doped aluminas are shown in Fig. 1. The dopant levels for the various impurity ions were as follows: Zr (100 p.p.m.), Nd (100 p.p.m.), La (500 p.p.m.), and Y (1000 p.p.m.). Note that for the purposes of comparison, the creep rates were normalized to the same value of grain size ( $d = 2.4 \mu\text{m}$ ) using a grain size exponent of 3. (Experimental results supporting the validity of this procedure are discussed in detail in Section 2.4.) It can be seen that compared to undoped alumina, the creep rates of the Y-, Nd-, and La-doped specimens were reduced by almost two to three orders of magnitude [1–3]. This is a dramatic enhancement in creep resistance, especially considering that earlier studies in the literature have all reported that dopant ions either increased the creep rates in alumina, or had little effect [12, 13].

If one considers the influence of dopant ionic size on the creep data, the results show that although the larger rare-earth ions [ $\text{Y}^{3+}$  (0.89 Å),  $\text{Nd}^{3+}$  (1.00 Å) and  $\text{La}^{3+}$  (1.06 Å)] were more effective in inhibiting creep than  $\text{Zr}^{4+}$  (0.72 Å), the beneficial effect of the impurity ions appears to saturate. Interestingly (see Fig. 1), all the doped systems exhibited significantly higher activation energies than undoped alumina (483 kJ/mol), with the La-

doped system having the highest value (800 kJ/mol). In undoped alumina, quantitative mechanistic analyses of previous diffusional creep and sintering studies have concluded that oxygen grain boundary diffusion is much faster than either aluminum grain boundary diffusion or oxygen lattice diffusion [14]. It has been further concluded that, over the range of temperatures, stresses and grain sizes employed in the current study, boundary aluminum diffusion controls diffusional creep [14]. Furthermore, the value of the activation energy derived from the creep experiments conducted at Lehigh ( $\sim 468$  kJ/mol) [1, 2] was much closer to the published activation energy values for aluminum grain boundary diffusion ( $\sim 420$  kJ/mol) than that for oxygen grain boundary diffusion ( $\sim 226$  kJ/mol) [15, 16]. The issue of whether the creep rate is controlled by grain boundary diffusion or reactions at the interface will be discussed in Section 5.

### 2.2. Effect of codoping

Given the foregoing results, where it was shown that beyond a certain size, increasing ionic radius did not result in any further enhancement of the creep behavior, it was decided to test the strategy of codoping [3]. The rationale was based on simple packing considerations, namely that by incorporating ions of differing sizes, it might be possible to block the grain boundary sites more effectively. Figure 2 shows the creep response of alumina codoped with both Nd and Zr (nominally 100 p.p.m. of each dopant ion), and compares it with the corresponding behavior of the undoped and singly doped materials. It can be seen that doping with 100 p.p.m.  $\text{Zr}^{4+}$  alone, reduced the creep rate by a factor of 15 as compared with undoped alumina. The singly Nd-doped alumina exhibited a

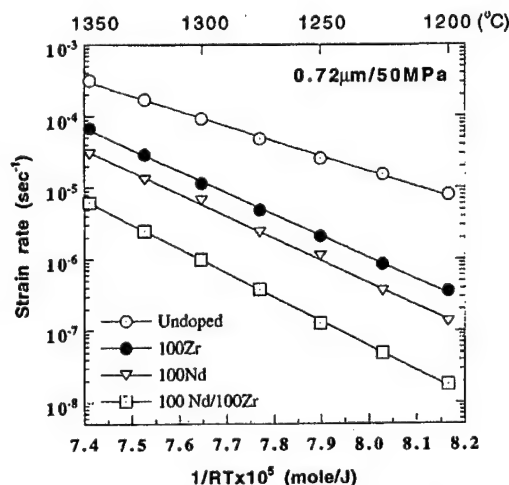


Fig. 2. Arrhenius plot of normalized steady-state creep rates for undoped, 100 p.p.m. Zr-doped, 100 p.p.m. Nd-doped, and 100/100 p.p.m. Nd/Zr-codoped alumina. The plots were normalized to a 0.72  $\mu\text{m}$  grain size.



further reduction in creep rate, but the codoped specimen showed the best creep behavior of all, thus confirming the effectiveness of the codoping approach. In contrast, a Sc/Zr codoped system (1000 p.p.m. Sc/100 p.p.m. Zr) showed similar creep behavior to the singly Zr-doped system [3]. Since the  $\text{Sc}^{3+}$  ion has a similar ionic radius to  $\text{Zr}^{4+}$  ( $R_{\text{Sc}} \sim 0.73 \text{ \AA}$ ,  $R_{\text{Zr}} \sim 0.72 \text{ \AA}$ ), this result is consistent with the premise that a disparity of ionic size is necessary for codoping to have a significant benefit over the singly doped case.

### 2.3. Solid solution effect

In the original study by French *et al.* [1], it was observed that the 1000 p.p.m. Y-doped alumina contained a small number of YAG ( $\text{Y}_3\text{Al}_5\text{O}_{12}$ ) precipitates. As a result, it was not clear whether the second phase particles played a role in enhancing the creep behavior. To clarify this issue, a series of studies was undertaken whereby the creep rates for alumina containing various dopant ions (Y, La, Nd/Zr) were compared for concentrations both above and below the solubility limit [3, 4]. The creep curves for the La-doped materials are shown in Fig. 3. Note that in this study, the samples were annealed (prior to creep testing) to achieve very similar mean grain size values. As a result, no grain size correction was required in order to directly compare the data. It can be seen that the creep rates for the 100 p.p.m. sample (below solubility limit), and the 500 p.p.m. sample (above solubility limit), are very close. The same general result was obtained in the case of Y doping [4], and Nd/Zr codoping [3]. Taken together, these findings provide very strong evidence that the beneficial influence of rare-earth dopant ions is a solid solution effect, and unrelated to the presence of second phase precipitates. Clearly, it would also be of interest to measure the variation of creep rate with dopant

level for concentrations *below* the solubility limit. Such studies are currently underway.

### 2.4. Values of inverse grain size exponent ( $p$ ), stress exponent ( $n$ )

In addition to the above described creep studies, values of the (inverse) grain size exponent ( $p$ ) and stress exponent ( $n$ ) were evaluated for the various dopant systems. These experiments were deemed pertinent for the following reasons. Firstly, since it was not always possible to creep test samples with the same grain size, an experimentally determined value of the grain size exponent was necessary in order to normalize the creep data for purposes of comparison. Secondly, it was hoped that the values of  $n$  and  $p$  might yield some insight into the creep mechanism. For the majority of compositions studied (100 p.p.m. Y, 100 p.p.m. La, 100 p.p.m. Nd, 100 p.p.m. Zr), the grain size exponent ( $p$ ) was determined to be close to 3 [3, 4]. This value is consistent with grain boundary diffusion controlled (Coble) creep. The only exceptions to this result were the Nd/Zr codoped samples (100 p.p.m. Nd/100 p.p.m. Zr, 350 p.p.m. Nd/100 p.p.m. Zr), which showed a grain size exponent of 2. (Note that the above data were derived from creep testing at  $1275^\circ\text{C}$ , under an applied stress of 50 MPa.) The change in grain size exponent from 3 (for the Nd and Zr singly doped samples) to 2 (for the Nd/Zr codoped material) was rationalized by arguing that the degree of suppression of grain boundary diffusivity achieved by the codoping was sufficiently great that lattice diffusion (rather than grain boundary diffusion) was now the rate-controlling mechanism [3].

With regard to the stress exponent, however, all the above doped systems exhibited a stress exponent very close to 2 [3, 4]. This result is troubling, in that it is difficult to reconcile with the previously derived value of 3 for the grain size exponent. Instead,  $n = 2$  indicates either grain boundary sliding accommodated by the formation of cavities [17], or interface-reaction controlled creep [18]. To date, with the exception of the purely phenomenological equation frequently found in many metal systems by Sherby and Wadsworth [19, 20] which describes superplastic behavior, no theory has been put forward which predicts the observed combination of  $n = 2$  and  $p = 3$ .

## 3. STRUCTURE AND CHEMISTRY OF GRAIN BOUNDARIES

Even before the discovery of enhanced creep resistance in alumina, it was well known that Y acted as a *reactive element additive*, and improved the oxidation resistance of FeCrTiAl and NiAl alloys [21, 22]. As a consequence, the distribution of Y in polycrystalline alumina had been the subject of a wide variety of analytical techniques [6, 23–29].

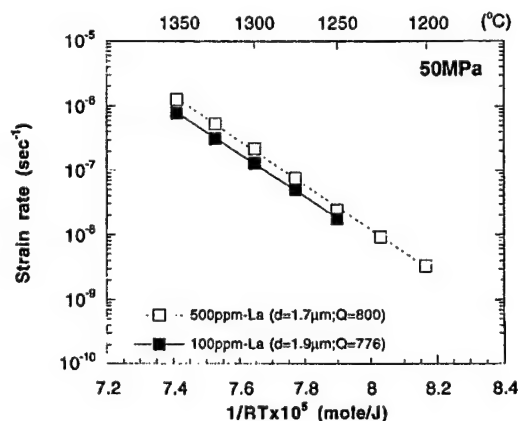


Fig. 3. Comparison of the creep behavior of two La-doped aluminas: 100 p.p.m. La (below solubility limit), 500 p.p.m. La (above solubility limit).

Although the results of these studies consistently indicated that Y segregated to the alumina grain boundaries, what was missing was the ability to correlate directly chemical and microstructural information for a statistically meaningful number of grain boundaries. For example, compositional line profiling using X-ray energy dispersive spectroscopy in the TEM or STEM can probe individual grain boundaries at high spatial resolution, but typically the number of grain boundaries studied is limited. In contrast, the signal from surface techniques such as Auger electron spectroscopy and conventional SIMS is averaged over a large number of grain boundaries, but the link between chemistry and microstructural features is missing. Clearly, in terms of understanding the role of dopant ions on a bulk deformation behavior such as creep, it is desirable to map the segregation behavior over a large number of grains.

It was with this in mind that a collaborative study was undertaken with researchers at the University of Chicago to utilize its unique imaging SIMS capability. The instrument is described in detail in Ref. [30]. Essentially, a focused gallium beam (probe diameter 35 nm) is used to sputter atoms/molecules from the uppermost layers of the specimen surface. Chemical information is derived from analyzing the mass to charge ratio of the secondary ions created by the sputtering process. Two-dimensional elemental distribution maps are subsequently obtained by rastering the beam across the specimen, and recording the signal intensity corresponding to a given chemical species at every position of the beam. In this way, SIMS maps were obtained for both singly doped (Y, La, Nd, Zr) and codoped (Nd/Zr, Sc/Zr) alumina samples [3, 6]. An example of such a map is shown in Fig. 4, which depicts the La map for a sample doped with

500 p.p.m. La. This result was typical of the singly doped systems, in that the SIMS confirmed that there was localized enrichment of the dopant ion concentration at the alumina grain boundaries [3, 6]. Furthermore, there did not appear to be any gross non-uniformity in segregation behavior, either along a given grain boundary, or from boundary to boundary. SIMS maps of the codoped samples revealed that both dopant ions were segregated to the grain boundaries [3], thus providing support for the contention that codoping may provide a synergistic effect in terms of inhibiting creep.

The advantage of the SIMS mapping lies in its excellent analytical sensitivity (typically at the p.p.m. level), though the lateral resolution is limited by the probe diameter (~35 nm). In order to gain more insight into the width of the segregation layer, quantitative line profile analyses of grain boundaries in Y- and La-doped alumina were carried out by Bruley *et al.* [5]. These workers found that in both cases, the segregation was confined to a layer thickness less than 3 nm. In addition, the amount of excess solute was found to be similar for both dopants:  $9 \pm 3$  and  $10 \pm 2$  at.%, for Y and La, respectively. Note that in no instance was any evidence of a continuous grain boundary phase detected.

Most recently, high-resolution STEM has been used to generate compositional maps of the dopant concentration in the grain boundary region. The work was carried out in a dedicated STEM (VG HB603) at 300 kV. Very high spatial resolutions can be achieved in this instrument because the probe size is only of the order of 2 nm (even taking into account beam broadening). Figure 5 shows a STEM high-resolution X-ray map taken from 1000 p.p.m. Y-doped alumina, and the corresponding intensity profile. The map clearly shows a distinct segregation layer, which is enriched in Y. The corresponding result for an alumina sample doped with 500 p.p.m. La is shown in Fig. 6. As in the previous case, there is solute enrichment at the grain boundary, but note also the evidence for a corresponding depletion in Al.

Observation of the segregation behavior of the rare-earth ions led Lehigh researchers to propose that the beneficial effect on creep resulted from an inhibition of grain boundary diffusion due to a site-blocking effect. This view is also supported by results from a recent creep study of rare-earth doped alumina by Yoshida *et al.* [31]. An alternative school of thought, however, is that the addition of dopant ions modifies the grain boundary structure. Based on a series of detailed TEM studies of grain boundaries in crept alumina specimens (Mg doped and Mg/Y codoped), Lartigue and co-workers [32–35] postulated that the role of the dopant ions was to limit grain boundary sliding by impeding the accommodation of lattice dislocations. Further, these workers reported evidence that dop-

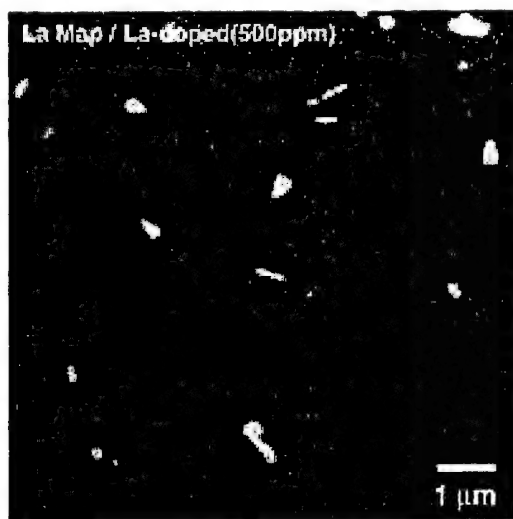


Fig. 4. SIMS map showing the La distribution in the as-hot pressed 500 p.p.m. La-doped alumina.



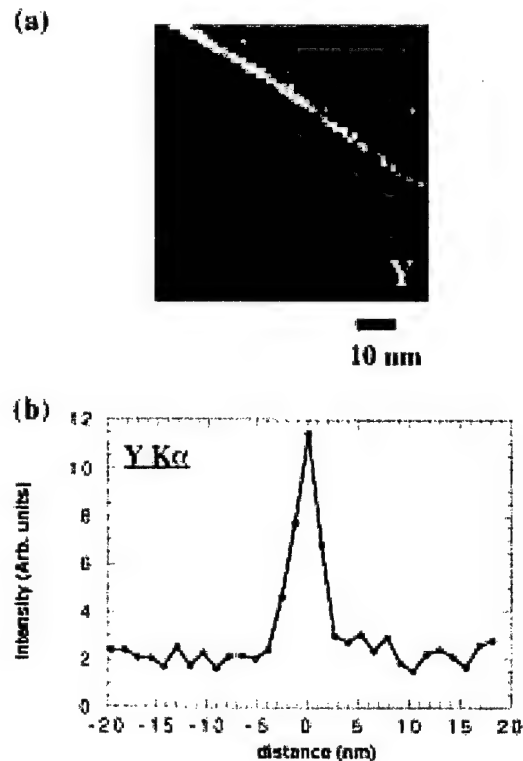


Fig. 5. STEM high-resolution X-ray map taken from 1000 p.p.m. Y-doped alumina: (a) Y map; (b) the corresponding intensity line profile across the boundary that appears in (a).

ing favors the formation of special boundaries, i.e. coincidence site lattice (CSL) and/or coincidence axis direction (CAD) boundaries, which in turn leads to improved creep resistance [36, 37]. In an effort to distinguish between these two models, Cho and co-workers used electron backscattered Kikuchi diffraction (EBKD) (also called OIM) to characterize the grain boundaries in both undoped and doped alumina [4, 7]. A comparison of the misorientation angle histograms for pure alumina, and alumina doped with 1000 p.p.m. Y is given in Fig. 7. It can be seen that Y-doping does not result in a significant difference in the misorientation distribution. Further, the study showed that the proportion of CSL boundaries in the Y-doped sample was very low (1–5%), and that there was little difference between the doped and undoped alumina. The EBKD results for the Y doping were representative of all the dopant systems tested (La, Nd, Zr, Nd/Zr) in that, for each system, the number of CSL boundaries detected was only a very small fraction of the total and there was no discernible difference in boundary fractions when compared with the undoped alumina. The very low frequency of CSL boundaries in Y-doped alumina was also confirmed by the TEM study of Gülgün *et al.* [38]. These findings provided strong evidence in support of the site-

blocking model, although clearly, subtle modifications of the grain boundary structure due to the presence of the rare-earth ions cannot be completely excluded.

To this end, work is in progress using EXAFS to study the local environment of the dopant ions at the alumina grain boundaries. In brief, preliminary EXAFS analyses of  $Y_2O_3$  and  $ZrO_2$  doped alumina indicate that dopants at the level of 100 p.p.m. are mainly segregated to the alumina grain boundaries. On average Y ions in the grain boundaries are coordinated by four oxygens at a distance of 2.3 Å, which corresponds to the Y–O bond length in cubic  $Y_2O_3$ , and Zr ions are coordinated by five oxygens at a distance of 2.14 Å, which is approximately the same as the average Zr–O bond length in monoclinic  $ZrO_2$ . From EXAFS, the Y grain boundary saturation concentration is estimated to be 6.0 atoms/ $nm^2$ , which is consistent with the estimation from STEM of 4.4 atoms/ $nm^2$  [8].

#### 4. COMPUTER SIMULATION OF SEGREGATION AND TRANSPORT

In light of the results of the mechanical, microstructural and microchemical studies summarized in the previous sections, and the associated conclusion that grain boundaries probably play a dominant

role in the enhancement of creep resistance in doped oxides, we now begin to systematically characterize and correlate grain boundary structure, chemistry and transport in doped aluminas. For this purpose we employ atomistic computer simulation to model idealized, periodically repeated bicrystals containing special, CSL boundaries. These boundaries were selected, though not realistic, due to their computational convenience [9]. In this context, simulation is a particularly useful tool that permits the interrogation of boundary structure and chemistry in a simplified description of a "clean" system with a controlled introduction of impurities. We note, however, that given the idealized nature of the systems under consideration, and the vagueness associated with available interionic potentials, our goal is really to obtain generic information which can then be extrapolated to a relatively broad spectrum of boundaries.

As the details of the simulation methodology and a description of the interionic potential are given elsewhere [9], we merely outline here the salient fea-

tures of the procedure employed in this study. In brief, a charge neutral combination of cations and anions is placed on either a perfect or defected lattice in a spatially periodic rectangular (or rhombic) simulation supercell [39], with ionic interactions described by a combination of empirical pair potentials including: (i) a short-range combination of Born-Mayer and attractive van der Waals potentials [40, 41], (ii) a long-range Coulombic interaction, and (iii) an elastic interaction between ionic cores and shells that reflects the electric polarizability of the lattice [42]. The conditionally convergent nature of the summations required to determine the Coulombic interactions was remedied, as usual, by using an Ewald summation [43]. In the case of grain boundary defects, the height of the simulation cell in the direction normal to the boundary was adjusted in order to eliminate, or at least reduce, extended defect-defect interactions (sometimes via extrapolation), while excess volume was introduced through interfacial gaps when appropriate. After constructing the desired perfect crystal or defect,

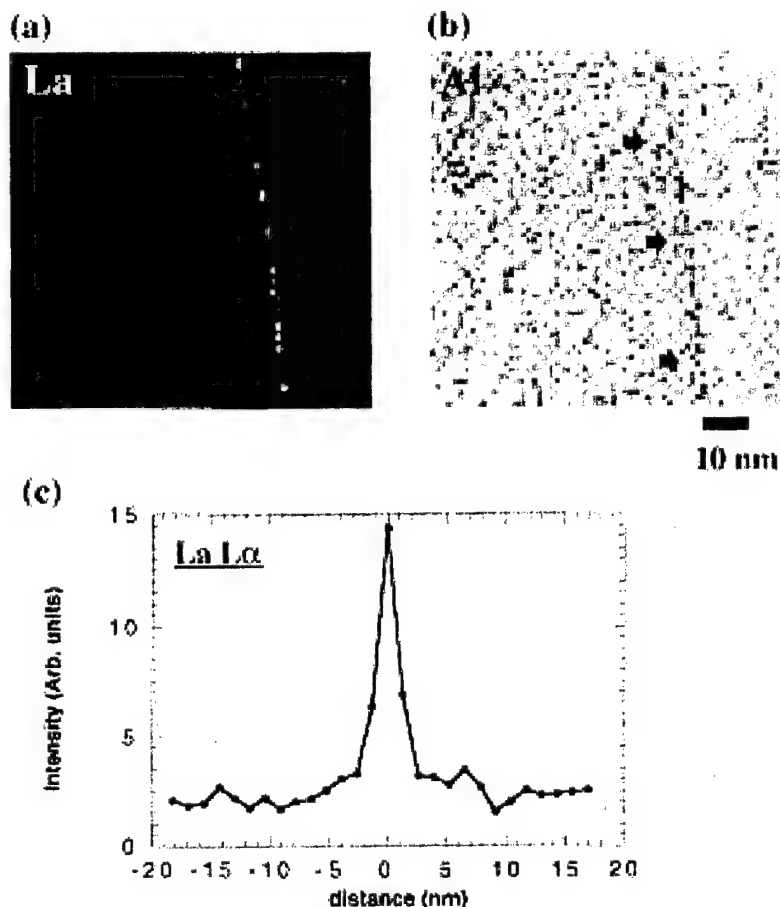


Fig. 6. STEM high-resolution X-ray map taken from 500 p.p.m. La-doped alumina: (a) La map; (b) Al map; (c) the corresponding intensity line profile across the boundary that appears in (a).

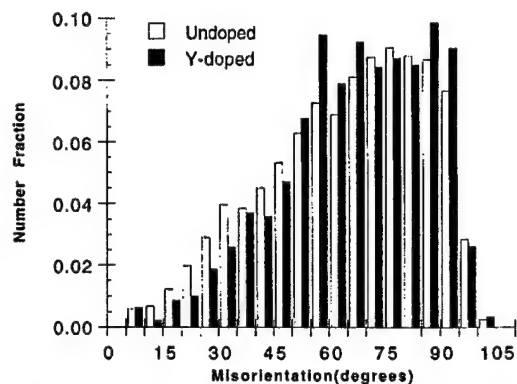


Fig. 7. Misorientation angle histogram for undoped and 1000 p.p.m. Y-doped alumina.

the equilibrium, ground state energy is obtained by employing a conjugate-gradient energy minimization technique [44], wherein the forces calculated at each iteration in the relaxation determine the subsequent configurational evolution of the system. In some cases, we validated our results by comparing these equilibrium energies with those obtained by zero-temperature Monte Carlo (MC) simulation.

An effective strategy for characterizing boundary structure and implicitly, to some degree, boundary chemistry, is to assess the volume associated with grain boundaries. Our approach has been to partition space in a slab of prescribed thickness near a (fully relaxed) boundary using a Voronoi construction [45]. In particular, two measures of interfacial volume were determined, the spatial distribution of cation volume as well as the distribution of void volume. In the cation case, a Voronoi polyhedron can be constructed from the envelope of planes that bisect each line which connects a given cation to its neighboring anions. A similar construction was used for the interstitial case. In both cases, an average "radius" was extracted for each Voronoi cell, yielding a spatially local measure of cell size [9]. As will be seen below, this construction, although complicated by ambiguities in identifying void locations and while not explicitly incorporating local charge considerations, is, nevertheless, quite informative for highlighting potential dopant segregation sites.

For concreteness, we focus here on two prototypical grain boundaries, a  $\Sigma 3$  basal twin, the relatively more ordered structure formed by a  $60^\circ$  rotation about the  $[0001]$  axis, and the  $\Sigma 13$  boundary, a relatively disordered structure formed by a  $27.8^\circ$  rotation about the same axis. In order to identify likely segregation sites for oversized dopants, frequency histograms of Voronoi volumes associated with substitutional and interstitial sites for both boundaries were compiled by using the procedure outlined above. The results, presented in Figs 8(a)–(d), indicate, for example, that the effect of the  $\Sigma 3$  boundary is to break the bulk unimodal size distribution of substitutional sites into an essen-

tially bimodal distribution with widely disparate cell sizes. The distribution of interstitial sites is somewhat similar, yet complicated by the fact that both octahedral and (more numerous) tetrahedral sites exist in the bulk region. The lower symmetry of the  $\Sigma 13$  boundary leads to several potential substitutional sites for segregation, some larger than the corresponding bulk sites, as well as some interstitial sites. In addition, by extending this Voronoi analysis to other ionic layers near a given boundary, and calculating a local excess volume per layer [9], it was found that the  $\Sigma 3$  boundary had a relatively localized excess volume, implying that the segregation profile associated with this boundary is likely to be quite narrow. The relative occupancy of these boundary sites by dopant ions in equilibrium can now be estimated by assigning each an energy and associated Boltzmann weight. Indeed, electron microscopy studies have reported essentially no segregation of Y to the basal twin boundary in alumina and some segregation to other boundaries [38], though this observation must be interpreted in view of the fact that the best resolution currently obtainable with these instruments is about 1–2 nm.

It has also been possible to obtain semi-quantitative kinetic information on Al migration at both segregated and unsegregated boundaries via computer simulation. Such information is especially useful given, for example, the paucity of cation boundary diffusion data, and because transport properties in alumina are governed strongly by the presence of impurities [46]. It may also aid in the interpretation of the aforementioned site-blocking model advanced to describe improved creep properties in ceramic oxides. Based on earlier work which characterized bulk cation diffusion [4], we explored the energy surface associated with the migration paths of Frenkel pairs on the  $\Sigma 3$  boundary. This type of defect was selected so that charge compensation effects (i.e. additional vacancies or interstitials) can be ignored. For a given Frenkel pair, three possible migration paths were identified in both the bulk and the twin boundary environments. These paths are illustrated schematically for undoped configurations in Fig. 9 [4]. We note that our approach was somewhat oversimplified in that we did not consider longer range diffusive processes and that we determined only approximate saddle point configurations. This latter approximation was adopted here given the geometric complexities inherent in identifying possible diffusive paths, especially in the presence of dopants. Nevertheless, we believe that the preliminary results presented below are indicative of important trends relating cation diffusion to dopant size.

Generally speaking, the presence of oversized, segregated dopants significantly modify grain boundary diffusion paths. In particular, the migration energies associated with various paths near the twin boundary were found to be lower than the

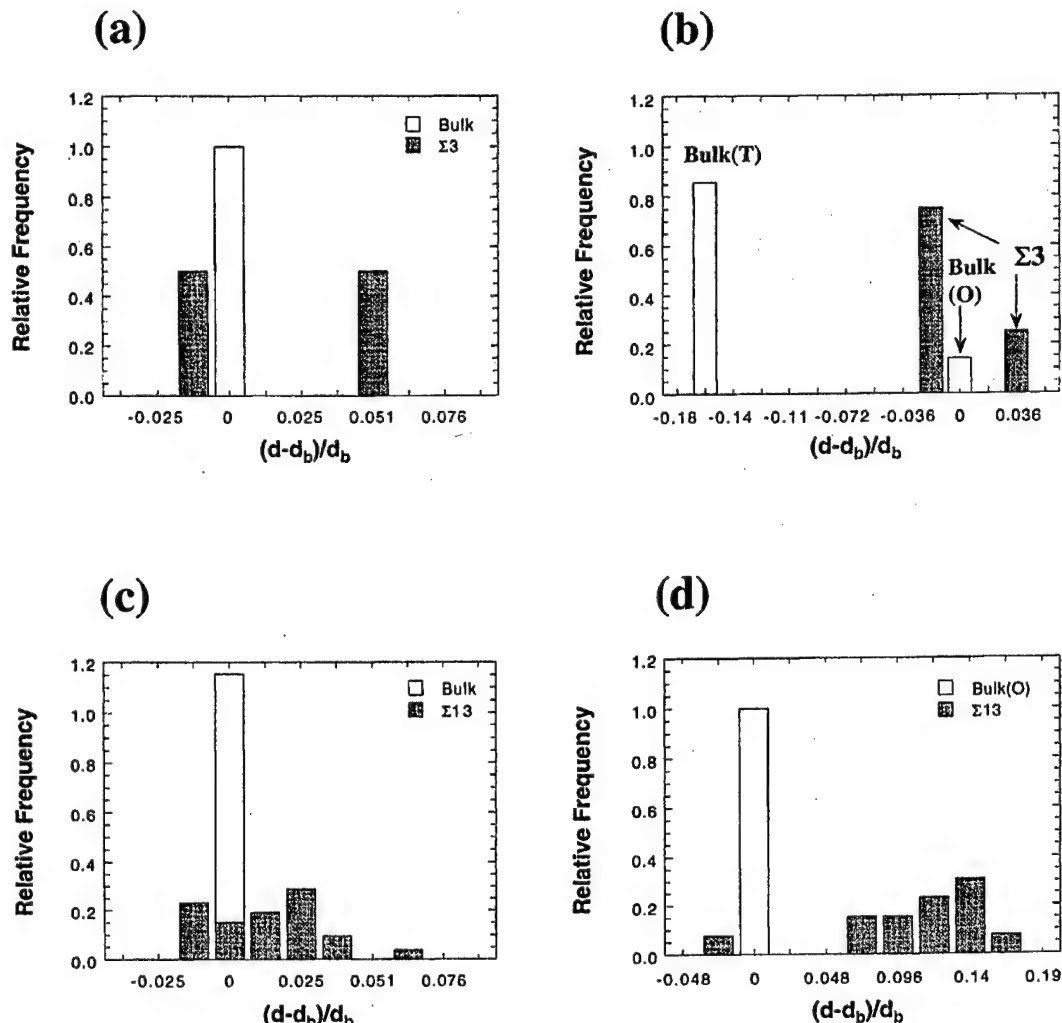


Fig. 8. A Voronoi cell characterization of a boundary plane, as compared to bulk environment: (a)  $\Sigma 3$ , substitutional; (b)  $\Sigma 3$ , interstitial; (c)  $\Sigma 13$ , substitutional; (d)  $\Sigma 13$ , interstitial. T, tetrahedral site; O, octahedral site;  $d$ , Voronoi cell radius;  $d_b$ , Voronoi cell radius for the bulk sites.

corresponding bulk paths (by as much as a factor of 5) and, in some cases, increased upon doping with Yb [4]. For example, the energy associated with the fastest unsegregated twin path increased by a factor of 2.75. If, instead, the system were doped with three (larger) La ions, the migration energy became about five to six times higher than the fastest unsegregated path and more isotropic. Further calculations for other boundaries and dopants are currently planned to amplify on these results.

## 5. DISCUSSION AND CONCLUSIONS

A variety of techniques, both experimental and theoretical have been employed to probe the role of segregating dopants in enhancing the creep behavior of alumina. The first important point which can be made is that because comparable creep behavior

was obtained for dopant levels above and below the solubility limit, the phenomenon is undoubtedly a solid solution effect, and unrelated to the presence of second phase particles. The possible role of the dopant ions in modifying grain boundary properties was highlighted by analytical studies, which revealed that the dopant ions were strongly segregated to the alumina grain boundaries. This result was not unexpected, given their greater size relative to the  $Al^{3+}$  ion. In a complementary study, the relation between ionic size and segregation enthalpy was confirmed by atomistic modeling [4]; the results of which underscored the idea that segregation was driven by the elastic strain energy due to size mismatch. Experiments aimed at elucidating the influence of dopant ionic size on the creep behavior revealed that the degree of enhancement saturates at higher ionic radii, suggesting that there is a limi-

tation on the amount of excess solute which can be accommodated at the grain boundaries. This is borne out by the STEM measurements of Bruley *et al.* [5], which showed very similar dopant ion concentrations at the boundaries for Y- and La-doped aluminas. The codoping studies [3] revealed that the addition of two dopant ions of differing size was more beneficial (in terms of the creep behavior) than doping with one type of ion alone. This result was rationalized in terms of greater efficiency of packing for ions with different ionic radii, and again was consistent with the site-blocking role of the dopant ions.

This concept of a volume distribution of cation grain boundary sites, which perhaps could be filled more efficiently by a range of different ions, was explored further by Cho *et al.* using computer simulation [9]. As described earlier (Section 4), these workers showed that for a  $\Sigma 3$  boundary, the Voronoi cation and interstitial volumes exhibit an essentially bimodal distribution, with widely disparate sizes. Furthermore, it was generally observed that a significant proportion of the boundary sites was larger than the corresponding bulk sites. The modeling results, therefore, supported the contention that a combination of large and small ions could fill the grain boundary region more efficiently than either ion individually.

From the outset, the contention of the Lehigh researchers was that the primary effect of the rare-earth ions was to inhibit grain boundary diffusion, most likely by 'site blocking' of rapid transport paths. We note that a similar mechanism for diffusive retardation, involving the "clogging" of important boundary paths by segregants, was proposed by others to explain the decrease in boundary diffusivity in Fe that attends Sn segregation [47]. An alternative possibility was raised by the work of Lartigue and Priester [36], however, wherein the deformation behavior was modified because the presence of Mg dopant ions favored the formation of special boundaries. In addition, these workers assessed the role of Y on grain boundary structure in Mg and Y codoped alumina, speculating that the proportion of near CSL boundaries increased after creep deformation [34] as found in metallic systems [48]. In this regard the EBKD results of Cho *et al.* [4, 7] were critical, in that they showed that rare-earth doping had very little influence on either the misorientation distribution, or the frequency of selected CSL boundaries.

As mentioned earlier in Section 2.4, the experimental values of the stress exponent ( $n \sim 2$ ) and (inverse) grain size exponent ( $p \sim 3$ ) are difficult to reconcile, in that they predict different rate-controlling mechanisms. Such apparent contradictions, however, are not uncommon in the creep literature, e.g. see Refs [19, 20, 49], and measurements carried out at Lehigh on undoped alumina also showed similar exponent values [1, 4]. Overall, we are per-

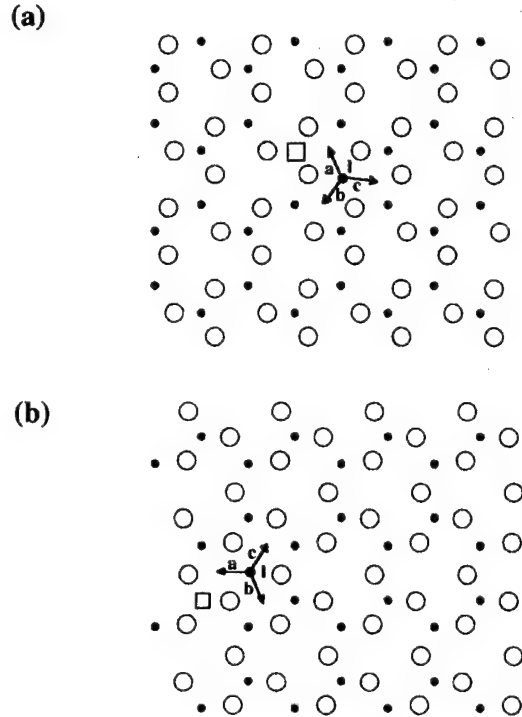


Fig. 9. Schematic diagram for three different migration paths in undoped alumina viewed along the [0001] axis: (a) bulk lattice; (b) (0001) twin boundary plane. (I: interstitial, a, b, c: migration paths,  $\square$ : vacancy, O: oxygen,  $\bullet$ : aluminum).

sued that the case for grain boundary diffusion control (vs interface control) is more convincing based on the following. Firstly, the study of Fang *et al.* [50] showed that for Y- and La-doped alumina, the densification kinetics exhibited a grain size exponent of 4, which again is consistent with grain boundary diffusion being the predominant mechanism. Secondly, the observed change in grain size exponent (from  $p \sim 3$  to 2) for the singly doped (Nd, Zr) to codoped (Nd/Zr) compositions [3] agrees well with the concept of a transition from grain boundary diffusion to lattice diffusion control. If however, for the sake of argument, the mechanism in the singly doped samples was indeed interface control (with  $p = 1$ ), it would be very difficult to rationalize the subsequent change in grain size exponent. In the absence of definitive evidence to the contrary, therefore, we believe that site blocking of rapid grain boundary diffusion paths by oversized ions is a reasonable model for the observed behavior, and intuitively preferable, because of its more straightforward physical basis.

Clearly, understanding in this area has been impeded by the lack of direct diffusion data on the effect of rare-earth doping on  $\text{Al}^{3+}$  grain boundary diffusion. However, an  $^{18}\text{O}$  tracer study by Le Gall *et al.* [51] suggested that Y doping decreased the diffusivity of oxygen at grain boundaries by two to

three orders of magnitude, raising the question of whether the rare-earth dopant ions have any effect on the anion diffusion. Strictly, because the creep rate is determined by the slower ion (on the faster route), any effect on the non-rate-controlling ion would not have an appreciable influence. The implications for oxidation rates, however, which depend on the faster moving species, are far greater; in this regard it would certainly be of interest to extend the simulation work to look into the motion of the oxygen ions.

Taken as a whole, the experimental and theoretical studies paint a reasonably self-consistent picture of outsize ions segregating to more energetically favorable grain boundary sites, and improving creep resistance by blocking a few critical diffusive pathways. As such, the mechanism is not reliant on any material specific defect mechanisms, and would thus seem to be generally applicable to other ceramic systems. The only proviso, however, would be that diffusional creep along the grain boundaries was the rate controlling mechanism. Implicit in the foregoing arguments is that it is the grain boundary diffusion of the Al ions which is being impeded by the rare-earth dopants. In this regard, there are interesting parallels with the reactive element (RE) effect in oxidation. For example, there is evidence that the addition of RE elements such as Y causes a change in mechanism of the scale growth from outward diffusion of aluminum ions, to inward diffusion of oxygen ions [52, 53]. The arguments put forward to explain this behavior are very similar to the one proposed above, namely that the RE cations inhibit the diffusivity of the Al ions at the grain boundary.

Although there is a firm basis for a general, phenomenological understanding of the creep behavior of doped alumina, several outstanding issues remain. For dopant levels below the solubility limit, it is not known whether there is a threshold concentration for creep inhibition, and how the creep behavior depends on dopant concentration. There are also unresolved questions concerning ionic size. The experimental data show both a saturation in the creep effect with increasing atomic size, and the dopant concentration at the grain boundary. Intuitively, however, one might expect a trade-off in terms of more effective blocking by a larger dopant ion, but a lower solubility due to fewer available sites. This in turn suggests that for dopant ions larger than  $Al^{3+}$ , there may be a range of ionic size, outside of which, the effect on grain boundary diffusivity is negligible. It is believed that further computer simulation, coupled with ongoing EXAFS studies on the local environment of the dopant ions as a function of concentration and size, may cast light on these issues. There is also the question as to whether a dopant ion which is smaller than the aluminum ion will also be effective in inhibiting creep. Here the lack of suitable trivalent dopant

ions provides an experimental constraint, but fortunately no such limitation exists for the modeling work.

In summary, a comprehensive integrated study has yielded significant progress in understanding the behavior of dopant systems where the creep behavior of alumina is improved. The field, however, is still not at a stage where it would be possible to predict, for a given host system, the optimal dopant ion and dopant level. Many of the obstacles to greater detailed understanding of the segregation and diffusion behavior arise from uncertainties in the structure of general (as opposed to special), grain boundaries in alumina. It is believed that the modeling of such boundaries, and their transport properties, is a fertile and important area for future work.

*Acknowledgements*—This work was supported by the U.S. Air Force Office of Scientific Research (under Contract No. F49620-98-1-0117, monitored by A. Pechenik). The authors would like to thank R. F. Krause at NIST for help with hot pressing the 3 in. billets. Helpful discussions with G. S. Cargill III are greatly appreciated. We are also indebted to V. Keast for her help with the STEM work.

## REFERENCES

- French, J. D., Zhao, J., Harmer, M. P., Chan, H. M. and Miller, G. A., *J. Am. Ceram. Soc.*, 1994, 77, 2857.
- Cho, J., Harmer, M. P., Chan, H. M., Rickman, J. M. and Thompson, A. M., *J. Am. Ceram. Soc.*, 1997, 80, 1013.
- Li, Y.-Z., Wang, C., Chan, H. M., Rickman, J. M., Harmer, M. P., Chabala, J. M., Gavrilov, K. L. and Levi-Setti, R., *J. Am. Ceram. Soc.*, 1999, 82, 1497.
- Cho, J., Ph.D. thesis, Lehigh University, 1998.
- Bruley, J., Cho, J., Chan, H. M., Harmer, M. P. and Rickman, J. M., *J. Am. Ceram. Soc.*, in press.
- Thompson, A. M., Soni, K. K., Chan, H. M., Harmer, M. P., Williams, D. B., Chabala, J. M. and Levi-Setti, R., *J. Am. Ceram. Soc.*, 1997, 80, 373.
- Cho, J., Chan, H. M., Harmer, M. P. and Rickman, J. M., *J. Am. Ceram. Soc.*, 1998, 81, 3001.
- Wang, C. M., Cargill III, G. S., Harmer, M. P., Chan, H. M. and Cho, J., *Acta Mater.*, in press.
- Cho, J., Rickman, J. M., Chan, H. M. and Harmer, M. P., *J. Am. Ceram. Soc.*, in press.
- Carroll, C. and Mocellin, A., *Ceram. Int.*, 1987, 13, 89.
- Carroll, D. F., Wiederhorn, S. M. and Roberts, D. E., *J. Am. Ceram. Soc.*, 1989, 72, 1610.
- Hollenberg, G. W. and Gordon, R. S., *J. Am. Ceram. Soc.*, 1973, 56, 140.
- Lessing, P. A. and Gordon, R. S., *J. Mater. Sci.*, 1977, 12, 2291.
- Cannon, R. M. and Coble, R. L., in *Deformation of Ceramic Materials, Proc. Symp. on Plastic Deformation of Ceramic Materials*, ed. R. C. Bradt and R. E. Tressler. Plenum Press, New York, 1975, p. 61.
- Chokshi, A. H. and Langdon, T. G., in *Defect and Diffusion Forum*, ed. F. J. Kedves and D. L. Beke, *Diffusion in Metals and Alloys DIMETA 88*, Vol. 66-9. Sci-Tech Publications, Brookfield, VT, 1990, p. 1205.
- Paladino, A. E. and Coble, R. L., *J. Am. Ceram. Soc.*, 1963, 46, 133.

17. Langdon, T. G., *Phil. Mag.*, 1970, **22**, 689.
18. Ashby, M. F. and Verrall, R. A., *Acta metall.*, 1973, **21**, 149.
19. Sherby, O. D. and Wadsworth, J., in *Deformation, Processing, and Microstructure*, Proc. ASM Materials Science Seminar, ed. G. Krauss. American Society for Metals, Metals Park, OH, 1984, p. 355.
20. Sherby, O. D. and Wadsworth, J., *Prog. Mater. Sci.*, 1989, **33**, 169.
21. Przybylski, K., Garratt-Reed, A. J., Pint, B. A., Katz, E. P. and Yurek, G. J., *J. electrochem. Soc.*, 1987, **134**, 3207.
22. Pint, B. A., Martin, J. R. and Hobbs, L. W., *Oxid. Met.*, 1993, **39**, 167.
23. Nanni, P., Stoddart, C. T. H. and Hondros, A. H., *Mater. Chem.*, 1976, **1**, 297.
24. Bender, B., Williams, D. B. and Notis, M. R., *J. Am. Ceram. Soc.*, 1980, **63**, 542.
25. Li, C.-W. and Kingery, W. D., in *Structure and Properties of MgO and Al<sub>2</sub>O<sub>3</sub> Ceramics*, ed. W. D. Kingery, *Advances in Ceramics*, Vol. 10. American Ceramic Society, Columbus, OH, 1984, p. 368.
26. Loudjani, M. K., Roy, J. and Huntz, A. M., *J. Am. Ceram. Soc.*, 1985, **68**, 559.
27. McCune, R. C., Donlon, W. T. and Ku, R. C., *J. Am. Ceram. Soc.*, 1986, **69**, C196.
28. Tawancy, H. M. and Abbas, N. M., *Scripta metall. mater.*, 1993, **29**, 689.
29. Gruffel, P. and Carry, C., *J. Eur. Ceram. Soc.*, 1993, **11**, 189.
30. Chabala, J. M., Soni, K. K., Gavrilov, K. L. and Levi-Setti, R., *Int. J. Mass Spectrosc. Ion Proc.*, 1995, **143**, 191.
31. Yoshida, H., Ikuhara, Y. and Sakuma, T., *J. Mater. Res.*, 1998, **13**, 2597.
32. Lartigue, S., Priester, L., Dupau, F., Gruffel, P. and Carry, C., *Mater. Sci. Engng*, 1993, **A164**, 211.
33. Lartigue, S. and Priester, L., *J. Am. Ceram. Soc.*, 1988, **71**, 430.
34. Korinek, S. L. and Dupau, F., *Acta metall. mater.*, 1994, **42**, 293.
35. Lartigue-Korinek, S., Carry, C., Dupau, F. and Priester, L., *Mater. Sci. Forum*, 1994, **170-172**, 409.
36. Lartigue, S. and Priester, L., *J. Physique*, 1988, **C5-49**, 451.
37. Priester, L., *Rev. Phys. Appl.*, 1989, **24**, 419.
38. Gülgün, M. A., Putlayev, V. and Rühle, M., *J. Am. Ceram. Soc.*, 1999, **82**, 1849.
39. Rittner, J. D., Udler, D. and Seidman, D. N., *Interface Sci.*, 1996, **4**, 65.
40. Catlow, C. R. W., James, R., Mackrodt, W. C. and Stewart, R. F., *Phys. Rev. B*, 1982, **25**, 1006.
41. Bush, T. S., Gale, J. D., Catlow, C. R. A. and Battle, P. D., *J. Mater. Chem.*, 1994, **4**, 831.
42. Dick, B. G. and Overhauser, A. W., *Phys. Rev.*, 1958, **112**, 90.
43. Allen, M. P. and Tildesley, D. J., *Computer Simulation of Liquids*. Oxford University Press, Oxford, 1987.
44. Press, W. H., Teukolsky, S. A., Vetterling, W. T. and Flannery, B. T., *Numerical Recipes in Fortran: The Art of Scientific Computing*. Cambridge University Press, New York, 1992.
45. Srolovitz, D. J., Maeda, K., Takeuchi, S., Egami, T. and Vitek, V., *J. Phys. F: Metal Phys.*, 1981, **11**, 2209.
46. Cannon, R. M. and Hou, P. Y., in *High Temperature Corrosion and Materials Chemistry*, ed. M. McNallan *et al.* Electrochemistry Society, Pennington, NJ, 1998, in press.
47. Sutton, A. P. and Balluffi, R. W., in *Interfaces in Crystalline Materials*. Clarendon Press, Oxford, 1995, p. 477.
48. Kokawa, H., Watanabe, T. and Karashima, S., *Phil. Mag. A*, 1981, **44**, 1239.
49. Robertson, A. G., Wilkinson, D. S. and Caceres, C. H., *J. Am. Ceram. Soc.*, 1991, **74**, 915.
50. Fang, J., Thompson, A. M., Harmer, M. P. and Chan, H. M., *J. Am. Ceram. Soc.*, 1997, **80**, 2005.
51. Le Gall, M., Huntz, A. M., Lesage, B., Monty, C. and Bernardini, J., *J. Mater. Sci.*, 1995, **30**, 201.
52. Pint, B. A., *Oxid. Met.*, 1996, **45**, 1.
53. Pint, B. A., Garratt-Reed, A. J. and Hobbs, L. W., *J. Am. Ceram. Soc.*, 1998, **81**, 305.



# Codoping of Alumina to Enhance Creep Resistance

Yan-Zun Li, Chongmin Wang,\* Helen M. Chan,\* Jeffrey M. Rickman,\* and Martin P. Harmer\*

Department of Materials Science and Engineering and Materials Research Center, Lehigh University, Bethlehem, Pennsylvania 18015

Jan M. Chabala, Konstantin L. Gavrilov,\* and Riccardo Levi-Setti

Enrico Fermi Institute and Department Physics, University of Chicago, Chicago, Illinois 60637

The tensile creep behavior of both singly and multiply doped alumina samples has been investigated in order to understand better the impact of dopant segregation to grain boundaries on observed creep resistance. Previous studies have suggested that the segregation of the oversized dopant ions reduces the grain boundary diffusivity and thus the creep rate. The aims of the present work are to examine the possibly beneficial effects of selective codoping in enhancing creep resistance, and to elucidate the role (if any) of precipitates in creep inhibition. The specific singly and codoped systems considered in this work were as follows: hot-pressed alumina samples containing nominally (i) 100 ppm zirconium, (ii) 100 ppm neodymium, (iii) 100 ppm zirconium codoped with either 100, 350, or 1000 ppm neodymium, (iv) 100 ppm zirconium codoped with 1000 ppm scandium. Microchemical mapping using secondary ion mass spectrometry revealed direct evidence of cosegregation of the dopant ions to grain boundaries. Tensile creep tests were carried out in the temperature range of 1200–1350°C, utilizing stresses ranging from 20 to 100 MPa. In the case of the Nd/Zr codoped alumina, it was found that the creep rate decreased by 2 to 3 orders of magnitude relative to undoped alumina. This improvement was greater than that achieved by doping with either Nd or Zr alone, and demonstrates that the incorporation of ions of differing sizes may be beneficial. The observed enhancement in creep resistance was obtained for compositions both above and below the solubility limit of Nd in alumina; hence the phenomenon is primarily a solid solution effect.

## I. Introduction

RECENTLY it has been shown that rare-earth dopant additions can significantly improve the creep resistance of polycrystalline alumina. For example, the results of French *et al.*<sup>1</sup> and Cho *et al.*<sup>2</sup> demonstrated that the addition of 1000 ppm (atomic ratio) Y or 500 ppm La gave rise to a 2 orders of magnitude reduction in the tensile creep rate of alumina. Lartigue *et al.*<sup>3</sup> and Robertson *et al.*<sup>4</sup> showed a reduction (by factors of 5 and 15) in the creep rate of magnesia-doped alumina with the addition of 500 and 360 ppm Y, respectively. Finally, Wakai *et al.*<sup>5</sup> reported a decrease in the creep rate by a factor of 15 with the addition of 1000 ppm Zr to Al<sub>2</sub>O<sub>3</sub>.

The enhancement in creep resistance resulting from yttrium and lanthanum additions is believed to be a result of segregation of the oversized solute ions to the grain boundaries.<sup>6–12</sup>

Assuming a diffusional creep mechanism, segregants at the grain boundaries could inhibit grain boundary diffusion<sup>8–10</sup> or possibly retard the interface reaction believed to be controlling the rate of ion transport along the grain boundaries.<sup>11,13</sup> Indeed, grain boundary diffusion experiments by Le Gall *et al.*<sup>10</sup> recently revealed a 3 orders of magnitude reduction in diffusivity by doping alumina with 500 ppm Y. In a study by Wakai *et al.*,<sup>5</sup> the creep rate reduction due to Zr addition was attributed to a decrease in the interface reaction rate resulting from zirconia particles formed at the alumina grain boundaries. In a more recent study, however, the same group observed a similar beneficial effect when the Zr doping was at a level below the solubility limit.<sup>6</sup>

With these results in mind, it is of particular interest to identify the dopant or combination of dopants that best enhance creep resistance. The belief that the rate of grain boundary diffusion determines the creep rate suggests at least two possibilities. First, it might be advantageous to introduce dopants with large ionic radii in order to effectively block fast diffusion paths along the boundary. Previous studies of Y- and La-doped alumina indicate, however, that this approach may be of limited utility as the steady-state creep behavior of these materials was quite similar despite a significant difference in dopant ionic radii. An enhancement of this blocking effect might be achievable by a second option, namely *selective codoping*. That is, by employing dopants of varying size, it should be possible to more efficiently fill the free volume associated with a grain boundary, and thereby hinder transport along numerous potential paths.

In this paper we consider this latter, more promising option. Specifically, we compare and contrast the results of creep studies involving singly doped alumina (Nd, Zr) with those of Nd/Zr and Sc/Zr codoped alumina. Both tensile creep tests and complementary microstructural analyses will be used to correlate enhanced creep resistance with dopant segregation to grain boundaries. The goal of this work is to explore any synergistic effects associated with selective codoping that enhance mechanical properties, and to identify the critical parameters (e.g., relative ionic size) that determine the observed creep behavior.

## II. Experimental Procedure

### (1) Specimen Preparation

Ultrapure  $\alpha$ -Al<sub>2</sub>O<sub>3</sub> powders (AKP-53, 99.995%, mean particle size of 0.35  $\mu$ m, Sumitomo Chemical America, New York, NY), neodymium nitrate (Nd(NO<sub>3</sub>)<sub>3</sub>·6H<sub>2</sub>O, 99.99%), scandium nitrate (Sc(NO<sub>3</sub>)<sub>3</sub>·4H<sub>2</sub>O, 99.99%), and aluminum nitrate (Al(NO<sub>3</sub>)<sub>3</sub>·9H<sub>2</sub>O, 99.999%) (Alfa AESAR, Ward Hill, MA) were used as the starting powders. Alumina slurries of roughly equal mass of alumina powders and DDI (deionized + distilled) water were prepared. Doping levels (atomic ratio) of 100 ppm, 350 ppm, 1000 ppm Nd (Nd/Al ratio), and 1000 ppm Sc were achieved by adding the appropriate amount of neodymium or scandium nitrate aqueous solution to the alumina

R. Raj—contributing editor

Manuscript No. 190400. Received February 9, 1998; approved October 21, 1998.  
\*Member, American Ceramic Society.

slurries. A few drops of aluminate nitrate aqueous solution (equivalent of 250 ppm doping level of Al ions) were added to all of the slurries as a deflocculant. For selected compositions, codoping with Zr was achieved by ball-milling the slurries with ZrO<sub>2</sub> grinding media (Tosoh U.S.A. Inc., Bridgewater, NJ) for 20 h. The slurries were dried in a Teflon evaporating dish under an infrared heat lamp; magnetic stirring was used to minimize differential settling. The dried cakes were then placed in a polyethylene bag and crushed with a rolling pin. The powders were subsequently calcined in high-purity alumina crucibles (99.8%, Vesuvius McDanel Ceramic Co., Beaver Falls, PA) at 850°C for 10 h to remove possible organic contaminants, and then recrushed. A new set of labware was used for each composition to avoid cross contamination. Typical powder batch sizes were 200–250 g each. All powder preparation was carried out in a class 100 clean environment using acid-washed containers. A list of all the compositions studied, together with the results of chemical analysis using ICP-OES (inductively coupled plasma-optical emission spectroscopy), is given in Table I.

Hot-pressing was carried out under vacuum, in a graphite resistance furnace (Vacuum Industries, Inc., Somerville, MA) at NIST (National Institute of Standards and Technology, Gaithersburg, MD). Graphite foil liners and BN powder were used to facilitate specimen removal after hot pressing. For all compositions the heating rate was 1000°C/h, and the soaking time was 30 min with an applied pressure of 45 MPa. The Zr-doped and Sc/Zr codoped Al<sub>2</sub>O<sub>3</sub> were hot-pressed at 1320°C, the Nd/Zr codoped Al<sub>2</sub>O<sub>3</sub> containing 100 ppm Nd was hot-pressed at 1400°C, whereas the 350 ppm and 1000 ppm Nd samples were hot-pressed at 1475°C. The 100 ppm singly Nd-doped sample was hot-pressed at 1425°C. After soaking, the specimens were furnace cooled to room temperature while maintaining 45 MPa applied pressure.

## (2) Microstructural Characterization

Microstructural characterization was performed using scanning electron microscopy (SEM, JEOL 6300F). The grain structures were revealed by taking polished specimens (1 µm diamond finish) and thermally etching in a box furnace at 1300–1400°C for 30–60 min. The grain size was determined from SEM micrographs using the linear intercept technique, with at least 600 intercepts counted for each measurement. In order to obtain creep specimens with differing initial grain size, a few tensile specimens for each material were acid washed and given further annealing treatments (see Table II).

Imaging secondary ion mass spectrometry (SIMS) maps of Zr, Nd, and Sc distributions were obtained from polished specimens of the doped materials. The samples were coated with a thin layer of gold (~10 nm thick) to prevent charging during analysis. The SIMS instrument is described in detail in Ref. 14. Briefly, a primary beam of Ga<sup>+</sup> ions, extracted from a liquid ion source, is focused to a spot approximately 40 nm in diameter, and scanned in a raster pattern over the samples. The spatial resolution, assuming adequate signal statistics, is equivalent to the probe diameter. For each point in the scanned raster, secondary ions (emerging from the upper two monolayers of the sample) are collected and mass-discriminated by a magnetic sector mass spectrometer. It is important to note that the background signal for the SIMS technique is essentially zero; i.e., no background subtraction is necessary, and any small signal corresponds to an actual material concentration.

## (3) Creep Testing

The hot-pressed billets were machined by a commercial shop (Bomas Machine Specialties, Inc., Somerville, MA) into dog-bone tensile specimens of the 2-in. specimen design developed at NIST by French and Wiederhorn.<sup>15</sup> SiC flags were attached to the specimen with carbon cement to establish the gauge length; at elevated temperatures, the flags remain attached due to frictional forces. A laser extensometer (LaserMike, Inc., Dayton, OH) was used to measure the gauge length (precision of ±1 µm) as a function of time under load. During testing, the specimen was subjected to a constant load using either a lever-arm or hydraulic testing machine (Applied Test Systems, Inc., Butler, PA). Tensile tests were performed in air under a constant load in the temperature range of 1200–1350°C. Since all of the experimental data (except for the creep rupture tests) were collected under a total strain of 2–3%, the tests could be considered to be under constant stress. The range of stress values was 20–100 MPa. The maximum strains at rupture were as follows: (a) 8–12% for the Nd-doped sample, (b) 10–12% for Zr-doped, Nd 100/Zr and Sc/Zr codoped samples, (c) 4% for Nd 350/Zr, and (d) 1.5% for Nd 1000/Zr.

Three types of creep tests were performed: (i) standard creep rupture tests in which the specimen experienced a constant load and temperature until failure, (ii) temperature step tests in which the stress was kept constant but the temperature was altered periodically, and (iii) stress step tests in which temperature was held constant while the stress was altered periodically. For most compositions, the creep rate under each set of conditions was measured two or three times on a given specimen to ensure that the strain rate was not dependent on strain history. It was found that the strain rates under the same conditions were typically within about 10%. With the exception of a 20% increase in grain size associated with the 0.48 µm Zr-doped alumina after being crept 12% at rupture, the grain size changes for all other compositions were found to be less than 5% after being crept.

## III. Results and Discussion

### (1) Microstructure and Segregation Behavior

The grain size and density values for all of the specimens studied are summarized in Table II. Figure 1 shows as-fired microstructures for all of the alumina compositions. For the Zr-doped, Nd-doped, Nd 100/Zr, and Sc/Zr samples, it can be seen that the microstructures were fairly uniform, consisting of roughly equiaxed grains. In addition, high-resolution SEM did not reveal the presence of second phase particles for any of the above compositions. In general, it was observed that with increasing Nd doping there was an increase in the tendency for abnormal grain growth, and hence the degree of microstructural inhomogeneity. Hence for the Nd 350/Zr composition, there were isolated abnormal grains, whereas the grain structure for the Nd 1000/Zr sample was bimodal. The range of the grain sizes for the Nd/Zr codoped materials with 350 and 1000 ppm Nd was very broad, 0.2–5.0 µm for Nd 350/Zr and 0.2–10 µm for Nd 1000/Zr. Furthermore, second phase particles were clearly visible for these two compositions (see Fig. 2). In the 350 Nd/Zr material, the second phase particles were isolated and uniformly distributed in the microstructure. In contrast, for Nd 1000/Zr, the second phase particles occurred in clusters. Since precipitates were observed only for the Nd 350/Zr and

Table I. Compositions of Doped Specimens

	Singly doped (ppm)		Codoped (ppm)			
	Nd	Zr	Nd 100/Zr	Nd 350/Zr	Nd 1000/Zr	Sc/Zr
Nominal	100	100	100/100	350/100	1000/100	1000/100
Measured†	143	110	40/70	270/220	735/190	610/200

†All analyses were carried out using ICP-OES (inductively coupled plasma-optical emission spectroscopy, which has an estimated error of ±20%).

Table II. Density and Grain Size Values for Samples Tested

	Singly doped		Co-doped			
	Nd	Zr	Nd 100/Zr	Nd 350/Zr	Nd 1000/Zr	Sc/Zr
Nominal doping (ppm)	100	100	100/100	350/100	1000/100	1000/100
Density (%)	99.4	97.0	98.0	100	100	95.0
Grain size ( $\mu\text{m}$ )						
As hot-pressed	1.31	0.48	0.72	1.50	5.2	0.66
Annealed at 1450°C	1.79 <sup>†</sup>	1.45 <sup>‡</sup>	1.31 <sup>‡</sup>	2.30 <sup>‡</sup>		1.66 <sup>§</sup>
Annealed at 1500°C	2.45 <sup>†</sup>	1.64 <sup>‡</sup>	1.97 <sup>‡</sup>	3.90 <sup>‡</sup>		1.93 <sup>§</sup>

<sup>†</sup>Annealed for 15 h. <sup>‡</sup>Annealed for 10 h. <sup>§</sup>Annealed for 5 h.

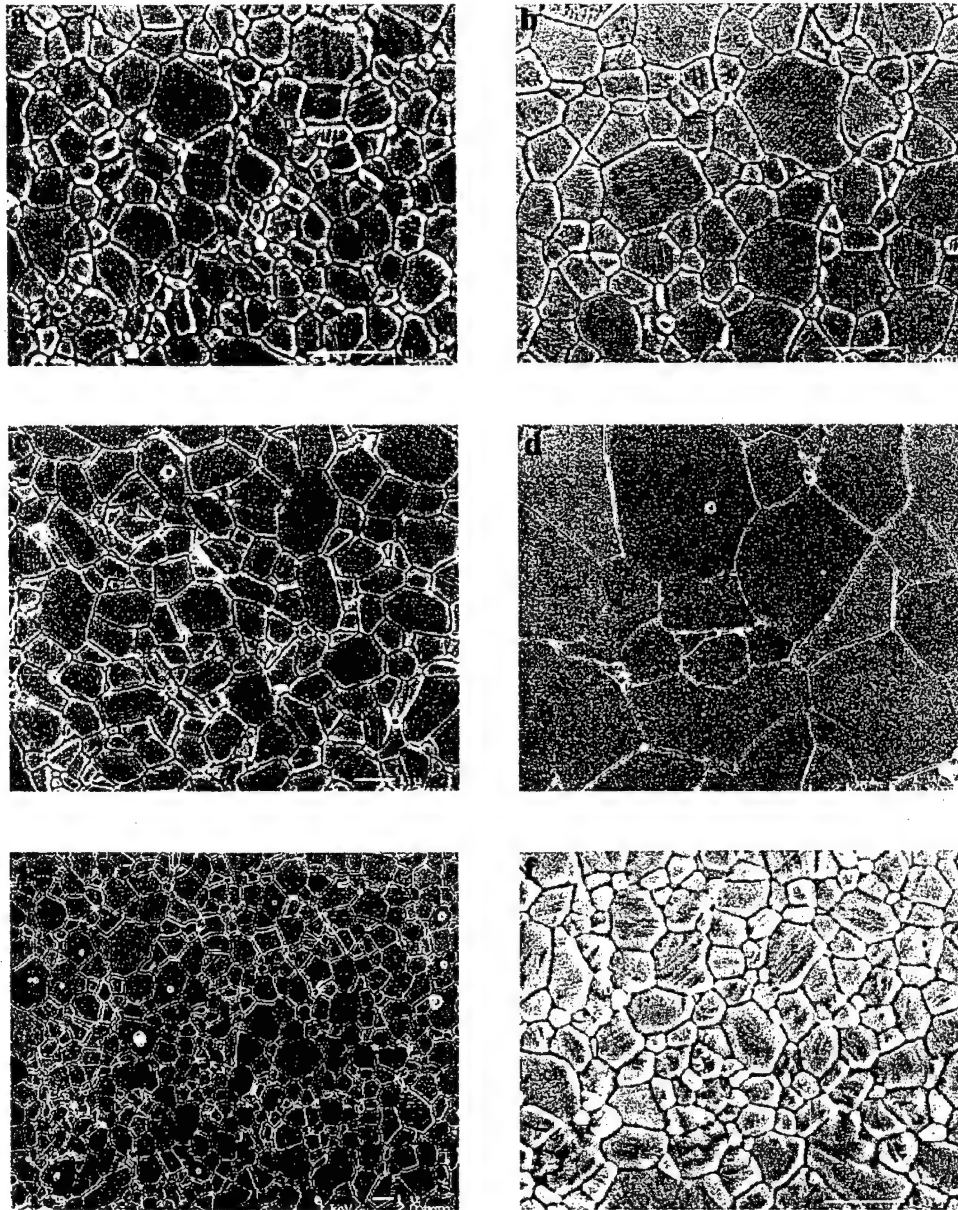


Fig. 1. SEM micrographs showing microstructures of as-hot-pressed doped alumina: (a) 100 ppm Zr doped; (b) 100 ppm Nd/100 ppm Zr codoped; (c) 350 ppm Nd/100 ppm Zr codoped; (d) 1000 ppm Nd/100 ppm Zr codoped; (e) 100 ppm Nd doped; and (f) 1000 ppm Sc/100 ppm Zr codoped.

Nd 1000/Zr compositions, we can infer that the solubility limit of (a) Zr in alumina is >110 ppm (and >200 ppm in the presence of Sc), (b) Nd in alumina is in the range of 143 and 270 ppm, and (c) Sc in alumina is >610 ppm in the presence of Zr. The observed difference in the relative solubilities of Sc and Nd is consistent with the degree of size mismatch with  $\text{Al}^{3+}$ .

The  $\text{Sc}^{3+}$  ion is smaller and closer in atomic radius to  $\text{Al}^{3+}$ , and hence more soluble.  $\text{Zr}^{4+}$  is the same size as  $\text{Sc}^{3+}$ , but the lower solubility in alumina can be rationalized in terms of the higher charge, and the need to form compensating point defects.

SIMS maps showing the distribution of dopant ions for the codoped specimens are given in Fig. 3. Note that the corre-



Fig. 2. SEM micrographs showing second phase precipitates (arrowed): (a) 350 ppm Nd/100 ppm Zr codoped; and (b) 1000 ppm Nd/100 ppm Zr codoped.

sponding maps for the different dopant ions were obtained from the same area of the specimen. Clearly, all the dopant ions utilized in this study ( $Zr^{4+}$ ,  $Nd^{3+}$ , and  $Sc^{3+}$ ) segregate to the alumina grain boundaries. The same type of segregation behavior was also observed for the singly Zr- and Nd-doped samples. In the case of  $Zr^{4+}$  and  $Sc^{3+}$ , it appears qualitatively from the SIMS images that the width of the grain boundary segregation layer is greater than for  $Nd^{3+}$ ; this observation is consistent with the lesser degree of size mismatch discussed earlier, and is the subject of current, more detailed study.

Absolute concentration calibration is difficult with SIMS, but relative concentrations (e.g., between bulk and grain boundaries), can be estimated.<sup>7</sup> The procedure adopted was as follows. For each sample, the SIMS signal from the grain interior was determined by averaging the intensity from a large number (>1000) of image pixels. The intensity from selected grain boundaries was obtained from operator-defined line profiles oriented normal to the boundary, and averaged over a width of 10 pixels ( $\sim 0.2 \mu m$ ) to reduce statistical noise. At least 20 boundaries were analyzed for each sample. The maximum signal intensity along these scans was taken as the dopant signal from the grain boundary region. Since the primary beam diameter is significantly larger than the grain boundary width, the dopant signal was corrected for unit area assuming a boundary width of 1 nm and a probe size of 40 nm. In the case of  $Nd^{3+}$ , the ratio of the grain boundary signal to that of the bulk ( $I_{gb}/I_{bulk}$ ) was  $\sim 7000$ , and there was no significant difference in this result between the singly doped and codoped samples. For the codoped samples,  $I_{gb}/I_{bulk}$  for  $Zr^{4+}$  was  $\sim 4800$ , and for  $Sc^{3+}$  the ratio was  $\sim 260$ . The experimental scatter in the ratio values

was  $\sim 20\%$ ; this uncertainty could be attributed to variation in the bulk signal (which, in the case of Nd and Zr, was so low as to be essentially at the limit of detectability). Nonetheless, the SIMS results clearly demonstrate that  $Sc^{3+}$  segregates to a lesser degree at the alumina grain boundaries than the other two dopant ions. Most importantly, the simultaneous segregation to the boundaries by the different ions in the codoped compositions strongly supports the contention that there may be an additive effect on the grain boundary transport process.

## (2) General Creep Behavior

Most of the doped materials exhibited an initial primary stage of creep, although the strain range and the difference between the primary and the steady-state creep rates were not the same for each composition. It was found that an initial annealing treatment at  $1250^\circ C$  for 24 h under a low applied stress ( $< 5$  MPa) significantly shortened or completely suppressed the primary stage of creep. Without this pre-annealing step, primary creep up to 0.5% strain was observed for most of the doped aluminas. The reason for this phenomenon is not clear. Possible explanations include dopant redistribution, local stress relaxation, and subtle changes in the microstructure. In order to facilitate the accurate measurement of the steady-state creep rate, all of the specimens were pre-annealed, including those for the creep rupture tests.

The strain-time curves from creep rupture tests are shown in Fig. 4. It can be seen from the figure that Zr-doped and Sc/Zr codoped alumina exhibit reasonably well-defined steady-state and tertiary creep regimes. For the Nd/Zr codoped aluminas, however, the strain rate difference between the different stages of creep was less than 10%, which is within experimental scatter. For this reason, the entire creep regime for the Nd/Zr codoped aluminas was considered to be steady-state for the purpose of creep rate measurements.

The as-measured creep rates from temperature step tests under a constant stress of 50 MPa are shown in Fig. 5(a). It should be emphasized here that, because of differences in grain size, the effect of the dopant ions alone on the creep rates is obscured. Comparison of the creep behavior for the different dopant systems when normalized to a constant grain size is discussed in detail in Sections III(3) to III(5). Note that corrections to the creep rate<sup>16</sup> taking into account the slight differences in porosity from system to system were found to be of the same order as experimental scatter in the creep measurements, i.e., 10–15%, and hence neglected.

(A) *Activation Energy:* The apparent activation energy for creep in pure alumina was previously determined to be 450 kJ/mol.<sup>1</sup> In this study it was found that for the singly doped alumina, the addition of 100 ppm Zr increased the activation energy to 690 kJ/mol, whereas for the 100 ppm Nd sample, it was 720 kJ/mol. For the Nd/Zr codoped compositions, the activation energies were determined to be 780, 990, and 1060 kJ/mol, for Nd 100/Zr, Nd 350/Zr, and Nd 1000/Zr, respectively. In the case of the Sc/Zr codoped sample, the activation energy was 720 kJ/mol. Higher activation energies resulting from dopant additions were also reported by Cho *et al.*<sup>2</sup> in Y and La doped alumina, where the activation energy was 745 and 760 kJ/mol for 1000 ppm Y and 500 ppm La doped aluminas, by Sato and Carry<sup>17</sup> in Y and Mg codoped alumina, and by Wakai *et al.*<sup>6</sup> in Zr-doped alumina.

(B) *Stress Exponent ( $n$ ) and Inverse Grain Size Exponent ( $p$ ):* The steady-state creep rate predicted by diffusional mechanisms is commonly expressed in the form

$$d\epsilon/dt = A(\sigma)^n(d)^{-p} \exp(-Q/RT)$$

where  $A$  is the constant determined by the slowest diffusing species along the most rapid diffusion path,  $\sigma$  the applied stress,  $n$  the stress exponent,  $d$  the grain size,  $p$  the inverse grain size exponent,  $Q$  the apparent activation energy for creep, and  $T$  the absolute temperature.

The effect of stress on the steady-state creep rate was investigated in the stress range of 20–100 MPa and at a constant



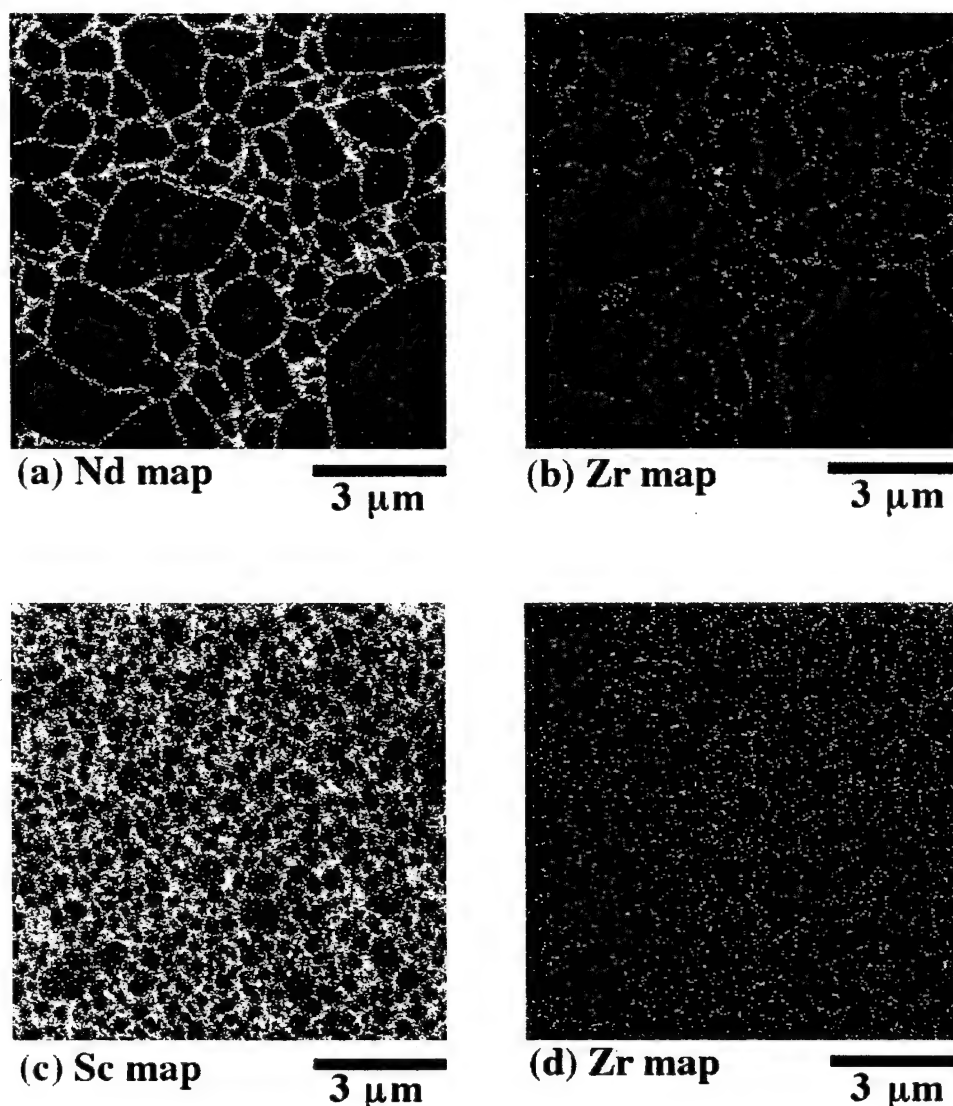


Fig. 3. SIMS maps showing the dopant distributions in the as-hot-pressed codoped alumina materials: (a) Nd map and (b) Zr map of the same area in the specimen codoped with 350 ppm Nd/100 ppm Zr; (c) Sc map and (d) Zr map of the same area in the specimen codoped with 1000 ppm Sc/100 ppm Zr.

temperature of 1275°C. The results for all of the compositions are shown in Fig. 5(b). The stress exponent ( $n$ ) was measured to be close to 2 for all of the materials, which is consistent with the results of French *et al.*<sup>1</sup> and Robertson *et al.*<sup>4</sup> This value reflects a possible role of interface-reaction in the creep process.

The effect of grain size on the creep rate was investigated for all of the compositions except for the Nd 1000/Zr alumina; this is because of the large starting grain size (5.2 μm) of the as-hot-pressed material for this composition. The strain rates at temperature steps in the range of 1200–1350°C (under a constant stress of 50 MPa) were obtained for each specimen. Three specimens with different grain sizes were tested for each composition. Figure 5(c) shows the dependence of the strain rates on grain size at 1275°C. It can be seen that the inverse grain size exponent ( $p$ ) was measured to be greater than 3 for the Zr-doped, Nd-doped, and Sc/Zr codoped materials, and close to 2 for the Nd/Zr codoped materials. The dependence of the strain rates on the grain size was the same for all of the temperatures studied.

In order to directly compare the strain rates associated with the different dopant systems, the strain rates shown in Fig. 5(a)

were adjusted to reflect a grain size of 0.72 μm, the grain size of the Nd 100/Zr sample. The strain rates of Zr-doped, Nd-doped, and Sc/Zr codoped aluminas were corrected taking the measured value of  $p = 3$  (grain boundary diffusion controlled creep), while that of the other Nd/Zr codoped aluminas were corrected assuming  $p = 2$  (lattice diffusion controlled creep). In previous work, French *et al.*<sup>1</sup> and Cho *et al.*<sup>2</sup> determined the inverse grain size exponent for undoped alumina to be close to 3. This value was used to obtain corrected strain rates for the undoped alumina data. The influence of the various doping parameters as evidenced by the normalized creep curves is discussed in detail in the following sections.

### (3) Solid Solution Effect

Before considering the role of dopant size on creep rate, it is useful to establish to what extent the diminution of creep rates in the alumina compositions studied is essentially a solid solution effect, as opposed to a consequence of the presence of second-phase particles. This information can be inferred from Fig. 6, which shows the dependence of observed strain rate on temperature for alumina doped with 100 ppm Nd/Zr (below the solubility limit) and 1000 ppm Nd/Zr (above the solubility

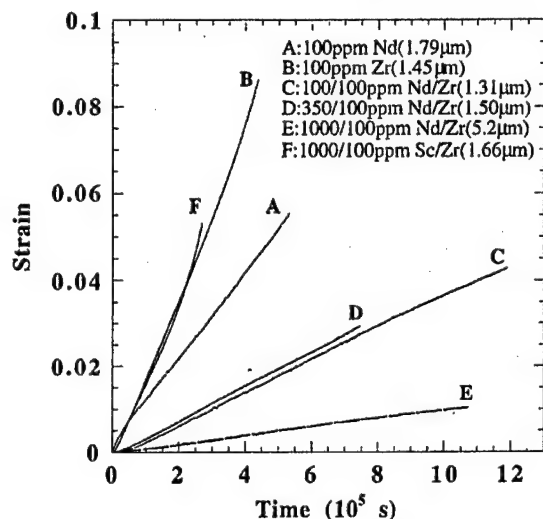


Fig. 4. Typical creep deformation curves of the doped alumina samples. The average grain size is shown in parentheses. For all specimens, the applied stress was 50 MPa. The temperature of testing was 1250°C except for specimens A and E, which were crept at 1275°C.

limit). As compared with undoped alumina, the Nd/Zr codoped aluminas show essentially the same secondary creep behavior over the temperature range explored. As discussed previously (Section III(2)), for the Nd/Zr codoped compositions, the creep activation energies were determined to be 780, 990, and 1060 kJ/mol, for Nd 100/Zr, Nd 350/Zr, and Nd 1000/Zr samples, respectively. If we assume that the difference between the values for Nd 350/Zr and Nd 1000/Zr are within experimental scatter, then the activation energy results are consistent with an increasing activation energy with increasing Nd content up to the solubility limit, which is known to lie between the dopant concentrations corresponding to Nd 100/Zr and Nd 350/Zr. The creep results thus support the contention that second phase precipitates do not play a significant role in promoting creep resistance in this system. Wakai *et al.*<sup>6</sup> have reached essentially the same conclusion in their study of the effect of zirconium addition on the creep of alumina.

#### (4) Size Effect—Single Dopants

Having established that the enhanced creep behavior most likely results from a solid solution of dopant in an alumina solvent, as opposed to the creation of a distinct second phase, we now explore the impact of various dopant parameters on observed creep rates. Consider first Fig. 7, which shows the measured strain rate for several singly doped aluminas as a function of temperature. It is clear that for a range of dopant sizes, larger dopant ions are associated with smaller strain rates and correspondingly larger creep activation energies. For dopant radii around 1 Å (e.g.,  $Y^{3+}$  and  $La^{3+}$ ), however, increases in dopant radius do not result in improved creep resistance. This apparent saturation of creep resistance is highlighted in Fig. 8, which shows the dependence of strain rate on ionic radius at fixed temperature. It should be emphasized here that our focus is on steady-state creep behavior, and that the primary and tertiary creep regimes for these doped aluminas often show markedly different behaviors.<sup>2</sup>

Our belief is that the improvement in creep resistance results from the lowering of grain boundary diffusivity due to the segregation of the oversized dopant ions to the boundaries. There are several compelling reasons for this conclusion. First, results of sintering/densification studies of yttrium- and lanthanum-doped alumina<sup>18</sup> were consistent with grain boundary diffusion control, and revealed a reduction of densification rate by a factor of 10 and 20 for 1000 ppm Y and 1000 ppm La

addition to alumina, respectively. Second, direct measurement of the coefficient of oxygen grain boundary diffusion by Le Gall *et al.*<sup>10</sup> recently showed a 3 orders of magnitude reduction with a doping level of 500 ppm Y, while the oxygen lattice diffusivity increased slightly. Finally, although it has been proposed<sup>19–21</sup> that the role of the dopant ions is to modify the grain boundary structure and increase the frequency of special boundaries, recent research by the present group<sup>22</sup> utilizing EBKD (electron backscatter Kikuchi diffraction) has found no evidence of this. This emerging picture of inhibited Coble creep, in turn, implies that blocking effectiveness is essentially a geometrical issue related to dopant size and the local geometry of a particular boundary. The interesting question which arises is whether we can improve blocking effectiveness by the simultaneous addition of dopants of varying size.

#### (5) Selective Codoping

As revealed by the SIMS mapping, simultaneous segregation to the boundaries by different ions occurs. It is likely, therefore, that grain boundary transport, and thereby the creep rate, can be modified by selective codoping. Additional information as to the impact of codoping on transport mechanisms can be obtained by examining Fig. 9, which shows the dependence of the measured steady-state strain rate on temperature for both singly and multiply doped samples. First, let us consider the creep behavior of the Zr-doped and Sc/Zr codoped compositions. It can be seen that the addition of 1000 ppm Sc does not result in any further improvement in the creep rate. The relative similarity between these two systems is, perhaps, not too surprising given that the disparity in ionic radius ( $R$ ) is quite small (i.e.,  $R_{Zr} \sim 0.72$  Å and  $R_{Sc} \sim 0.73$  Å). On the other hand, a comparison of the creep curves for the Nd/Zr codoped specimen and the corresponding singly doped (Zr, Nd) compositions shows that the presence of both Nd and Zr results in an additive beneficial effect. This difference in behavior between the Sc/Zr and Nd/Zr systems suggests that ionic size, rather than charge, is a key parameter in understanding the effect of dopant ions in inhibiting creep in alumina. It is postulated that for segregating dopant ions with different ionic radii, more efficient packing of the ions can occur in the grain boundary region, which in turn results in enhanced inhibition of grain boundary transport processes. An exhaustive and systematic investigation of other multiply doped oxides would, of course, be desirable to validate these conclusions.

Finally, by contrast with the creep results for singly doped aluminas, for the Nd/Zr codoped compositions we find a grain size exponent  $p = 2$ , suggesting that creep is lattice diffusion controlled. One possible explanation for this is that the degree of suppression of grain boundary diffusivity achieved by 100 ppm Nd and Zr codoping is sufficiently great that lattice diffusion (rather than grain boundary diffusion) becomes the rate-controlling mechanism. Interestingly, the observed 2 to 3 orders of magnitude suppression of the creep rate is consistent with literature estimates of the relative magnitude of the diffusion coefficients.<sup>23,24</sup> If it is indeed the case that lattice diffusion is now the rate-controlling process in creep, further improvements in creep resistance will necessitate inhibition of intragranular transport processes. Work is ongoing to test this proposal.

At this point, it is perhaps pertinent to compare the results of the present study with those obtained by earlier workers. Hollenberg and Gordon<sup>25</sup> reported that trivalent ions such as  $Fe^{3+}$  ( $R_{Fe^{3+}} \sim 0.65$  Å) and  $Cr^{3+}$  ( $R_{Cr^{3+}} \sim 0.62$  Å) have little influence on the creep rate of alumina. Given that both these ions have similar ionic radii to  $Al^{3+}$ , this result is fully consistent with our contention that relative ionic size plays an important role in determining the effect on creep. Previous studies on aliovalent dopant ions, however, e.g.,  $Fe^{2+}$ ,  $Ni^{2+}$ , and  $Ti^{4+}$ , have generally been found to increase the rate of creep in alumina.<sup>25,26</sup> In the past, these observations have been rationalized on the basis of defect chemistry arguments, although other factors (such as impurity contamination and the formation of liquid phases)

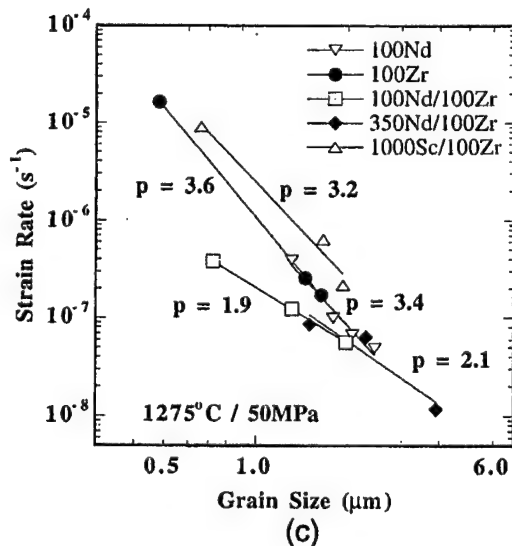
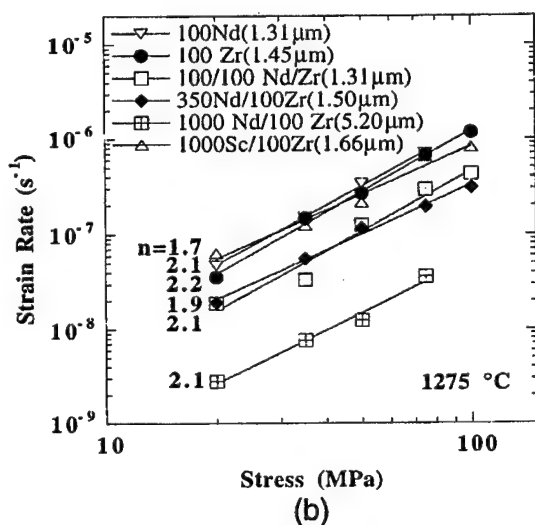
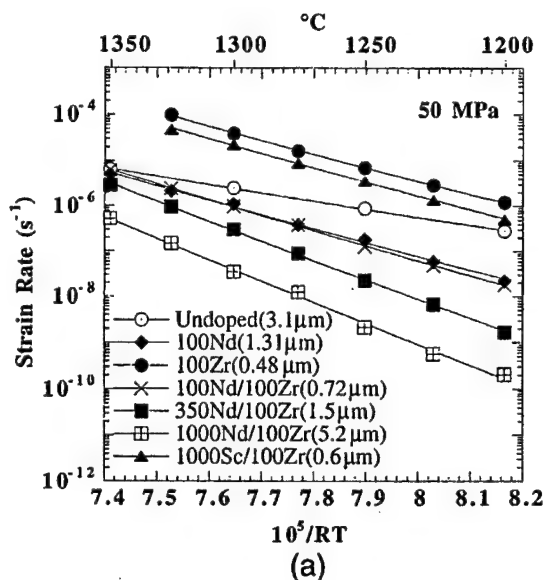


Fig. 5. (a) Strain rate as a function of temperature. (b) Strain rate as a function of stress. (c) Strain rate as a function of grain size.

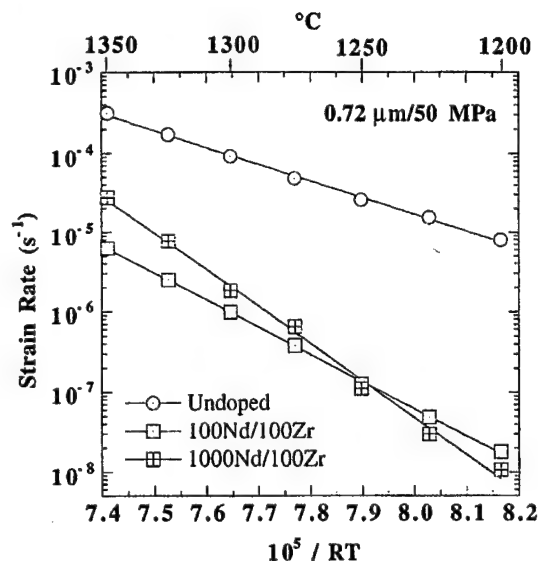


Fig. 6. Strain rate (normalized to 0.72  $\mu\text{m}$  grain size) as a function of temperature for undoped alumina, 100 ppm Nd/100 ppm Zr codoped alumina (below solubility limit), and 1000 ppm Nd/100 ppm Zr codoped alumina (above solubility limit).

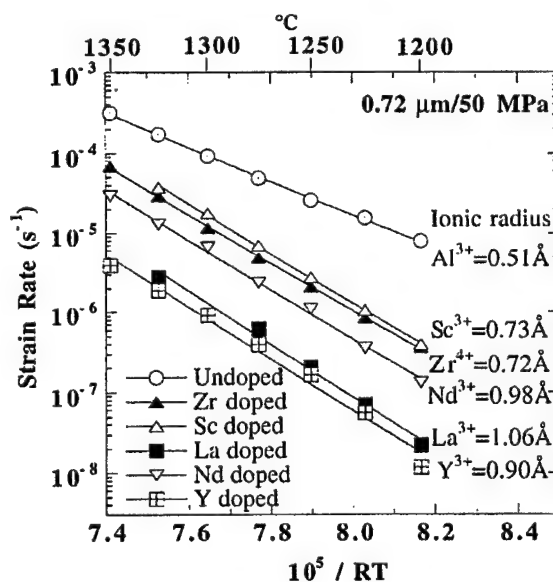


Fig. 7. Strain rate (normalized to 0.72  $\mu\text{m}$  grain size) as a function of temperature, showing the influence of dopant size on the tensile creep rate for various dopant systems.

have clouded the defect interpretations.<sup>27,28</sup> The reported deleterious effect of doping with titanium is particularly intriguing, because the  $\text{Ti}^{4+}$  and  $\text{Zr}^{4+}$  ions possess the same valency, and have comparable ionic radii. Such discrepancies highlight the need for continued careful research in this area.

#### IV. Summary

The tensile creep behavior of both singly doped (Zr, Nd) and codoped (Zr/Nd, Zr/Sc) hot-pressed fine-grained alumina ceramics has been studied in the temperature range of 1200–1350°C and the stress range of 20–100 MPa. An extensive steady-state creep regime was observed for each material. A stress exponent of approximately 2 was found for all of the



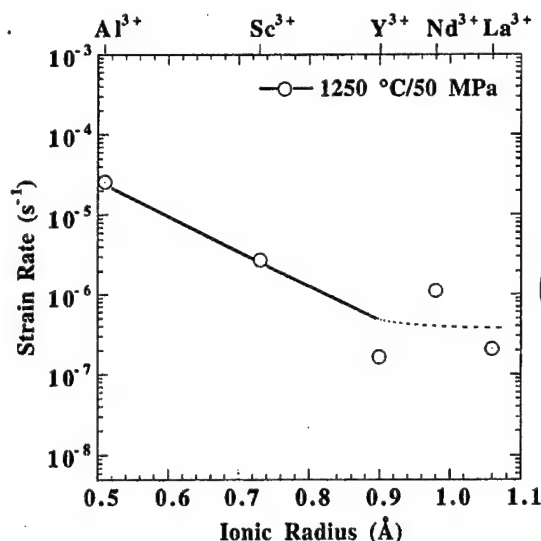


Fig. 8. Strain rate of doped alumina (normalized to 0.72  $\mu\text{m}$  grain size) as a function of isovalent dopant ionic radius.

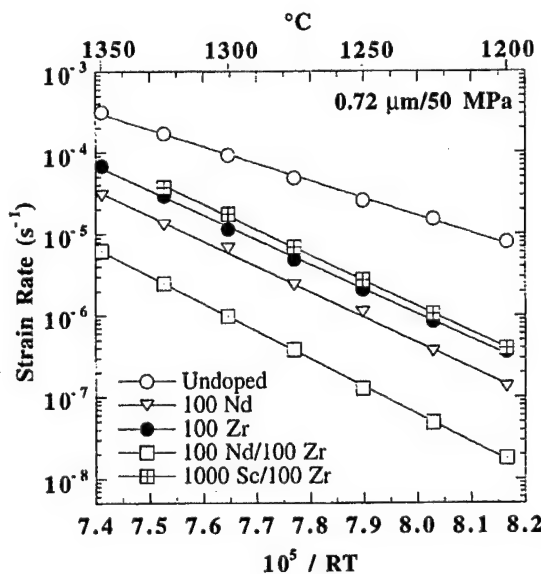


Fig. 9. Strain rate (normalized to 0.72  $\mu\text{m}$  grain size) as a function of temperature for undoped, Nd and Zr singly doped, and Nd/Zr and Sc/Zr codoped alumina.

compositions. The inverse grain size exponent was measured to be close to 3 for Zr-doped, Nd-doped, and Sc/Zr codoped alumina, and approximately 2 for the Nd/Zr codoped materials. It was found that in comparison to undoped alumina normalized to the same grain size, the creep rate of Zr-doped alumina and Sc/Zr codoped alumina was lowered by 1 order of magnitude, and that of the Nd/Zr codoped aluminas was lowered by 2 to 3 orders of magnitude. The improvement in the creep resistance of alumina by these dopant ions was shown to be a solid solution effect. For both the singly doped and codoped aluminas, direct evidence of segregation to the alumina grain boundaries by the Nd, Sc, and Zr ions was obtained by SIMS analysis. It is suggested that the segregation of the oversized dopant ions to the alumina grain boundaries reduces the grain boundary diffusivity and thus the creep rate. Further, the study shows that codoping with ions of differing size can result in improved behavior compared to the singly doped compositions. We pos-

tulate that this synergy is the result of more efficient packing of the dopant ions at the grain boundaries, further reducing the free volume available for grain boundary transport.

**Acknowledgments:** We would like to thank Drs. R. Krause and E. R. Fuller, Jr., at NIST for help with hot-pressing the 3-in. billets, and Dr. W. Luecke at NIST for providing the design specifications of the 2-in. tensile specimen and valuable discussions regarding the creep testing. We are also grateful to J. Cho for providing the original creep data of pure and 1000 ppm Y and 500 ppm La doped aluminas, and Drs. J. D. French and A. M. Thompson for helpful discussions. This work was supported by AFOSR under Grant No. F49620-94-1-0284 (monitored by Dr. A. Pechenik). At the University of Chicago, this work was supported by the MRSEC program of NSF under award No. DMR-9400379.

## References

- J. D. French, J. Zhao, M. P. Harmer, H. M. Chan, and G. A. Miller, "Creep of Duplex Microstructures," *J. Am. Ceram. Soc.*, **77**, 2857-65 (1994).
- J. Cho, M. P. Harmer, H. M. Chan, J. M. Rickman, and A. M. Thompson, "Effect of Y and La on the Tensile Creep Behavior of Aluminum Oxide," *J. Am. Ceram. Soc.*, **80**, 1013-17 (1997).
- S. Lartigue, C. Carry, and L. Priester, "Grain Boundaries in High Temperature Deformation of Yttria and Magnesia Co-doped Alumina," *J. Phys. (Paris)*, **C1**, 51, 985-90 (1990).
- A. G. Robertson, D. S. Wilkinson, and C. H. Cáceres, "Creep and Creep Fracture in Hot-Pressed Alumina," *J. Am. Ceram. Soc.*, **74**, 915-21 (1991).
- F. Wakai, T. Iga, and T. Nagano, "Effect of Dispersion of  $\text{ZrO}_2$  Particles on Creep of Fine-Grained Alumina," *J. Am. Ceram. Soc. Jpn.*, **96**, 1206-209 (1988).
- F. Wakai, T. Nagano, and T. Iga, "Hardening in Creep of Alumina by Zirconium Segregation at the Grain Boundary," *J. Am. Ceram. Soc.*, **80**, 2361-66 (1997).
- A. M. Thompson, K. K. Soni, H. M. Chan, M. P. Harmer, D. B. Williams, J. M. Chabala, and R. Levi-Setti, "Dopant Distributions in Rare-Earth-Doped Alumina," *J. Am. Ceram. Soc.*, **80**, 373-76 (1997).
- P. Gruffel and C. Carry, "Effect of Grain Size on Yttrium Grain Boundary Segregation in Fine Grained Alumina," *J. Eur. Ceram. Soc.*, **11**, 189-99 (1993).
- B. A. Pint, "Experimental Observations in Support of the Dynamic Segregation Theory to Explain the Reactive Element Effect," *Oxid. Met.*, **45**, 1-37 (1996).
- M. Le Gall, A. M. Huntz, and B. Lesage, "Self-Diffusion in  $\alpha\text{-Al}_2\text{O}_3$  and Growth Rate of Alumina Scales Formed by Oxidation: Effect of  $\text{Y}_2\text{O}_3$  Doping," *J. Mater. Sci.*, **30**, 201-11 (1995).
- S. Lartigue-Korinek, C. Carry, F. Dupau, and L. Priester, "Transmission Electron Microscopy Analysis of Grain Boundary Behavior in Superplastic Doped Aluminas," *Mater. Sci. Forum*, **170-172**, 409-14 (1994).
- J. Bruley, J. Cho, J. C. Fang, A. M. Thompson, Y.-Z. Li, H. M. Chan, J. M. Rickman, and M. P. Harmer, "STEM Analysis of Grain Boundaries of Creep Resistant Y and La Doped Alumina," unpublished work.
- E. Arzt, M. F. Ashby, and R. A. Verrall, "Interface Controlled Diffusional Creep," *Acta Metall.*, **31**, 1977-89 (1983).
- J. M. Chabala, K. K. Soni, K. L. Gavrilov, and R. Levi-Setti, "High Resolution Chemical Imaging with Scanning Probe SIMS," *Int. J. Mass. Spectrom. Ion Processes*, **143**, 191-212 (1995).
- J. D. French and S. M. Wiederhorn, "Tensile Specimens from Ceramic Components," *J. Am. Ceram. Soc.*, **79**, 550-52 (1996).
- W. D. Kingery, H. K. Bowen, and D. R. Uhlmann, *Introduction to Ceramics*, 2nd ed., p. 745. Wiley, New York, 1976.
- E. Sato and C. Carry, "Yttria Doping and Sintering of Submicrometer-Grained  $\alpha\text{-Alumina}$ ," *J. Am. Ceram. Soc.*, **79**, 2156-60 (1996).
- J. Fang, A. M. Thompson, M. P. Harmer, and H. M. Chan, "Effect of Y and La on the Final-Stage Sintering Behavior of Ultra-High-Purity  $\text{Al}_2\text{O}_3$ ," *J. Am. Ceram. Soc.*, **80**, 2005-12 (1997).
- S. Lartigue and L. Priester, "Influence of Doping Elements on the Grain Boundary Characteristics in Alumina," *J. Phys. Colloq. (C5)*, **49**, 451-56 (1988).
- S. Lartigue, L. Priester, F. Dupau, P. Gruffel, and C. Carry, "Dislocation Activity and Differences Between Tensile and Compressive Creep of Yttria Doped Alumina," *Mater. Sci. Eng.*, **A164**, 211-15 (1993).
- S. Lartigue-Korinek, C. Carry, F. Dupau, and L. Priester, "Transmission Electron Microscopy Analysis of Grain Boundary Behavior in Superplastic Doped Aluminas," *Mater. Sci. Forum*, **170-172**, 409-14 (1994).
- J. Cho, H. M. Chan, M. P. Harmer, and J. M. Rickman, "Influence of Yttrium Doping on Grain Misorientation in Aluminum Oxide," *J. Am. Ceram. Soc.*, **81** [11] 3001-3004 (1998).
- A. H. Chokshi and T. G. Langdon, "Diffusion Creep in Ceramics: A Comparison with Metals," *Defect Diffus. Forum*, **66-69**, 1205-26 (1989).
- R. M. Cannon and R. L. Coble, "Review of Diffusional Creep of  $\text{Al}_2\text{O}_3$ ," in *Deformation of Ceramic Materials*. Edited by R. C. Bradt and R. E. Tressler. Plenum Press, New York, 1975.
- G. W. Hollenberg and R. S. Gordon, "Effect of Oxygen Partial Pressure on the Creep of Polycrystalline  $\text{Al}_2\text{O}_3$  Doped with Cr, Fe, or Ti," *J. Am. Ceram. Soc.*, **56**, 140-47 (1973).
- P. A. Lessing and R. S. Gordon, "Creep of Polycrystalline Alumina, Pure and Doped with Transition Metal Impurities," *J. Mater. Sci.*, **12**, 2291-302 (1977).
- J. E. Blendell and C. A. Handwerker, "Effect of Chemical Composition on Sintering of Ceramics," *J. Cryst. Growth*, **75**, 138 (1986).
- P. E. D. Morgan and M. A. Kousoutsis, "Phase Studies Concerning Sintering in Aluminas Doped with  $\text{Ti}^{4+}$ ," *J. Am. Ceram. Soc.*, **68**, C-156-C-158 (1985).

# Influence of Yttrium Doping on Grain Misorientation in Aluminum Oxide

Junghyun Cho,\* Helen M. Chan,\* Martin P. Harmer,\* and J. M. Rickman\*

Department of Materials Science and Engineering and Materials Research Center, Lehigh University, Bethlehem, Pennsylvania 18015

Oversized dopant ions such as yttrium and lanthanum segregate to grain boundaries and reduce the tensile creep rate of  $\alpha$ - $\text{Al}_2\text{O}_3$  by 2–3 orders of magnitude. One explanation for this behavior is that the oversized segregants give rise to a “site-blocking” effect for grain boundary diffusion. It has also been speculated that the dopant ions modify the grain boundary structure in alumina and reduce the creep rate by promoting the formation of special (e.g., coincidence site lattice (CSL)) grain boundaries. In order to test the latter hypothesis, we have used electron backscattered Kikuchi diffraction to characterize the misorientation and special grain boundary distribution for undoped and 1000-ppm-yttrium-doped alumina. The results show that the grain boundary structure in alumina (as characterized by the frequency of selected CSLs and misorientation distribution) was not significantly changed by the addition of yttrium, indicating that creep retardation results mainly from site-blocking.

## I. Introduction

IT HAS been reported that the tensile creep rate of  $\alpha$ - $\text{Al}_2\text{O}_3$  can be dramatically reduced by the addition of 1000 ppm  $\text{Y}_2\text{O}_3$ .<sup>1,2</sup> This was a surprising result since most previous studies of isovalent dopants such as  $\text{Cr}^{3+}$  and  $\text{Fe}^{3+}$  (whose ionic radii are similar to  $\text{Al}^{3+}$ ) have revealed no improvement in the creep properties.<sup>3,4</sup> In addition, it is well known that yttrium (Y) doping reduces the growth rate of polycrystalline alumina scales formed by oxidation.<sup>5,6</sup> Segregation of Y to grain boundaries in  $\alpha$ - $\text{Al}_2\text{O}_3$ , which arises from a large size (radius) mismatch between  $\text{Al}^{3+}$  (0.51 Å) and  $\text{Y}^{3+}$  (0.89 Å), has been clearly demonstrated in many studies.<sup>7–10</sup> It was suggested by Cho *et al.*, therefore, that the observed reduction in creep rate was the result of a “site-blocking” effect of oversized segregant ions on grain boundary diffusion.<sup>2</sup> This hypothesis is consistent with recent studies on the self-diffusivity in  $\alpha$ - $\text{Al}_2\text{O}_3$  which have shown that Y-doping decreases oxygen diffusivity at grain boundaries, with little effect on bulk diffusion.<sup>11–15</sup> Furthermore, Fang *et al.* observed that the densification rate of alumina was significantly reduced by the presence of Y, and the data were consistent with a grain boundary diffusion-controlled mechanism.<sup>16</sup>

An alternative school of thought to the “site-blocking” model is that the presence of the dopant ions modifies the grain boundary structure. The argument is that certain types of “special” boundaries are favored, which play a limiting role in

the transmission of grain boundary sliding due to the difficulty in accommodating lattice dislocations.<sup>17,18</sup> In fact, there is evidence that special grain boundaries in metals can decrease the grain boundary diffusivity and deformation rate;<sup>19–21</sup> however, there is little direct evidence of such effects in ceramics. Using transmission electron microscopy (TEM), Lartigue *et al.* reported that magnesium (Mg) doping increased the proportion of special (coincidence site lattice (CSL) and coincidence axis direction (CAD)) grain boundaries in alumina.<sup>22</sup> Further, the role of Y on the grain boundary structure was investigated in Mg and Y codoped alumina, where it was speculated that the proportion of near-coincidence grain boundaries increased after creep deformation,<sup>23</sup> consistent with the observations in metallic systems.<sup>17</sup> Thus, an alternative role of Y is that it increases the proportion of special grain boundaries in alumina.

The aim of this study was to test this postulate by obtaining grain misorientation information for both undoped and Y-doped alumina utilizing electron backscattered Kikuchi diffraction (EBKD) in the scanning electron microscope (SEM).<sup>24,25</sup> This technique has several advantages over the TEM; most importantly, it can characterize a large number of grains in a single scan, and in addition specimen preparation is relatively easy.

## II. Experimental Procedure

Undoped (designated “Pure A”) and Y-doped alumina (designated “YA-UN”) used in this study were prepared from commercial powders of  $\alpha$ - $\text{Al}_2\text{O}_3$  (AKP-HP and AKP-53, respectively; Sumitomo Chemical America, New York, NY).<sup>1,26</sup> The powder was mixed with a suitable proportion of yttrium nitrate solution to achieve dopant levels of 1000 ppm (Y/Al ion). Fully dense materials were obtained by hot-pressing under vacuum at 50 MPa; the conditions were 30 min at 1475°C and 15 min at 1400°C for the Y-doped and undoped alumina, respectively. The resultant grain size was around 2–3  $\mu\text{m}$  for both materials. A specimen of the Y-doped alumina was creep-ruptured at 1300°C under a tensile stress of 50 MPa in air with a final strain of ~5.5% (designated “YA-DEF”).

For the investigation of grain misorientation, the surfaces of bulk specimens were polished down to a 1  $\mu\text{m}$  finish with diamond slurry, followed by polishing with 0.02  $\mu\text{m}$  colloidal  $\text{SiO}_2$  in the vibratory polisher (Vibromet II, Buehler, Lake Bluff, IL). In order to avoid charging, a thin carbon layer (<5 nm) was deposited on the polished surface. The (Kikuchi) diffraction patterns were obtained in the SEM (Camscan Series II) at an accelerating voltage of 25 kV and a working distance of 33 mm. The backscattered Kikuchi patterns were captured using a silicon intensified target (SIT) camera (Customs Camera 27, Somerset, UK) and its live image was improved by subtracting background noises through an image processor (Hamamatsu Argus 10). Subsequent analysis of the EBKD patterns was carried out with the aid of computer software (TSL, Inc., Draper, UT). The total number of grains analyzed

C. A. Handwerker—contributing editor

Manuscript No. 190583. Received November 10, 1997; approved July 28, 1998.  
Supported by the U.S. Air Force Office of Scientific Research under Contract No. F49620-94-1-0284 (monitored by Dr. A. Pechenik).  
\*Member, American Ceramic Society.

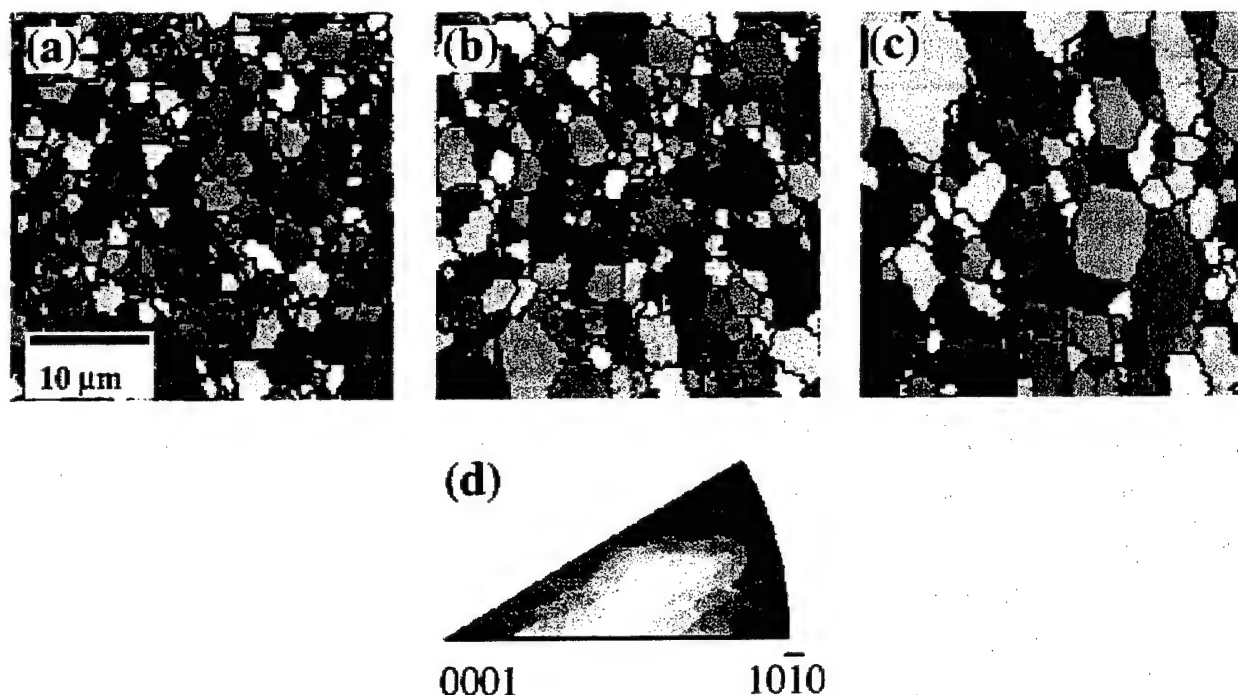


Fig. 1. Orientation image maps (OIM) for (a) pure alumina, (b) undeformed Y-doped alumina, (c) deformed Y-doped alumina, and (d) stereographic triangle. Color-shading in OIMs corresponds to those of the stereographic triangle, and represents the orientation normal to the specimen surface.

in this study was approximately 1400, 1000, and 800 for the Pure A, YA-UN, and YA-DEF samples, respectively.

### III. Results and Discussion

Figure 1 shows the orientation image maps (OIM) for pure, undeformed Y-doped, and deformed Y-doped alumina; the grains are color coded, where each color represents an orientation normal to the specimen surface, as shown in the stereographic triangle. All the OIMs have the same magnification. It is apparent from the OIMs that none of the specimens exhibit a very pronounced texture. This inference was confirmed by pole figures generated from the EBKD data, which revealed that although the degree of preferred orientation was weak for all three specimens, the YA-DEF specimen showed (relatively) the strongest texture. A detailed study on the influence of creep

deformation on the texture is the subject of ongoing work, and will be reported separately. It should be noted that the stereographic projection (and the calculated misorientation angles) was determined assuming hexagonal (rather than rhombohedral) symmetry. This approximation, which has been adopted in other studies,<sup>22,27-29</sup> is considered to be acceptable, given that we are mainly interested in the comparison between undeformed and Y-doped alumina.

The distribution of grain boundary misorientation is shown in Fig. 2; it can be seen that Y doping does not have a significant influence on the frequency of occurrence of these boundaries. The only slight difference between the misorientation distributions is the higher proportion of low-angle (<5°) boundaries in the YA-UN sample. These low-angle boundaries constitute less than 4% of the total number of boundaries sampled.

In addition, OIMs revealed a bimodal grain structure and

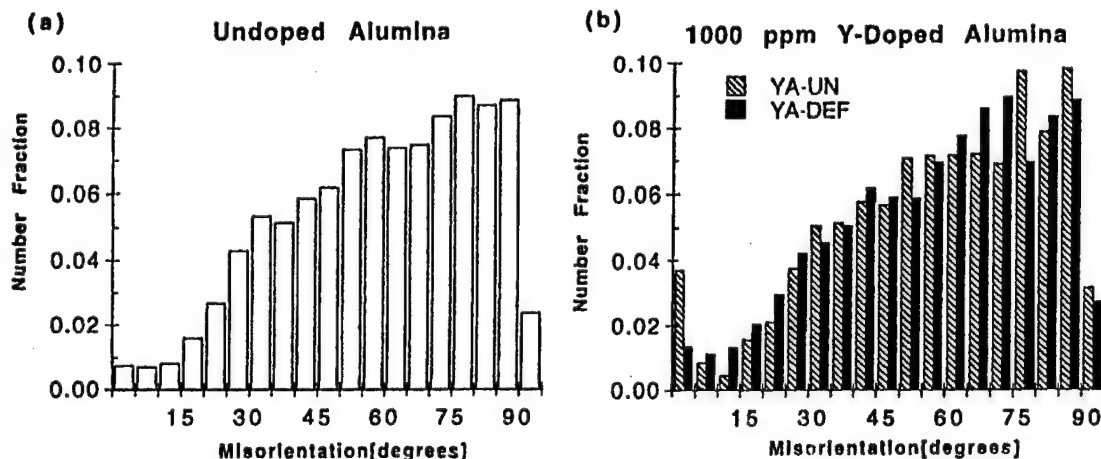


Fig. 2. Misorientation angle histograms for (a) pure alumina and (b) Y-doped alumina.

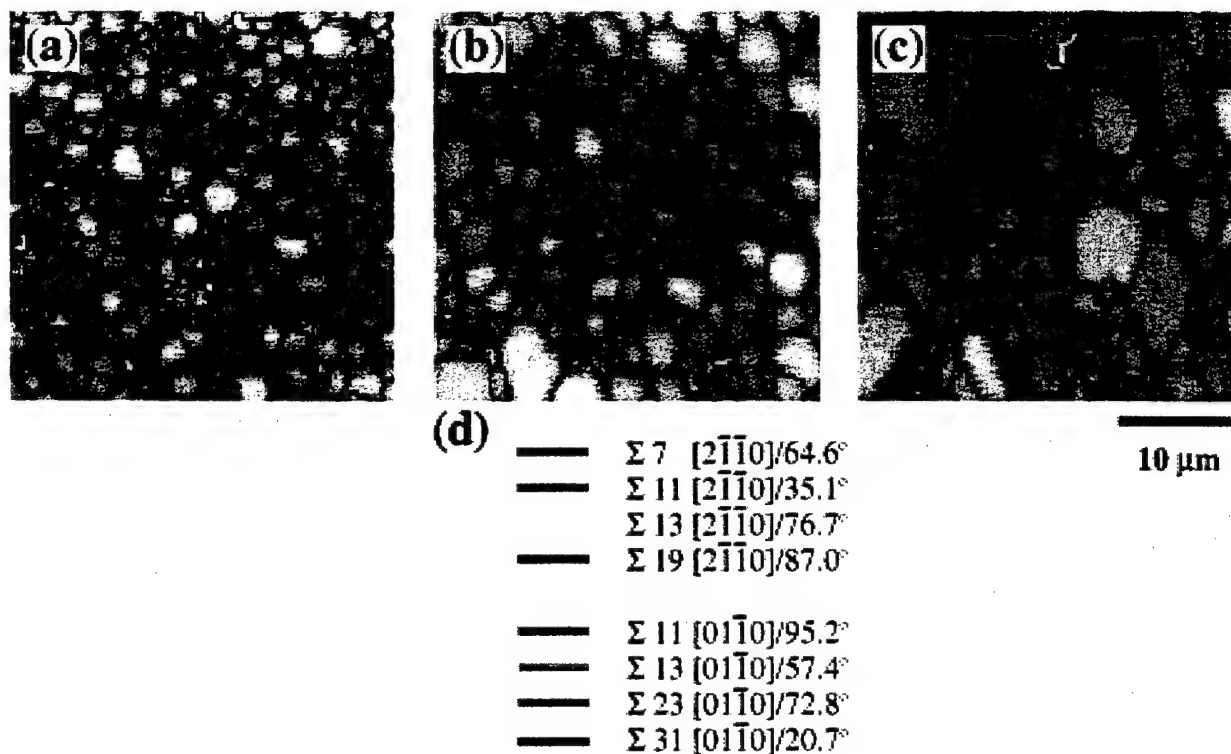


Fig. 3. Orientation images showing grain boundary shading by CSL criterion for the same area as in Fig. 1. The types and angles of CSLs for each color are tabulated in (d): (a) pure alumina; (b) undeformed Y-doped alumina; (c) deformed Y-doped alumina.

several YAG ( $\text{Y}_3\text{Al}_5\text{O}_{12}$ ) precipitates (nonuniformly distributed) in Y-doped alumina. This structure became more nonuniform after creep deformation, possibly because the precipitates may have pinned grain boundaries in those regions of higher precipitate concentration. The origin of this abnormal grain growth is under investigation. Unlike the undeformed structure, some areas in the deformed Y-doped system clearly showed much distorted (elongated) grain shapes due to uniaxial tensile loading, as shown in Fig. 1(c).

CSL boundaries, characterized by the reciprocal of the proportion of common lattice sites, were systematically examined to test the effect (if any) of yttrium on grain boundary structure. In this case, the permissible angular deviation,  $\theta$ , from the exact coincidence was determined using Brandon's criterion:

$$\theta = \theta_0 / \sqrt{\Sigma} \quad (1)$$

where  $\theta_0$  is a constant ( $\approx 15^\circ$ ) and  $\Sigma$  a multiplicity.<sup>30</sup> Note that in hexagonal symmetry, a change in axial ratio,  $c/a$  can be accommodated by both a deviation in misorientation and a dislocation array. In the present studies, the influence of

temperature on the  $c/a$  ratio was neglected.<sup>31</sup> Selected CSLs for rotation axes of  $[2\bar{1}\bar{1}0]$  and  $[0\bar{1}\bar{1}0]$  along with misorientation angles<sup>27</sup> were identified by color-shading grain boundaries in the OIMs. In the case of all specimens (Fig. 3), the proportion of special boundaries was low, and their concentration did not vary much between specimens. In general, the observed special boundaries tended to occur in the smaller grains. For clarification, several special boundaries selected from among those in Fig. 3 are tabulated in Table I, where deformed Y-doped alumina contains about 200 grains and undoped and (undeformed) Y-doped alumina contains 300–400 grains. Again, both Y-doping and creep deformation did not result in any significant increase of CSL boundaries compared to undoped alumina.

In addition, we checked CSLs for a rotation axis of  $[0001]$  and found similar results. The above results were also supported by independent work by another group on the same Y-doped samples. These workers used TEM to characterize more than 100 grain boundaries, and found very few special boundaries.<sup>32</sup> It would seem, therefore, that the proportion of special boundaries in Y-doped alumina is not as high as that reported in Mg-doped alumina ( $\sim 30\%$  CSLs).<sup>22</sup> The similarity

Table I. The Number of Special Boundaries in Fig. 3 ( $30 \times 30 \mu\text{m}^2$ ) along with Misorientation Angles and Axes for Three Specimens

	$\Sigma 7$ 64.6° [2 $\bar{1}\bar{1}0$ ]	$\Sigma 11$ 35.1° [2 $\bar{1}\bar{1}0$ ]	$\Sigma 13$ 76.7° [2 $\bar{1}\bar{1}0$ ]	$\Sigma 19$ 87.0° [2 $\bar{1}\bar{1}0$ ]	$\Sigma 11$ 95.2° [0 $\bar{1}\bar{1}0$ ]	$\Sigma 13$ 57.4° [0 $\bar{1}\bar{1}0$ ]	$\Sigma 23$ 72.8° [0 $\bar{1}\bar{1}0$ ]	$\Sigma 31$ 20.7° [0 $\bar{1}\bar{1}0$ ]
Pure A ( $\approx 400$ grains) <sup>†</sup>	9	8	11	3	12	0	1	1
YA-UN ( $\approx 300$ grains) <sup>‡</sup>	9	6	6	4	14	1	3	2
YA-DEF ( $\approx 200$ grains) <sup>§</sup>	9	3	5	3	8	2	0	1

<sup>†</sup>Undoped alumina. <sup>‡</sup>Undeformed Y-doped alumina. <sup>§</sup>Deformed Y-doped alumina.

in our findings for the YA-UN and YA-DEF samples contrasts with the work of Kokawa *et al.*<sup>17</sup> and Korinek and Dupau,<sup>23</sup> who speculated that creep deformation results in an increase in the proportion of special boundaries.

Despite its several advantages, the EBKD technique has some limitations. In the present study, the CSL information is based solely upon misorientation angle and axis, and the boundary plane is not taken into account. In addition, special boundaries consisting of dislocation networks that do not exhibit CSL orientations are not accessible using this technique.

This study represents the first in which EBKD/OIM has been used to determine the effect of an isovalent dopant ion on the grain boundary structure of alumina. As mentioned above, although the possibility of more subtle structural differences cannot be entirely ruled out, it is believed that given the large number of grains sampled, the study shows convincingly that there is no significant difference in the overall grain boundary structure in undoped alumina and Y-doped alumina (before and after creep testing). Furthermore, since the average grain sizes in the undoped and Y-doped (as hot-pressed) samples were similar, possible complications with regard to the evolution of grain boundary orientation distribution with grain growth are circumvented. The present results support the hypothesis that the improvement in creep behavior results primarily from a lowering of grain boundary diffusion due to site-blocking by the dopant ions, as opposed to induced differences in grain boundary structure. Research utilizing the EBKD technique to study the influence on grain misorientation of other dopants which have also been shown to improve creep ( $\text{La}^{3+}$ ,  $\text{Nd}^{3+}$ )<sup>2,33</sup> is ongoing.

#### IV. Summary

In an effort to explain the basic mechanism for creep rate reduction in rare-earth-doped alumina, we have used the EBKD technique to study (a) differences in grain misorientation and (b) frequency of selected CSL boundaries between undoped and Y-doped  $\text{Al}_2\text{O}_3$ . It was found that in both cases, the addition of yttrium produced no significant effect for the subset of boundaries examined. Furthermore, the creep deformation process did not produce an increased proportion of special grain boundaries (CSLs) in Y-doped alumina. These results therefore favor the hypothesis that the beneficial influence of Y-doping is not primarily through its effect on the grain boundary structure, though a more exhaustive characterization study is clearly warranted. Instead, we argue that it most likely reduces the creep rate by blocking grain boundary diffusion.

**Acknowledgments:** We would like to thank Dr. Arthur H. Heuer for valuable discussions regarding this work. The efforts of Gary S. Thompson are gratefully acknowledged for processing the pure alumina specimen. We are also indebted to Dr. David P. Field and Matthew M. Nowell (TSL, Inc., Draper, UT) for their help with the orientation image microscopy.

#### References

- J. D. French, J. Zhao, M. P. Harmer, H. M. Chan, and G. A. Miller, "Creep of Duplex Microstructures," *J. Am. Ceram. Soc.*, **77** [11] 2857-65 (1994).
- J. Cho, M. P. Harmer, H. M. Chan, J. M. Rickman, and A. M. Thompson, "Effect of Yttrium and Lanthanum on the Tensile Creep Behavior of Aluminum Oxide," *J. Am. Ceram. Soc.*, **80** [4] 1013-17 (1997).
- P. A. Lessing and R. S. Gordon, "Creep of Polycrystalline Alumina, Pure and Doped with Transition Metal Impurities," *J. Mater. Sci.*, **12**, 2291-302 (1977).
- G. W. Hollenberg and R. S. Gordon, "Effect of Oxygen Partial Pressure on the Creep of Polycrystalline  $\text{Al}_2\text{O}_3$  Doped with Cr, Fe, or Ti," *J. Am. Ceram. Soc.*, **56** [3] 140-47 (1973).
- K. Przybylski and G. J. Yurek, "Segregation of Y to Grain Boundaries in  $\text{Cr}_2\text{O}_3$  and  $\text{Al}_2\text{O}_3$  Scales," *J. Electrochem. Soc.*, **134** [8B] C469 (1987).
- A. M. Huntz, "Influence of Active Elements on the Oxidation Mechanism of M-Cr-Al Alloys," *Mater. Sci. Eng.*, **87**, 251-60 (1987).
- C.-W. Li and W. D. Kingery, "Solute Segregation at Grain Boundaries in Polycrystalline  $\text{Al}_2\text{O}_3$ ," pp. 368-78 in *Advances in Ceramics*, Vol. 10, *Structure and Properties of  $\text{MgO}$  and  $\text{Al}_2\text{O}_3$  Ceramics*. Edited by W. D. Kingery. American Ceramic Society, Columbus, OH, 1984.
- M. K. Loudjani, A. M. Huntz, and R. Cortes, "Influence of Yttrium on Microstructure and Point Defects in  $\alpha\text{-Al}_2\text{O}_3$  in Relation to Oxidation," *J. Mater. Sci.*, **28**, 6466-73 (1993).
- A. M. Thompson, K. K. Soni, H. M. Chan, M. P. Harmer, D. B. Williams, J. M. Chabala, and R. Levi-Setti, "Rare Earth Dopant Distributions in Creep-Resistant  $\text{Al}_2\text{O}_3$ ," *J. Am. Ceram. Soc.*, **80** [2] 373-76 (1997).
- J. Bruley, J. Cho, J. C. Fang, A. M. Thompson, Y. Z. Li, H. M. Chan, and M. P. Harmer, "STEM Analysis of Grain Boundaries of Creep Resistant Y and La Doped Alumina," unpublished work.
- M. Le Gall, A. M. Huntz, B. Lesage, C. Monty, and J. Bernardini, "Self-diffusion in  $\alpha\text{-Al}_2\text{O}_3$  and Growth Rate of Alumina Scales formed by Oxidation: Effect of  $\text{Y}_2\text{O}_3$  Doping," *J. Mater. Sci.*, **30**, 201-11 (1995).
- M. Le Gall, B. Lesage, and J. Bernardini, "Self-diffusion in  $\alpha\text{-Al}_2\text{O}_3$ . I. Aluminum Diffusion in Single Crystals," *Philos. Mag. A*, **70** [5] 761-73 (1996).
- D. Prot and C. Monty, "Self-diffusion in  $\alpha\text{-Al}_2\text{O}_3$ . II. Oxygen Diffusion in 'Undoped' Single Crystals," *Philos. Mag. A*, **73** [4] 899-917 (1996).
- M. Le Gall, A. M. Huntz, B. Lesage, and C. Monty, "Self-diffusion in  $\alpha\text{-Al}_2\text{O}_3$ . III. Oxygen Diffusion in Single Crystals Doped with  $\text{Y}_2\text{O}_3$ ," *Philos. Mag. A*, **73** [4] 919-34 (1996).
- D. Prot, M. Le Gall, B. Lesage, A. M. Huntz, and C. Monty, "Self-diffusion in  $\alpha\text{-Al}_2\text{O}_3$ . IV. Oxygen Grain-Boundary Self-diffusion in Undoped and Yttria-Doped Alumina Polycrystals," *Philos. Mag. A*, **73** [4] 935-49 (1996).
- J. Fang, A. M. Thompson, M. P. Harmer, and H. M. Chan, "Effect of Y and La on the Sintering Behavior of Ultrahigh-Purity  $\text{Al}_2\text{O}_3$ ," *J. Am. Ceram. Soc.*, **80** [8] 2005-12 (1997).
- H. Kokawa, T. Watanabe, and S. Karashima, "Sliding Behavior and Dislocation Structures in Aluminum Grain Boundaries," *Philos. Mag. A*, **44** [6] 1239-54 (1981).
- S. Lartigue and L. Priester, "Grain Boundaries in Fine-Grained Magnesium-Doped Aluminas," *J. Am. Ceram. Soc.*, **71** [6] 430-37 (1988).
- J. W. Wyrzykowski and M. W. Grabski, "The Hall-Petch Relation in Aluminum and Its Dependence on the Grain Boundary Structure," *Philos. Mag. A*, **53** [4] 505-20 (1986).
- Z. Pakielna, M. Krasnowski, and J. W. Wyrzykowski, "Changes in Distributions of Grain Boundary Diffusion Properties after Grain Growth in Austenitic Steel," *Mater. Sci. Eng. A*, **112**, 199-204 (1989).
- A. Garbacz and J. W. Wyrzykowski, "Correlation between Diffusivity of Grain Boundaries and Distribution of Coincidence Site Lattice Boundaries in Polycrystals," *Mater. Sci. Eng. A*, **172**, 137-44 (1993).
- S. Lartigue and L. Priester, "Influence of Doping Elements on the Grain Boundary Characteristics in Alumina," *J. Phys. (Paris)*, **C5-49**, 451-56 (1988).
- S. L. Korinek and F. Dupau, "Grain Boundary Behavior in Superplastic Mg-Doped Alumina with Yttria Codoping," *Acta Metall. Mater.*, **42** [1] 293-302 (1994).
- D. J. Dingley and V. Randle, "Review Microstructure Determination by Electron Back-scatter Diffraction," *J. Mater. Sci.*, **27**, 4545-66 (1992).
- S. J. Wright and B. L. Adams, "Automatic Analysis of Electron Backscatter Diffraction Patterns," *Metall. Trans. A*, **23**, 759-67 (1992).
- G. S. Thompson, unpublished work.
- F.-R. Chen, C.-C. Chu, J.-Y. Wang, and L. Chang, "Atomic Structure of  $\Sigma 7(01\bar{1}2)$  Symmetrical Tilt Grain Boundaries in  $\alpha\text{-Al}_2\text{O}_3$ ," *Philos. Mag. A*, **72** [3] 529-44 (1995).
- S. Lartigue and L. Priester, "Grain Boundaries in Polycrystalline Alumina," *J. Phys. (Paris)*, **C4-46**, 101-106 (1985).
- H. Grimmer and D. H. Warrington, "Coincidence Orientations of Grains in Hexagonal Materials," *J. Phys. (Paris)*, **C4-46**, 231-36 (1985).
- D. G. Brandon, "The Structure of High-Angle Grain Boundaries," *Acta Metall.*, **14**, 1479-84 (1966).
- K. Shin and A. H. King, "Grain-Boundary Structure and Behavior in Zinc," pp. 25-41 in *Structure and Property Relationships for Interfaces*. Edited by J. L. Walter, A. H. King, and K. Tangri. ASM International, Materials Park, OH, 1991.
- M. A. Gülgün, private communication.
- M. P. Harmer, H. M. Chan, J. M. Rickman, J. Cho, and C. M. Wang, "Grain Boundary Chemistry and Creep Resistance of Oxide Ceramics," pp. 139-44 in *The Science of Engineering Ceramics II, Proceedings of the 2nd International Symposium on the Science of Engineering Ceramics* (Osaka, Japan, September 1998). Edited by K. Niihara, T. Sekino, E. Yasuda, and T. Sasa. The Ceramic Society of Japan, 1998. □



# Influence of Dopant Concentration on Creep Properties of Nd<sub>2</sub>O<sub>3</sub>-Doped Alumina

Chong-Min Wang,\* Junghyun Cho,\* Helen M. Chan,\* Martin P. Harmer,\* and Jeffrey M. Rickman

Materials Research Center, Lehigh University, Bethlehem, Pennsylvania 18015

The microstructural features and tensile creep behavior of Al<sub>2</sub>O<sub>3</sub> doped with Nd<sub>2</sub>O<sub>3</sub> at levels ranging from 100 to 1000 ppm (Nd:Al atomic ratio) were systematically investigated. Compositional mapping, using both high-resolution scanning transmission electron microscopy and secondary ion mass spectroscopy revealed that, for all of the compositions studied, the Nd<sup>3+</sup> ions were strongly segregated to the Al<sub>2</sub>O<sub>3</sub> grain boundaries. Microstructural observations revealed that the solubility of Nd<sub>2</sub>O<sub>3</sub> was between 100 and 350 ppm. Tensile creep tests were conducted over a range of temperatures (1200°–1350°C) and stresses (20–75 MPa). Both the stress and grain-size exponents were analyzed. In selected experiments, controlled grain-growth anneals were used to enable creep testing of samples of the same average grain size but different neodymium concentrations. Independent of dopant level, the neodymium additions decreased the creep rate by 2–3 orders of magnitude, compared with that of undoped Al<sub>2</sub>O<sub>3</sub>. The value of the apparent creep activation energy increased with increased dopant concentration and then saturated at dopant levels exceeding the solubility limit. Overall, the results of the present study were consistent with a creep-inhibition mechanism whereby oversized segregant ions reduce grain-boundary diffusivity by a site-blocking mechanism.

## I. Introduction

In recent years, a series of studies has established the beneficial role of rare-earth-dopant ions on the creep behavior of Al<sub>2</sub>O<sub>3</sub>.<sup>1–7</sup> Thus, work by Lartigue *et al.*<sup>1</sup> and Robertson *et al.*<sup>8</sup> showed reductions in the creep rate of MgO-doped Al<sub>2</sub>O<sub>3</sub>, with the addition of yttrium, by factors of 5 and 15, respectively. The study of Cho *et al.*<sup>4</sup> demonstrated a more dramatic effect, whereby doping with yttrium or lanthanum improved the steady-state strain rate by 2–3 orders of magnitude (versus that of undoped Al<sub>2</sub>O<sub>3</sub>). In related work, Wakai *et al.*<sup>9,10</sup> observed that the addition of zirconium to Al<sub>2</sub>O<sub>3</sub> (at levels both above and below the solubility limit) reduced the creep rate by a factor of 15.

More recently, Li *et al.*<sup>7</sup> reported the additional benefit that can derive from codoping with ions of disparate sizes. These workers showed that the enhancement in creep resistance for Nd/Zr codoped Al<sub>2</sub>O<sub>3</sub> was greater than that achieved by doping with either neodymium or zirconium alone. The study of Li *et al.* also highlighted the influence of ionic size on the creep rate; thus, doping with Sc<sup>3+</sup> (0.74 Å) or Zr<sup>4+</sup> (0.72 Å), although still beneficial, was markedly less effective than doping with either La<sup>3+</sup> (1.03 Å) or Y<sup>3+</sup> (0.90 Å). Although previous work has

suggested that the creep inhibition is primarily a solid-solution effect,<sup>7,11</sup> the influence of dopant concentration on creep behavior has not been systematically studied. Therefore, the objective of the present study was to address this issue, with regard to neodymium doping. In particular, it was hoped that any changes in behavior for the different solute levels would lend further insight to the creep mechanism.

## II. Experimental Procedure

### (1) Sample Preparation

The starting materials were ultra-pure α-Al<sub>2</sub>O<sub>3</sub> powder (AKP-53, 99.995%, mean particle size 0.35 μm and specific surface area 12.7 m<sup>2</sup>/g, Sumitomo Chemical America, Inc., New York, NY) and semiconductor-grade neodymium nitrate. Al<sub>2</sub>O<sub>3</sub> samples with the following nominal Nd<sub>2</sub>O<sub>3</sub> dopant levels were prepared: 100, 350, and 1000 ppm (Nd:Al atomic ratio). Details of the powder-processing and doping procedures are described elsewhere.<sup>4,7</sup> Dense billets (>99.5%) were obtained by hot-pressing the samples in a graphite die 76.2 μm in diameter, at 50 MPa for 30 min, in vacuum. The hot-pressing temperatures (which were tailored to achieve microstructures with comparable average grain sizes for the different compositions) were as follows: pure Al<sub>2</sub>O<sub>3</sub>, 1350°C; 100 ppm Al<sub>2</sub>O<sub>3</sub>, 1425°C; 350 and 1000 ppm neodymium, 1450°C.

### (2) Creep Testing

Dog-bone-shaped tensile samples were machined from the hot-pressed billets, according to specifications described by French and Wiederhorn.<sup>12</sup> The sample gauge lengths were defined by two SiC flags attached to each sample and measured, using a laser extensometer (Beta LaserMike, Inc., Dayton, OH), to an accuracy of 1 μm. For each sample, possible flag slippage was monitored by measuring the projected flag thickness both before and after the creep test. If the change in projected flag thickness was >20 μm, the creep data were disregarded.

Previous work<sup>4</sup> showed that preannealing the creep samples under a slight load (5 MPa) significantly decreased the extent of primary creep. The microstructure was examined both before and after the preannealing treatment, and no change in grain size was detected. Therefore, before creep testing, all of the present samples were annealed at 1250°C for 24 h, under an applied stress of 5 MPa. Tensile creep tests were performed in air, whereby the sample was subjected to a constant load, using either a lever arm or a hydraulic testing machine (Applied Test Systems, Butler, PA). Testing was conducted in the temperature range 1200°–1350°C, with applied stresses ranging from 20 to 75 MPa. Three types of creep tests were performed: (i) a standard stress-rupture test, at 1275°C and 50 MPa; (ii) a temperature-step test, in which the stress was nominally kept constant, but the temperature was altered periodically; and (iii) a stress-step test, in which the temperature was held constant, but the stress was varied. The latter two types of tests enabled the measurement of the strain rate, under a given set of test conditions, two to three times per sample. For the range of stress and temperatures studied, no dependence of the steady-state strain rate on strain history was observed.

R. Raj—contributing editor

Manuscript No. 188999. Received October 22, 1999; approved October 12, 2000. Supported by the U.S. Air Force Office of Scientific Research, under Grant No. F49620-98-1-0117.

\*Member, American Ceramic Society.

The values of the stress exponent ( $n$ ) and inverse grain-size exponent ( $p$ ), as defined by the following constitutive equation, were also evaluated.

$$\dot{\epsilon} = A \left( \frac{\sigma^n}{d^p} \right) \exp \left( - \frac{Q}{RT} \right) \quad (1)$$

Here,  $\dot{\epsilon}$  is the strain rate,  $d$  the grain size,  $\sigma$  the applied stress,  $A$  a constant of proportionality determined by the slowest diffusive species along the fastest diffusion path,  $Q$  the activation energy,  $R$  the gas constant, and  $T$  the absolute temperature. To obtain  $n$ , stress-step testing was used to evaluate the steady-state strain rate at different stresses (at constant temperature and grain size). To evaluate  $p$ , the as-hot-pressed materials were annealed at 1450° and 1500°C for different times, to obtain a range of grain sizes for each composition; the samples were then tested at 1275°C, under a constant tensile loading of 50 MPa, until rupture.

Two distinct approaches were adopted to assess the dependence of creep resistance on the grain-boundary dopant concentration. In the first case, samples of the different dopant compositions were annealed to the same average grain size ( $2.4 \pm 0.2 \mu\text{m}$ ), and stress-rupture tests were conducted at 1275°C, under an applied stress of 50 MPa. In the second case, the creep behavior of samples with different grain sizes and dopant levels was normalized to the same grain size, using an experimentally determined value of  $p$ .

### (3) Microstructure Analysis and Compositional Mapping

The microstructures of samples both before and after creep testing were evaluated by polishing each sample to a 1  $\mu\text{m}$  diamond finish and thermally etching at 1400°C for 1 h. Grain size was determined from scanning electron micrographs, using the linear intercept method. The distribution of the neodymium dopant ions was characterized by both imaging secondary ion mass spectrometry (SIMS) (conducted at the University of Chicago) and analytical electron microscopy (AEM). Details of the SIMS procedure are given elsewhere.<sup>6</sup> In the case of the AEM, thin foils of both as-hot-pressed and deformed materials were prepared by standard techniques, including ultrasonic cutting, thinning, and dimpling, to a foil thickness of 120  $\mu\text{m}$ , followed by ion-beam milling to perforation. A thin layer of carbon was evaporated on the sample to eliminate charging. Compositional mapping of the dopant distribution was conducted on a dedicated scanning transmission electron microscope (STEM; Model 603, VG Microscopes, West Sussex, U.K.) operating at 300 keV, fitted with a windowless Si(Li) detector (Link Systems, Boston, MA). The probe size was of the order of 0.6 nm, yielding an areal resolution of  $\sim 1 \text{ nm}^2$ .

## III. Results

### (1) Microstructure and Neodymium Segregation Behavior

Scanning electron micrographs of the polished and thermally etched surfaces of the as-hot-pressed samples are shown in Fig. 1.

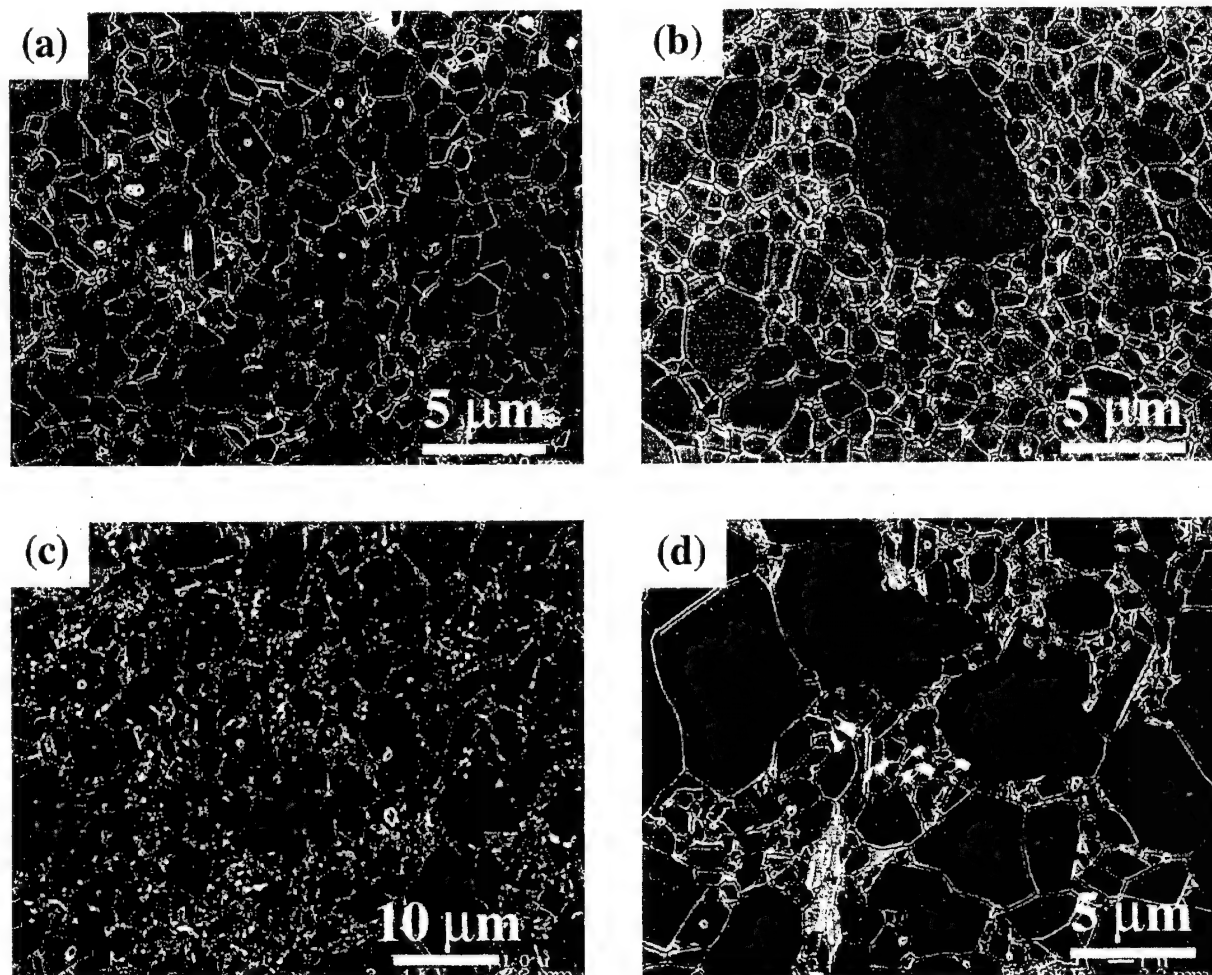


Fig. 1. SEM micrographs showing the microstructures of the as-hot-pressed neodymium-doped aluminas: (a) 100, (b) 350, and (c) and (d) 1000 ppm (arrows indicate secondary-phase precipitates).



The grains of the 100 ppm doped material are equiaxed and exhibit a uniform size distribution, with an average grain size of  $\sim 1.5 \mu\text{m}$  (see Fig. 1(a)). No second-phase precipitates were observed for this composition, either by scanning electron microscopy (SEM) or transmission electron microscopy (TEM). In contrast, neodymium-rich precipitates occasionally were observed at grain-boundary triple points in the 350 ppm neodymium-doped material. The grain structure also differed from the 100 ppm sample in that, interspersed in a background of fine ( $d \approx 1.5 \mu\text{m}$ ) grains, were larger grains up to  $10 \mu\text{m}$  in size (Fig. 1(b)). From the micrographs, it was estimated that the large abnormal grains made up  $\sim 3\%$  (by volume) of the structure. The microstructure of the 1000 ppm doped material was the most inhomogeneous of the three compositions, exhibiting essentially a bimodal grain-size distribution, with clusters of fine- and coarse-grain-size regions. For this dopant level, numerous second-phase particles were visible, preferentially situated in the fine-grain-size regions (Figs. 1(c) and (d)).

Figure 2 shows SIMS maps of the neodymium distribution in the as-hot-pressed materials; the regions of brighter contrast correspond to a locally higher neodymium content. As shown in the maps,  $\text{Nd}^{3+}$  ions are strongly segregated to the grain boundaries. The marked segregation behavior, even at the 100 ppm dopant level, confirms the very low solubility of neodymium in the  $\text{Al}_2\text{O}_3$  lattice.

TEM observation revealed that the microstructures of the crept materials were characterized by an occasional dislocation array and two distinct forms of cavity (Fig. 3 and Fig. 4). The first type of cavity consisted of intragranular pores, which often exhibited a

faceted morphology (Figs. 3(a) and 4(a)). Comparison of the deformed and undeformed materials established that these intragranular pores were residual pores following densification. The other type of cavity tended to be triangular in shape and located primarily at grain-boundary triple junctions (Fig. 3(b)). For the 1000 ppm sample (which essentially exhibited a bimodal grain size), these cavities occurred preferentially at the interface between large abnormal grains and surrounding small grains.

Similar cavitation features also have been reported by Chokshi and Porter<sup>13</sup> in crept  $\text{Al}_2\text{O}_3$  codoped with 250 ppm MgO and 250 ppm  $\text{ZrO}_2$  and possessing a bimodal grain-size distribution. A theoretical explanation for this cavitation phenomenon has been developed by Dalglish *et al.*<sup>14</sup> and Chokshi and Porter,<sup>13</sup> predicting a localized doubling of the effective stress at the coarse-grained clusters, therefore inducing cavitations in these regions. Dedicated STEM analysis of dopant distribution confirmed the SIMS findings, namely that neodymium is mainly segregated to grain boundaries (see Fig. 5). However, no evidence was obtained for the segregation of neodymium ions to dislocation cores.

## (2) Creep Behavior

The stress-rupture tests revealed that, independent of dopant level, the general features of the creep-deformation behavior were similar, with well-defined primary, steady-state, and tertiary deformation stages. Typically, the creep-rupture strain was  $\sim 15\%$  for the 100 ppm doped material,  $\sim 8\%$  for the 350 ppm doped material, and  $\sim 3\%$  for the 1000 ppm doped material.

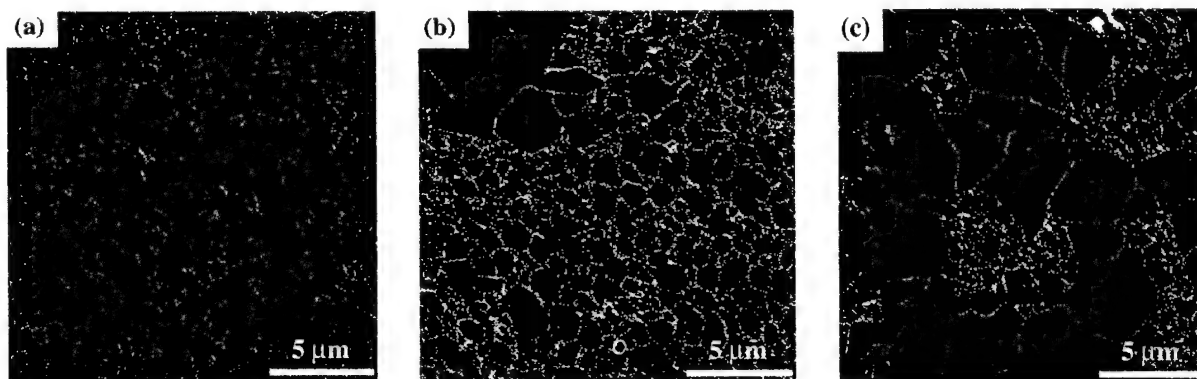


Fig. 2. SIMS map showing the neodymium distribution in the as-hot-pressed materials: (a) 100, (b) 350, and (c) 1000 ppm.

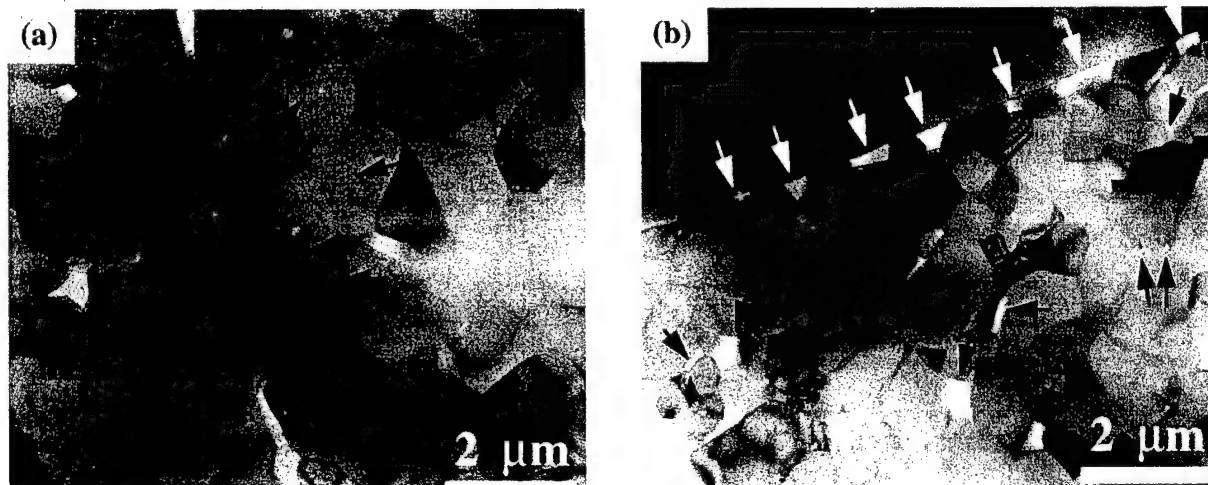


Fig. 3. TEM micrographs of the 350 ppm neodymium-doped material deformed at  $1200^{\circ}$ – $1350^{\circ}\text{C}$  and a stress of 50 MPa, for an accumulated strain of  $\sim 7\%$ : (a) residual intragranular pores (indicated by arrows), (b) deformation-induced cavities within fine-grain-size regions (black arrows) and at the boundary between coarse and fine-grain-size clusters (white arrows).

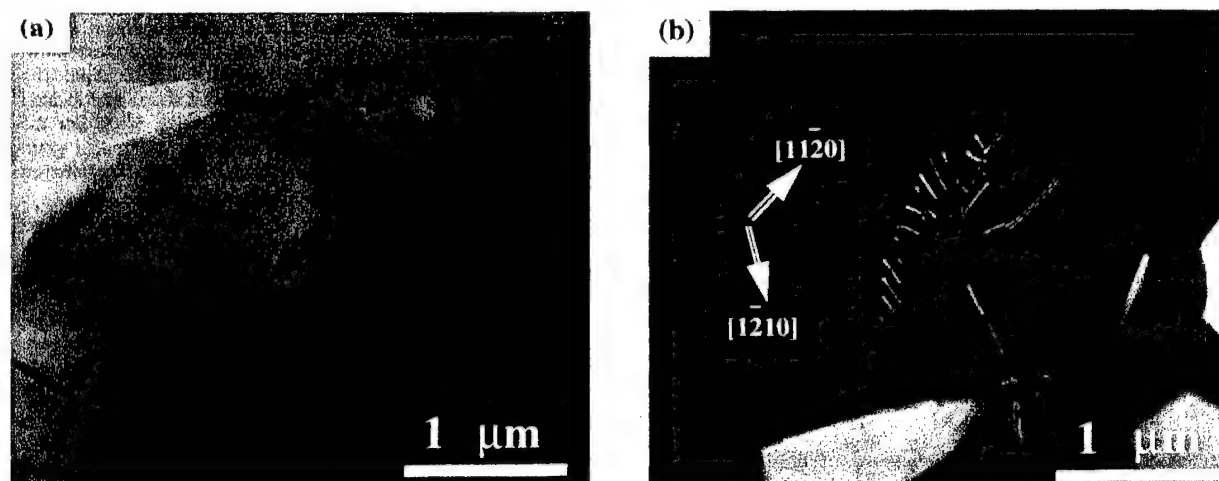


Fig. 4. TEM micrographs showing (a) faceting of the residual intragranular pores (indicated by arrows) and (b) dislocation arrays, which have a Burgers vector of  $1/3\langle 110 \rangle$ .

The strain-rate data (at a constant tensile stress of 50 MPa) for the doped compositions are shown in Fig. 6; corresponding data for undoped  $\text{Al}_2\text{O}_3$ <sup>4</sup> are included, for reference. The apparent activation energy for tensile creep was derived from the slope of the curves and is plotted, as a function of dopant concentration, in Fig. 7. For comparison, values of the activation energy obtained by densification experiments on the same powder compositions are also plotted. (These latter experiments will be discussed in more detail in a separate paper.) Reasonable agreement exists between the two sets of data, and both sets suggest a trend whereby the activation energy first increases as the neodymium content increases and then saturates at a neodymium-dopant level of  $\sim 350$ – $400$  ppm.

The effect of the stress on the steady-state strain rate is shown in Fig. 8(a); the values of the stress exponent,  $n$ , were determined to be 2.1, 1.8, and 2.4 for the 100, 350, and 1000 ppm doped compositions, respectively. Hence, for the range of stress tested (20–75 MPa), the stress exponent is  $\sim 2$  for all three dopant concentrations. This result is consistent with studies on other dopant systems obtained by the present group<sup>2,4,7,15</sup> and with work on undoped  $\text{Al}_2\text{O}_3$  by Robertson *et al.*<sup>8</sup> As described earlier, the

grain-size exponent,  $p$ , was determined by creep testing samples of different starting grain sizes at constant stress (50 MPa) and temperature (1275°C). Unfortunately, in the case of the 1000 ppm sample, annealing treatments did not provide a sufficient increase in the average grain size to enable the evaluation of  $p$ . However, for the 100 and 350 ppm doped samples, the values of  $p$  were 3.4 and 3.7, respectively (Fig. 8(b)).

In evaluating  $p$ , we used the average grain size, acquired by the linear-intercept method. In the 350 ppm neodymium-doped  $\text{Al}_2\text{O}_3$  sample, some grains had a rather large grain size ( $>10$  μm). Consequently, the validity of the linear-intercept method for obtaining the average grain size and, therefore, the grain-size exponent,  $p$ , is questionable in the present context. However, a compilation of the grain-size distributions for the 350 ppm neodymium-doped sample (Fig. 9) revealed that these outliers in the distribution comprise  $<3$  vol% and are spatially isolated in the system. Thus, this small proportion of large grains is not expected to influence the strain rate of the material significantly. Detailed discussion of the effect of grain-size distribution on the creep strain rate will be discussed in a separate paper.

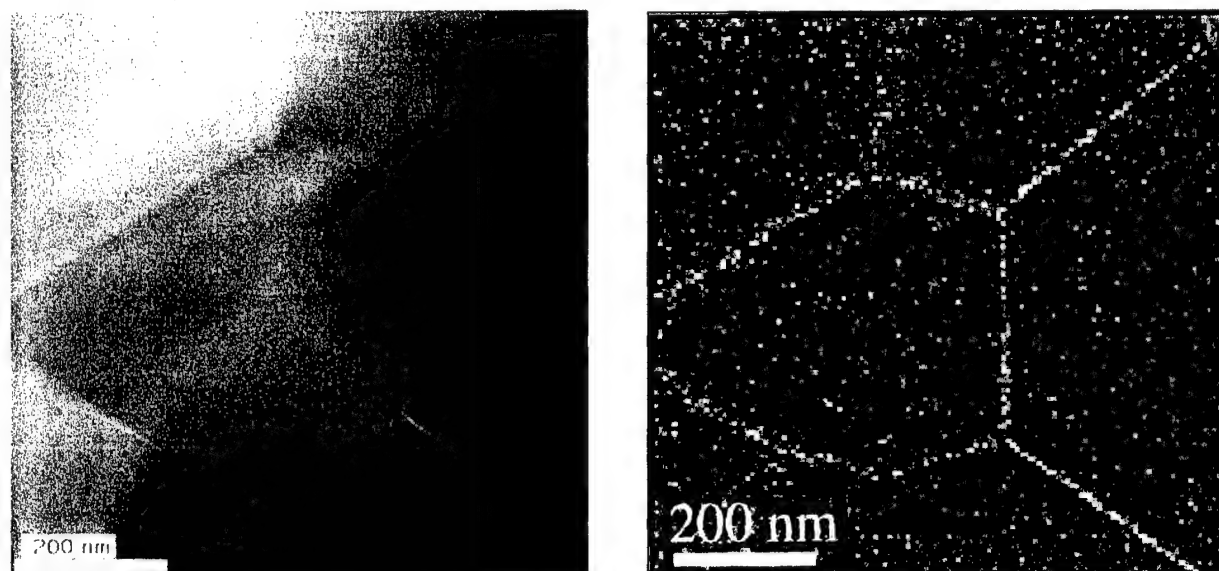


Fig. 5. (a) Annular-aperture dark-field STEM image and (b) energy-dispersive X-ray analysis map of neodymium distribution.

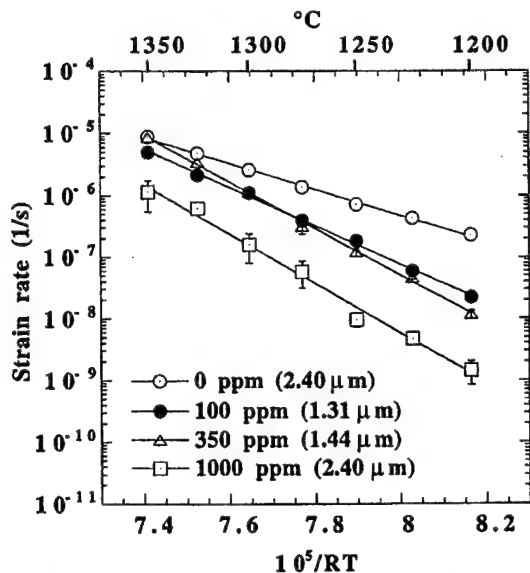


Fig. 6. Strain rate, as a function of temperature, for different neodymium dopant levels (50 MPa applied stress).

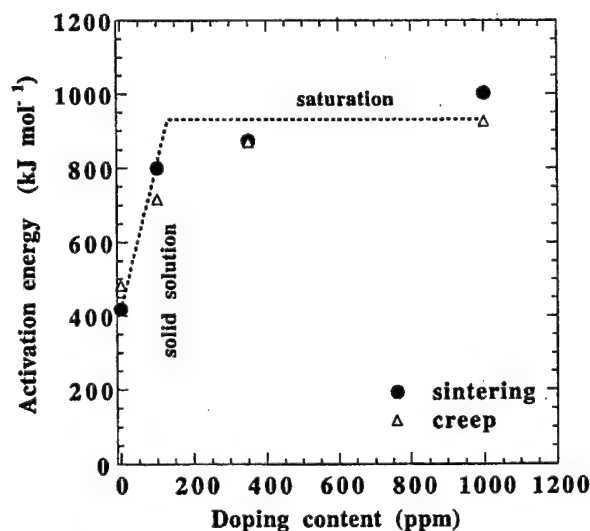


Fig. 7. Apparent activation energy (measured by both creep and sintering experiments), as a function of neodymium-doping content.

The effect of neodymium-dopant concentration on the creep behavior was evaluated by two distinct methods. Figure 10 shows the results of one of these approaches, in which creep data for the as-hot-pressed 100 and 350 ppm samples were corrected to the grain size of the 1000 ppm sample, using the  $p$  values determined previously. Under this approach, the creep data of the doped materials form a band that is distinct from that of the undoped  $\text{Al}_2\text{O}_3$ . Closer observation also reveals that the slope of the creep curves for the doped compositions reflect the difference in activation energy discussed earlier; hence, there is a crossover in the behavior at  $\sim 1275^\circ\text{C}$ . Thus, depending on the creep temperature, the higher dopant level may be more or less beneficial, in terms of the strain rate.

In the second approach, the steady-state strain rate was compared for samples of different dopant compositions that had been annealed to achieve similar average grain sizes ( $2.4 \pm 0.2 \mu\text{m}$ ). Figure 11 shows that the degree of improvement in creep resistance is essentially independent of dopant composition. However,

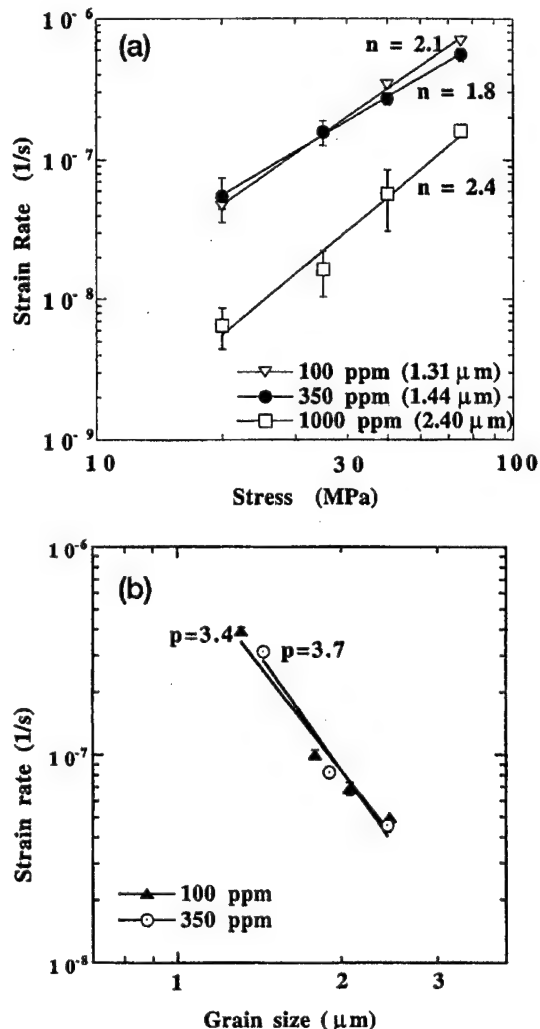


Fig. 8. Strain rate as a function of (a) stress (tested at  $1275^\circ\text{C}$ ) and (b) grain size (50 MPa,  $1275^\circ\text{C}$ ).

(coincidentally) the conditions tested (50 MPa,  $1275^\circ\text{C}$ ) correspond to the region of the "crossover" of the strain-rate curves (see Fig. 10); hence, any dispersion in the strain rates is minimized. Nonetheless, the two sets of data are entirely consistent, and, taken as a whole, they show that the neodymium-dopant concentration (over the range 100–1000 ppm) does not have a strong effect on the degree of creep inhibition.

#### IV. Discussion

The present work demonstrates that singly doping  $\text{Al}_2\text{O}_3$  with neodymium lowers the tensile creep rate by 2–3 orders of magnitude. Thus, the influence of neodymium is consistent with that of yttrium and lanthanum,<sup>4</sup> a result not altogether unexpected, given that the ionic radius of neodymium (0.98 Å) is intermediate between those of yttrium (0.90 Å) and lanthanum (1.03 Å). However, the present study was the first in which the neodymium-dopant concentration was systematically studied. The results show that the creep behavior, when normalized to account for grain size, is practically independent of the neodymium content. Because the dopant levels studied spanned the solubility limit, this finding confirms that the creep inhibition mechanism is primarily a solid-solution effect. The relative insensitivity of the creep behavior to dopant concentration is interesting and would seem to point

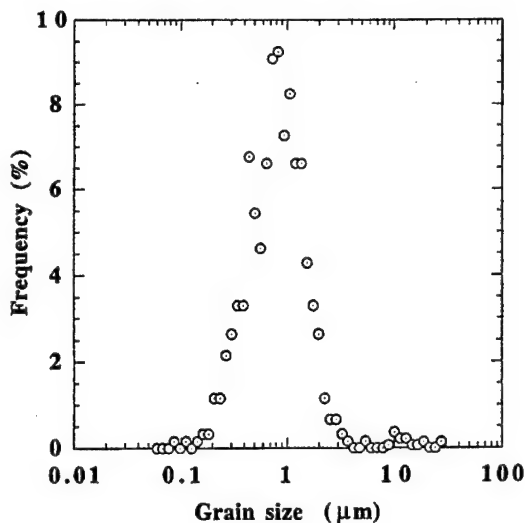


Fig. 9. Grain-size distribution of 350 ppm neodymium-doped  $\text{Al}_2\text{O}_3$  (as-hot-pressed).

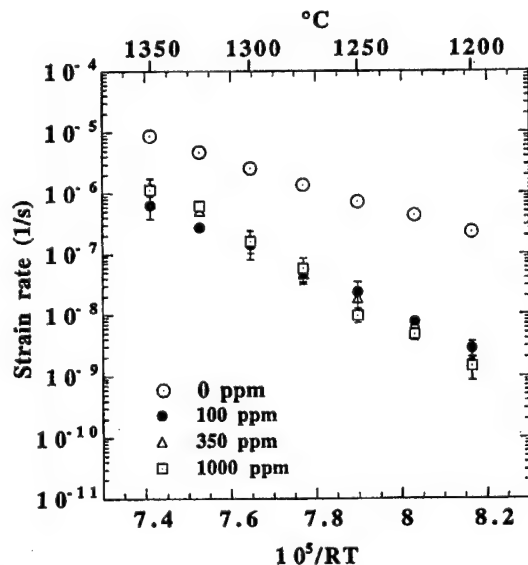


Fig. 10. Strain rate as a function of temperature (50 MPa applied stress). For all compositions, data were normalized to a grain size of  $2.4 \mu\text{m}$ , according to the measured grain-size exponent.

to a saturation of  $\text{Nd}^{3+}$  ions at the grain boundary, and, hence, an upper limit to their effectiveness as obstacles to grain-boundary diffusion. However, the situation is more complex, because the present study also shows that the apparent activation energy (derived from both creep and densification experiments) increases as the dopant level increases.

One could speculate that the increase in the overall neodymium content correlates with an increase in the grain-boundary concentration and that interaction between the neodymium-occupied sites causes an initial increase in the activation energy. However, at the grain-boundary saturation level, no further increases would occur. Evidence to support this general picture is provided by ongoing AEM and extended X-ray absorption fine-structure studies,<sup>16,17</sup> which suggest that the local atomic environment of grain-boundary-segregated yttrium ions changes with yttrium concentration.

Similarly, in the  $\text{Al}_2\text{O}_3$ - $\text{ZrO}_2$  composite system, Wang and Raj<sup>18</sup> found that the apparent activation energy of  $\text{Al}_2\text{O}_3$  during

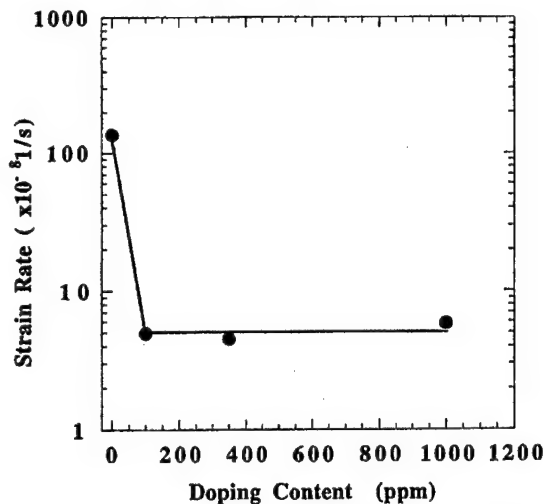


Fig. 11. Strain rate as a function of  $\text{Nd}_2\text{O}_3$ -doping level (50 MPa at  $1275^\circ\text{C}$ ). All samples were preannealed to achieve a grain size of  $2.4 \pm 0.2 \mu\text{m}$ .

sintering increased initially as the  $\text{ZrO}_2$  content increased (up to 5 vol% of  $\text{ZrO}_2$ ), after which the apparent activation energy reached a saturation value. However, the trend of increasing activation energy with dopant level is in contrast to the results of Cho,<sup>15</sup> who reported that, in the case of lanthanum doping, the activation energies for 100 and 500 ppm samples were approximately the same (776 and 800 kJ/mol, respectively). However, for yttrium-doped  $\text{Al}_2\text{O}_3$ , Cho observed that the activation energy was lower for a 1000 ppm doped sample than for a 100 ppm sample (685 versus 832 kJ/mol). The reasons for this discrepancy are not well understood.

As proposed earlier, site-blocking of rapid grain-boundary diffusive paths seems to be the most logical explanation for the observed creep inhibition. The evidence supporting this mechanism (versus, for example, interface control) has been discussed in a previous work.<sup>11</sup> One compelling argument is that, for the range of grain sizes and stress and temperature conditions studied, grain-boundary diffusion is widely accepted as the rate-controlling step for  $\text{Al}_2\text{O}_3$ .<sup>19</sup> Furthermore, densification studies on doped aluminas have confirmed that grain-boundary diffusion is rate-controlling,<sup>20</sup> and the present study has shown that the values of the activation energy determined from creep and densification experiments are very comparable. Finally, orientation-image-mapping (OIM) studies do not reveal a significant difference between either the grain-boundary misorientation distribution or the proportion of coincident-site-lattice (CSL) boundaries in neodymium-doped  $\text{Al}_2\text{O}_3$  versus undoped  $\text{Al}_2\text{O}_3$ .<sup>21</sup> This result rules out any possible role of the dopant ions in promoting particular boundaries with creep-resistant properties. However, the measured values of the grain size ( $p \approx 3-4$ ) and stress exponent ( $n \approx 2$ ), although once again consistent with previous results, cannot be reconciled with any generally accepted creep mechanism.<sup>19,22-24</sup>

In addition to its influence on the creep properties, the neodymium-dopant level also has a marked effect on the  $\text{Al}_2\text{O}_3$  grain structure. The present study shows that neodymium concentrations in excess of the solubility limit result in an increased tendency for abnormal grain growth. This phenomenon is not processing-related, but rather a result of the effect of grain-boundary solute levels on the grain-boundary mobility. Recent STEM and grain-growth studies suggest that the onset of abnormal grain growth corresponds to a supersaturation of the solute at the  $\text{Al}_2\text{O}_3$  grain boundary; these results are reported in a separate paper.<sup>25</sup>

## V. Conclusions

Doping  $\text{Al}_2\text{O}_3$  with 100 ppm  $\text{Nd}_2\text{O}_3$  (which is below the solubility limit) reduces the tensile creep rate by 2–3 orders of magnitude. Dopant levels in excess of the solubility limit (350 and 1000 ppm) do not result in further substantial improvements in the creep, thus confirming that the beneficial influence of neodymium is primarily a solid-solution effect. The apparent creep activation energy increases with neodymium content and then saturates at  $\sim 950$  kJ/mol for neodymium concentrations greater than the solubility limit. This trend is confirmed by activation energies derived from sintering experiments. The increase in activation energy (relative to that of undoped  $\text{Al}_2\text{O}_3$ ) is probably attributable to site-blocking by the oversized  $\text{Nd}^{3+}$  ions, which segregate to the  $\text{Al}_2\text{O}_3$  grain boundaries. It is tentatively suggested that the saturation in the activation energy subsequent to increasing the neodymium concentration corresponds to a greater likelihood of interaction between adjacent neodymium-occupied sites.

Given that the present grain structures were markedly less homogeneous in the case of the 350 and 1000 ppm dopant concentrations, the saturation in the creep benefit suggests an optimum dopant level at which the grain-boundary dopant concentration just exceeds the solubility limit. The results of the present study are completely consistent with creep studies conducted on other rare-earth dopant systems (yttrium and lanthanum) and, once more, suggest a site-blocking mechanism whereby the oversized dopant ions impede grain-boundary diffusion.

## Acknowledgments

The authors are grateful to R. Krause, National Institute of Standards and Technology, for his assistance with hot-pressing of the materials and for helpful suggestions regarding improved accuracy in acquiring the creep data. We also wish to thank G. Thompson for assistance in determining the grain-size distribution and J. M. Chabala, K. L. Gavrilov, and R. Levi-Setti, University of Chicago, for conducting the SIMS characterizations. This work was monitored by Dr. A. Pechenik.

## References

- <sup>1</sup>S. Lartigue, C. Carry, and L. Priester, "Grain Boundaries in High Temperature Deformation of Yttria and Magnesia Co-Doped Alumina," *J. Phys. (Paris)*, **C1-51**, 985–90 (1990).
- <sup>2</sup>J. D. French, J. Zhao, M. P. Harmer, H. M. Chan, and G. A. Miller, "Creep of Duplex Microstructure," *J. Am. Ceram. Soc.*, **77**, 2857–65 (1994).
- <sup>3</sup>S. Korinek and F. Dupau, "Grain Boundary Behavior in Superplastic Mg-Doped Alumina with Yttria Co-doping," *Acta Metall. Mater.*, **42**, 293–302 (1994).
- <sup>4</sup>J. Cho, M. P. Harmer, H. M. Chan, J. M. Rickman, and A. M. Thompson, "Effect of Yttrium and Lanthanum on the Tensile Creep Behavior of Aluminum Oxide," *J. Am. Ceram. Soc.*, **80**, 1013–17 (1997).
- <sup>5</sup>A. M. Thompson, H. M. Chan, and M. P. Harmer, "Tensile Creep of Alumina-Silicon Carbide Nanocomposites," *J. Am. Ceram. Soc.*, **80**, 2221–28 (1997).
- <sup>6</sup>A. M. Thompson, K. K. Soni, H. M. Chan, M. P. Harmer, D. B. Williams, J. M. Chabala, and R. L. Setti, "Dopant Distribution in Rare-Earth-Doped Alumina," *J. Am. Ceram. Soc.*, **80**, 373–76 (1997).
- <sup>7</sup>Y. Z. Li, C. M. Wang, H. M. Chan, J. M. Rickman, M. P. Harmer, J. M. Chabala, K. L. Gavrilov, and R. Levi-Setti, "Codoping of Alumina to Enhance Creep," *J. Am. Ceram. Soc.*, **82**, 1497–504 (1999).
- <sup>8</sup>A. J. Robertson, D. S. Wilkinson, and C. H. Caceres, "Creep and Creep Fracture in Hot-Pressed Alumina," *J. Am. Ceram. Soc.*, **74**, 915–20 (1991).
- <sup>9</sup>F. Wakai, T. Nagano, and T. Iga, "Hardening in Creep of Alumina by Zirconium Segregation at the Grain Boundary," *J. Am. Ceram. Soc.*, **80**, 2361–66 (1997).
- <sup>10</sup>F. Wakai, T. Iga, and T. Nagano, "Effect of Dispersion of  $\text{ZrO}_2$  Particles on Creep of Fine-Grained Alumina," *J. Ceram. Soc. Jpn.*, **96**, 1206–209 (1988).
- <sup>11</sup>J. Cho, C. M. Wang, H. M. Chan, M. P. Harmer, and J. M. Rickman, "Role of Segregation Dopants on the Improved Creep Resistance of Aluminum Oxide," *Acta Mater.*, **47**, 4197–207 (1999).
- <sup>12</sup>J. D. French and S. M. Wiederhorn, "Tensile Specimens from Ceramic Composites," *J. Am. Ceram. Soc.*, **79**, 550–52 (1996).
- <sup>13</sup>A. H. Chokshi and J. R. Porter, "Cavity Development during Creep Deformation in Alumina with a Bimodal Grain Size Distribution," *J. Am. Ceram. Soc.*, **70**, 197–202 (1987).
- <sup>14</sup>B. J. Dalgleish, S. M. Johnson, and A. G. Evans, "High-Temperature Failure of Polycrystalline Alumina: I, Crack Nucleation," *J. Am. Ceram. Soc.*, **67**, 741–50 (1984).
- <sup>15</sup>J. Cho, "Role of Rare-Earth Dopant on the Improved Creep Properties of Aluminum Oxide," Ph.D. Thesis, Lehigh University, Bethlehem, PA, 1998.
- <sup>16</sup>C. M. Wang, G. S. Cargill III, M. P. Harmer, H. M. Chan, and J. Cho, "Atomic Structural Environment around Grain Boundary Segregated Y and Zr in Creep Resistant Alumina," *Acta Mater.*, **47**, 3411–22 (1999).
- <sup>17</sup>C. M. Wang, G. S. Cargill III, H. M. Chan, and M. P. Harmer, "Structural Features of Y-Saturated and Supersaturated Grain Boundaries in Alumina," *Acta Mater.*, **48**, 2579–91 (2000).
- <sup>18</sup>J. Wang and R. Raj, "Activation Energy for the Sintering of Two-Phase Alumina/Zirconia Ceramics," *J. Am. Ceram. Soc.*, **74**, 1959–63 (1991).
- <sup>19</sup>R. M. Cannon and R. L. Coble, "Review of Diffusional Creep of  $\text{Al}_2\text{O}_3$ ," pp. 61–100 in *Deformation of Ceramic Materials*. Edited by R. C. Bradt and R. E. Tressler. Plenum Press, New York, 1975.
- <sup>20</sup>J. Fang, A. M. Thompson, M. P. Harmer, and H. M. Chan, "Effect of Yttrium and Lanthanum on the Sintering Behavior of Ultra-High-Purity  $\text{Al}_2\text{O}_3$ ," *J. Am. Ceram. Soc.*, **80**, 2005–12 (1997).
- <sup>21</sup>J. Cho, C. M. Wang, H. M. Chan, M. P. Harmer, and J. M. Rickman, "A Study of Grain Boundary Structure in Rare-Earth-Doped Alumina Using the EBKD Technique," submitted to *J. Mater. Sci.*
- <sup>22</sup>P. A. Lessing and R. S. Gordon, "Creep of Polycrystalline Alumina, Pure and Doped with Transition Metal Impurities," *J. Mater. Sci.*, **12**, 2291–302 (1977).
- <sup>23</sup>F. R. N. Nabarro, "Deformation of Crystals by Motion of Single Ions," p. 231 in *Report of a Conference on the Strength of Solids*. Physical Society, London, U.K., 1948.
- <sup>24</sup>C. Herring, "Diffusional Viscosity of a Polycrystalline Solid," *J. Appl. Phys.*, **21**, 437–41 (1950).
- <sup>25</sup>C. M. Wang, H. M. Chan, M. P. Harmer, and J. M. Rickman; unpublished research. □

### **3. AWARDS, HONORS, AND PATENTS**



### **3. AWARDS, HONONRS, AND PATENTS**

#### **3.1 Awards**

American Ceramic Society's Roland B. Snow award for "Best of Show" in national ceramographic contest (1999, 2000).

Martin P. Harmer, 2004 Hillman Faculty Award from Lehigh University for excellence in teaching and research and for doing the most to advance the interests of the university.

#### **4. PERSONNEL**

#### **4. PERSONNEL**

Dr. Martin P. Harmer, Principal Investigator

Dr. Helen M. Chan, Co-Principal Investigator

Dr. Jeffrey M. Rickman, Co-Principal Investigator

##### **Research Associates/Assistants:**

Michael Drahus

Kwame Bedu-Anissah